NEW FUNCTIONAL POLYMERS FOR SENSORS, SMART MATERIALS AND SOLAR CELLS

by
JOSE MIGUEL LOBEZ COMERAS

Lic. Chemistry (Premio Extraordinario / Premio Nacional – Mención Especial)
Universidad de Zaragoza (2006)

Submitted to the Department of Chemistry
in Partial Fulfillment of the Requirements for the Degree of

DOCTOR OF PHILOSOPHY IN CHEMISTRY
AT
THE MASSACHUSETTS INSTITUTE OF TECHNOLOGY

June 2012

v. 1

Signature of Author _____
Department of Chemistry
April 17, 2012

Certified by _____
Timothy M. Swager
John D. MacArthur Professor of Chemistry
Thesis Supervisor

Accepted by _____
Robert W. Field
Haslam and Dewey Professor of Chemistry
Chairman, Departmental Committee on Graduate Students

This doctoral thesis has been examined by a Committee of the Department of Chemistry as follows:

Prof. Stephen L. Buchwald _____
Department of Chemistry
Chairman

Prof. Timothy M. Swager _____
Department of Chemistry
Thesis Supervisor

Prof. Paula T. Hammond _____
Department of Chemical Engineering
Committee Member

Dedicated to My Family

NEW FUNCTIONAL POLYMERS FOR SENSORS, SMART MATERIALS AND SOLAR CELLS

by

JOSE MIGUEL LOBEZ COMERAS

Submitted to the Department of Chemistry on April 30, 2012
in Partial Fulfillment of the Requirements for the Degree of
Doctor of Philosophy in Chemistry

ABSTRACT

Organic polymers can be used as the active component of sensors, smart materials, chemical-delivery systems and the active layer of solar cells. The rational design and modification of the chemical structure of polymers has enabled control over their properties and morphology, leading to the advancement of nanotechnology. A deeper understanding of structure-property relationships, as described in this thesis, affords control over the nanostructure of devices made from these macromolecular materials, which is crucial to the optimization of their performance.

In Chapter 1, a new sensor for ionizing radiation based on composites of electron beam lithography resists, poly (olefin sulfone)s (POSs), and multiwalled carbon nanotubes is presented. The polymeric active component is radiation labile and its degradation after a sensing event leads to morphological and electrical changes in the composite at the nanoscale. As a result, a signal can be detected. Systematic sensitivity improvements can be accomplished by rational modifications of the chemical structure of the polymer side-chains. Orthogonal post-polymerization modifications performed using "click" chemistry, incorporate functional groups capable of increasing either the homogeneity of the composite, or its opacity towards radiation.

In Chapter 2, a smart hybrid polymer composed of a POS and a silicone linked by "click" chemistry is described. By tuning the chemical structure of these two components and varying their ratio, composites with different mechanical properties and hardness can be achieved. This elastomeric smart material exhibits switchable mechanical properties: exposure to mild bases triggers disassembly into its monomers and individual constituents.

In Chapter 3, the design, synthesis and properties of new polymer surfactant additives for photovoltaic devices is shown. The AB alternating regioregular polythiophene copolymer additives are obtained via a combinatorial approach, and contain functional groups in every other repeat unit. In Chapter 4 incorporation of small amounts of these polymer additives (0.25 weight %) is shown to result in large increases of up to 30% in the power conversion efficiency of organic solar cells consisting primarily of the benchmark system of poly (3-hexylthiophene) and Phenyl-C_{61}-butyric acid methyl ester (PCBM) as the active layer. This effect is mainly due to the presence of dipoles at the interface of the bulk heterojunction introduced by the additives, which prevent charge recombination and lead to increases in the photocurrent collected across the polymer-fullerene interface.

In Chapter 5, the synthesis of liquid crystalline polymer brushes is described, and their supramolecular and self-assembly properties are studied. The solid-state ordering and alignment

properties of these highly substituted polymers can be affected by chemically tuning their mesogenic oligomeric side-chains, the length of the polymer backbone and the degree of cross-linking. The morphologies obtained with these macromolecules are interesting from the point of view of future photovoltaic applications.

Thesis Supervisor: Timothy M. Swager
Title: John D. MacArthur Professor of Chemistry

TABLE OF CONTENTS

LIST OF FIGURES

CHAPTER 1

CHAPTER 2

CHAPTER 3

LIST OF TABLES

LIST OF SCHEMES

CHAPTER 4

CHAPTER 5

CHAPTER 1

Sensing Ionizing Radiation with Poly (Olefin Sulfone) / Carbon Nanotube Composites

Adapted and reprinted in part with permission from:

Lobez, J. M.; Swager, T. M. "Radiation Detection: Resistivity Responses in Functional Poly (Olefin Sulfone)/Carbon Nanotube Composites" *Angew. Chem. Int. Ed.* **2010**, *49*, 95-98

1.1 Introduction

Ionizing radiation is radiation capable of ejecting an electron from an atom upon interaction with matter. There are several types of ionizing radiation and they differ from each other depending on the mass or lack thereof, and on their charge or lack thereof (see Table 1.1 for a summary of the main types of ionizing radiation).[1] The degree of ionization, and the mechanisms by which ionization occurs are highly dependant on the nature of the ionizing radiation, and the composition of the matter being irradiated. For instance, charged radiation will tend to induce a higher degree of ionization as these charges interact strongly with the electrons to be ejected, and matter composed of heavier elements tends to interact more with high energy photons, as each atom contains more electrons.

Radiation	Type	Charge	Energy range	Penetration	Effect
alpha (α)	He^{2+}	+	3-7 MeV	Low	Highly Ionizing
beta (β)	e	+ or -	0-3 MeV (continuous)	Medium	Medium Ionizing
X-Ray*	$h\nu$	No	0.12-12keV	High	Ionizing
gamma (γ)*	$h\nu$	No	>100keV	Very High	Ionizing
neutron	n	No	0.025 eV (thermal) - MeV (fast)	High	Ionizing

Table 1.1. Summary of the main kinds of ionizing radiation and their properties. (*) More modern definitions distinguish X-Rays from γ-Rays not based on the energy, but depending on their origin: X-rays are originated from electrons, and γ-Rays are originated from nuclei

Sensing the presence of ionizing radiation[2] is crucial in several fields, including energy, national security, biological and nuclear research, and in environments where the levels of radiation are higher than average, such as in outer space. In all these situations, it becomes necessary not only to sense the presence of ionizing radiation, but also to quantify the cumulative dose of radiation absorbed over time using a dosimeter.[3] This is interesting from the point of view of personal protection, as well as monitoring materials attrition.

Dosimeter design usually involves a sensing event, in which the sensor undergoes an irreversible modification. This is the case for the most commonly used system for personal dosimetry of gamma radiation, which is based on the development of a photographic film. According to the Gurney-Mott model used to describe the interaction of a photographic film with ionizing radiation (Figure 1.1),[2b] after exposure to radiation and ionization, the film contains local densities of negative charge. This event is followed by migration of interstitial silver ions to compensate these charges, followed by reduction of the silver ions. The amount of silver metal (Ag^0) generated is proportional to the amount of radiation used for the exposure. In order to read the signal from this dosimeter, it is necessary to submit these photographic films to labs located off-site, so that the Ag^0 nuclei can be developed into larger domains in a controlled manner. Then, the remaining developed areas can be read with the bare eye. This system of analysis has been standardized, so that the size and number of the resulting stains remains proportional to the initial amount of radiation. The system has been perfected over time and is highly reliable, but has the disadvantage of the need for off-site development and reading, resulting in long waiting times to obtain a reading. This can be problematic from the point of view of personal dosimetry.

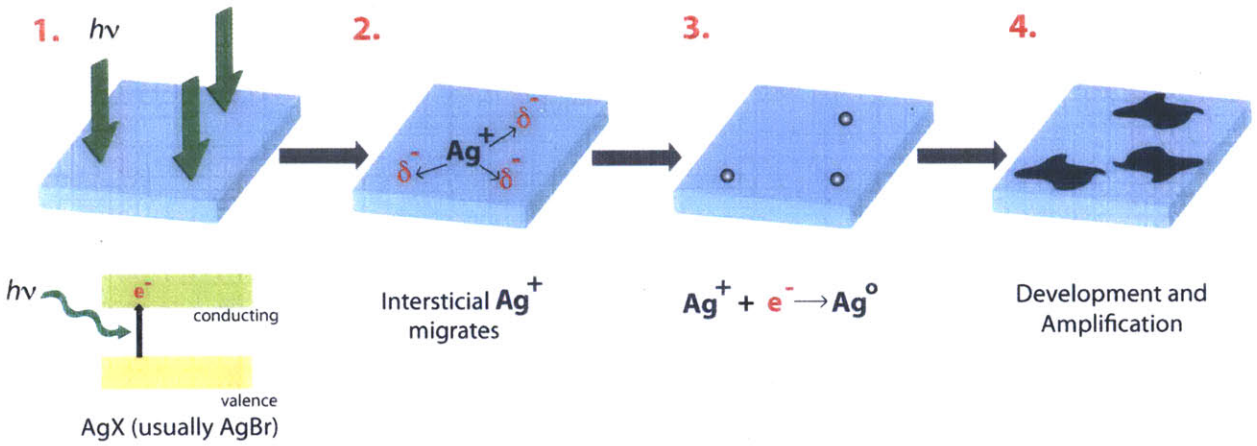

Figure 1.1. Gurney-Mott model explaining the basis of a photographic film radiation dosimeter. Step 4 and reading of the absorbed dose is performed off-site

In general, systems used for the detection and dosimetry of ionizing radiation usually have one or several of the following drawbacks: incapability to produce a real-time signal as is the case with the photographic film systems just described; expensive and/or complicated manufacturing like on CdZnTe based systems;[4] need for operation at low temperatures as most semiconductor based systems require;[5] low sensitivity to non-charged radiation which is particularly problematic for systems based on organic materials;[6] a voluminous size like the Geiger counter; relatively high fragility like for the case of smaller systems based in the ionization of a gas trapped inside a chamber. Although organic materials present the advantages of being easily processed, synthetic versatility, and relatively low cost, deployment of organic systems as small-size ionizing radiation sensors and dosimeters has been traditionally limited to the detection of charged particles, owing to the low cross sections for high energy photon absorption of the elements incorporated in these molecules.[7]

In this chapter, we report a new sensing scheme for gamma rays based on organic materials, in which the signal is not generated by scintillation or charge creation in a

semiconductor. The system herein described is based on the degradation of the radiation labile polymeric matrix of a composite film upon radiation exposure, which leads to large resistivity changes in a composite film. We also show how chemical design and tailoring of the side chains of this active polymer using an orthogonal post-polymerization modification can be used for the optimization of sensor performance, namely to influence the sensitivity of the resulting materials towards gamma radiation.

1.2 Sensing Scheme

The proposed sensor (Figure 1.2) is an irreversible sensor that could be used for dosimetry of high energy photons such as gamma rays, and the active component of this sensor is a thin composite film consisting of two elements:

1. A major component, which is a non-conducting polymeric matrix capable of degrading in the presence of radiation leading to depolymerization and generation of volatile monomers which can in turn escape from the film

2. A minor component, which is a semiconducting element with a high aspect ratio

In an initial state (left, Figure 1.2), the semiconducting component is dispersed in the non-conducting polymeric matrix above the percolation threshold, which means the composite has a high resistivity. Upon radiation exposure, the polymeric matrix degrades with unzipping polymeric chains transforming into volatile monomers, which can escape from the film. This leads to large changes in the morphology of the composite: the semiconducting elements that were previously dispersed in the matrix are no longer separated by the polymeric matrix, and will now come into contact (right, Figure 1.2). This means that new conduction pathways are

generated within the composite, leading to an increase in the conductivity. These changes in the film's resistivity can be detected by amperometry (measurement over time of the current intensity, **I**, between two electrodes at a constant potential **V**).

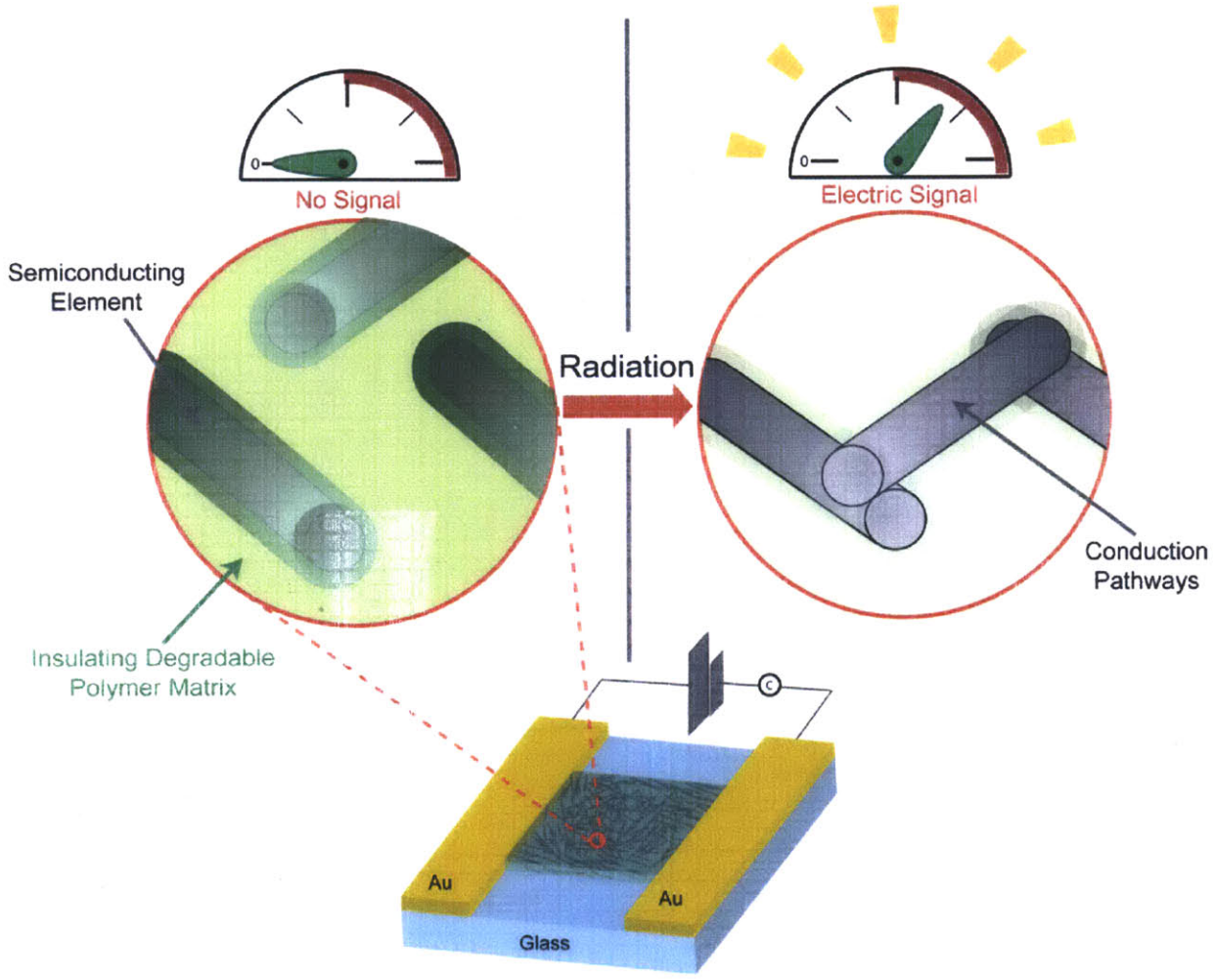

Figure 1.2. Proposed sensing scheme for gamma ray sensing. Radiation exposure leads to degradation of the polymeric matrix and to changes in the morphology of the active thin film, modifying the film conductivity. Conduction pathways are generated in this fashion. This irreversible modification can be detected by amperometry

For the aforementioned sensing scheme to work, the following requirements need to be met:

a) The polymer must degrade rapidly upon ionization

b) The semiconducting elements must have a large aspect ratio, so that small changes in the matrix morphology can lead to events where the semiconducting elements connect with each other

c) The initial homogeneity of the composite must be high. The semiconducting elements must be dispersed well in the polymeric matrix so that the initial state is above the percolation threshold

d) The system must be radiation opaque, in order to have a high radiation harvesting yield and to increase the probability of ionization and polymer degradation, which in turn increases the sensitivity

1.2.1 Polymeric Matrix: Poly (Olefin Sulfone)s

We have selected poly (olefin sulfone)s (**POSs**; Scheme 1.1) as our polymer matrix. POSs are sulfur dioxide (SO_2)/olefin copolymers, which have relatively low ceiling temperatures and degrade in the presence of ionizing radiation (high energy electrons,[8] gamma rays).[8,9] Due to this fact they are used as electron beam resists in electron beam lithography.[8,10]

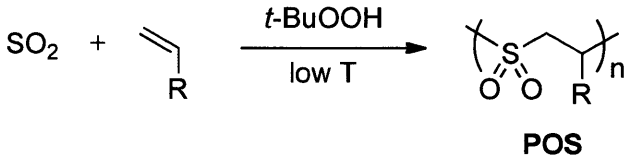

Scheme 1.1. Poly (olefin sulfone) (**POS**) synthesis

POSs were first reported in 1898, when Russian chemist Solonina first mixed liquid sulfur dioxide and an olefin in the presence of a radical initiator to obtain an unidentified white powder.[11] It was not until Staudinger developed his macromolecular theory that this initial white powder was correctly identified as a polymer.

Polymerization conditions usually involve low temperatures with a radical initiator such as *tert*-butyl hydroperoxide, and the solvent of choice is usually liquid sulfur dioxide.[12] The polymerization mechanism is that of a radical chain growth polymerization, in which the propagating species is an alternating electrophilic or nucleophilic radical (Scheme 1.2). Homopolymerization of sulfur dioxide is not favored, and homopolymerization of the olefin is prevented by running the reaction in an excess of sulfur dioxide, used as the solvent. For most olefin monomers of choice, the result is a 1:1 perfectly alternating copolymer of sulfur dioxide and olefin repeat units, as depicted in Scheme 1.1.[10b] This is true of most alkyl olefin monomers, whereas monomers that generate less nucleophilic radicals (such as styrene based monomers) tend to yield a lower ratio of incorporation of sulfur dioxide to olefin in the final polymer.

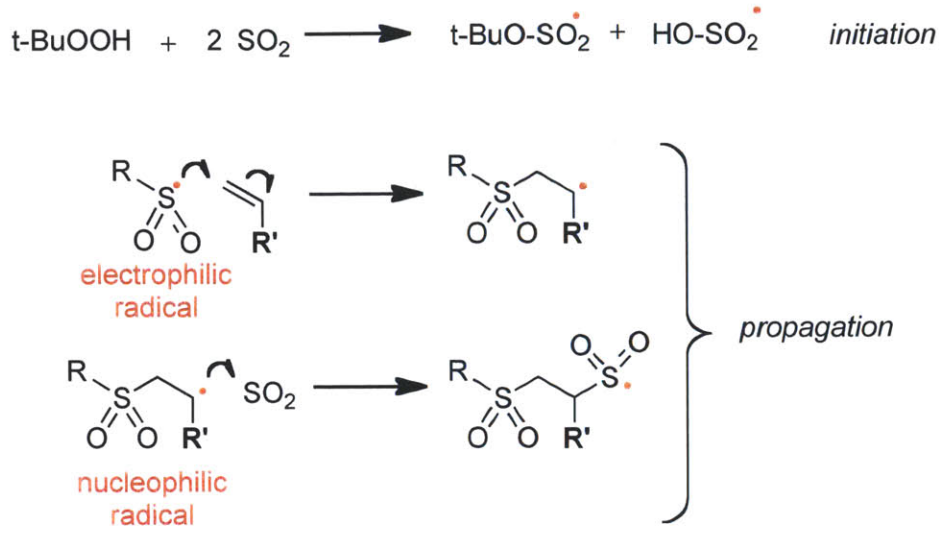

Scheme 1.2. Poly (olefin sulfone) polymerization mechanism. The propagating species is, alternatingly, an electrophilic radical and a nucleophilic radical

For the polymerization to take place in high yields and with a high degree of conversion, the monomer to be copolymerized with sulfur dioxide needs to meet the following requirements:[10b]

a) Exhibit good solubility in **SO_2**, the polymerization solvent

b) The unsaturation in the olefin must be electron rich, to favor reactivity with propagating electrophilic sulfur dioxide radicals

c) The unsaturation cannot be very sterically hindered

d) The olefin cannot bear any functional group incompatible with polymerization conditions. For instance, the olefin cannot have basic moieties (as sulfur dioxide is a strong Lewis acid) or any other chemical moiety capable of undergoing a side reaction with sulfur dioxide

POSs can be readily obtained in industrial scale and they exhibit good mechanical properties, which are tunable depending on the olefin of choice. However, they have not been more extensively deployed as commodity polymers due to their tendency to degrade under certain conditions (Scheme 1.3). Chain scission in the polymer backbone can occur when these polymers are exposed to ionizing radiation, bases or any other source of energy capable of cleaving the relatively weak carbon-sulfur bond in the backbone. Exposure to a single stimulus leads to a chain of events in which the whole polymer chain is decomposed, so this single interaction is amplified to generate large changes in the whole polymer chain.

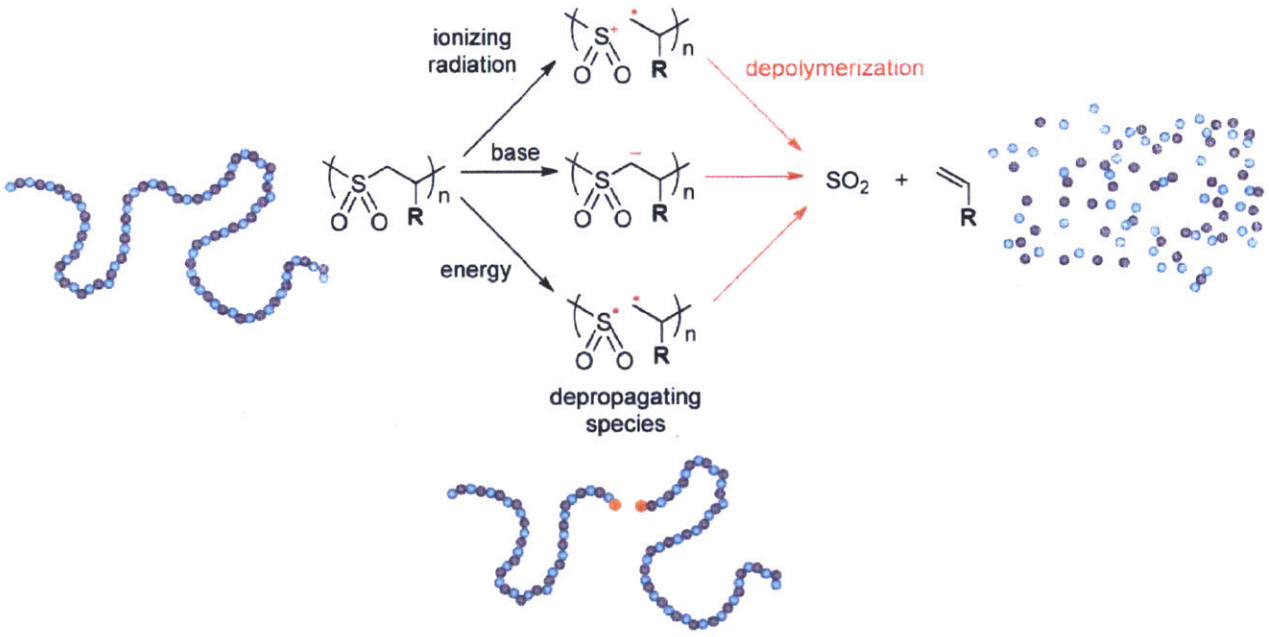

Scheme 1.3. Stimuli causing poly (olefin sulfone) degradation. C-S bond cleavage in the backbone leads to unzipping of the polymer chains, going back to volatile monomers

In the case of decomposition by ionizing radiation, irradiation induces chain-scission leaving behind a radical and cationic depropagating species. Depolymerization *via* the corresponding radical and cationic mechanisms occur,[13] releasing sulfur dioxide (**SO_2**) gas and a volatile olefin (Scheme 1.4).[12] Competing repolymerization reactions can be neglected if the depolymerization takes place in an open system. Owing to the high sensitivity to ionizing radiation and the capability of showing amplification upon exposure, **POSs** are the ideal candidates for the polymeric matrix in the proposed sensing scheme.

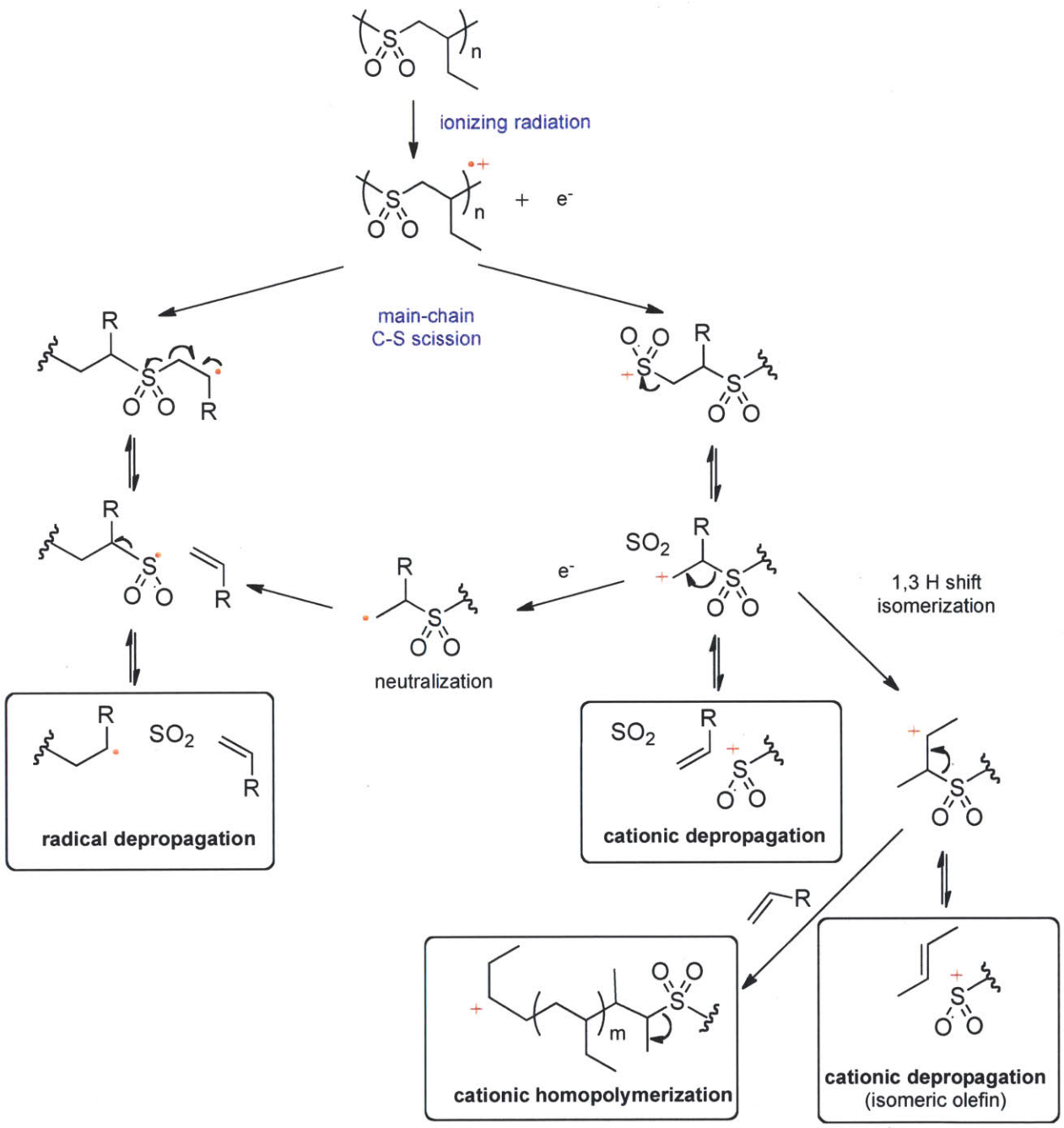

Scheme 1.4. Degradation of poly (olefin sulfone) by ionizing radiation. Chain-scission leads to depolymerization into volatile monomers following a radical and cationic depropagation mechanism

1.2.2 Semiconductor Elements: Carbon Nanotubes

Carbon nanotubes (**CNTs**)[14] are carbon based materials that show unique mechanical and electronic properties ranging from semiconducting to metallic depending on their molecular structure. These materials have become readily available in the recent years, which has enabled their modification and deposition for deployment as sensors, electrodes, supercapacitors, catalysts, filters and for organic electronic applications.[14b]

One of the main criteria used to classify **CNTs** is according to the number of graphitic layers they contain: when the **CNTs** only contain one layer, they are called single-walled carbon nanotubes (**SWCNTs**), and when they contain several layers, they are called multi-walled carbon nanotubes (**MWCNTs**). **SWCNTs** of extremely high purity and monodispersity can be readily obtained, and, depending on their molecular structure, their electric properties range from semiconducting to metallic. **MWCNTs** are by nature more polydisperse in size and number of layers, and they are only semiconducting. Owing to the larger degree of polydispersity, **MWCNTs** are easier to disperse in organic solvents and polymeric organic matrices.

One of the most important characteristics of carbon nanotubes is their large aspect ratio, due to which they can be considered one dimensional nanowires. It is worth noting that since these materials are carbon based, they are also relatively cheap and light. For these reasons, they were the material of choice as the semiconducting element in the proposed sensing scheme.

1.3 Proof of Principle: Ionizing Radiation Detection

In order to test these ideas, devices containing a thin film of a poly (1-hexene sulfone) (**P1HS**) and **MWCNTs** (Figure 1.3) were fabricated. Thin films of these composites were drop-

cast on an inert substrate (glass), and gold electrodes were deposited on top as described in the sensing scheme (Figure 1.2).

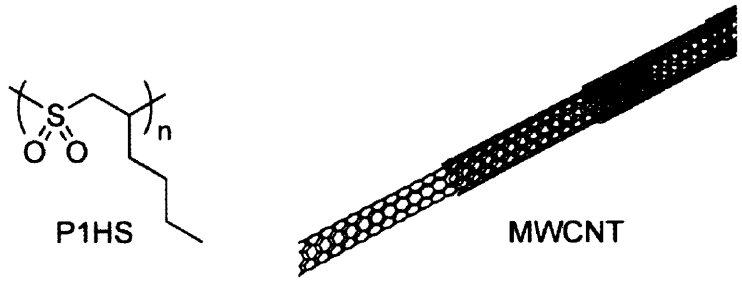

Figure 1.3. Structure of Poly (1-hexene sulfone) and schematic representation of **MWCNTs**

When the current measured under a constant potential of devices fabricated with different ratios of **P1HS** to **MWCNTs** was investigated, it was evidenced that increasing loadings of **P1HS** yielded lower conductivities for the composite films. This was expected, since a lower ratio of **MWCNTs** to **P1HS** means a higher degree of separation of the **MWCNTS** in the blend (Figure 1.4).

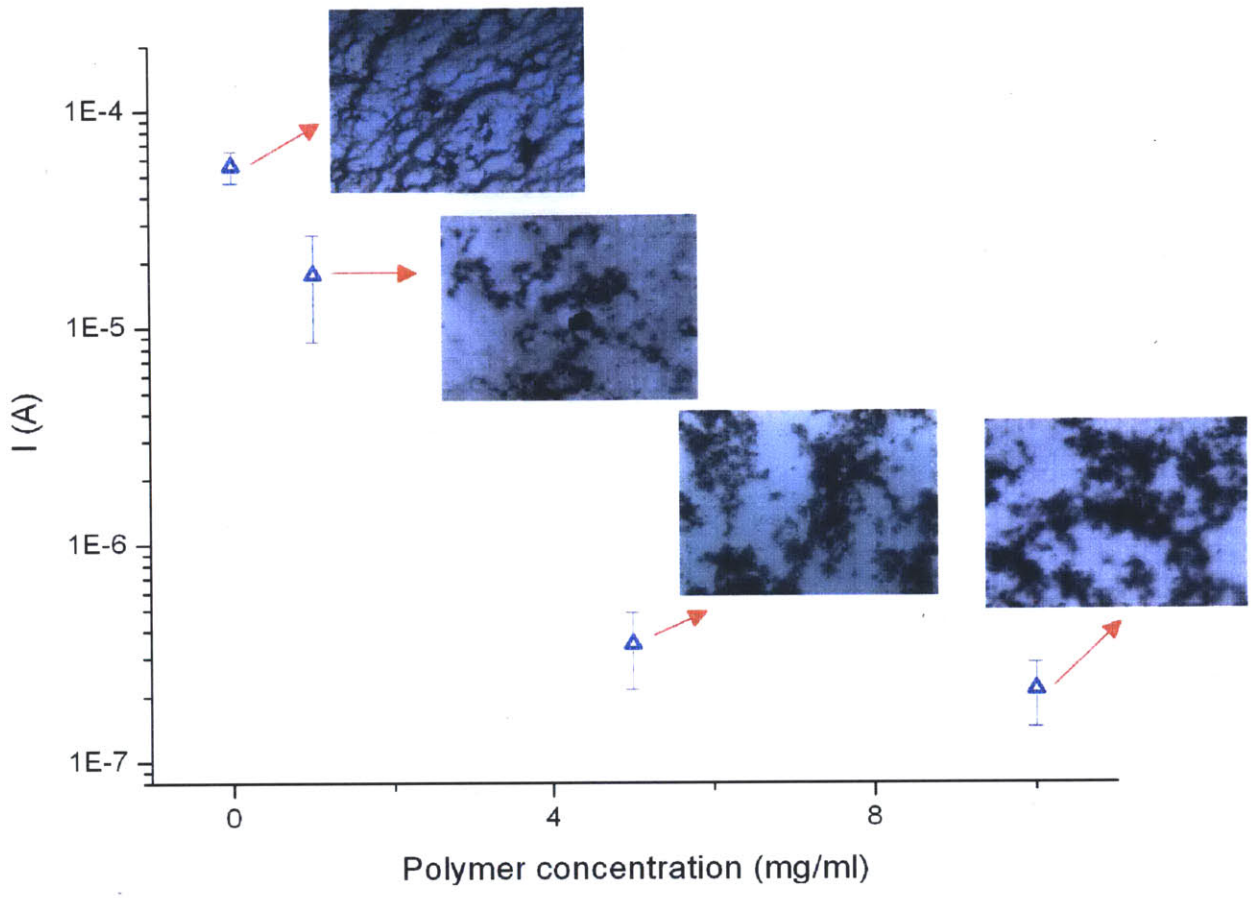

Figure 1.4. Amperometric measurements (constant voltage 1V, average of 18 devices) for films containing different ratios of **P1HS** to **MWCNTs**. Inset: Optical microscopy pictures of the films (40x magnification)

When an array of devices containing such films were exposed to high doses of radiation ($5 \cdot 10^6$ rad) emitted by the decaying elements of a nuclear reactor, an increase in the conductivity of up to 103-fold as compared to a non-irradiated reference of the same composition (Figure 1.5) was observed. This increase was larger for lower starting conductivities. As expected, when the matrix degrades, carbon nanotubes come into contact creating conducting pathways, which lead to higher overall conductivities.

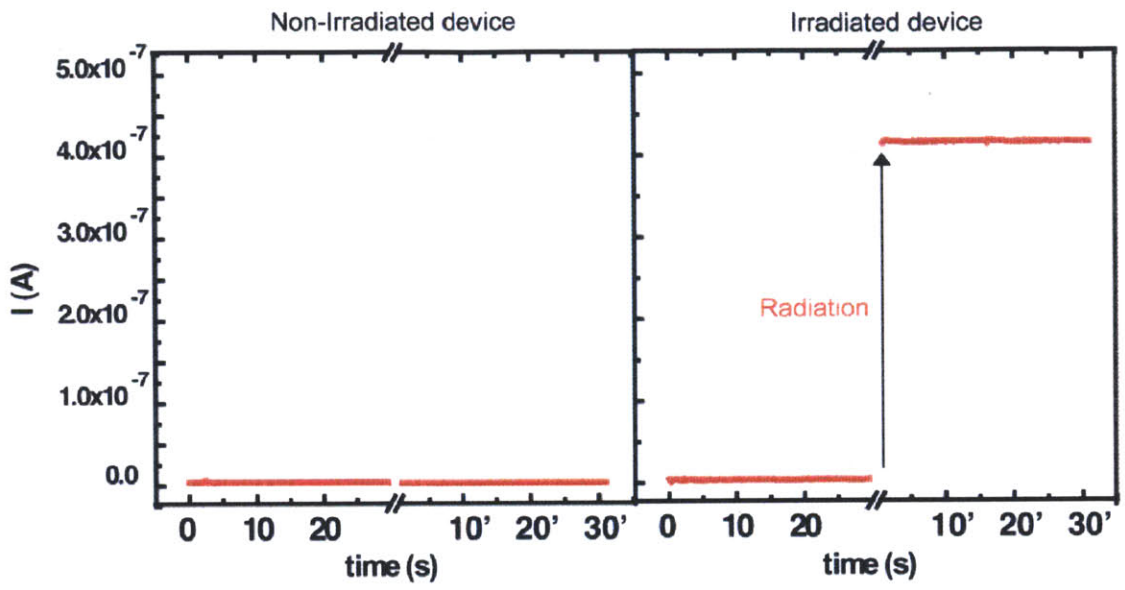

Figure 1.5. Amperometric measurements over time for devices of equal composition (**P1HS/MWCNTs**) that were not exposed to radiaiton (left), and that were exposed to radiation (right). An increase in conductivity is observed for devices that were exposed to radiation

Degradation of the polymeric matrix (**P1HS**) can be seen both by optical microscopy (Figure 1.6) and by scanning electron microscopy (SEM) (Figure 1.7). After irradiation, bubbles (pores) appear in the films, created by the volatile monomers generated after ionization and unzipping of the polymer chains.

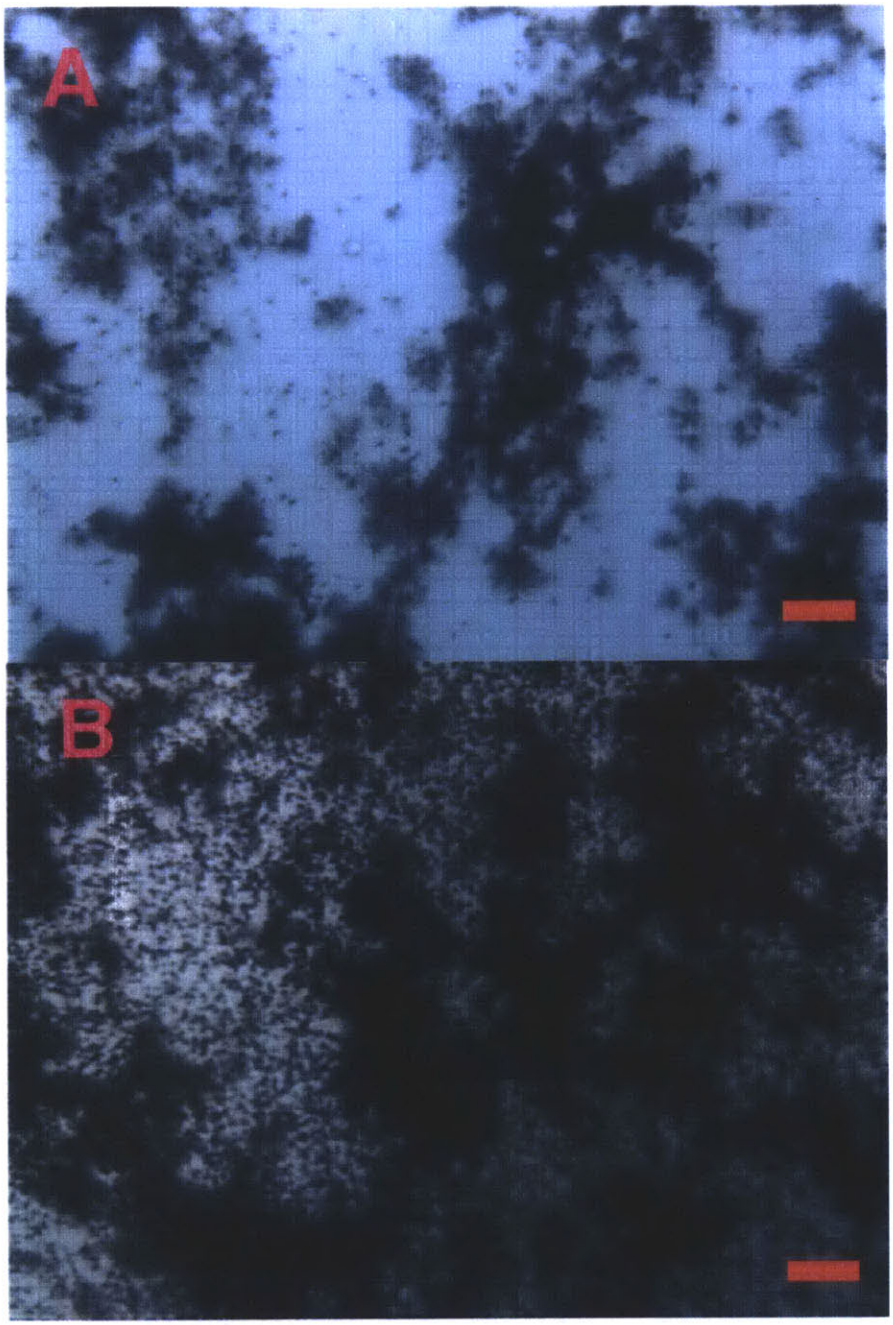

Figure 1.6. Optical Microscopy (40x, bright field mode, scale bar 20 μm) images of films composed of **P1HS/MWCNT** before (A), and after (B) irradiation with a high dose of radiation. The formation of pores in the film from gas development after polymer degradation is evident

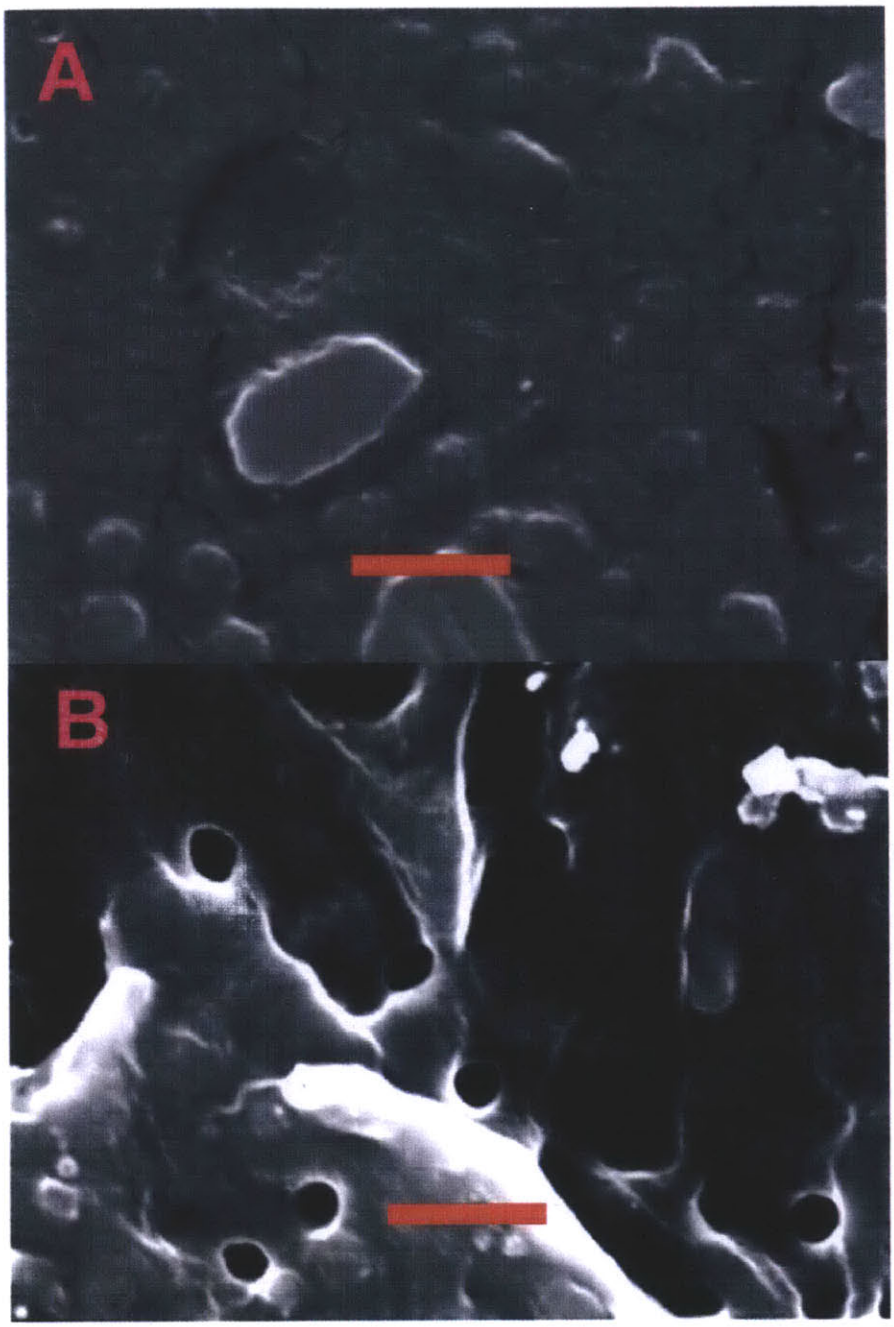

Figure 1.7. SEM (23000x, 15kV, SEI detector, no tilt, scale bar 1 μm) images of films composed of **P1HS/MWCNT** before (A), and after (B) irradiation with a high dose of radiation. The pictures show detail of the pores formed after irradiation

When organic matrices other than **P1HS** are used, the results are different. These results are summarized in Figure 1.8. Only when radiation labile polymers, traditionally used as electron beam resists such as **POSs** and poly (methyl methacrylate) (**PMMA**) are used, an increase in the conductivity can be seen. When more radiation robust polymer such as poly (styrene) (**PS**) are used, no change in the films and in the device signal is observed. The same can be said when small molecule analogues of **POSs**, such as 3-sulfolene are used as the matrix. Even though 3-sulfolene has also been reported to degrade in the presence of ionizing radiation, going back to butadiene and sulfur dioxide, this is an isolated event with no amplification. In the case of **POSs**, one bond cleavage event leads to unzipping of the whole polymer chain (amplification), which in turn leads to significant changes in the morphology.

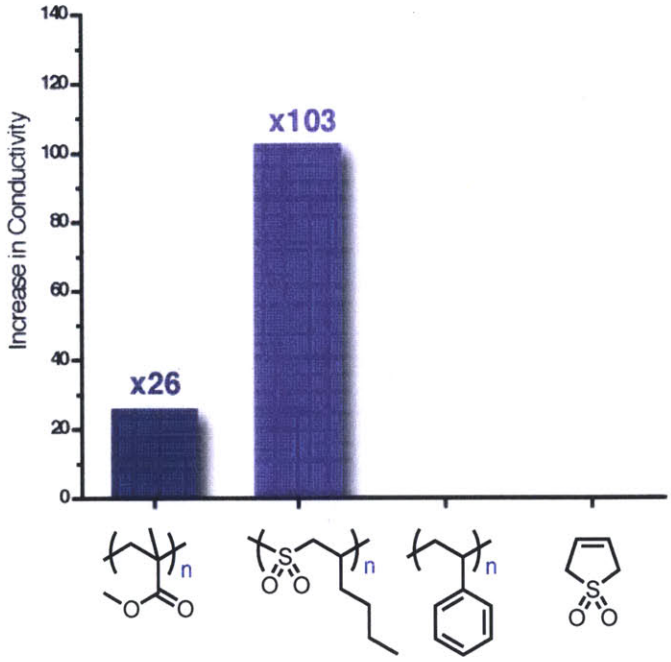

Figure 1.8. Increase in conductivity after irradiation (radiation dose: $5 \cdot 10^6$ rad) for devices using different organic matrices (from left to right: **PMMA**, **P1HS**, **PS** and 3-sulfolene) and **MWCNTs**

It is worth noting that when comparing **P1HS** and **PMMA** as a matrix, the sensitivity of devices is much higher for the case of **P1HS**. This is due to the fact that **P1HS** has a much higher tendency to degrade in the presence of ionizing radiation, which leads to larger changes in the morphology.

To test the dynamic range of the detectors, a lower dose of $5 \cdot 10^3$ rad was employed, and devices also showed a detectable increase in the conductivity as compared to a non-irradiated reference. However, the conductivity was at the lower detection limit of the amperometer used, and devices failed to show a response when exposed to even lower doses. The lack of signal at lower doses is mainly due to two problems:

a) The initial homogeneity of the films was very poor (Figure 1.9), owing to the lack of favorable interactions between the **POS** and the **CNTs**. Large **CNT** aggregates can be observed, and this is detrimental for sensor performance

b) The cross-sections for gamma ray absorption of the elements used in the active film were relatively low, so few gamma rays were scattered inside the film, leading to sensing events

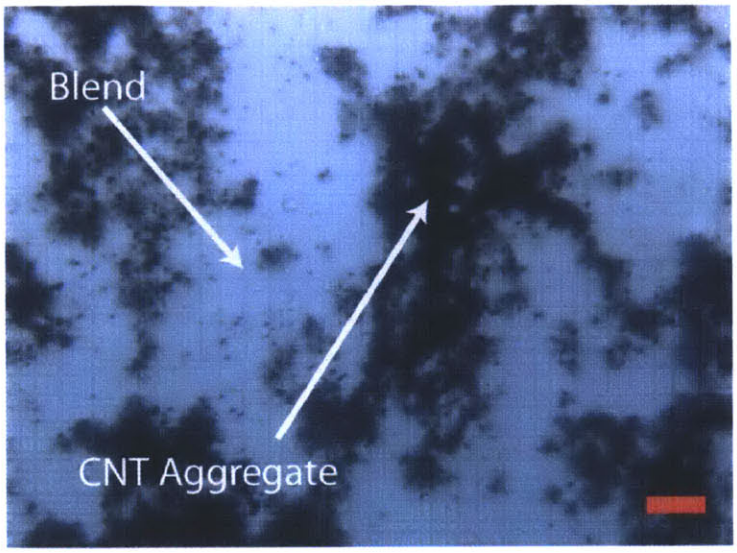

Figure 1.9. Detail of optical micrographs (40x, bright field mode, scale bar 20 μm) of films of **P1HS** and **MWCNT**

In order to address these concerns, and to improve device sensitivity, we decided to modify the chemical structure of the active element in the sensor. For this purpose, we embarked on the synthesis of **POSs** containing functional groups on the side chains.

1.4 Synthesis and modification of Side-Chain Functionalized Poly (Olefin Sulfone)s

Even though monomers with many different functional groups have been successfully incorporated into **POSs**,[15] several restrictions in the monomer choice arise from the nature and conditions of the polymerization process. In order to attach different functional groups and test the performance of these new **POSs**, a modular approach was taken, in which a parent polymer with versatile functional groups susceptible of undergoing orthogonal chemistry was synthesized, and then functional groups were attached in a post-polymerization modification.

The Huisgen 1,3-dipolar cycloaddition (one of the most prominent examples of the group of transformations commonly referred to as "click chemistry", Scheme 1.5) in which a terminal alkynyl group and an azide react to form a triazole ring has proven to be an extremely useful tool for the orthogonal post-polymerization functionalization of polymers.[16]

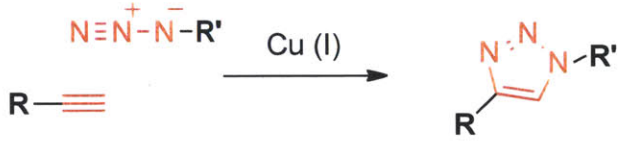

Scheme 1.5. Cu-catalyzed Huisgen 1,3-dipolar cycloaddition

Azide-containing olefins were synthesized and successfully incorporated into **POSs**. Copolymerization of 6-azido-1-hexene (obtained from 6-bromo-1-hexene) with **SO_2** and 1-hexene afforded a family of random monomodal terpolymers, azide-**POSs** (Scheme 1.6). The actual loading of azide on the side chain (defined as the molar fraction of repeat unit containing azides on the side-chain, X_b versus the molar ratio of repeat unit containing unfunctionalized side-chains, X_a) could be traced by ^{1}H-NMR and infrared (IR) spectroscopic techniques (Figure 1.10 and Figure 1.11 respectively).

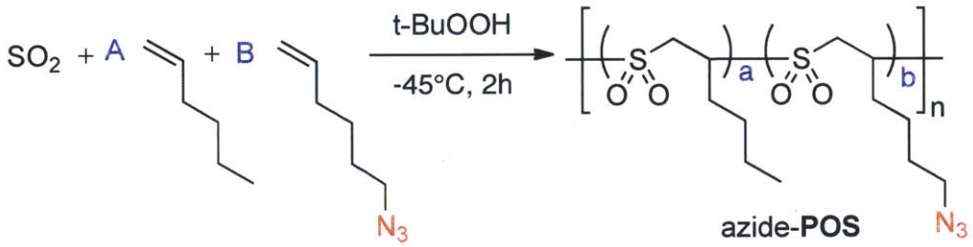

Scheme 1.6. Synthesis of azide-containing poly(olefin sulfone)s (azide-**POSs**)

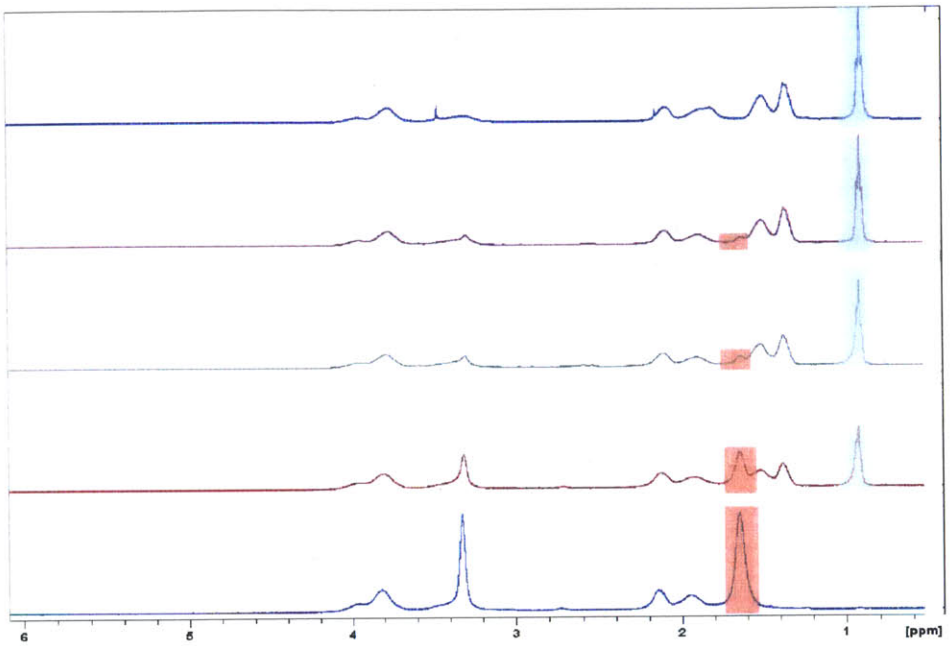

Figure 1.10. ^{1}H-NMR spectra for **POS** with different ratios of X_a, X_b ($X_a + X_b = 1$). From top to bottom: X_b (determined by ^{1}H-NMR)=0, 0.08, 0.14, 0.44, 1

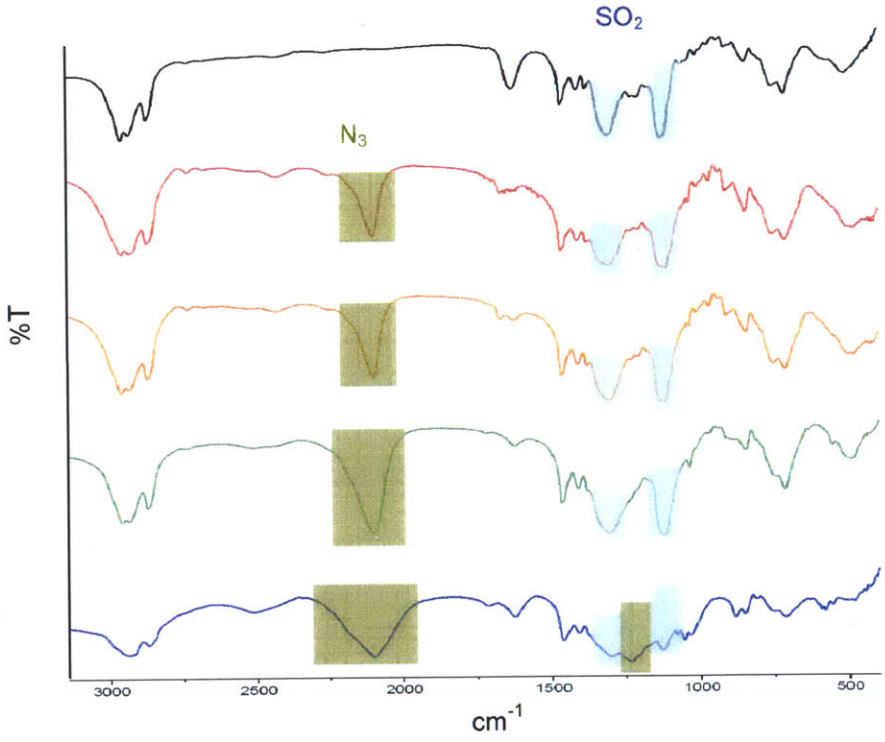

Figure 1.11. IR Spectra of POS with different ratios of X_a, X_b ($X_a + X_b = 1$). From top to bottom: X_b (determined by ^{1}H-NMR)=0, 0.08, 0.14, 0.44, 1

The amount of azido-olefin incorporated into the final polymer (X_b) was proportional to the amount in the initial feed (X_B) as shown in Figure 1.12. For copolymerizations, this is a perfect example for an ideal azeotropic copolymerization. This allows for perfect control over the loading of azide functionalities on the side chain of the polymer. Post-polymerization Huisgen 1,3-dipolar cycloaddition with alkynyl molecules provided these azide- **POSs** with the desired functionality.

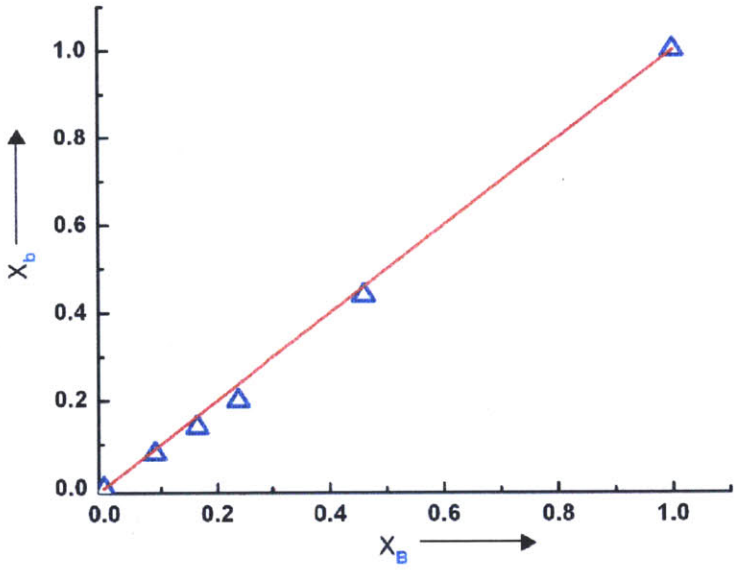

Figure 1.12. Molar ratio of 6-azido-1-hexene (X_B) in the feed (x axis) vs. molar ratio of repeat unit containing azide monomer (X_b), as determined by ^{1}H NMR spectroscopy

1.5 Pyrene – Modified Poly (Olefin Sulfone)s: Increase in Homogeneity

To improve the dispersion capabilities of **MWCNTs**, pyrene was attached to the side chains of our **POSs**. Pyrene binds to the surface of **MWCNTs** by π–π stacking,[17] improving polymer-**MWCNT** interactions. This interaction was first decribed in 2001 by Dai *et al.* and has since been used to tailor the surface of **CNTs** for functionalization purposes, leaving the electronic structure of the tubes intact.[18] Pyrene derivative propargyl pyrenebutyl ether **1** was synthesized from a pyrenebutanol precursor, and was incorporated into the **POSs** using click chemistry (Scheme 1.7), to yield pyrene-functionalized **POS 2**.

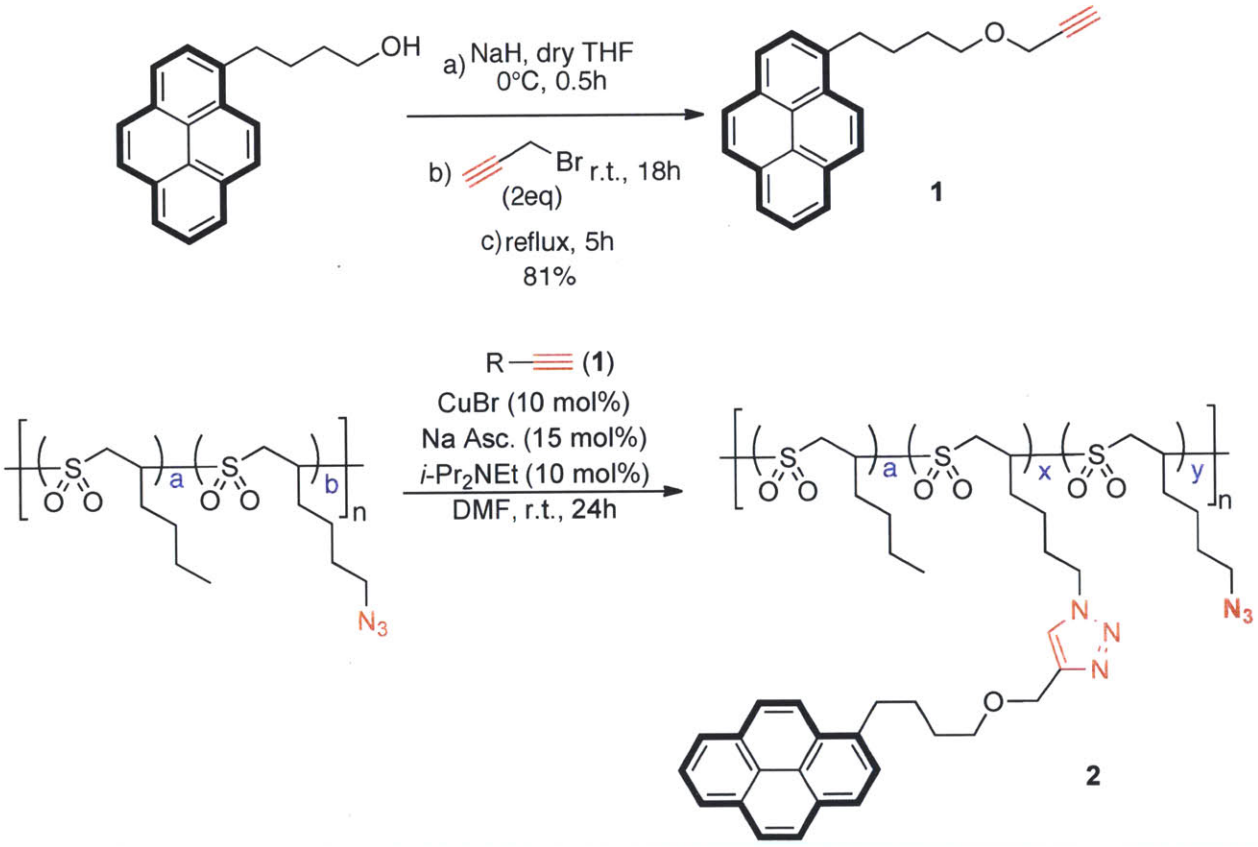

Scheme 1.7. Synthesis of propargyl pyrenebutyl ether **1** and post-polymerization click chemistry reaction to yield pyrene-functionalized **POS 2**

When films were cast using pyrene-modified **POS 2** and **MWCNTs**, it was clear that the initial homogeneity of the films was improved. The higher the content of pyrene molecules on the side chain of the **POS** used, the better the interaction between **POS** and **MWCNTs** and the smaller the size of the **CNT** aggregates observed by optical microscopy (Figure 1.13). Optical microscopy pictures reveal how the degree of aggregation of the **MWCNT** decreases with increasing content of pyrene in the side chains of the **POS** (from B to C, clear areas correspond to regions with transparent **POS** and **MWCNT** dispersed in aggregates too small to absorb visible light). **SEM** micrographs show that continuous films are formed when using a **POS** together with the **MWCNT** for film deposition.

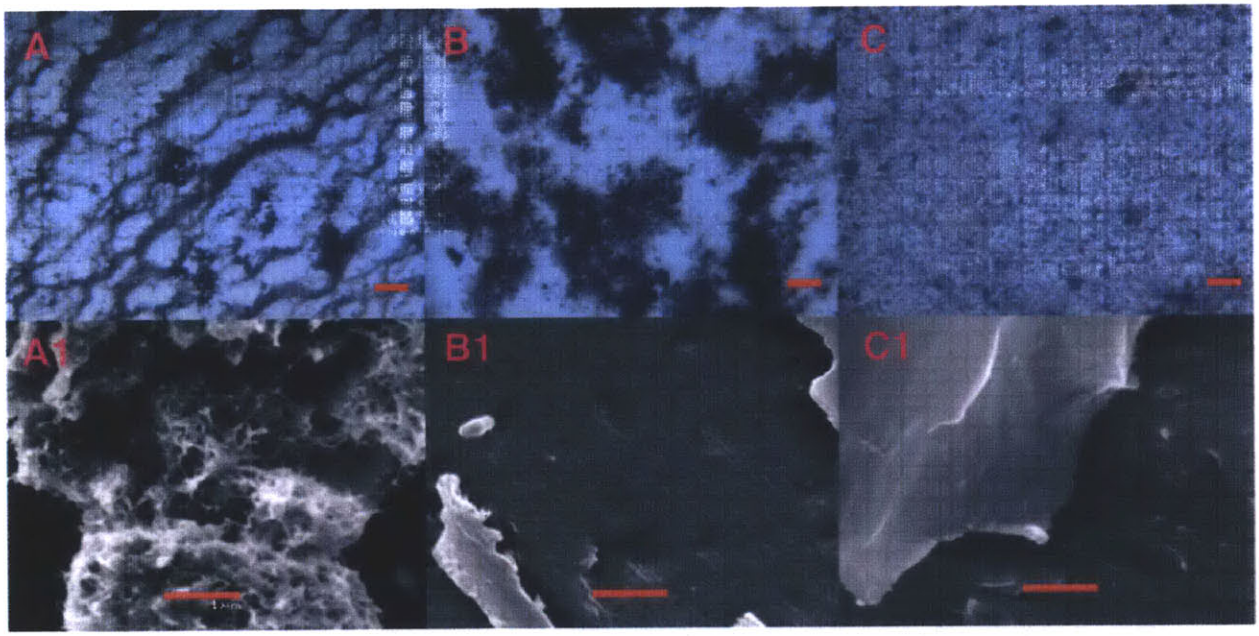

Figure 1.13. Optical Microscopy (A-C, 40x, bright field mode, scale bar 20 μm) and SEM (A1-C1, 23000x, 15kV, SEI detector, no tilt, scale bar 1 μm) images of films composed of bare **MWCNT** (A, A1), **P1HS/MWCNT** (B, B1), **2** (24 mol% pyrene)/**MWCNT** (C, C1)

When devices fabricated using pyrene-functionalized **POS 2** were exposed to gamma radiation, a more pronounced increase in conductivity was obtained as compared to devices with the unfunctionalized equivalent poly (1-hexene sulfone) (Figure 1.14). An increase in the initial homogeneity of the system improved the performance of the devices. Comparing the response of pyrene-functionalized polymers with varying ratios of pyrene on the side-chain under the same dose of radiation ($5{\cdot}10^3$ rad), the signal goes from barely detectable to an increase of about 14 %.

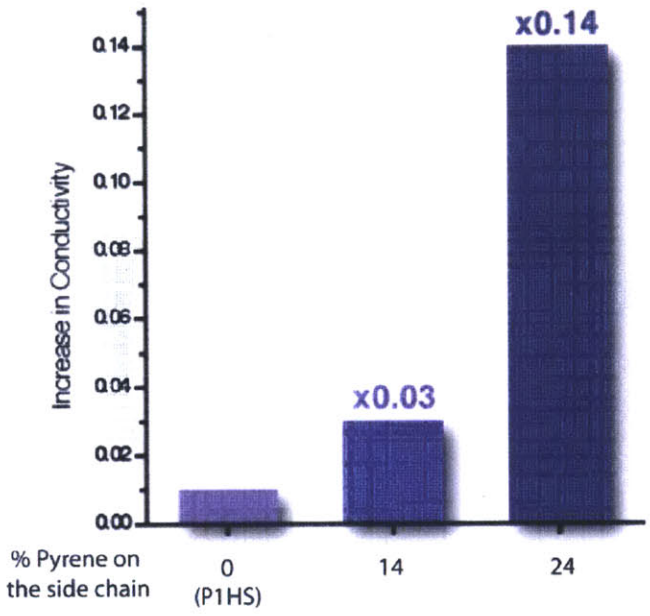

Figure 1.14. Increase in conductivity (y-axis) of irradiated devices fabricated using **POS** with different amounts of pyrene on the side-chain (x-axis) and **MWCNTs**. The sensitivity increases with increasing pyrene content

1.6 Bismuth – Modified Poly (Olefin Sulfone)s: Increase in Radiation Opacity

Cross-section values for ionization caused by gamma rays of different elements increase with increasing atomic number (Z) as shown in Figure 1.15.[7] Bismuth (**Bi**) is considered to be the heaviest non-radioactive element in the periodic table,[19] and doping polymers with **Bi** has been shown to increase the opacity of the resulting polymers towards ionizing radiation.[20] For this reason, **Bi** containing derivatives were synthesized and incorporated in the side-chains of the azide-**POSs**.

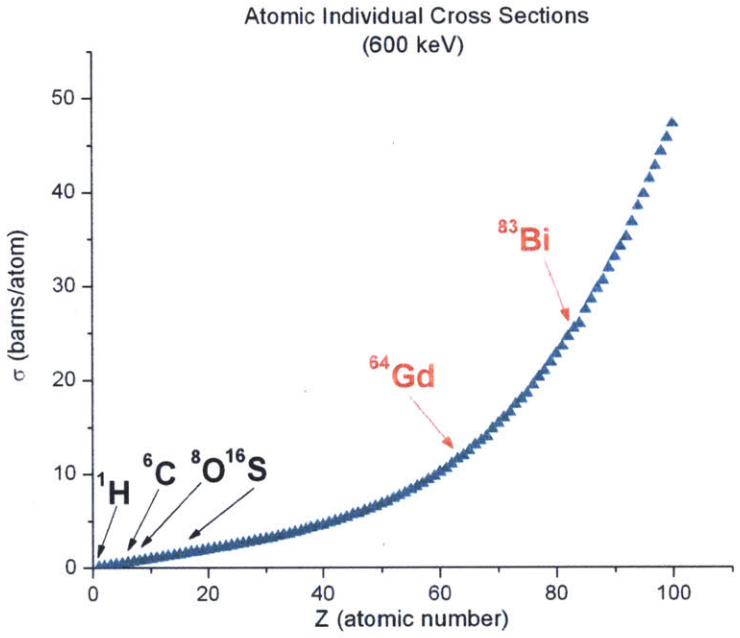

Figure 1.15. Atomic individual cross-sections (σ) for gamma ray absorption (600 keV). σ increases with increasing atomic number (Z)

Bi complex (4-ethynylphenyl)diphenylbismuthine (**4**, Scheme 1.8) was synthesized starting with the desproportionation of triphenylbismuth and bismuth trichloride to obtain

chlorodiphenylbismuthine **3**, which after ligand exchange with the organilithium derivative of TMS phenylacetylene and deprotection gave compound **4**. **Bi** complex **4** was then used for the side-chain modification of azide-**POS** (Scheme 1.8). Bismuth loadings as high as 20% (characterized by gel permeation chromatography (GPC), ^{1}H NMR spectroscopy, and IR spectroscopy) were achieved in this manner without any reduction in solubility. Presence of **Bi** in the polymer was further confirmed by X-ray photoelectron spectroscopy (XPS, Figure 1.17).

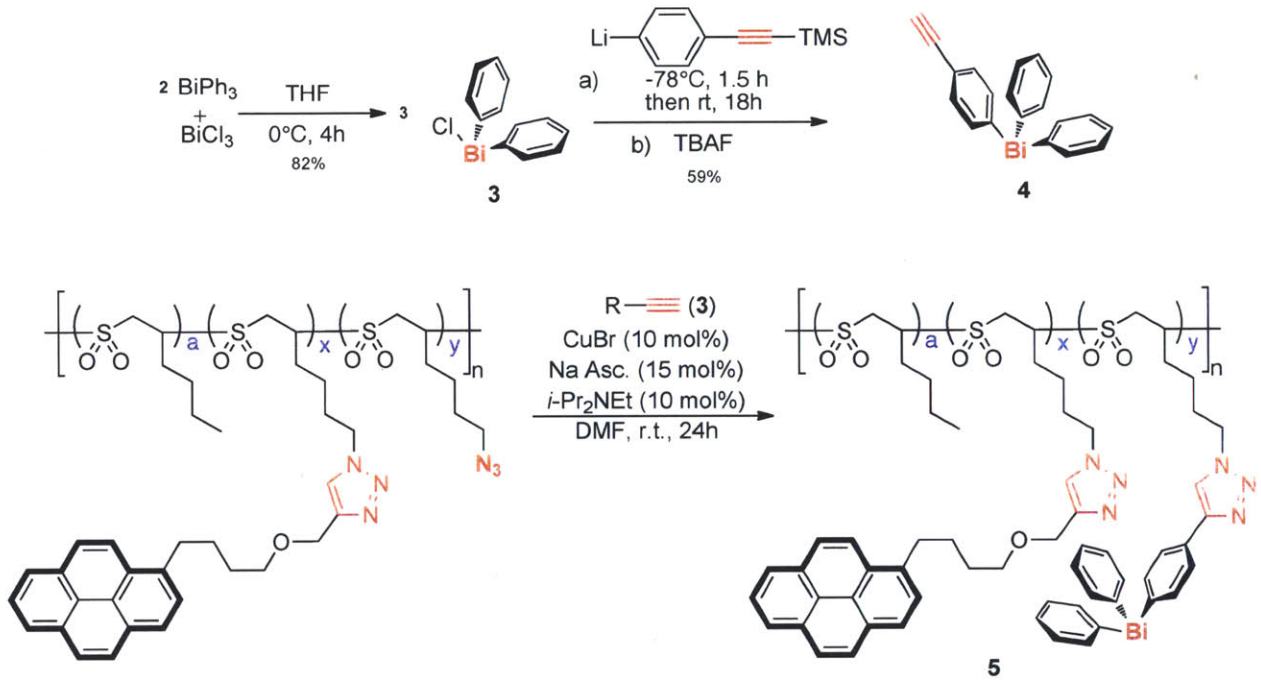

Scheme 1.8. Synthesis of (4-ethynylphenyl)diphenylbismuthine **3** and post-polymerization click chemistry reaction

Incorporation of **Bi** to increase the opacity of the system towards gamma rays proved to be an even more effective strategy for increasing device response towards radiation. In devices containing **POSs** functionalized with both pyrene and bismuth moieties in the side-chain and MWCNTs as the active layer (**5**), a 5.12-fold increase in the conductivity was detected. This

response is even higher than that obtained when using pyrene-only modified polymers (**2**, Figure 1.16).

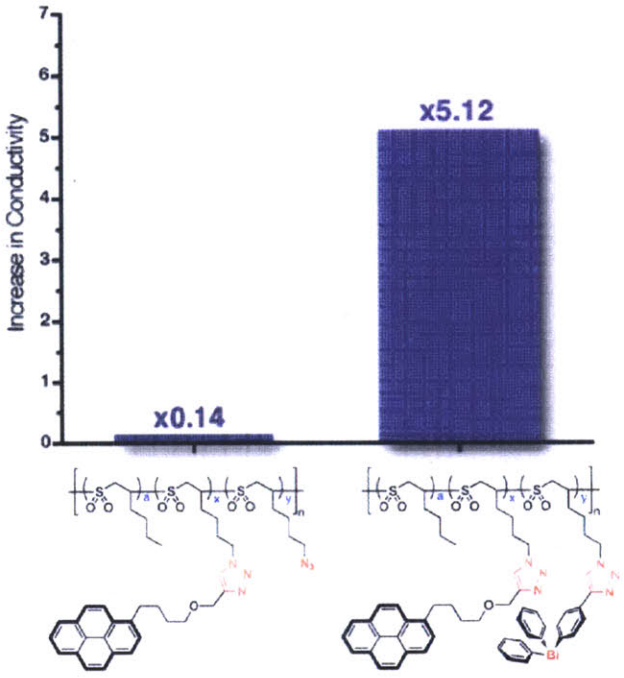

Figure 1.16. Increase in conductivity (*y*-axis) of irradiated devices fabricated using **POS** with and without bismuth on the side-chain (*x*-axis) and **MWCNTs**. The sensitivity increases when **POSs** with **Bi** in the side chain are used

The increased sensitivity is attributed to a higher opacity towards gamma rays (Figure 1.17). When the film doped with bismuth is exposed to radiation, more gamma rays are scattered within the film, increasing the chance of an ionization event to occur.

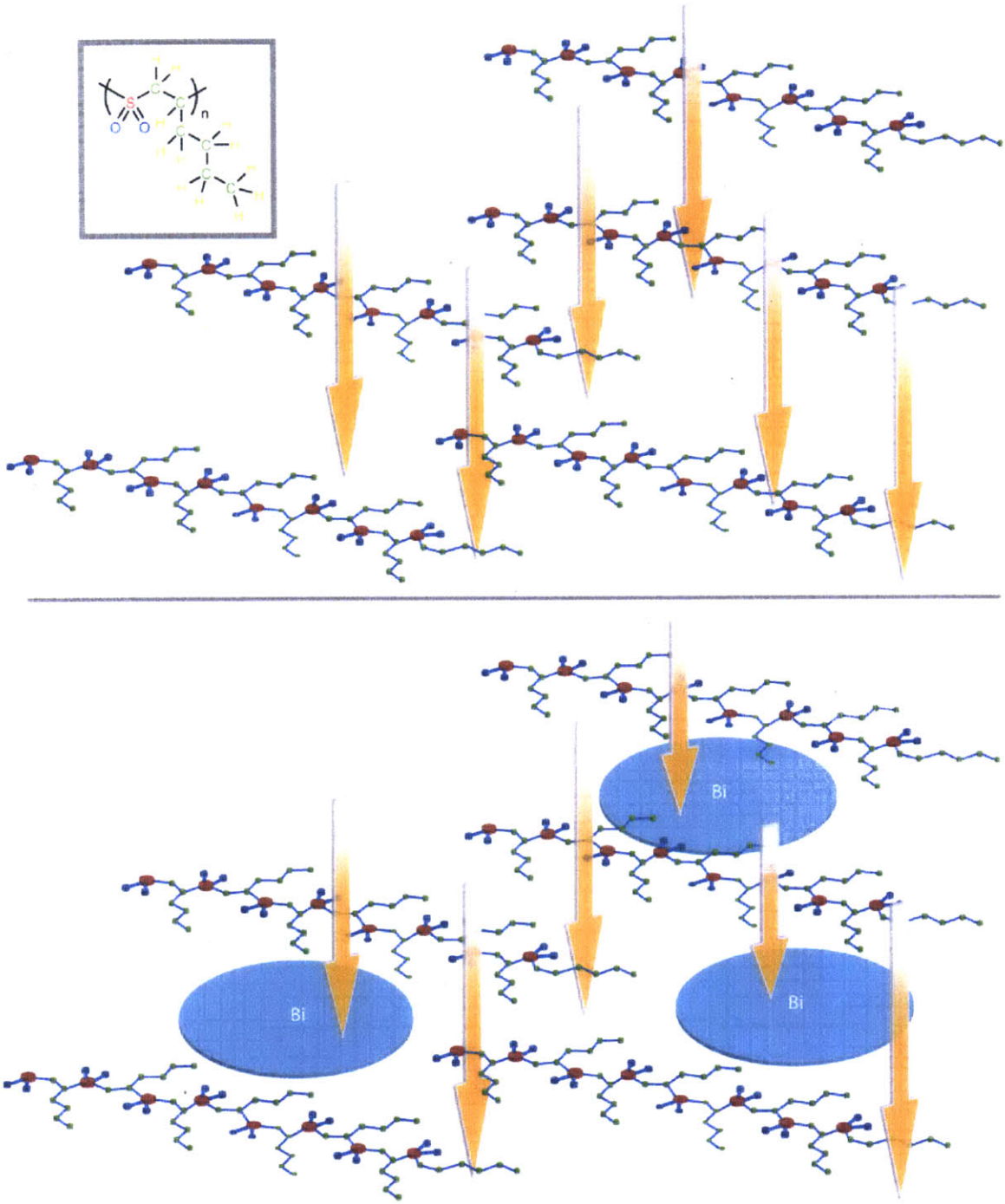

Figure 1.17. Model depicting the relative sizes of gamma ray absorption cross-sections (σ) as discs of the elements in **P1HS**. When bismuth atoms, with much larger σ, are incorporated in the formulation, the opacity of the films towards gamma-rays (represented as yellow arrows) is greatly increased

1.7 Conclusions

In summary, in this chapter we have shown how a novel sensing scheme that is not based on scintillation or charge generation in semiconductors can be deployed for the detection of uncharged ionization radiation using small devices. Our sensing mechanism (Figure 1) makes use of a polymer / multiwalled carbon nanotube (**MWCNT**) blend as the active layer of small devices for the detection of gamma rays. This system is capable of producing a real-time signal at room temperature, composed of relatively inexpensive starting materials, with nearly zero cost of operation.

In our system, the conducting **MWCNTs** form a percolated network and are partially isolated from each other in a non-conductive polymeric matrix. The turn-on detection mechanism is as follows: upon irradiation of the composite, ionization induces depolymerization of the matrix, creating a lower resistance connection between the **MWCNTs**. The depolymerization creates amplification and large changes in the electrical properties of the composite, increasing its conductivity.

Functional **POSs** were accessed by click chemistry methods, and several strategies were successfully deployed to increase sensor sensitivity. We have shown that systematic improvements in sensitivity can be accomplished by rational design, and incorporation of the appropriate chemical components to achieve sensitivities in the 10^3 rad range.[21] This is a good example of how rational design and chemical modification can lead to large changes in material performance.

1.8 Experimental Section

Materials: Unless otherwise noted, all reactions were performed under an oxygen-free atmosphere of argon. Graduated flasks were used for polymerization reactions with condensed sulfur dioxide. Anhydrous solvents were obtained using a solvent purification solvent (Innovative Technologies). All other chemicals were of reagent grade from Sigma-Aldrich and were used as received, except for sulfur dioxide, which was purchased from Airgas, and triphenylbismuthine, which was purchased from Alfa. Cuprous Bromide was purified as described somewhere else.[22] Multi-walled carbon nanotubes were donated by Bayer, AG (Baytubes 150 P, >95% purity).

General Notes on Organic-Azide Reactivity: Please note that organic-azides have been noted to be explosive. Even though no incidents happened during the manipulation of any of the chemicals described in this chapter, it is recommended to use extreme caution when working with this kind of compounds.

NMR Spectroscopy: NMR spectra were obtained on a Bruker Avance (400 MHz). NMR chemical shifts are given in ppm referenced to $CHCl_3$/TMS (7.24 ppm for ^1H, 77.24 ppm for ^{13}C), or THF (3.58 ppm for ^1H, 25.37 ppm for ^{13}C), or DMF (8.03 ppm for ^1H, 163.15 ppm for ^{13}C).

Mass Spectrometry: High-resolution mass spectra (HRMS) were obtained on a Bruker Daltonics APEXII 3 Tesla Fourier Transform Mass Spectrometer at the MIT Department of Chemistry Instrumentation Facility (DCIF).

Infrared (IR) Spectroscopy: Fourier Transform infrared (FT-IR) spectroscopy was performed on a Perkin- Elmer model 2000 FT-IR spectrophotometer using the Spectrum v. 2.00 software package.

Molecular Weight Determination: Polymer molecular weights were determined at room temperature on a HP series 1100 GPC system in THF at 1.0 mL/min (1 mg/mL sample concentrations), approximate molecular weights were estimated using a polystyrene calibration standard.

Device Fabrication: Thin-film deposition on a microscope slide was achieved by drop-casting from a THF solution containing both the **POS** and commercially available purified CNTs, dispersed by sonication. Gold electrodes were deposited by sputter- coating with a spacing of 1.5 mm between electrodes to enable amperometric measurements.

Amperometry: Amperometric measurements were performed with an AUTOLAB PGSTAT 20 potentiostat (Eco Chemie) at constant potential (1 V). Gold electrodes were deposited using a SC7620 Sputter Coater from Quorum Technologies. Devices were measured before and after irradiation, and its I (A) signal (variation of I normalized to the initial I) under constant voltage was compared to non-irradiated devices with the same formulation.

Irradiation Experiments: The decaying element from the core of a nuclear reactor was used for the high dose gamma ray source at the gamma irradiation facility from the nuclear reactor at MIT. Devices were irradiated for 72h to achieve a radiation dose of $5 \cdot 10^6$ rad. A Gammacell irradiator Gammacell 40 with a ^{137}Cs source (Model C-161, Type 8) was used for the lower radiation doses. Typically, devices were irradiated for 77 min to achieve a radiation dose of $5 \cdot 10^3$ rad.

Optical Microscopy: Pictures were obtained using a Leica DMRXP optical microscope.

Scanning Electron Microscopy: SEM images were obtained using a JEOL JSM 6060 Scanning Electron Microscope. Samples for SEM were coated with a Sputterer with a Au/Pd target to prevent radiation damage.

X-Ray Photoelectron Spectroscopy: XPS spectra were recorded on a Kratos AXIS Ultra X-ray Photoelectron Spectrometer.

General POS Synthesis. A typical poly (olefin sulfone) (**POS**) synthesis was carried out following literature procedures.[12] In general, sulfur dioxide (6ml) was condensed into a graduated vessel at -78°C. The reaction vessel was then transferred into a -45°C bath. Olefin monomers were added to the reaction mixture in the desired ratio, and the solution was stirred for 5 minutes. Initiator for the polymerization (tert-Butyl hydroperoxide in decane, solution 5.0-6.0M, 5-10 mol% relative to total amount of olefin) was added, and the mixture was stirred at -45°C for 2h. The polymerization was stopped by pouring the reaction mixture into MeOH. The resulting white powder was redissolved in $CHCl_3$ and reprecipitated from MeOH, then washed with MeOH. The white solid obtained was dried under vacuum.

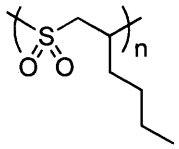

Poly (1-hexene sulfone) (P1HS). See general **POS** synthesis (98% yield). ^{1}H-NMR ($CDCl_3$) 0.9 (3H, br t), 1.3-1.4 (2H, br), 1.4-1.6 (2H, br), 1.8-2.0 (1H, br), 2.0-2.2 (1H, br), 3.2-3.5 (1H, br), 3.7-4.1 (2H, br). ^{13}C-NMR ($CDCl_3$) 13.92. 22.67, 28.12, 28.46, 50.26, 57.34. IR (cm^{-1}): 2961, 2874, 1309, 1130, 715. GPC Mn = 102 KDa, Mw = 367 KDa, PDI = 1.97.

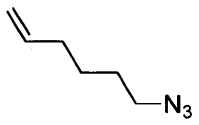

6-azido-1-hexene. To a solution of 6-bromo-1-hexene (1ml, 7.5 mmol) in DMSO (20ml) under argon was added sodium azide (1g, 15.4 mmol), and the solution was stirred for 42h at room temperature. A 1:1 mixture of H_2O/diethyl ether was added to the reaction mixture, and the aqueous phase was extracted three times with 20 ml Et_2O. The combined organic phases were washed twice with 20 ml H_2O, 20ml brine, and dried over $MgSO_4$. After removal of the solvent under reduced pressure, a colorless oil was obtained (652mg, 69%). ^{1}H-NMR ($CDCl_3$) 1.4 (2H, m), 1.6 (2H, m), 2.1 (2H, m), 3.2 (2H, t, J=6.8 Hz), 4.9 (2H, m,), 5.8 (1H, ddt, 6.7, 10.2, 16.9 Hz). ^{13}C-NMR ($CDCl_3$) 26.10, 28.44, 33.38, 51.51, 115.19, 138.35.

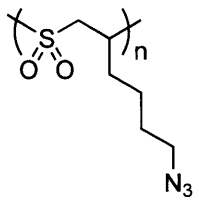

Poly (6-azido-1-hexene sulfone), (a/(a+b)=0). See general **POS** synthesis (96% yield). ^{1}H-NMR ($CDCl_3$) 1.5-1.8 (4H, br), 1.8-2.1 (1H, br), 2.1-2.3 (1H, br), 3.3-3.6 (3H, br), 3.7-4.1 (2H, br). ^{13}C-NMR ($CDCl_3$) 23.19, 28.18, 28.58, 49.78, 51.00, 57.00. IR (cm^{-1}): 2942, 2098, 1299, 1234, 1128. GPC Mn=2.9 KDa, Mw=5.0 KDa, PDI=1.71.

Poly (1-hexene 6-azido-1-hexene sulfone), (a/(a+b)≠ 0). See general **POS** synthesis (96% yield). ^{1}H-NMR ($CDCl_3$) (Figure 1.10) mixture of signals at the same positions as for **P1HS** and poly (6-azido-1-hexene sulfone) X_a, X_b were determined by comparison of the integration of the signal at 0.9 ppm (3H from repeat unit a, highlighted in blue on Figure 1.10) and at 1.5-1.8 ppm

(4H from repeat unit b, highlighted in red on Figure 1.10). Corresponding IR Spectra are shown on Figure 1.11. For a polymer where X_a=0.56, X_b=0.44, Mn= 4.7KDa, Mw= 9.3KDa, PDI=1.99.

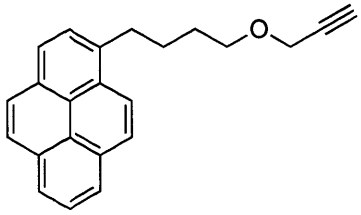

Propargyl pyrenebutyl ether (1). To a solution of 1-pyrenebutanol (1 g, 3.6 mmol) in anhydrous THF (15ml) was added NaH (160 mg, 6.7mmol) at 0°C. The solution was stirred at 0°C for 30 min, and propargyl bromide (80% in toluene, 880 mg, 7.4 mmol) was added. The reaction was stirred at 0°C in the dark for 30 min, and then allowed to warm to room temperature. After stirring for 15 h, the reaction was refluxed for 8h, after which ethyl acetate (10 ml) and water (10 ml) were added. The aqueous phase was extracted twice with 10 ml ethyl acetate. The combined organic phases were washed twice with 15 ml H_2O, and then twice with 15 ml brine, and dried over $MgSO_4$. After removal of the solvent under vacuum, the crude materials was purified by column chromatography using toluene as the eluent to give **1** as a pale yellow powder (911 mg, 81%). ^{1}H-NMR ($CDCl_3$): 1.8 (2H, m), 1.9 (2H, m), 2.6 (1H, t, J=2.4 Hz), 3.4 (2H, t, J=8 Hz), 3.6 (2H, t, J=6.4 Hz), 4.2 (2H, d, J=2.4 Hz), 7.8-8.3 (9H, m). ^{13}C-NMR ($CDCl_3$): 26.19, 29.49, 33.06, 58.00, 69.83, 74.35, 80.15, 123.33, 124.59, 124.71, 124.74, 124.94, 124.96, 125.68, 126.46, 127.07, 127.08, 127.45, 128.50, 129.67, 130.82, 131.34, 135.67. IR (cm^{-1}): 3294, 3040.51, 2933, 2860, 2116, 1102, 844 cm-1. m/z (HR-MS) found $(M+H)^+$ 313.1620, theoretical 313.16.

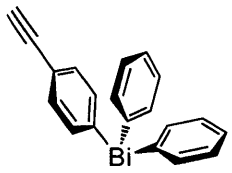

Chlorodiphenylbismuthine was synthesized from triphenylbismuthine and bismuth trichloride *via* a ligand redistribution reaction as described in the literature.[23]

(4-ethynylphenyl)diphenylbismuthine (4). To a solution of (4-bromophenylethynyl) trimethylsilane (640 mg, 2.5 mmol) in anhydrous THF (26 ml) at -78°C was added butyl lithium (1.6 ml solution in THF, 2.6 mmol) and stirred for 1h. Chlorodiphenylbismuthine (1g, 2.5 mmol) dispersed in 13 ml anhydrous THF was added to the reaction mixture, and stirred at -78°C for 1.5 h. The reaction was allowed to warm to room temperature, and stir for 14 h, after which TBAF (3.8 ml in THF solution 1.0 M, 3.8 mmol) was added to the reaction mixture. After 4 h of stirring at room temperature, the solvent was removed under vacuum, and the residue was purified by column chromatography using hexanes/ethyl acetate 19:1 as the eluent. **4** was obtained as a colorless oil (685 mg, 59%). ^{1}H-NMR (THF-d^{8}): 3.6 (1H, s), 7.2-7.8 (14H, m). ^{13}C-NMR (THF-d^{8}): 79.48, 84.72, 115.38, 122.70, 128.68, 131.44, 134.47, 138.46, 158.59, 158.63 (the signals for the quaternary carbons directly bound to bismuth are very weak, as reported in previous compounds). IR (cm^{-1}): 3288, 3058, 2924, 2106, 1570, 1474, 1428, 997, 817, 726, 695, 657, 533, 515, 446 cm-1. m/z= 386 (M+ - C6H5), 363 (M+ - C8H5), 310 (M+ - 2C6H5), 286 (M+ - C6H5, C8H5), 209 (Bi+ = M+ - 2C6H5, C8H5).

Conditions for the Click-Chemistry post-polymerization reaction. In a typical synthesis of polymers **2**, **5**, using standard Schlenk techniques, the alkynyl coupling partner (1mmol) was dissolved in dry DMF (15 ml). Azide-containing **POS** (1 eq of azide-containing repeat unit) dissolved in 5 ml of anhydrous DMF was added to the reaction mixture. CuBr (14.3 mg, 0.1 mmol) and sodium ascorbate (29.7 mg, 0.15 mmol) dispersed in 5 ml anhydrous DMF were

added to the reaction mixture, then addition of N,N-diisopropylethylamine (17 µl, 0.1 mmol) followed. The mixture was stirred at room temperature for 24 h, after which the solvent was removed under vacuum. The polymer was redissolved in THF, precipitated from MeOH, and washed with copious amounts of saturated aqueous solution of NH_4Cl. After washing with H_2O, MeOH, the resulting white solid was dried under vacuum.

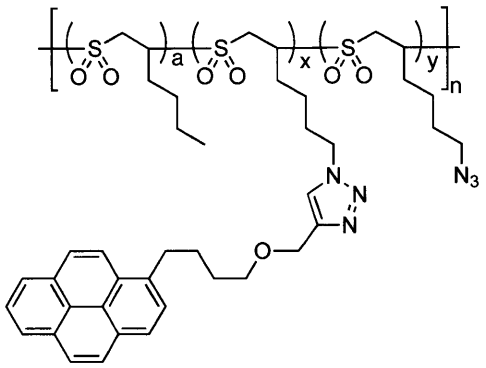

Pyrene-functionalized POS (2, 24 mol% Pyr): See conditions for the click-chemistry post-polymerization reaction. ^{1}H-NMR ($CDCl_3$): 0.9 (sb), 1.0-2.1 (m), 3.0-4.5 (m), 7.8-8.2 (m). ^{13}C-NMR ($CDCl_3$): 13.96, 22.64 (2), 28.19 (3), 28.44, 28.58, 29.76, 32.95, 33.33, 33.44, 36.67, 49.75 (2), 51.00, 57.35 (2), 58.31, 64.55, 70.17, 70.77, 74.40, 123.59, 123.67, 124.86, 124.99 (4), 125.02, 125.97, 126.76, 127.49, 128.69, 129.89, 131.00, 131.12, 131.53, 136.95, 145.00. Mol% determined by ^{1}H-NMR, comparing the relative ratio of the broad signal between ^{1}H-NMR ($CDCl_3$): 7.8-8.2 (9H, pyrene moiety), and 0.9 (3H, methyl group of hexane repeat unit). Mn= 4.9 KDa, Mw= 7.2 KDa, PDI=1.46. IR: See Figure 1.19 for decrease in the intensity of the azide stretching band.

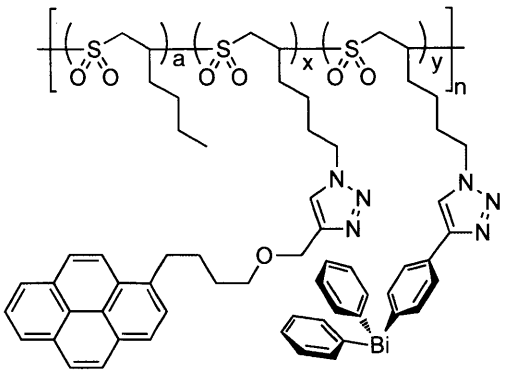

Pyrene / bismuth-functionalized POS (5, 24 mol% Pyr, 20 mol% Bi): See conditions for the click-chemistry post-polymerization reaction. ^{1}H-NMR (DMF-d^{7}): 0.9 (sb), 1.5-2.3 (m), 3.7-4.6 (m), 7.2-8.2 (m). ^{13}C-NMR (DMF-d^{7}): 10.43, 13.10, 13.85, 25.88, 25.94, 33.10, 33.17, 33.23, 49.76, 50.02, 64.34, 69.95, 115.69, 119.28, 122.07, 124.07, 125.23, 125.41, 125.64, 126.51, 126.97, 127.68, 127.98 (4), 128.03, 128.75, 128.91, 129.27, 129.78, 130.79, 131.83 (2), 137.86 (2), 138.83, 157.11, 158.89. Mn= 6.7 KDa, Mw= 7.5 KDa, PDI= 1.11. IR: See Figure 1.19 for decrease in the intensity of the azide stretching band.

1.9 Additional Figures

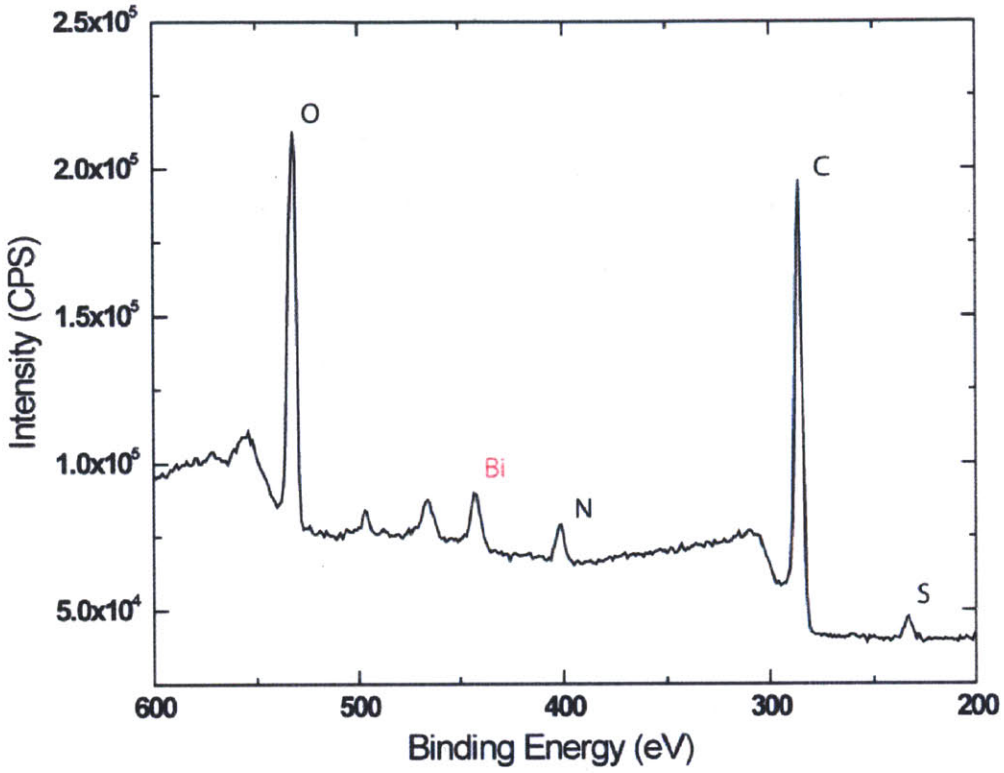

Figure 1.18. XPS Spectrum of polymer **5**

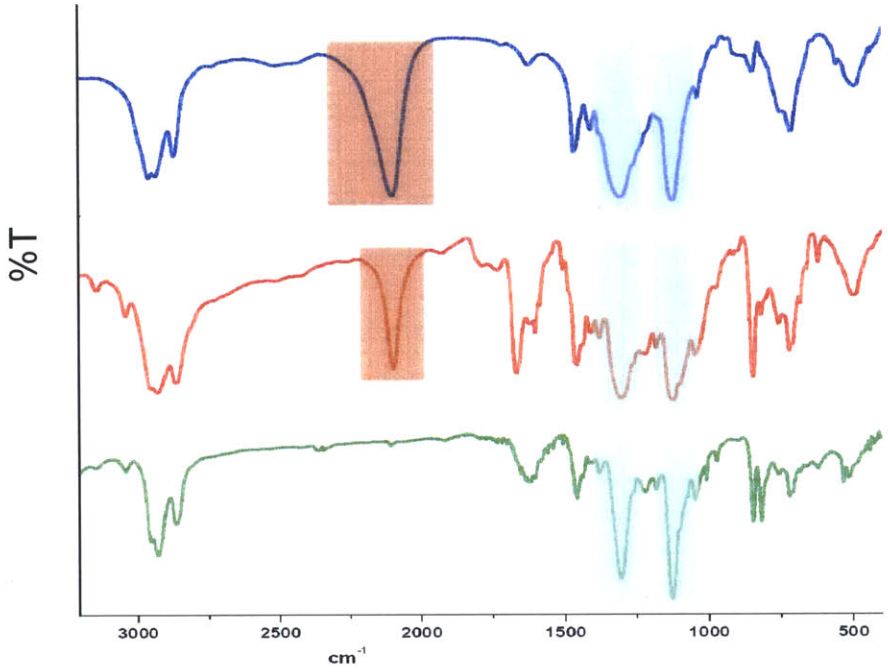

Figure 1.19. IR Spectra of **POS** with different degrees of functionalization. Red blocks indicate characteristic stretching bands for azide groups, blue blocks indicate characteristic stretching bands for sulfone groups. From top to bottom: azide-**POS**, with 44 mol% of azide-containing repeat unit (X_b =0.44); **2**, with 24 mol% pyrene containing repeat unit, 20 mol% repeat unit containing azide groups; **5**, with 24 mol% pyrene containing repeat unit, 20 mol% bismuth containing repeat unit. Mol% were determined by ^{1}H-NMR

1.10 References and Notes

(1) Esam M. A. Hussein. *Handbook on Radiation Probing, Gauging, Imaging and Analysis*; Kluwer Academic Publishers, 2003.

(2) (a) Knoll, G. F. *Radiation Detection and Measurement*; Wiley, New York, 1979. (b) Herz, R. H; *The Photographic Action of Ionizing Radiations*; Wiley-Interscience, London, 1969.

(3) The units for radiation dose vary depending on the field of science and the source, but generally for *Absorbed Dose* the units are either the *Gray* (Gy, SI) = 1J/kg rad or the *rad*=1cGy. When irradiating live specimens, often times the term *Equivalent Dose* is used, for which the units are either the *Sievert* (Sv, SI) = 1J/kg rem or the *rem*=1cSv.

(4) Owens, A. *J. Synchrotron Radiat.* **2006**, *13*, 143 – 150.

(5) Webster, J. G. *The Measurement, Sensors and Instrumentation Handboo*; CRC, 1999, pp. 66-12.

(6) Graham, S. C; Friend, R. H; Fung, S; Moratti, S. C. *Synth. Met.* **1997**, *84*, 903-904.

(7) Storm, E.; Israel, H. I. *At. Data Nucl. Data Tables* **1970**, *7*, 565-681.

(8) Bowden, M. J.; O Donnell, J. H. *Developments in Polymer Degradation*, Elsevier, Barking, 1985, Vol. 6, pp. 21 – 61.

(9) Brown, J. R.; O'Donnell, J. H. *Macromolecules* **1972**, *5*, 109-114.

(10) (a) Bowden, M. J.; Thompson, L. F. *J. Appl. Polym. Sci.* **1973**, *17*, 3211-3221. (b) Pampalone, T. R. *J. Imaging Sci.* **1986**, *30*, 160-166. (c) Yao, N.; Wang, Z. L. *Handbook of Microscopy for Nanotechnology*, Kluwer, Boston, 2005, pp. 287-319.

(11) Solonina, W. *Russ. J. Phys. Chem.* **1898**, *30*, 826-842.

(12) Bowmer, T. N.; O'Donnell, J. H. *J. Macromol. Sci. Part A* **1982**, *17*, 243-263.

(13) Ayscough, P. B.; Ivin, K. J.; O'Donnell, J. H. *Trans. Faraday Soc.* **1965**, *61*, 1110-1117.

(14) (a) Iijima, S. *Nature* **1991**, *354*, 56–58. (b) Schnorr, J. M.; Swager, T. M. *Chem. Mater.* **2010**, 1–12.

(15) Fawcett, A.H. *Encylopedia of Polymer Science & Engineering*; Wiley-VCH, Weinheim, 1987, Vol. 10, pp. 408 – 432.

(16) Numerous examples for post-polymerization modification of other families of polymers have been described in the literature. For a look at the scope of examples on click chemistry for post- polymerization modification and main chain polymerization, see *Macromolecules 2009*, virtual issue, issue 1.

(17) Chen, R. J.; Zhang, Y.; Wang, D.; Dai, H. *J. Am. Chem. Soc.* **2001**, *123*, 3838-3839.

(18) Paloniemi, H.; Äaritalo, T.; Laiho, T.; Liuke, H.; Kocharova, N.; Haapakka, K.; Terzi, F.; Seeber, R.; Lukkari, J. *J. Phys. Chem. B* **2005**, *109*, 8634-8642.

(19) Even though it has traditionally been considered that ^{209}Bi was the heaviest stable isotope in the periodic table, it was actually shown that the half-life is just extremely long (1.9×10^{19} years). However, this supposition can be considered correct for our system. De Marcillac, P.; Coron, N.; Dambier, G.; Leblanc, J.; Moalic, J.-P. *Nature* **2003**, *422*, 876-878.

(20) Tamber, H.; Smid, J.; Cabasso, I. *Chem. Mater.* **1997**, *9*, 1335-1341.

(21) Comparable organic-based small-size solid state systems in which the sensing mechanism relies on other phenomena present the following detection limits: Scintillation of conjugated polymers: (a) $>10^5$ rad (undoped system), Silva, E. A. B.; Borin, J. F.; Nicolucci, P.; Graeff, C. F. O.; Ghilardi Netto, T.; Bianchi, R. F. *Appl. Phys. Lett.* **2005**, *86*, 131902. (b) $0.5{\cdot}10^3$ rad (doped system), Zhao, Y. S.; Zhong, H.; Pei, Q. *Phys. Chem.*

Chem. Phys. **2008**, *10*, 1848-1851. (c) Charge generation in organic semiconductors: $4.1 \cdot 10^6$ rad, Raval, H. N.; Tiwari, S. P.; Navan, R. R.; Rao, V. R. *Appl. Phys. Lett.* **2009**, *94*, 123304.

(22) Armarego, W. L. F.; Chai, C. L. L. *Purification of Laboratory Chemicals*; ELSEVIER, 2003.

(23) Barton, D. H.; Bhatnagar, N. Y.; Finet, J.-P.; Motherwell, W. B. *Tetrahedron* **1986**, *42*, 3111-3122.

CHAPTER 2

Smart Poly (Olefin Sulfone) / Silicone Hybrid Polymers for Recyclable Composites

Adapted and reprinted in part with permission from:

Lobez, J. M.; Swager, T. M. "Disassembly of Elastomers: Poly (olefin sulfone)-Silicones with Switchable Mechanical Properties" *Macromolecules* **2010**, *43*, 10422-10426

2.1 Introduction

Stimulus responsive materials (often called "smart materials") are materials whose properties can be changed at will by applying an external signal. Polymers and polymeric composite materials can show this behavior, and there are numerous examples of polymeric systems that exhibit piezoelectricity (generation of an electric field or potential under mechanical stress),[1] shape memory,[2] biodegradability,[3] responses to thermal variations,[4] mechano-chromism,[5] or self-healing behavior.[6]

Smart materials that can be decomposed on demand are interesting from the point of view of recycling of composite materials. For instance, silicones can be used to bind the different layers of a composite, or to attach different components together in construction. This is achieved by placing a silicone precursor in between the parts to be bound together and then curing the silicone (Figure 2.1). However, when the two different components have to be separated in order to recycle the different layers of a composite or to recover the initially bound parts, silicone degradation requires extremely harsh conditions. Because cross-linked elastomeric silicones are chemically robust and do not degrade easily with temperature, they are not generally attractive components for recyclable composite materials. As a result, an equivalent material with similar properties to those of silicones that could be easily transformed into its processable precursors on command is a worthy goal. Such system could also find application for the controlled release of chemicals.[7]

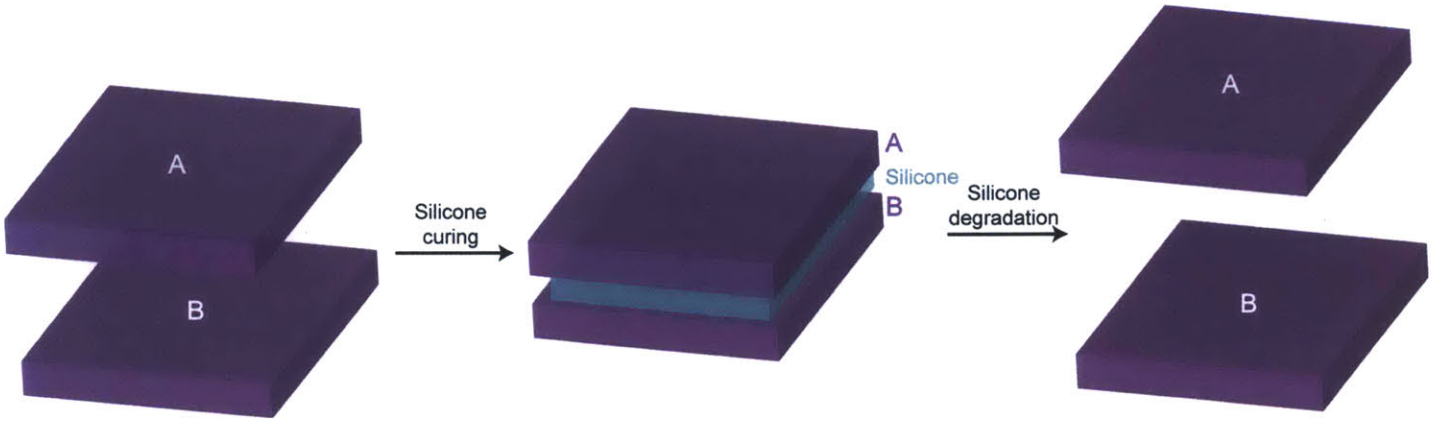

Figure 2.1. Composite assembly mediated by silicone as a binding agent and subsequent composite recycling after silicone degradation

In this chapter we present a hybrid polymer formed of a poly (olefin sulfone) (**POS**) and a silicone linked by "click" chemistry that exhibits switchable mechanical properties, namely it can disassemble into its monomers and individual constituents when exposed to mild bases. This new hybrid polymer is flexible, transparent, colorless and is also easily processed. By tuning the chemical structure of its two components and varying their ratio, a wide range of mechanical properties can be accessed. Additional properties such as coloring can be rapidly added to the system by virtue of a "click chemistry" reaction.

2.2 Smart Material Design

The proposed new hybrid polymer is formed by mixing two components: a silicone component and a poly (olefin sulfone) (**POS**) component (Figure 2.2).

Silicones[8,9] (Figure 2.2a) are among the most used elastomeric polymers and have found widespread use owing to their versatility, chemical and thermal stability,[10] and mechanical properties.

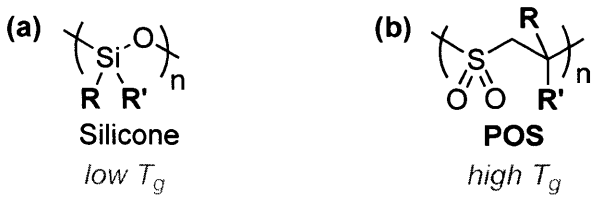

Figure 2.2. Structure of (a) silicones and (b) poly (olefin sulfone)s (**POSs**)

One of the most widely used silicone-based elastomers is poly (dimethylsiloxane) (**PDMS**, Figure 2.3), which is transparent, chemically inert and heat resistant. PDMS can be transformed into silica by calcination, and has widely tunable mechanical properties.[11] Linear **PDMS** has a glass-transition temperature (T_g) of -123°C,[12] and its cross-linked version is used as an elastomer. The mechanical properties of PDMS elastomers can be controlled by the length of the polymer chains, their branching, their cross-linking density, and the use of fillers.[13] Aside of applications that utilize its mechanical properties, **PDMS** has been crucial in the development of soft lithography[14] and in the field of microfluidics.[15] In the absence of air, **PDMS** starts decomposing at about 350 °C into cyclic compounds consisting of 3-11 repeat units.[16] **PDMS** also decomposes in the presence of base, but relatively harsh conditions are required to observe weight loss and macroscopic material failure (aprox. 190 °C in the presence of KOH).[17]

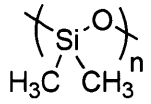

Figure 2.3. Structure of polydimethylsiloxane (**PDMS**)

From a synthetic point of view, silicone cyclic and linear oligomers are typically obtained from the hydrolysis of chlorosilanes[8,18] or hydrolysis of alkoxysilanes.[16] These oligomers can be converted into higher molecular weight silicones by any of the following procedures:

a) Equilibration with cyclic oligomers in the absence of a solvent[9]

b) Use of catalysts to polymerize oligomeric silanols either via condensation (using phosphoronitrile halides[19] or bases such as n-hexylamine)[10a] or via condensation and cleavage (using strong acids[20] or bases)[8]

c) Via ring-opening polymerization of cylic oligomers, either in its anionic[21] or cationic[22] form.

These polymers range from fluids to very viscous liquids and are usually cross-linked to obtain resins, coatings, and elastomers. Cross-linking has been traditionally performed by:

a) Room temperature vulcanization processes using either acid/base catalysts,[23] tin catalysts,[24] high-energy electrons,[25] or photoinitiated reactions,[26]

b) Heat-activated radical curing with peroxides,[27]

c) Mixing of two different polymeric silicone components, one of which contains a transition metal catalyst, typically Pt.[28]

The Huisgen 1,3-dipolar cycloaddition[29] ("click" reaction)[30] was introduced in the first chapter of this thesis and has been extensively used for post-polymerization modification of many polymer systems[31] but was only recently reported as a method for the cross-linking of silicones.[32] In this report the thermal or Cu-catalyzed "click" reaction was described to functionalize azide-containing silicone oligomers[33] and thermal curing was used for the formation of elastomeric silicones.[32] This approach has the advantage that no catalysts need to be

used in the process of cross-linking, so there is no need to remove/quench metal impurities after the cross-linking has occurred.

Poly (olefin sulfone)s (**POSs**)[34] (Figure 2.2b) and their synthesis from sulfur dioxide (SO_2) and olefins have been introduced in the first chapter of this thesis. They can be used not only as electron beam resists, but also as expanded foam insulation materials,[35] to improve the compatibility of certain materials with polymeric hydrocarbon chains,[36] and as antistatic additives for fuels.[37]

POSs have tunable glass-transition temperatures (T_gs) depending on the olefin moiety, although their T_gs are usually relatively high with values ranging from 77 °C for poly (1-hexadecene sulfone)[34b] to 177-200 °C for poly (styrene sulfone).[38] However, the use of **POSs** has been limited because as also described in detail in the first chapter of this thesis, **POSs** have low ceiling temperatures and tend to depolymerize, with polymer chains unzipping into volatile monomers (SO_2 and an olefin)[39] when an external stimulus produces chain scission.[40] Events that lead to depolymerization are exposure to ionizing radiation, either in the form of high-energy electrons[41] or γ rays[42,43] or exposure to base.[44] Their tendency to degrade has been exploited in the creation of electron beam resists[41,45] and sensors (see chapter 1).[43]

Given that **POSs** degrade into their volatile monomers in the presence of base following a mechanism similar to that of depolymerization in the presence of ionizing radiation (Scheme 2.1), an elastomeric **POS** could be used as a material to replace silicones capable of being disassembled. However, **POSs** have high T_gs and elastomeric **POSs** have not been reported. The low T_gs of silicones are usually attributed to the long silicon-oxygen (Si-O) bond and the wide Si-O-Si angle.[46] In contrast, the rigidity and high T_gs of **POSs** are the result of strong electrostatic interactions between adjacent sulfone dipoles, which induces a higher degree of

order.[47] Even POS copolymers containing 1-hexadecane as one of the monomers, with a long alkyl chain as a plasticizing element, are brittle powders at room temperature.

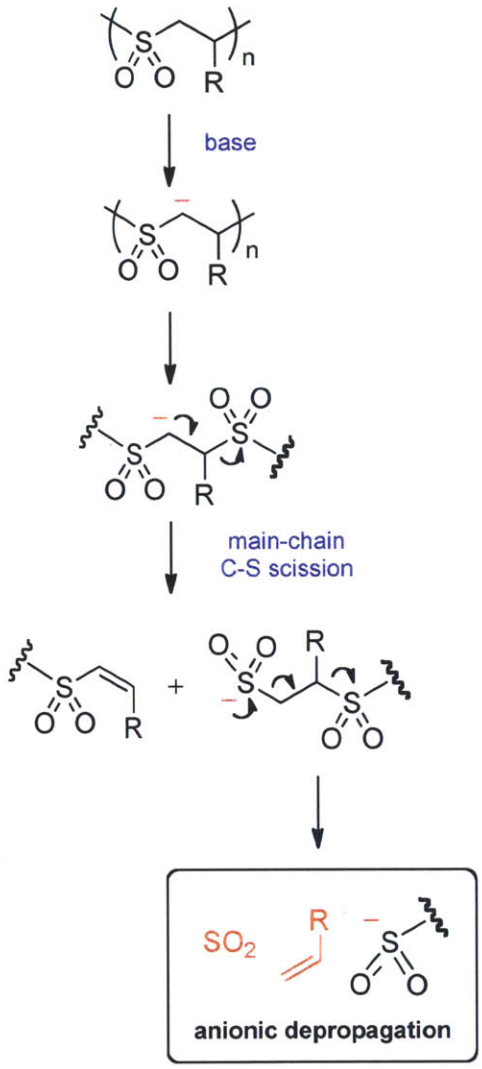

Scheme 2.1. Degradation mechanism of **POSs** in the presence of base

In chapter 1 we described the synthesis of **POSs** with azide functionalities in the side chains (**1**, Figure 2.4).[43] Copolymerization of azide-containing monomers with SO_2 and an olefin afforded a family of random terpolymers with monomodal molecular weight distributions, and

since it is an ideal azeotropic copolymerization, the ratio of azide incorporation into the polymer can be precisely controlled by the feed ratio.

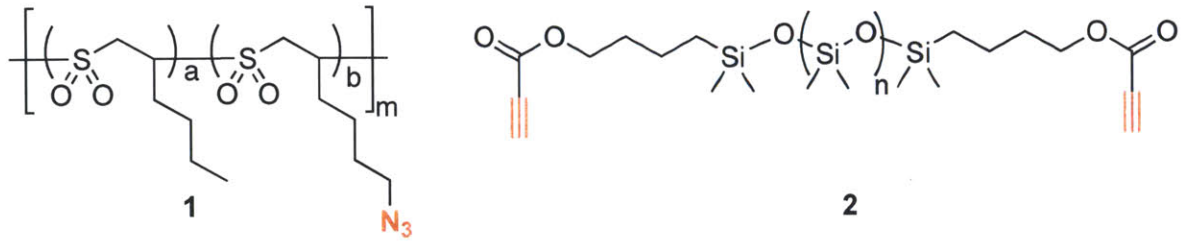

Figure 2.4. Structure of of azide-**POSs** (**1**) and alkynyl-terminated oligomeric siloxane (**2**)

As a result, we set to explore the possibility of using azide-POSs (**1**) as the cross-linker of oligomeric silicones terminated with alkynyl moieties (**2**). The resulting hybrid POS-silicone polymer formed using azide-alkyne cycloaddition reactions (Figure 2.5) could be used as a "smart material" capable of being decomposed upon exposure to base.

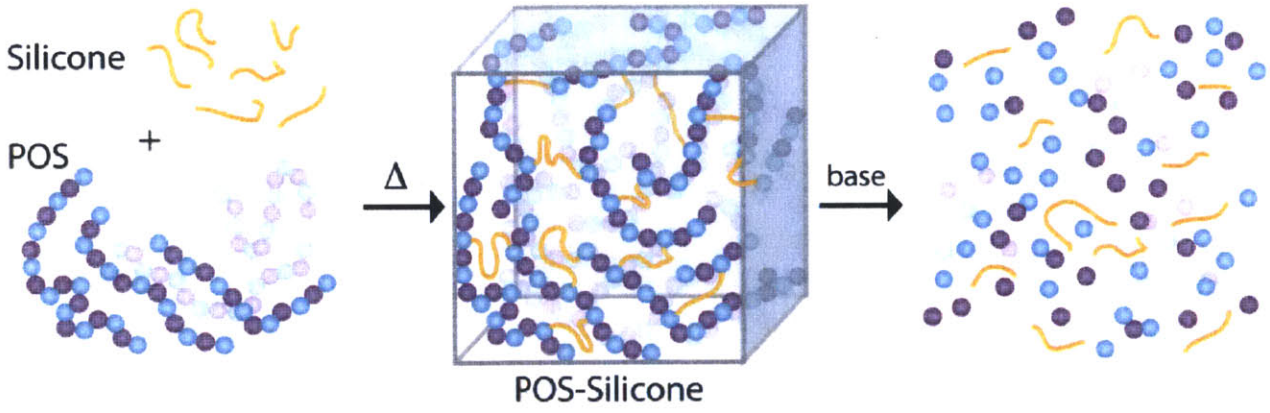

Figure 2.5. Formation of elastomeric cross-linked **POS**-silicone hybrid and its decomposition via unzipping of **POS** when exposed to base

2.3 Base-Initiated Depolymerization of Poly (Olefin Sulfone)s

One of the most important choices in our smart material design was the choice of the monomer for the POS element of the smart material, since this would have a great impact in the degradability of this component of the hybrid polymer.

The tendency of **POSs** to depolymerize with base depends on several factors, including the choice of base. Even though the pKa of the protons in the backbone of a poly (1-alkenyl sulfone) are expected to be between the pKas of bis(methylsulfonyl)methane (15.0 in DMSO)[48] and dimethylsulfone (31.1 in DMSO) (Figure 2.6),[49] POSs can be degraded into their monomers by milder bases.

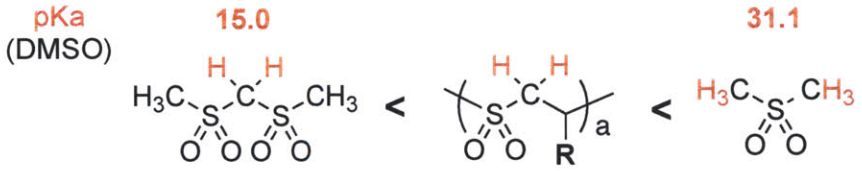

Figure 2.6. Expected range for the pKa of protons in the polymer backbone of poly (1-alkenyl sulfone)s

This can be seen by following the depolymerization of poly(2-methyl-1-pentene) (**P2MPS**, Figure 2.7) chains by ^{1}H NMR (Figure 2.8). The disassembly of the polymer is revealed by the increase of the signal for the olefinic monomer (2-methyl-1-pentane) at 4.7 ppm over time. After 30 min at rt with 0.7 M of base a clear signal can be seen for the olefinic monomer when using butylamine or piperidine as the base, and after 20 h even the comparatively less basic NH_4OH has almost completely degraded the polymer chains.

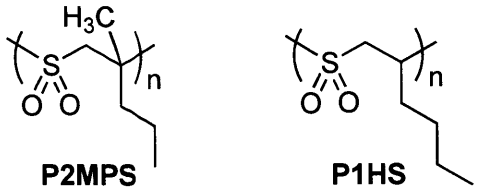

Figure 2.7. Structure of poly (2-methyl-pentene sulfone) (**P2MPS**) and poly (1-hexene sulfone) (**P1HS**)

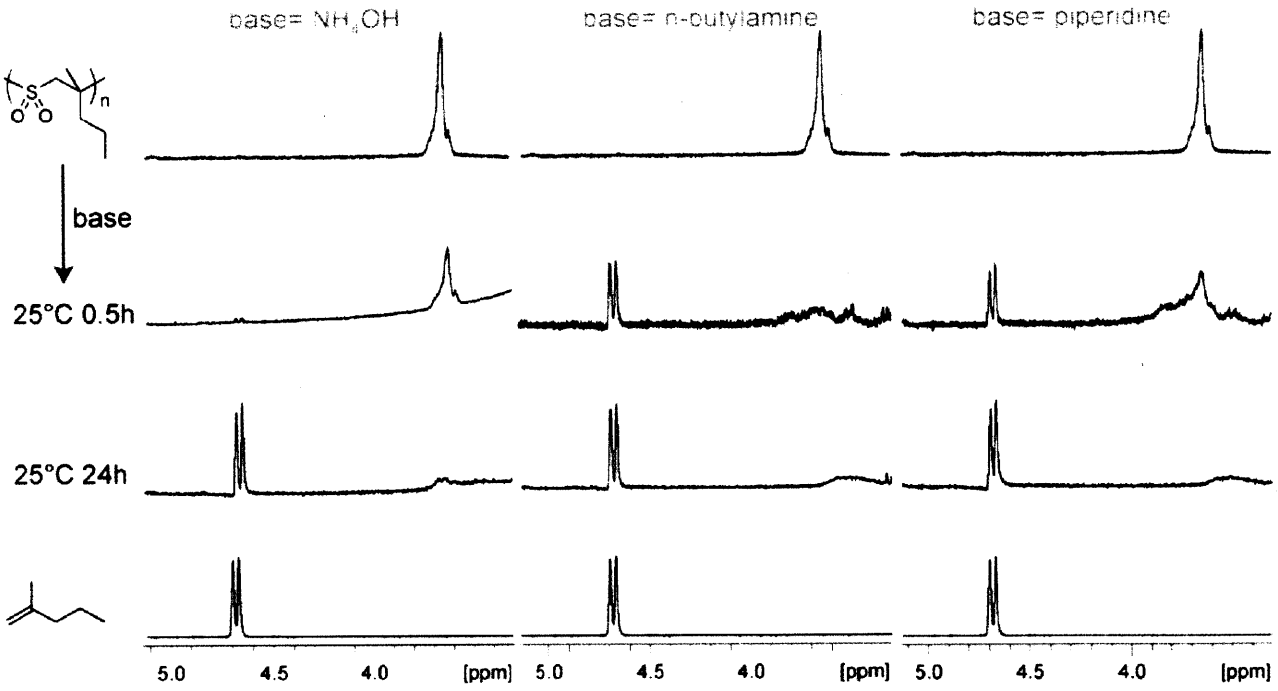

Figure 2.8. ^{1}H-NMR spectra showing the decomposition of **P2MPS** by different bases under different conditions

Another factor that dictates the ease of degradation of POSs with base is the choice of olefin comonomer. Upon comparing the degradation of poly (1-hexene sulfone), **P1HS** (Figure 2.7), to poly (2-methyl-1-pentene), **P2MPS**, at 80°C after 30 min, it is clear from the ratio of monomer to polymer ^{1}H NMR signals that **P1HS** degrades faster (Figure 2.9).

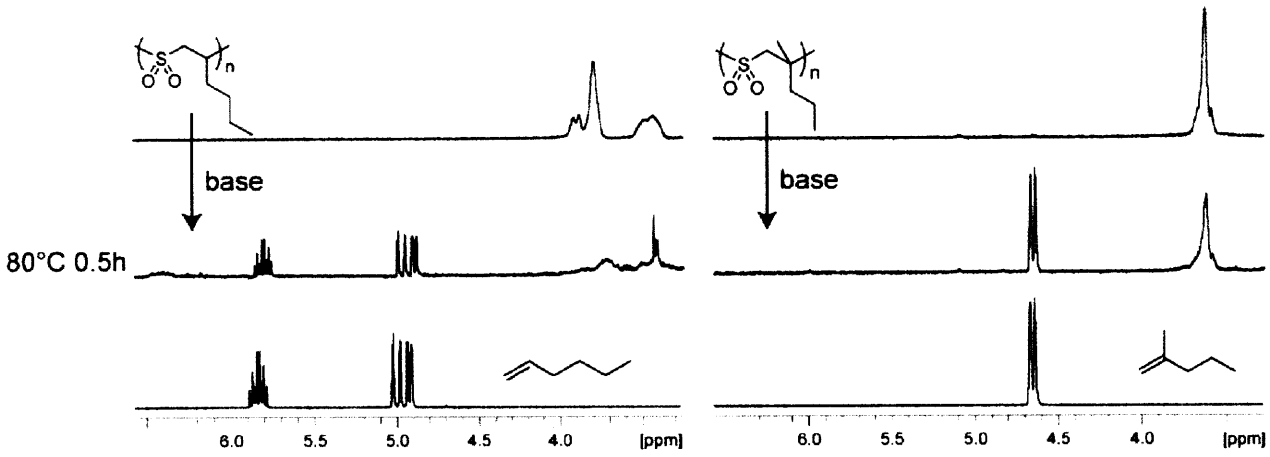

Figure 2.9. ^{1}H-NMR spectra showing the decomposition of **P2MPS** and **P1HS** after treatment with 0.3 eq. of piperidine at 80°C (30 min)

As expected, the degradation is even more accelerated when using a higher concentration of base (Figure 2.10). **P1HS** unzips into its monomers faster than **P2MPS**: a larger amount of base is needed for **P2MPS** to completely decompose into its olefinic monomer under the same conditions as **P1HS**. The olefinic monomer reacts with the excess base when using an excess of base for **P1HS**.

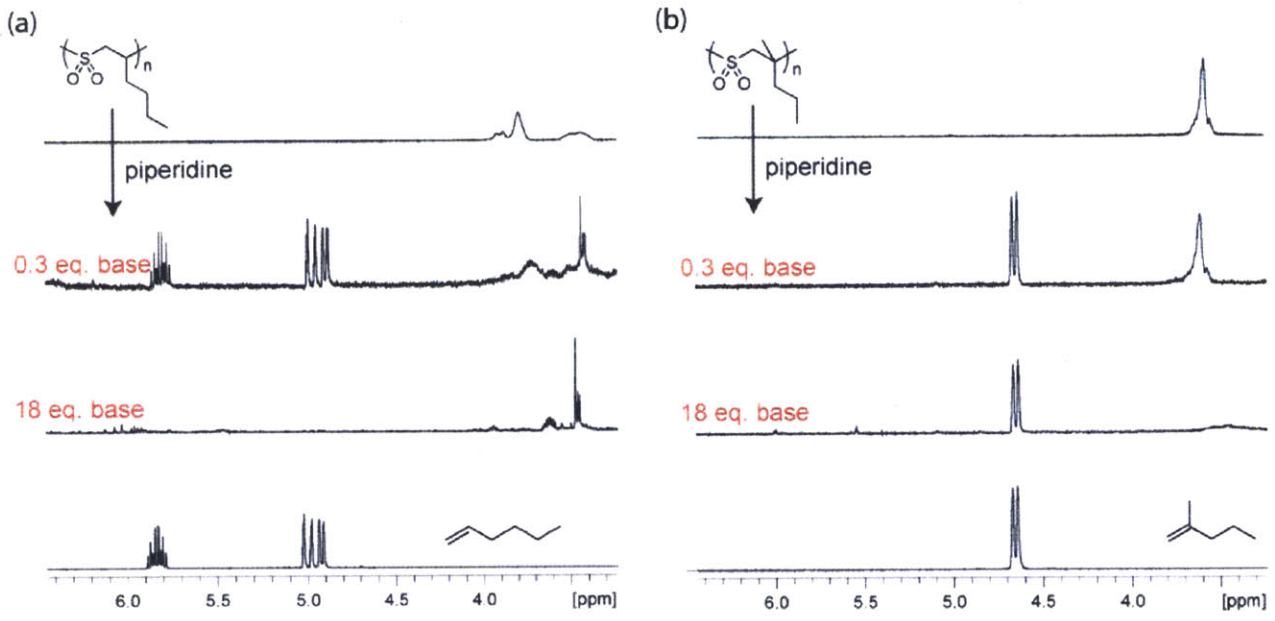

Figure 2.10. Unzipping of (a) **P1HS** and (b) **P2MPS** into their olefinic monomers as seen by ^{1}H-NMR (acetonitrile-d^{6}) with different amounts of piperidine at 80°C

The extent to which depolymerization occurs also depends on the depolymerization temperature. After 60 min of stirring with piperidine at room temperature, almost no degradation of the polymer can be observed (Figure 2.11). However, when heated to 80°C the signal for the olefinic monomer can be clearly seen for both **POSs** studied.

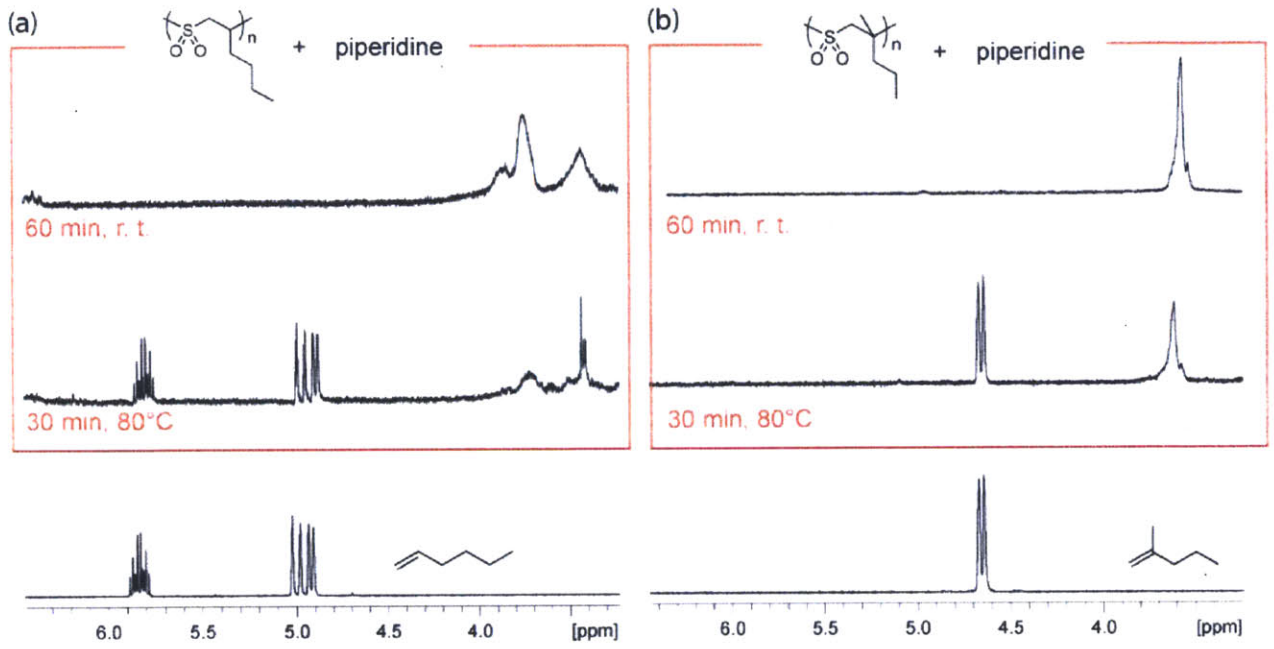

Figure 2.11. Unzipping of (a) **P1HS** and (b) **P2MPS** into their olefinic monomers by action of 0.3 eq. of piperidine as seen by ^{1}H-NMR (acetonitrile-d^{6}) under different conditions (time, temperature)

P1HS-based copolymers were chosen for composite preparation due to their superior tendency to be degraded by base. The fact that **P1HS** is more prone to base degradation than **P2MPS** is at first counterintuitive, since this is the opposite effect that one would expect when comparing the ceiling temperatures (T_c) of both polymers. Specifically, **P1HS** with an observed T_c of 60°C should be less prone to degradation than **P2MPS** with an observed T_c of -34°C.[50] As

a result, the slower reaction of **P2MPS** is attributed to higher steric hindrance that decreases deprotonation rates.

2.4 Hybrid Polymer Synthesis and Characterization

Dialkynyldimethylsiloxane oligomers (**2**) of varying lengths were synthesized by first end-capping an alcohol siloxane precursor (bis-(hydroxybutyl)tetramethyldisiloxane) via esterification with propargylic acid to attach alkynyl moieties on both ends, yielding **2a**. Posterior equilibration with octamethyl-cyclotetrasiloxane in the presence of trifluoroacetic acid[32] yielded compounds **2b** and **2c**, depending on the ratio of **2a** to octamethyl-cyclotetrasiloxane (Scheme 2.2).

THF solutions containing azide-**POS** and dialkynyldimethylsiloxane oligomers (**1** and **2** respectively, Figure 2.4) in different ratios were thermally cured in the oven at 80°C. After 120 min, depending on the initial ratio of polymers in the mixture, composites of different hardness ranging from elastomeric monoliths to highly viscous oils were obtained (Figure 2.12a). The elastomeric nature of the monoliths contrasts with the brittle nature of the POS solids and the liquid oligomeric silicones (Figure 2.12a). The polymer mixture can also be cured in different molds, yielding flexible and transparent films (Figure 2.12b, c).

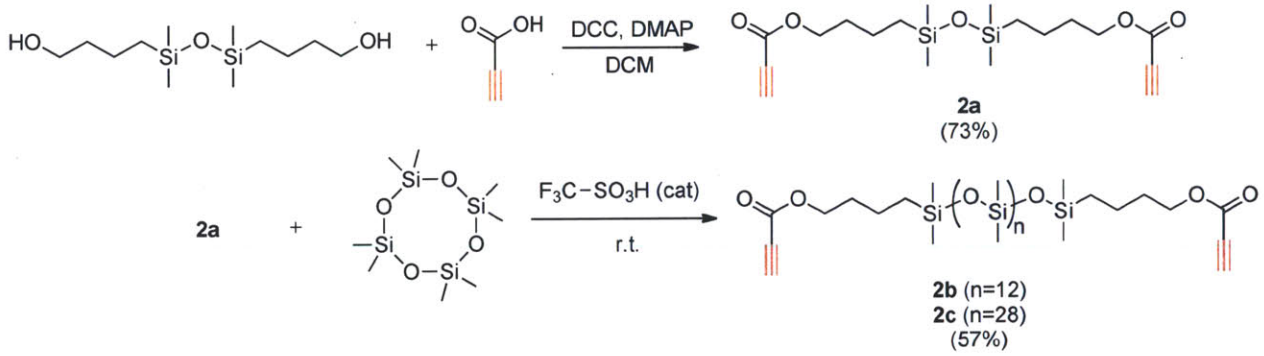

Scheme 2.2. Synthesis of **2a**, **2b** and **2c**

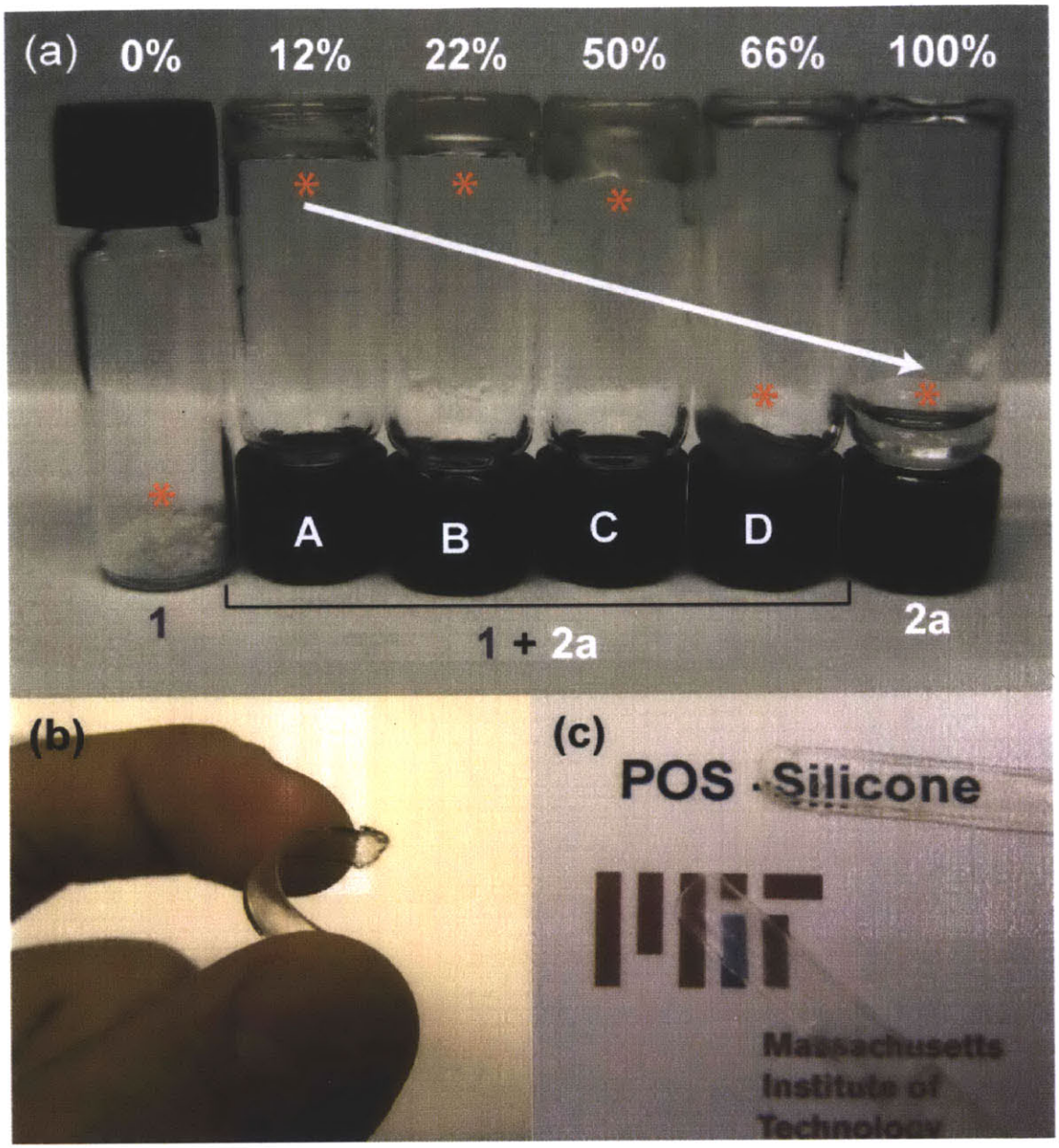

Figure 2.12. POS-silicone hybrid polymers. (a) Vials containing **1** (far left), **2a** (far right), and composites of **1** and **2a** (composition in wt%: A: 88%**1**, 12%**2a**; B: 78%**1**, 22%**2a**; C: 50%**1**, 50%**2a**; D: 33%**1**, 66% **2a**). The red star indicates the position of the hybrid polymer. (b) Flexible film of **1** + **2a**. (c) Transparent films of **1** + **2a**

The mechanical properties of the final hybrid polymer depend on the weight ratio of **POS** (**1**) to alkynyl silicone (**2**), the length of both polymers, the amount of functional groups for each component, and the cross-linking density.

The degree to which cross linking takes place can be related to the amount of side-chain azide groups reacted as determined by infrared spectroscopy (IR, Figure 2.13) and the number of azide groups per polymer chain (for this polymer a calculated average of 5 azide groups per polymer chain was determined considering the azide % and the length of the polymer).

By using IR, one can measure the decrease in intensity of the azide band (2120 cm^{-1}) compared to one of the sulfone bands (1308 cm^{-1}). The higher the content of POS **1**, the more cross linked the composites will be, which can be seen by the relative decrease in intensity of the band at 1718 cm^{-1} compared with the band at 2120 cm^{-1}, and the fact that the composites flow or form monoliths, depending on the composition (Figure 2.14).

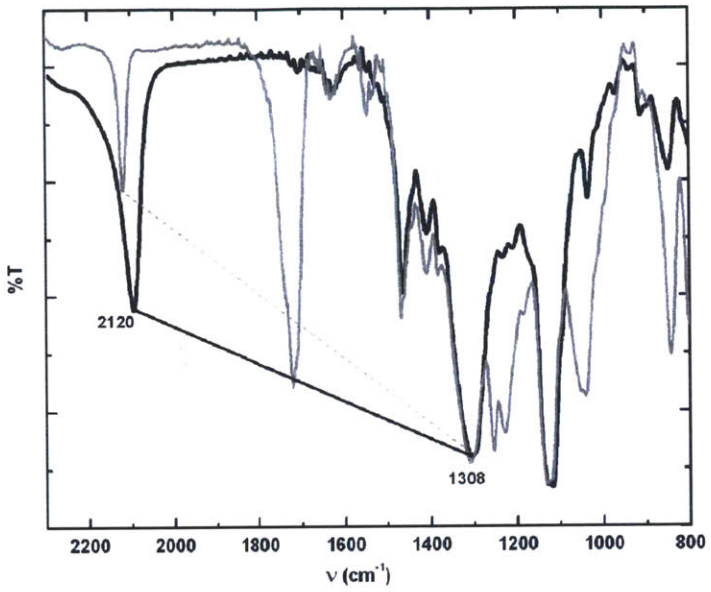

Figure 2.13. IR spectra of hybrid polymers of **POS 1** and silicone **2a**, for **POS 1** (bold) and a hybrid polymer containing 88 wt % of **POS 1** and 12 wt % of **2a** (light gray)

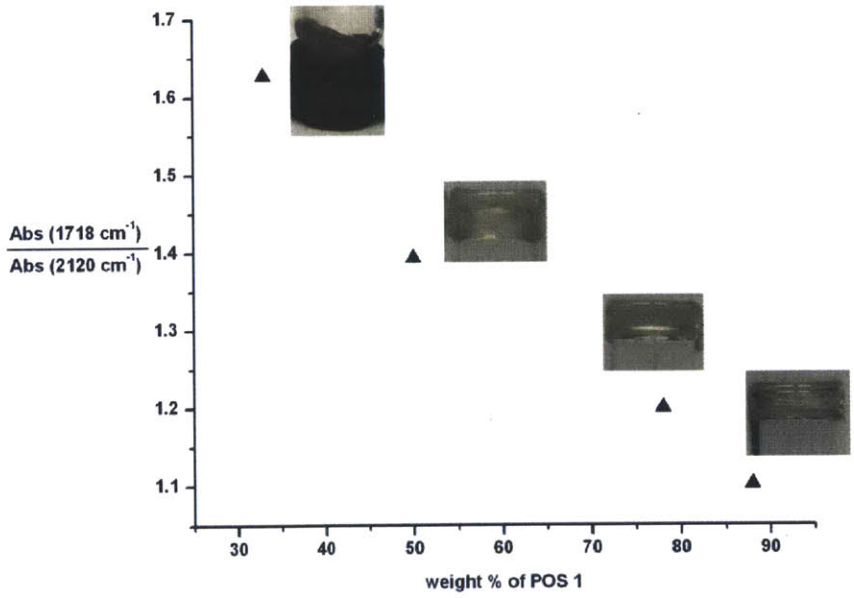

Figure 2.14. Relative intensity of the IR alkynyl band (1718 cm^{-1}) over the intensity of IR azide band (2120 cm^{-1}) plotted versus the weight % of **POS** (inset: pictures of the corresponding hybrid polymers)

The measured hardness of the hybrid polymers can range from that of a high viscosity oil like D, depicted in Figure 2.12a, to a monolith of a measured Shore A hardness of 90 (PDMS has a Shore A hardness of 50). Increasing the length of **2** has the effect of decreasing the hardness of the composite (Figure 2.15). The longer the silicone chain, the lower the measured hardness. This has to do with the incorporation of more flexible linkers in the composite, as the length of the silicone grows.

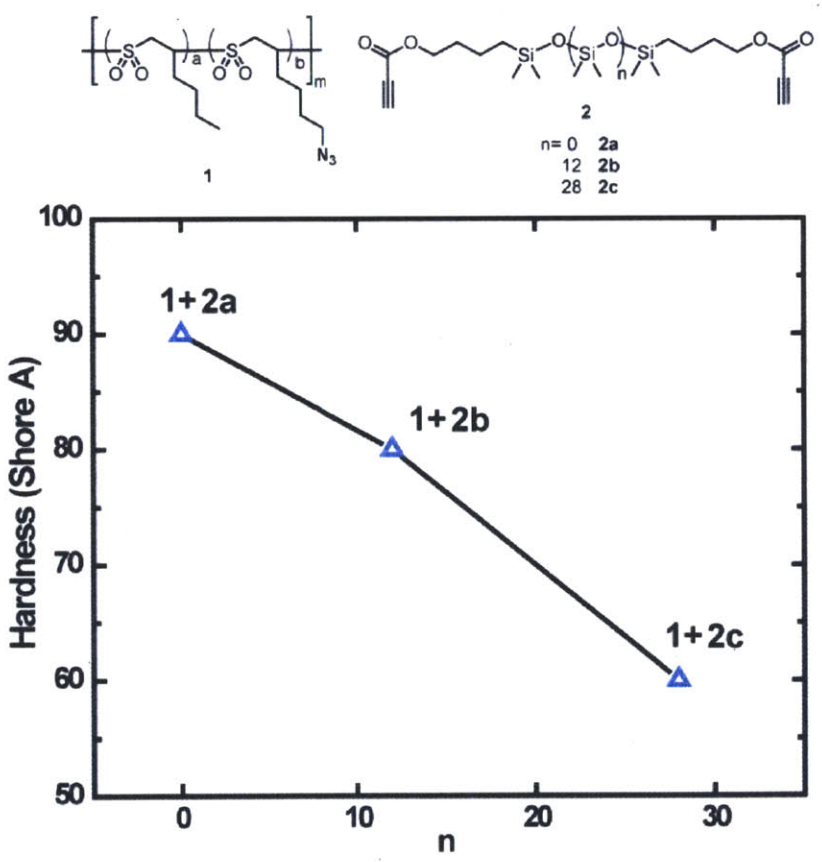

Figure 2.15. Shore A hardness of hybrid polymers formed of equimolar mixtures of azide and alkynyl moiety of the respective **POS** and silicone where the silicone has different lengths

Figure 2.16 shows an overall picture for the range of mechanical properties that can be achieved by varying several factors: the proportions of each component, different % of azide-containing repeat unit in the **POS** backbone, and different silicone lengths (each formulation with a different silicone chain length or azide content is denoted by a different geometrical shape, see legend). The hardness of **PDMS** is given as a reference value (red line). Unfilled data points represent formulations where the final composite was transparent and colorless; for filled data points the composite was opaque, probably due to phase segregation and microdomain formation.

It can be seen that the higher the content of silicone, or the longer the chain of the silicone component, the more opaque the composite is, so more phase segregation was induced. In general, the higher the weight content of **POS**, the higher the hardness, which correlates with the T_g values. A higher hardness of composites formed of **1** (12% azide) and **2** (n=0), represented with squares as compared to the composites formed of **1** (12% azide) and **2** (n=12) represented with triangles, can be attributed to a higher degree of cross-linking, since the mixtures are in general more homogenous and the click reaction will go to a higher extent. The higher hardness of composites formed of **1** (50% azide) and **2** (n=0), represented with a star as compared to the composites formed of **1** (12% azide) and **2** (n=0) represented with squares, can be attributed to the higher number of azide functionalities per **POS** chain, which results in a higher degree of cross-linking. The monolithic hybrid polymers were not transparent when the longest alkynyl silicone, **2c**, is used. This latter result is probably due to microprecipitation induced by phase segregation of both polymeric components.

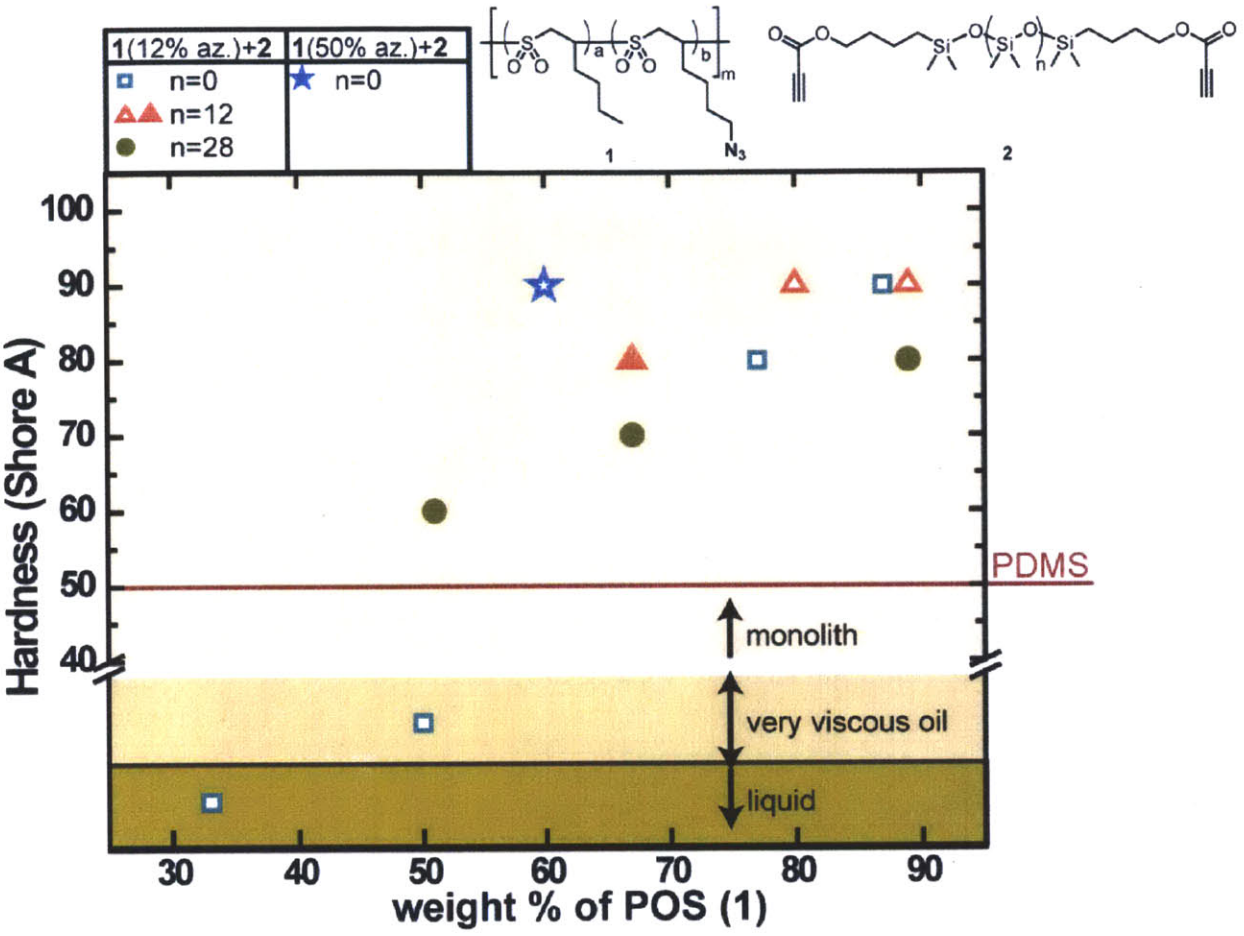

Figure 2.16. Shore A hardness of hybrid polymers formed from **POS 1** and silicone **2**, with varying ratios of **1**/**2**, different % of azide-containing repeat unit in the **POS** backbone, and different silicone lengths

The measured yield modulus for composites of **1** and **2a** (n=0) with 80 wt % of **POS** was in the 10 mPa range, which is in accordance with the incorporation of the high-T_g **POS** in the polymeric network. Measured yield modulus values of commercial **PDMS** using the same conditions and sample configuration were an order of magnitude lower.

2.5 Degradation Capabilities of the Hybrid Polymers

The decomposition of these composite materials when exposed to base was studied using a hybrid polymer labeled with a dye, Fat Brown B (**FBB**, Figure 2.17).

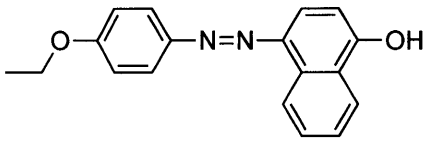

Fat Brown B **(FBB)**

Figure 2.17. Structure of dye Fat Brown B (**FBB**)

To form this hybrid polymer, alkynyl-**FBB** (**3**) was synthesized by a nucleophilic substitution reaction to attach an alkynyl moiety and then covalently tethered to the side chain of **POS 1** (Scheme 2.3) using conditions similar to those described on the first chapter of this thesis. Then, the hybrid polymer containing both the **FBB**-modified **POS** and a silicone was formed by reaction with compound **2a** under standard hybrid polymer formation conditions.

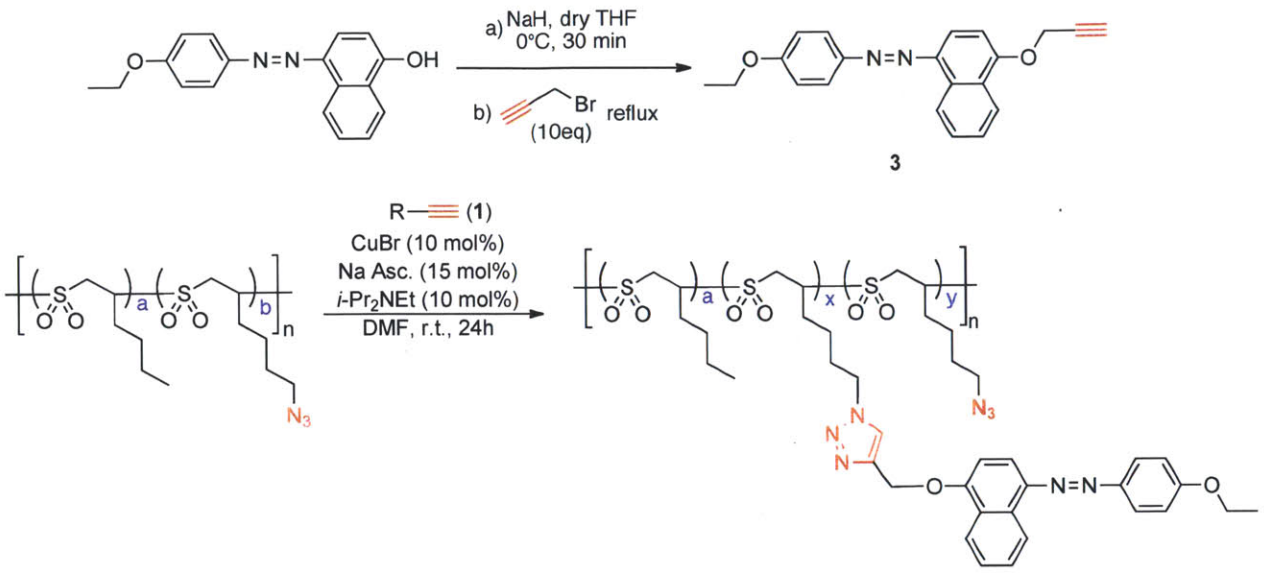

Scheme 2.3. Synthesis of alkynyl-**FBB** (**3**) and post-polymerization modification of **1**

The colored cross-linked hybrid polymer was expectedly insoluble in acetonitrile (the solution was not colored, Figure 2.18a). After addition of piperidine, the elastomer decomposed into its monomeric counterparts, releasing the monomer-tethered dye (FBB) into the acetonitrile solution. After only 5 min in a 0.03 M solution of piperidine in acetonitrile at 80°C, macroscopic mechanical failure was observed, and no macroscopic pieces of elastomer could be noticed (Figure 2.18b). As a result, the dye is completely leached into the solution.

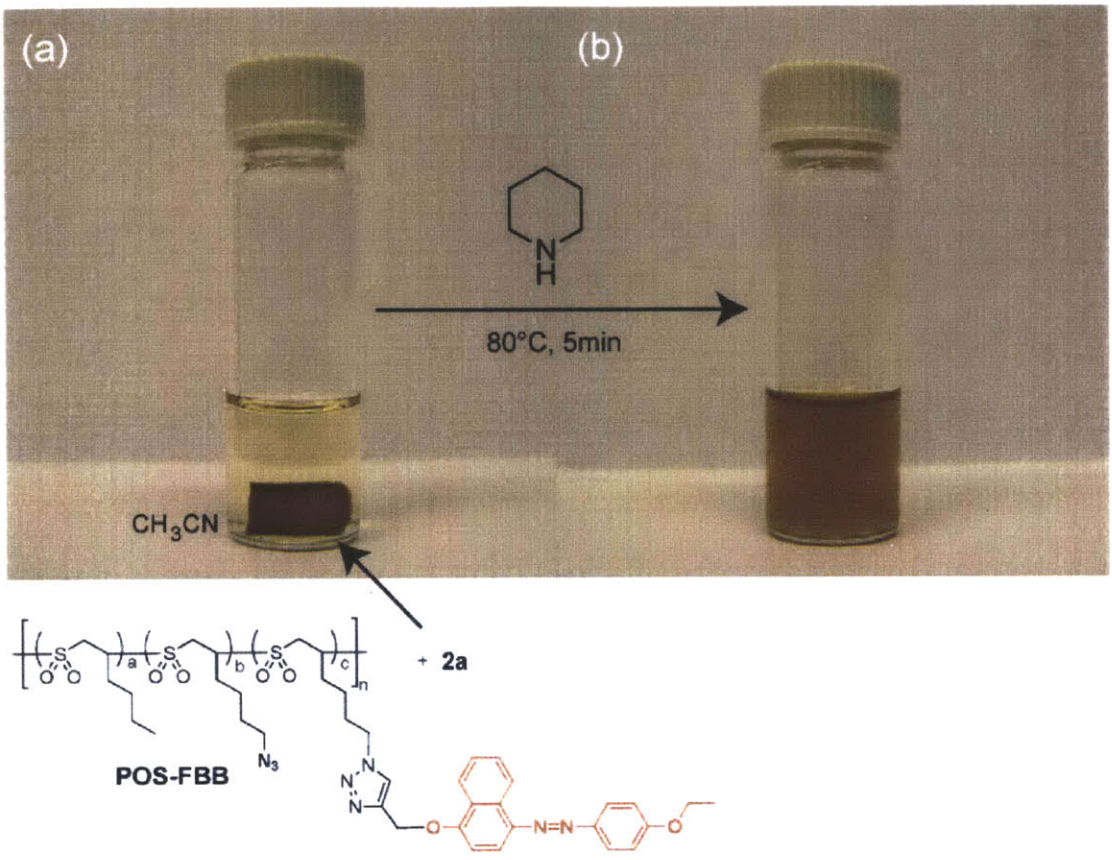

Figure 2.18. Hybrid polymer of **FBB**-tagged azide-containing **POS** with silicone **2a** (88 wt % of **POS-FBB**, 12 wt % of **2a**) in acetonitrile solution (a) before base addition and (b) after base addition

2.7 Conclusions

We have shown the synthesis of an elastomeric polymer composite that can be disassembled into its individual components when exposed to a mild base (piperidine). The composite is formed by curing a poly (olefin sulfone) and a silicone using "click" chemistry, and its components can be tailored to impart different properties to the final mixture. Different ratios of the two polymer components yield composites with varying mechanical properties/ hardness.

Its base-triggered decomposition is advantageous from the point of view of composite recycling and controlled release of chemicals.

2.8 Experimental Section

Materials: Unless otherwise stated, reagents were purchased from Sigma-Aldrich and used as received. Bis-(hydroxybutyl)tetramethyldisiloxane and octamethylcyclotetrasiloxane were obtained from Gelest and used as received.

NMR Spectroscopy: NMR spectra were obtained on a Bruker Avance (400 MHz). NMR chemical shifts are given in ppm referenced to referenced to either $CDCl_3$ (7.24 ppm for ^1H and 77.24 for ^{13}C) or acetonitrile-d^6 (1.94 ppm for ^1H) for the polymer degradation studies.

Infrared (IR) Spectroscopy: Fourier Transform infrared (FT-IR) spectroscopy was performed on a Perkin-Elmer model 2000 FT-IR spectrophotometer using the Spectrum v. 2.00 software package.

Molecular Weight Determination: Polymer molecular weights were determined at room temperature on a HP series 1100 GPC system in THF at 1.0 mL/min (1 mg/mL sample concentrations), approximate molecular weights were estimated using a polystyrene calibration standard.

Hardness Measurements: Hardness measurements were performed using a Rex 1500A Durometer Shore A type on samples with a thickness of 6 mm.

Hybrid Polymer Fabrication: In a typical composite synthesis, **POS 1** and alkynyl-silicone **2** were mixed in the desired ratio and dissolved in a minimal amount of THF (usually homogeneous solutions can be obtained with concentrations up to 400 mg/mL). The solution was vortexed for 15 min and poured in a Teflon mold. The composite was cured at 80°C in a vacuum oven for 120 min, after which time the hybrid polymer could be easily removed from the mold.

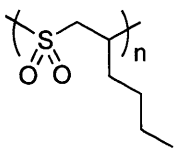

Poly (1-hexene sulfone) (P1HS). See Chapter 1 of this thesis for a detailed preparation.

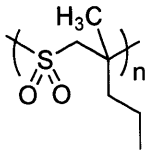

Poly (2-methyl-1-pentene sulfone) (P2MPS). See general **POS** synthesis in the first chapter of this thesis (98% yield). ^{1}H-NMR ($CDCl_3$) 0.9 (3H, br t), 1.53 (2H, br), 1.6-1.7 (3H, br), 2.0 (2H, br), 3.6 (2H, br). ^{13}C-NMR ($CDCl_3$) 14.63, 17.91, 20.21, 36.44, 36.82, 48.79, 67.96, 68.06. IR (cm^{-1}): 2967, 2876, 1715, 1470, 1297, 1117, 693, 460. GPC Mn = 5.3 KDa, Mw = 12.6 KDa, PDI = 2.39.

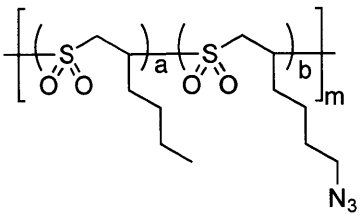

POS (1). See Chapter 1 of this thesis. In the composite formation experiments a polymer of Mn = 6.9K, PDI=1.38 was used. The ratio of 6-azido-1-hexenyl repeat unit to 1-hexenyl repeat unit was determined by ^{1}H NMR (Figure 2.19) from the relative integration of the peak highlighted in red, compared to the peak highlighted in blue and found to be of 12% azide-containing repeat. This is the azide content used for most experiments, unless otherwise specified.

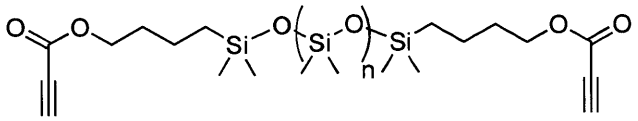

n= 0 **2a**
12 **2b**
28 **2c**

Alkynyl silicone 2a.[32] In a flame-dried and Ar-purged round bottom flask, bis-(hydroxybutyl)tetramethyldisiloxane (2.79g, 10 mmol) and propargyl alcohol (1.54 ml, 25 mmol) were dissolved at -45°C. DCC (4.13 g, 20 mmol) was added in small fractions over 20 min, during which time the reaction mixture turned turbid. DMAP (24 mg, 0.2 mmol) was added to the mixture, and after 30 min the reaction turned orange. The reaction was stirred and let warm-up to -10°C for 20h, after which 100 ml of anhydrous ether was added. The residual orange solid was filtered off and discarded, and the solvent was removed in vacuo. The crude was purified by column chromatography (hexanes:ethyl acetate, 95:5 to 75:25, TLC plates were revealed with a $KMnO_4$ solution) to yield the title compound as a colorless oil (2.80 g, 73%). ^{1}H-NMR ($CDCl_3$) 0.0 (12H, s), 0.5 (4H, t, J = 8.52 Hz), 1.4 (4H, m), 1.7 (4H, m), 2.9 (2H, s), 4.2 (4H, t, J = 6.62 Hz). ^{13}C-NMR ($CDCl_3$) 0.53, 18.02, 19.78, 31.92, 66.31, 74.65, 74.99, 153.05.

Alkynyl silicone 2b, 2c. Different lengths were obtained using modified conditions[32] for the equilibration reaction of previously reported compound **2a**. In a representative synthesis, compound **2a** (1 g, 2.6 mmol or 0.5 g, 1.3 mmol for the synthesis of **2b** and **2c**, respectively) and octamethyl-cyclotetrasiloxane (3 g, 10 mmol) were mixed together and stirred at room temperature with a magnetic stirbar at 600 rpm for 5 min in a flask connected to a drying tube. Trifluoromethylsulfonic acid (0.4 mL, 4.6 mmol or 0.2 mL, 2.3 mmol for **2b** or **2c**) was added, and the mixture was stirred for 72 h. Magnesium oxide (0.8 g for **2b** and 0.4 g for **2c**) and 40 mL of hexanes were added to the reaction mixture and stirred for 1 h. The reaction mixture was filtered through Celite, and the solvent was removed under reduced pressure. Purification by Kugelrohr distillation at 150°C for 2 h yielded **2b** (59%) or **2c** (57%) as transparent, colorless

oils. The number of dimethylsiloxane units was determined using ^{1}H NMR, by comparison of the integration signal of the terminal 2 alkynyl protons at 2.88 ppm to the signal of the silicon-linked methyl groups at 0.03 ppm to make 14 $Si(CH_3)_2$ repeat units (**2b**, n=12) or 30 $Si(CH_3)_2$ repeat units (**2c**, n=28) (Figure 2.20). The increase in molecular weight was also characterized by THF-GPC, and the Mn vs polystyrene standards were 2253, 4328, and 5981 for **2a**, **2b** and **2c**.

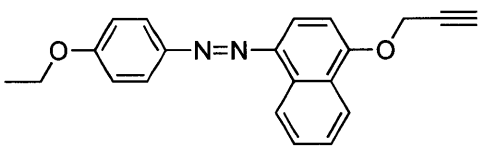

1-(4-ethoxyphenyl)-2-(4-(prop-2-yn-1-yloxy)naphthalen-1-yl)diazene (3). To a solution of Fat Brown B (FBB) (100 mg, 0.34 mmol) in anhydrous THF (6ml) was added NaH (9 mg, 0.37mmol) at 0°C. The solution was stirred at 0°C for 30 min and propargyl bromide (80% in toluene, 0.2ml, 1.8 mmol) was added. The reaction was refluxed for 6h, after which another fraction of propargyl bromide (80% in toluene, 0.2ml, 1.8 mmol) was added. After removal of the solvent under vacuum, the crude was purified by column chromatography using hexanes: ethyl acetate (9:1) as the eluent to give **3** as a dark orange powder (110 mg, 98%). ^{1}H-NMR ($CDCl_3$) 1.46 (3H, t, J = 6.8 Hz), 2.56 (1H, t, J = 2.4 Hz), 4.12 (2H, q, J = 6.8 Hz), 4.95 (2H, d, J = 2.4 Hz), 7.01 (d, 2H, J = 9.2 Hz), 7.56-7.64 (4H, m), 7.82 (1H, d, J = 8.4 Hz), 7.98 (2H, d, J=9.2 Hz), 8.31 (1H, d, J=8.4 Hz), 8.91 (1H, d, J=8.4 Hz). ^{13}C-NMR ($CDCl_3$) 15.03, 56.52, 64.05, 76.21, 77.45, 105.58, 112.28, 114.92, 115.63, 121.46, 122.29, 123.49, 124.96, 125.95, 126.15, 127.53, 132.66, 142.71, 147.85, 155.67, 161.35. IR (cm^{-1}): 3217, 2919, 2112, 1602, 1576, 1501, 1256, 1233, 1088, 921, 833, 823, 761. m/z (HR-MS) found $(M+H)^+$ 331.26, theoretical 331.14.

Click-chemistry reaction to tag azide-POS with FBB. The conditions for the Cu-catalyzed postpolymerizarion modification of azide-POS was described in the first chapter of this thesis. For the FBB-tagged composite studies, a POS containing 12% azide on the side chain was used, with a ratio of azide to alkynyl- FBB of 10 to 1 for the click chemistry reaction.

2.9 Additional Figures

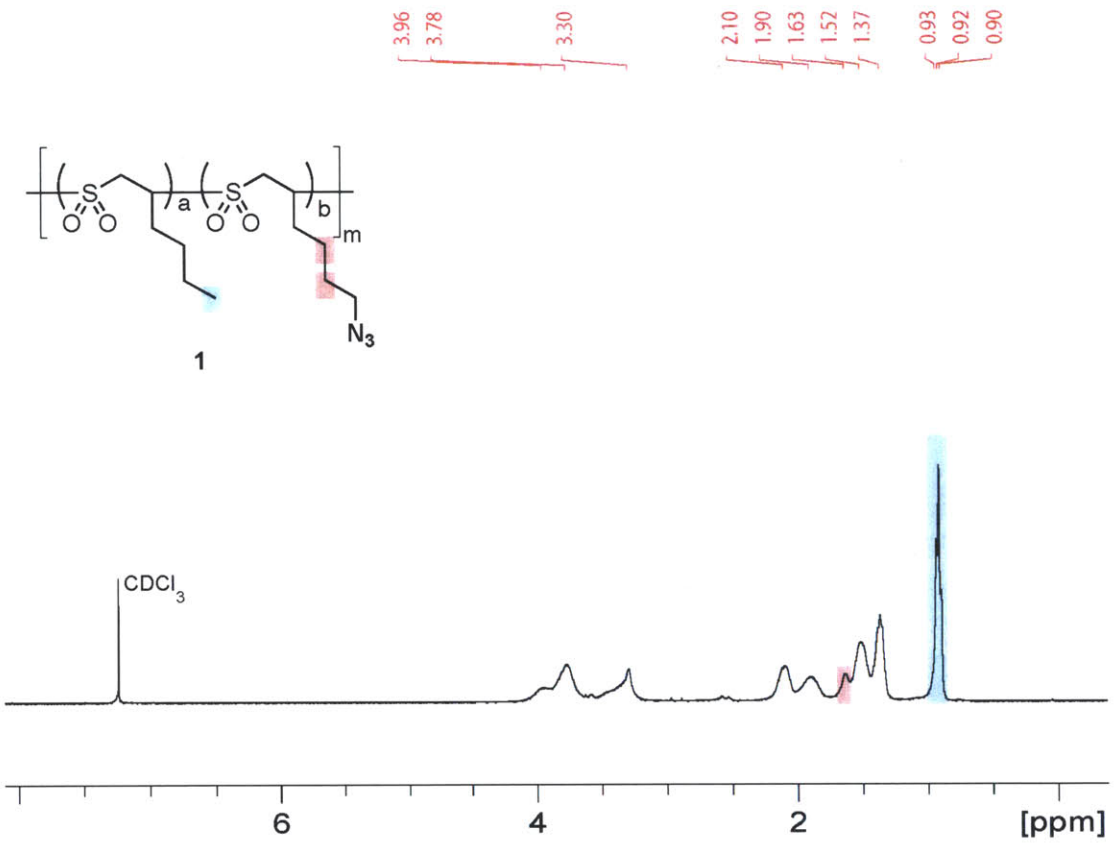

Figure 2.19. Determination of azide content from the ^{1}H-NMR ($CDCl_3$) spectrum of compound **1**

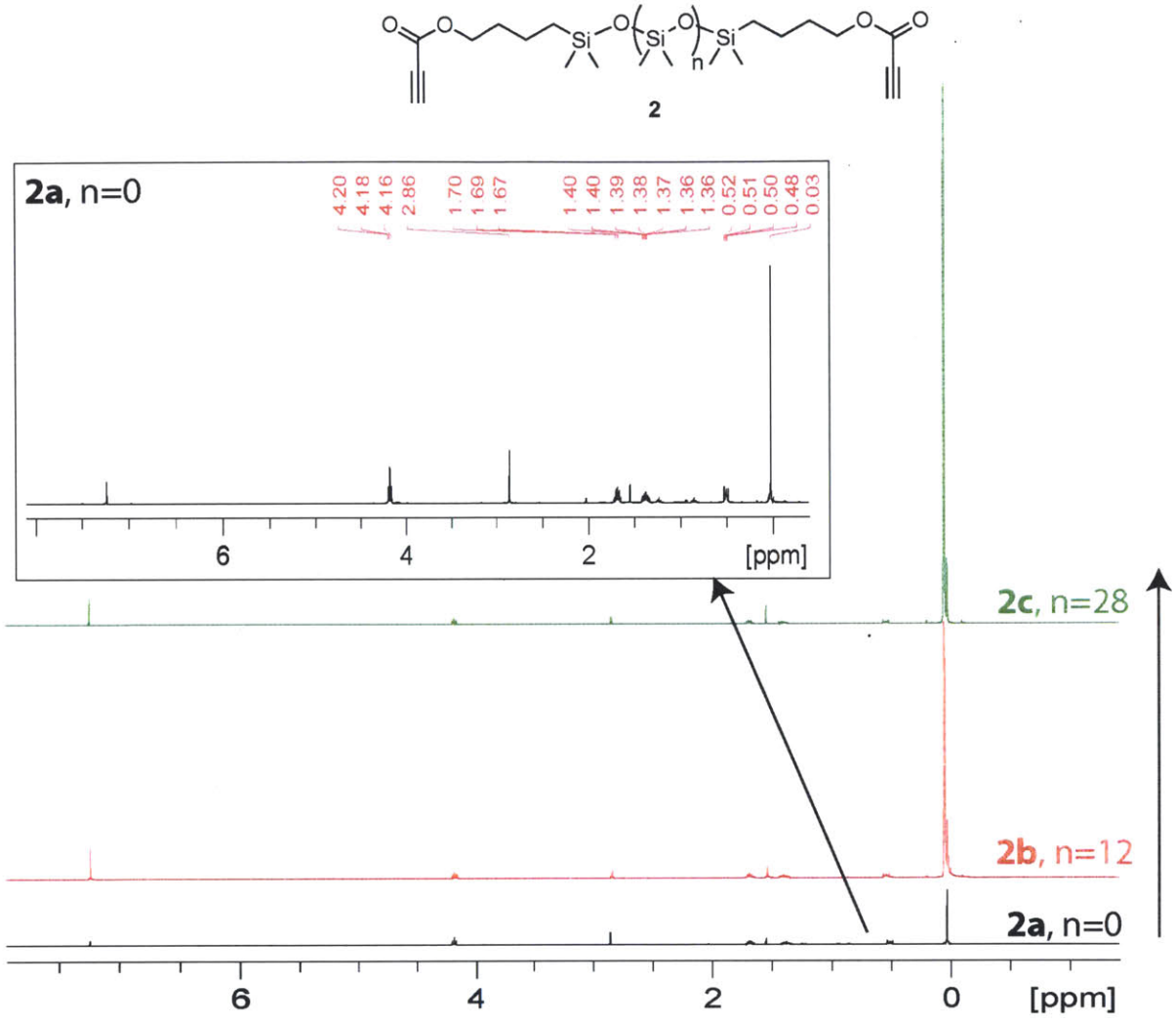

Figure 2.20. Determination of the length of compounds 2a, 2b, 2c by ^{1}H-NMR ($CDCl_3$)

2.10 References and Notes

(1) Vinogradov, A.; Schwartz, M. *Encyclopedia of Smart Materials*; John Wiley & Sons: Weinheim, 2002; Vols. 1 and 2, pp 780-792.

(2) Lendlein, A.; Kelch, S. *Angew. Chem. Int. Ed.* **2002**, *41*, 2034-2057.

(3) (a) Middleton, J. C.; Tipton, A. J. *Biomaterials* **2000**, *21*, 2335-2346. (b) Gilding, D. K.; Reed, A. M. *Polymer* **1979**, *20*, 1454-1458. (c) Gilding, D. K.; Reed, A. M. *Polymer* **1979**, *20*, 1459-1464.

(4) (a) Schild, H. G. *Prog. Polym. Sci.* **1992**, *17*, 163–249. (b) Heskins, M.; Guillet, J. E. *J. Macromol. Sci., Part A: Pure Appl. Chem.* **1968**, *2*, 1441–1455.

(5) Davis, D. A.; Hamilton, A.; Yang, J.; Cremar, L. D.; Van Gough, D.; Potisek, S. L.; Ong, M. T.; Braun, P. V.; Martinez, T. J.; White, S. R.; Moore, J. S.; Sottos, N. R. *Nature* **2009**, *459*, 68–72.

(6) (a) Bergman, S. D.; Wudl, F. *J. Mater. Chem.* **2008**, *18*, 41–62. (b) Yuan, Y. C.; Yin, T.; Rong, M. Z.; Zhang, M. Q. *Polym. Lett.* **2008**, *2*, 238–250.

(7) (a) Zelikin, A. N.; Li, Q.; Caruso, F. *Chem. Mater.* **2008**, *20*, 2655-2661. (b) Pastine, S. J.; Okawa, D.; Zettl, A.; Frechet, J. M. J. *J. Am. Chem. Soc.* **2009**, *131*, 13586-13587. (c) Johnston, A. P. R.; Such, G.; Caruso, F. *Angew. Chem., Int. Ed.* **2010**, *49*, 2664–2666. (d) Ochs, C. J.; Such, G. K.; Yan, Y.; van Koeverden, M. P.; Caruso, F. *ACS Nano* **2010**, *4*, 1653–1663. (e) Esser-Kahn, A. P.; Sottos, N. R.; White, S. R.; Moore, J. S. *J. Am. Chem. Soc.* **2010**, *132*, 10266–10268.

(8) Brook, M. A. *Silicon in Organic, Organometallic and Polymer Chemistry*; Wiley: New York, 2000; p 256.

(9) Clarson, S. J.; Semlyen, J. A. *Siloxane Polymers*; PTR PrenticeHall: Englewood Cliffs, NJ, 1993.

(10) (a) Noll, W. *Chemistry and Technology of the Silicones*; Academic Press: New York, 1968. (b) Rochow, E. G. *Silicon and Silicones*; Springer-Verlag: Berlin, 1987. (c) Warrick, E. L. *Forty Years of Firsts- The Recollections of a Dow Corning Pioneer*; McGraw-Hill: New York, 1990.

(11) Cademartiri, L.; Ozin, G. A. *Concepts of Nanochemistry*; Wiley- VCH: Weinheim, 2009; pp 113-139.

(12) Clarson, S. J.; Dodgson, K. *Polymer* **1985**, *26*, 930-934.

(13) Ward, I. M.; Sweeney, J. *An Introduction to the Mechanical Properties of Solid Polymers*; John Wiley and Sons: Weinheim, 2004.

(14) Xia, Y. N.; Whitesides, G. M. *Annu. Rev. Mater. Sci.* **1998**, 153-184.

(15) (a) Whitesides, G. M. *Nature* **2006**, *7101*, 368–373. (b) McDonald, J. C.; Duffy, D. C.; Anderson, J. R.; Chiu, D. T.; Wu, H. K.; Schueller, O. J. A.; Whitesides, G. M. *Electrophoresis* **2000**, *21*, 27–40.

(16) Patnode, W. J.; Wilcock, D. F. *J. Am. Chem. Soc.* **1946**, *68*, 358-363.

(17) Grassie, N.; MacFarlane, I. G. *Eur. Polym. J.* **1978**, *14*, 875–884.

(18) Eaborn, C. *Organosilicon Compounds*; Butterworths: London, 1960.

(19) Nitzsche, S.; Wick, M. German Patent 930481, 1953.

(20) Wilczek, L.; Chojnowski, *J. Makromol. Chem.* **1983**, *184*, 77-90.

(21) (a) McGrath, J. E. *Ring-Opening Polymerization: Kinetics, Mechanisms and Synthesis*; ACS Symp. Ser. 286; American Chemical Society: Washington, DC, 1985. (b) Frisch, K. C.; Reegen, S. L. *Ring-Opening Polymerization*; Dekker: New York, 1969.

(22) (a) Rashkov, I. B.; Gitsov, I. *J. Polym. Sci., Polym. Chem.* **1986**, *24*, 155-165. (b) Carmichael, J. B.; Heffel, J. *J. Phys. Chem.* **1965**, *69*, 2213-2217.

(23) Chu, H.-K.; Cross, R. P.; Crossan, D. I. *J. Organomet. Chem.* **1992**, *425*, 9-17.

(24) van der Weij, F. W. *Makromol.Chem.* **1980**, *181*, 2541-2548.

(25) Bueche, A. M. *J. Polym. Sci.* **1956**, *19*, 297-306.

(26) *Thiol/ene chemistry*: (a) Bokerman, G. N.; Colquhoun, J. A.; Gordon, D. J. Radiation-curable mercaptoalkyl vinyl polydiorganosiloxanes, method of coating there with and coated article. U.S. Patent 4,052,529, March 3, 1976. (b) Takamizawa, M.; Okada, F.; Hara, Y.; Aoki, H. Photocurable organopolysiloxane compositions. U.S. Patent 4,303,484, Aug 22, 1979. *Hydrosilane/ene addition*: (c) Gant, G. A. L. UV curable composition. U.S. Patent 4,064,027, Sept 28, 1973. (d) Chang, M. S. H. Radiation curable composition of vinyl polysiloxane and hydrogen polysiloxane with photosensitizer. U.S. Patent 4,435,259, Sept 1, 1982. *Acrylate polymerization*: (e) Cully, M.; Pines, A. N.; Metzler, R. B.; Babian, G. W. Radiation curable silicone release compositions. U.S. Patent 4,201,808, June 12, 1978. *Cationic polymerization of epoxy functionalities*: (f) Eckberg, R. P.; Riding, K. D.; Grenoble, M. E.; John, S. M. *Adhes. Age* **1989**, 24.

(27) Dunham, M. L.; Bailey, D. L.; Mixer, R. Y. *Ind. Eng. Chem.* **1957**, *49*, 1373-1376.

(28) (a) Lee, J. N.; Jiang, X.; Ryan, D.; Whitesides, G. M. *Langmuir* **2004**, *20*, 11684-11691. (b) Ye, H.; Gu, Z.; Gracias, D. H. *Langmuir* **2006**, *22*, 1863-1868.

(29) (a) Huisgen, R. *1,3-Dipolar Cycloaddition Chemistry*; Wiley: New York, 1984; pp 1-176. (b) Rostovtsev, V. V.; Green, L. G.; Fokin, V. V.; Sharpless, K. B. *Angew. Chem., Int. Ed.* **2002**, *41*, 2596–2599.

(30) Kolb, H. C.; Finn, M. G.; Sharpless, K. B. *Angew. Chem., Int. Ed.* **2001**, *40*, 2004-2021.

(31) (a) Sumerlin, B. S.; Vogt, A. P. *Macromolecules* **2010**, *43*, 1-13. (b) Lutz, J.-F. *Angew. Chem., Int. Ed.* **2007**, *46*, 1018-1025. (c) Fournier, D.; Hoogenboom, R.; Schubert, U. S. *Chem. Soc. Rev.* **2007**, *36*, 1369-1380. (d) Nurmi, L.; Lindqvist, J.; Randev, R.; Syrettb, J.; Haddleton, D. M. *Chem. Commun.* **2009**, *19*, 2727-2729. (e) Fijten, M. W. M.; Haensch, C.; van Lankvelt, B. M.; Hoogenboom, R.; Schubert, U. S. *Macromol. Chem. Phys.* **2008**, *209*, 1887-1895. (f) Saha, A.; Ramakrishnan, S. *Macromolecules* **2009**, *42*, 4028-4037. (g) Opsteen, J. A.; van Hest, J. C. M. *J. Polym. Sci., Part A: Polym. Chem.* **2007**, *45*, 2913-2924.

(32) Gonzaga, F.; Yu, G.; Brook, M. A. *Macromolecules* **2009**, *42*, 9220-9224.

(33) Gonzaga, F.; Yu, G.; Brook, M. A. *Chem. Commun.* **2009**, 1730-1732.

(34) (a) Solonina, W. Russ. *J. Phys. Chem.* **1898**, *30*, 826-842. (b) Fawcett, A. H. *Encylopedia of Polymer Science & Engineering*; Wiley-VCH: Weinheim, 1987; Vol. 10, pp 408-432.

(35) Chatelain, *J. Adv. Chem. Ser.* **1969**, *91*, 529-535.

(36) Takehisa, M.; Kurihara, H.; Yagi, T.; Watanabe, H.; Machi, S. Gypsum compositions for gypsum-thermoplastic composite. US Patent 3,873,492, Nov 22, 1972.

(37) Johnston, T. E.; Matt, J. W. Antistatic Additive Compositions. U.S. Patent 3,807,977, June 30, 1972.

(38) Bowden, M. J.; Thompson, L. F. *J. Electrochem. Soc.* **1974**, *121*, 1620-1623.

(39) Bowmer, T. N.; O'Donnell, J. H. *J. Macromol. Sci., Part A: Pure Appl. Chem.* **1982**, *A17*, 243-263.

(40) Ayscough, P. B.; O'Donnell, J. H. *Trans. Faraday Soc.* **1965**, *61*, 1110-1117.

(41) Bowden, M. J.; O'Donnell, J. H. *Developments in Polymer Degradation*; Elsevier Applied Science Publishers, Ltd.: Barking, 1985; Vol. 6, pp 21-61.

(42) Brown, J. R.; O'Donnell, J. H. *Macromolecules* **1972**, *5*, 109-114.

(43) Lobez, J. M.; Swager, T. M. *Angew. Chem., Int. Ed.* **2010**, *49*, 95-98.

(44) (a) Shinoda, T.; Nishiwaki, T.; Inoue, H. *J. Polym. Sci., Part A* **2000**, *3*, 2760-2766. (b) Yaguchi, H.; Sasaki, T. *Macromolecules* **2007**, *40*, 9332-9338. (c) Sasaki, T.; Yaguchi, H. *J. Polym. Sci., Part A: Polym. Chem.* **2009**, *47*, 602-613.

(45) (a) Bowden, M. J.; Thompson, L. F. *J. Appl. Polym. Sci.* **1973**, *17*, 3211-3221. (b) Pampalone, T. R. *J. Imaging Sci.* **1986**, *30*, 160-166. (c) Yao, N.; Wang, Z. L. *Handbook of Microscopy for Nanotechnology*; Kluwer Academic Publishers: Boston, 2005; pp 287-319.

(46) Odian, G. *Principles of Polymerization*; John Wiley & Sons: Hoboken, 2004; p 132.

(47) (a) Fawcett, A. H.; Fee, S. *Macromolecules* **1982**, *15*, 933-935. (b) Coleman, M. M.; Varnell, D. F. *Macromolecules* **1982**, *15*, 935-937.

(48) Bordwell, F. G.; Drucker, G. E.; McCollum, G. J. *J. Org. Chem.* **1982**, *47*, 2504-2510.

(49) Bordwell, F. G. *Acc. Chem. Res.* **1988**, *21*, 456-463.

(50) Cook, R. E.; Dainton, F. S. *J. Polym. Sci.* **1957**, *26*, 351-364.

CHAPTER 3

Side-Chain Functionalized Polythiophene Additives: Design, Synthesis and Properties

Adapted and reprinted in part with permission from:

Lobez, J. M.; Andrew, T. L.; Bulović, V.; Swager, T. M. "Improving the Performance of P3HT-Fullerene Bulk Heterojunction Solar Cells with Side-Chain Functionalized Polythiophene Additives: A New Paradigm for Polymer Design" *ACS Nano* **2012** DOI: 10.1021/nn204589u

3.1 Introduction

The increasing world demand for energy has created a great need for the development of cheap and efficient alternative energy sources. Solar cell technologies in which the incoming light of the sun is transformed into electric current are among the most promising candidates, since the amount of energy that could potentially be harnessed from the sun is much greater than the current demand for energy. The main kinds of solar cells are silicon (**Si**) based solar cells, dye-sensitized solar cells (**DSSC**) and organic-based solar cells

Silicon (**Si**) based solar cells make use of a semiconducting layer of **Si** as the active layer, which absorbs the incoming photons and generates charge carriers. **Si** solar cells are by far the most widespread photovoltaic systems available on the market. They can display the highest power conversion efficiencies (PCEs), of ~25% for single crystal individual cells, while commercial cells have an average PCE of about ~14%. However, they have the disadvantage of being relatively heavy, and can only be used on rigid, flat surfaces owing to the lack of flexibility of the Si films used as the active layer.

Dye-sensitized solar cells (**DSSC**, also known as Grätzel cells)[1] are hybrid solar cells based on both inorganic and organic materials. In a traditional device architecture, an organic dye is used to absorb most of the incoming photons. The generated excitons separate into the corresponding charges, which are transported by an inorganic semiconductor (such as TiO_2) acting as the electron conductor of the cell, and an electrolyte acting as the hole conductor in the cell. Dye-sensitized solar cells have moderate PCEs (of about 13% for individual cells)[2] and owing to the need to encapsulate the cells to prevent electrolyte leakage, this kind of cells are also mostly rigid and flat.

Organic-based solar cells show comparatively lower efficiencies than **Si** ones[3] (of up to about 9% for individual cells), but intensive research efforts over the past decade have made organic-based bulk heterojunction (BHJ)[4] solar cells viable market competitors,[5] and their stabilities have also been much improved.[6] Polymer-based solar cells have the advantages of any organic-based materials and are of particular interest since they can be easily printed or cast on both rigid and flexible surfaces.[7]

3.1.1 Organic Photovoltaics

As mentioned above, organic photovoltaic systems have the advantages of most organic systems: easy and cheap processing, chemical tunability to influence the final material properties, and they can be used flexible devices. Even though some advances have been made in the recent years for the development of thin film inorganic photovoltaic cells that are somewhat flexible and lighter, organic solar cells are the main choice when solar cells need to be deployed on non-flat surfaces, when the solar cell is going to be bent while being used or when the solar cell needs to be incorporated in fabrics.

In general, when solar cells are exposed to light, the processes that take place are the following: first, the photons are absorbed by the active layer of the solar cell, which leads to exciton generation in this active layer. Then, the excitons migrate and are eventually dissociated into two charges: a hole and an electron. Finally, charge migration and collection across the electrodes occurs under a bias voltage.

For the case of organic solar cells, usually at least two different components are regularly used for the active layer: a hole conducting (*p-type*) component or donor and an electron conducting (*n-type*) component or acceptor.[8] The need for a two-component system arises from

the fact that the dielectric constant of organic materials is relatively low, so for exciton dissociation to happen these two components are mixed and when excitons reach the interface, charge separation is favored.

Owing to the fact that the exciton diffusion length is relatively short, the most successful formulations of a *p-type* and an *n-type* component have been bulk heterojunctions (BHJ) of the two where the amount of interface is maximal, as supposed to a layered configuration. In these heterojunctions, the exciton dissociation occurs at the interface between the *p-type* and the *n-type* components, which are mixed and annealed with the purpose of creating an amorphous bicontinuous phase with the right morphology: the domain size needs to be small enough to maximize the amount of interface, while keeping conduction pathways for charges to reach the corresponding electrodes without yielding recombination.

For the specific case of an organic BHJ solar cell, the processes that take place after light absorption described above are summarized graphically on Figure 3.1. It is clear that since many of these phenomena occur at the interface of the heterojunction, this interface needs to fulfill some requirements: high surface area, right morphology, right alignment of molecular orbitals and appropriate environment to promote charge separation and prevent charge recombination once dissociation has already happened.

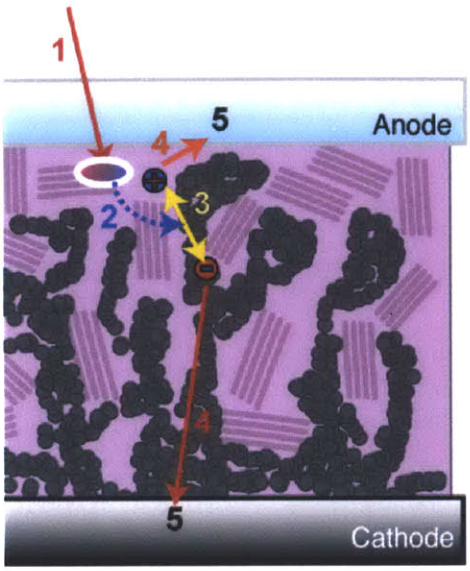

1. Photon absorption, exciton generation
2. Exciton migration to the interface
3. Exciton dissociation and charge separation at the interface
4. Charge migration
5. Charge collection

Figure 3.1. Summary of the processes that take place in an organic bulk heterojunction (BHJ) solar cell from the moment light absorption occurs until the charge is collected across the electrodes

The performance and efficiency of organic solar cells is evaluated by measuring the current (J) vs. voltage (V) curves of the solar cell under illumination conditions (typically the spectrum of wavelengths used and intensity are normalized to achieve 1 sun). The resulting J/V curve is depicted on Figure 3.2a. The ideal efficiency that could be obtained from the solar cell is determined by the area of the rectangle defined by the values of the short circuit current (J_{SC}) and the open circuit voltage (V_{OC}). In an ideal solar cell, this would be the actual efficiency and the shape of the J/V curve would be a perfect rectangle, but in real cells the actual power conversion efficiency (PCE) is determined by the rectangle *circumscribed* within the J/V curve. Therefore, the resulting formula to define the PCE of any given cell (Figure 3.2b) needs to take into account not only the J_{SC}, V_{OC} but also the fill factor (FF). In order to improve the PCE of any solar cell, one can either increase the J_{SC}, V_{OC} and/or the fill factor (FF) in the directions indicated on

Figure 3.2a. One of the main shortcomings of organic solar cells when compared to Si-based ones, is their significantly lower J_{SC}.

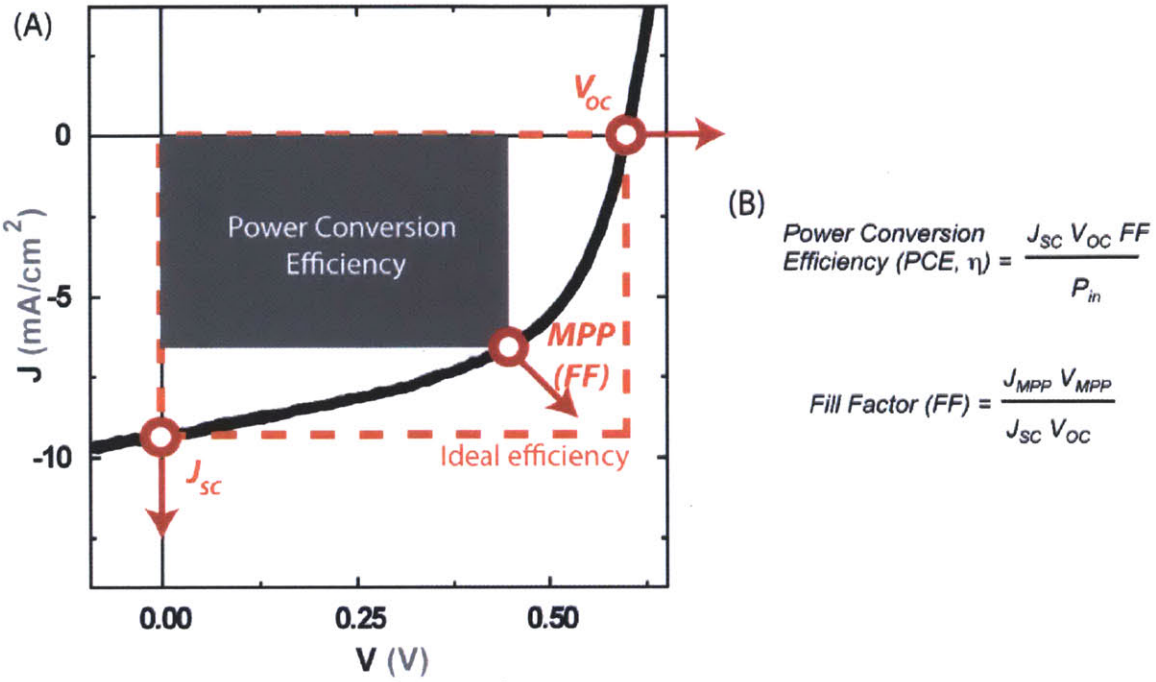

Figure 3.2. (A) J/V curves for a BHJ solar cell, showing the short circuit current (J_{SC}) and the open circuit voltage (V_{OC}). (B) Formula to calculate the power conversion efficiency (PCE) and fill factor (FF) of a solar cell

A variety of device and material factors limit the performance of BHJ solar cells, but the properties of the photoactive layer are the primary determinant of the maximum achievable PCE. The ideal donor–acceptor mixture in a BHJ structure should exhibit a bicontinuous network with domain widths within twice that of the exciton diffusion length and a high donor–acceptor interfacial area to favor exciton dissociation and efficient transport of separated charges to the respective electrodes.[9] In the specific case of polymer solar cells, the miscibility between the

donor and the acceptor, the crystallization of both phases, and the scale of the phase separation in the BHJ thin film are all critical to the overall performance of BHJ OPVs.[10,11,12,13,14]

Much work has been dedicated in the last years to the development of new conjugated polymers and small molecules to replace either the donor or the acceptor in BHJ solar cells, with two main goals:[15]

a) Improving band gap matching and increasing the V_{OC}

b) Increase the amount of excitons absorbed by the active layer by improving its near infra-red absorption, which leads to an increase in the J_{SC}

These approaches to improve PCE present the problems of having to design a new structure from scratch every time a new candidate is sought and having to employ lengthy multi-step syntheses, which are time and resource consuming and lead to polymers with dubious commercialization potential.

An alternative to improve solar cell power conversion has been the use of additives to increase the efficiency of already-optimized donor/acceptor BHJ systems. Most of these approaches are based on the addition of high boiling point dihaloalkanes (such as diiodooctane, DIO), which influences the annealing process during the fabrication of the active layer and helps reach optimized morphologies. However successful, these approaches are limited in the scope of additive choice and further optimization.

3.1.2 P3HT/PC_nBM Bulk Heterojunctions

Arguably one of the most studied organic photovoltaic systems is the donor–acceptor BHJ formed by mixtures of regioregular poly (3-hexylthiophene) (**rr-P3HT**) and soluble fullerene derivatives, such as phenyl-$C_{61/71}$-cetylbutyric acid methyl ester (**$PC_{61}BM$/$PC_{71}BM$**).[16]

These BHJs (Figure 3.3a) are a benchmark OPV structure, with average power conversion efficiencies (PCEs) of around 3%, being 5% the record under AM 1.5 conditions (100 mW/cm2).[17] The resulting domain size after annealing is about 10-15 nm, and direct imaging and characterization of these domains has proven difficult, owing to the small size of the features, their random distribution, and the lack of contrast between domains, since the elemental composition is similar. On Figure 3.3b, the picture of a **rr-P3HT/$PC_{61}BM$** BHJ is shown, for which defocused conditions are required. This makes the exact quantification of the domain size difficult, and affects the reproducibility of the measurement.

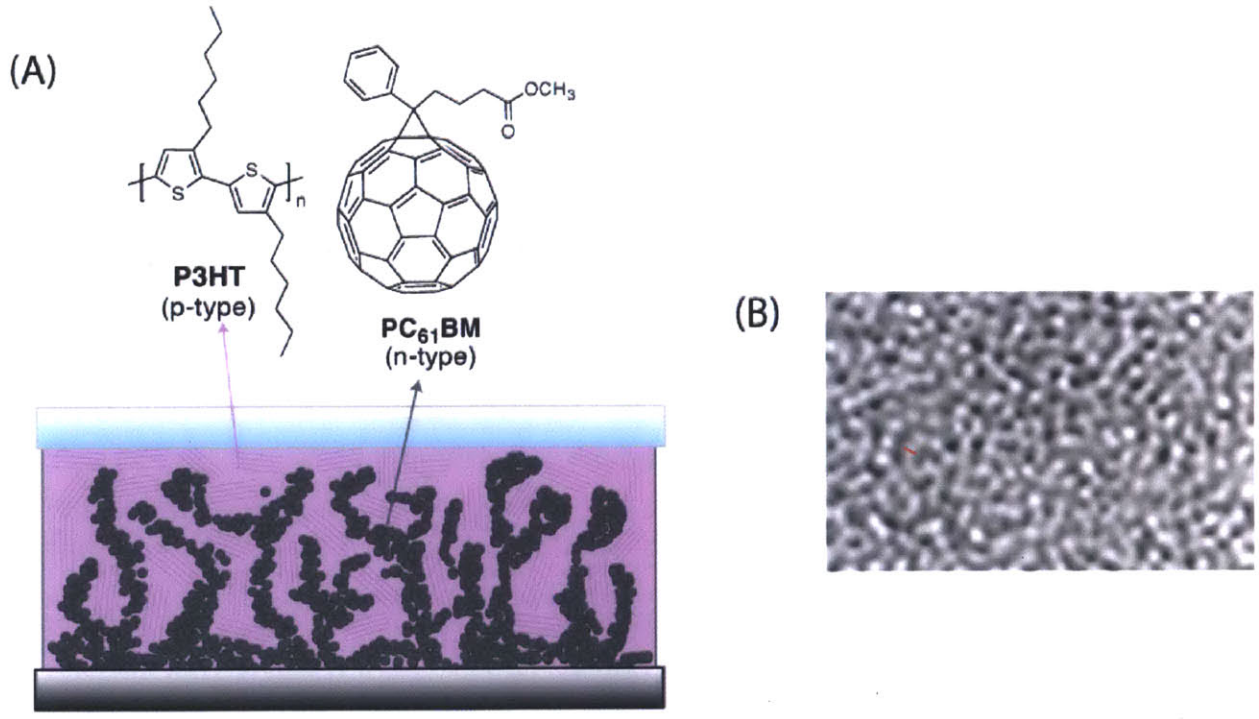

Figure 3.3. (A) Structures of regioregular poly (3-hexylthiophene) (**rr-P3HT**) and phenyl-C_{61}-cetylbutyric acid methyl ester (**$PC_{61}BM$**) in a BHJ. (B) TEM images of a **rr-P3HT/$PC_{61}BM$** BHJ under defocused conditions, the red line indicates the domain size (12 nm)

The best performing **P3HT/PC$_n$BM** solar cells reported to date make use of the regioregular variety of **P3HT** (**rr-P3HT**). For the case of **rr-P3HT**, the connectivity between adjacent repeat units in the polymer chain is always in a head to tail (HT) fashion (Figure 3.4).

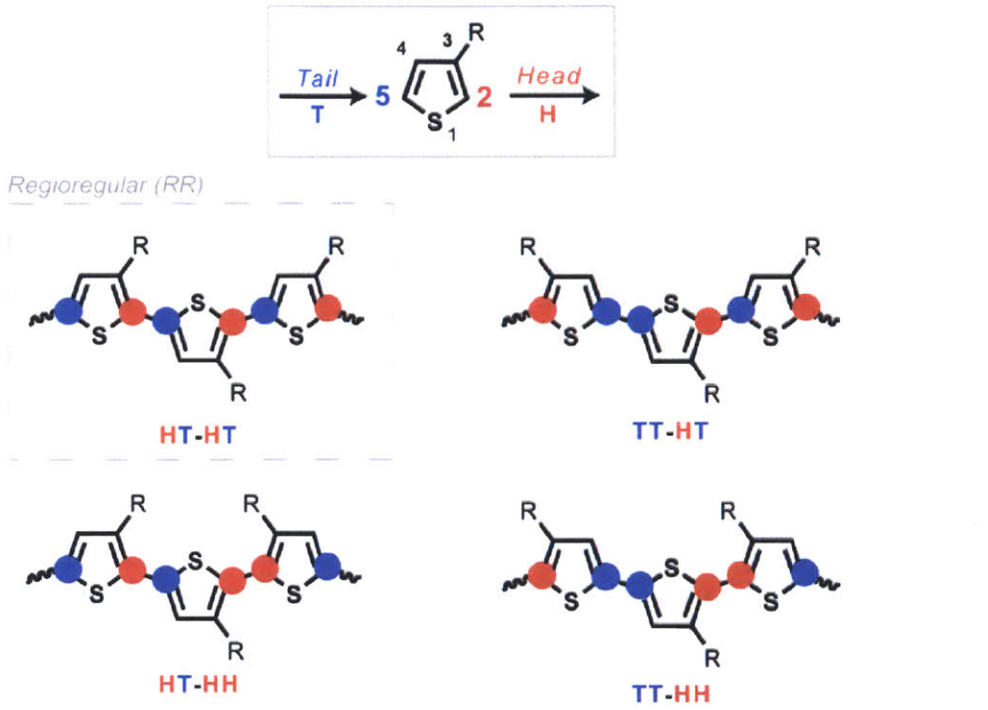

Figure 3.4. Connectivity of polythiophenes substituted in the 3 position

In the solid state, **rr-P3HT** packs itself partially into crystalline domains, in which the side-chains are ordered as described in Figure 3.5, with contiguous repeat units having their side-chans in opposite directions.[18] This prevalence of crystalline domains makes the conductivity of **rr-P3HT** be higher than its non-regioregular counterparts.

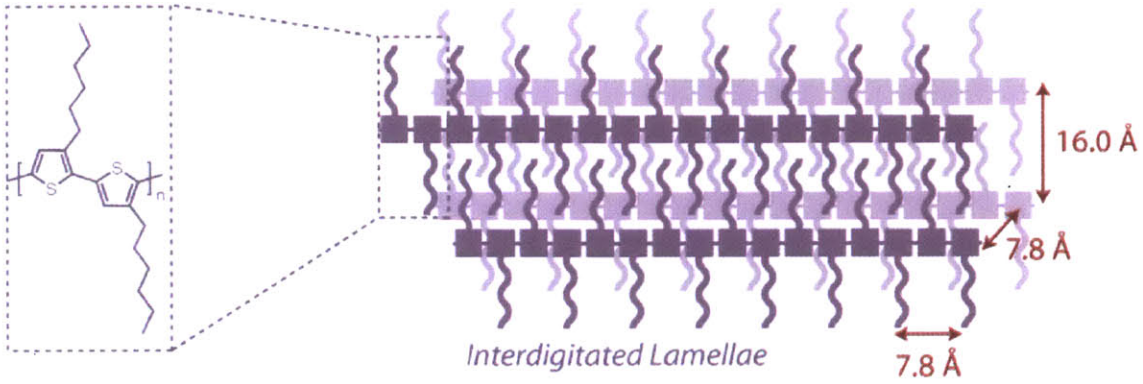

Figure 3.5. Interdigitation of the hexyl chains of **rr-P3HT** in the solid state into lamellar structures and dimensions of the individual cell of crystalline domains

The use of additives to improve the performance of **rr-P3HT/PC$_n$BM** (n = 61, 71) solar cells by changing the morphology of the active layer has been reported in the past, but examples have been limited to the use of high boiling point alkyl dihalides that act as cosolvents,[19] or main-chain block copolymers.[20,21,22] The use of **P3HT** with lower regioregularities as an additive has also been reported, and moderate increases in the open circuit voltage (V_{OC}) were observed, though accompanied by a decrease in the short circuit current (J_{SC}).[23] All of these approaches typically require extra processing steps, or a relatively large amount of additive (at least 5 wt %) to see an improvement in the PCE.

Both the length of the side chain on the repeat unit and the regioregularity of the polymeric donor material in PSCs have been shown to have a marked effect on solar cell performance.[24,25,26] In some cases, an optimal nanoscale morphology was achieved with random copolymers compared to highly-ordered regioregular analogs because the random copolymers could mix more effectively with the fullerene acceptor and form bicontinuous networks.[27] In comparison, fullerene molecules were found to intercalate between the side chains of an analogous highly-ordered polymer and form BHJs containing nanoparticles with poor electrical

connection to the top and bottom electrodes.[28,29] Different substituents have also been directly attached to a polythiophene backbone with the aim of changing its band gap,[30] but this approach has proven to be less effective than using the original **P3HT/PC$_{61}$BM** system. Further chemical modification of the side chains of **P3HT** and its resulting effect on solar cell performance is mostly unexplored, with reported examples of side-chain functionalization mainly centered on the exploration of solubility[31,32] and sensing applications.[33]

In this chapter we present the design and synthesis of a new class of designer additives based on side-chain functionalized polythiophene additives that can be used to greatly improve the efficiency of organic-based solar cells by only using a minuscule amount of additive. We hypothesized that ternary mixtures where these new polymers were used additives to the **rr-P3HT/PC$_n$BM** system would demonstrate better PCEs compared to binary **rr-P3HT/PC$_n$BM** mixtures. We designed our additives so that they would act as a surfactant locating itself at the interface between **rr-P3HT/PC$_n$BM**, firstly to improve interactions at the interface between the polymer and fullerene phases enabled by side-chain functionalization and secondly to locate a dipole at the interface that would prevent charge recombination. In the following chapter of this thesis we discuss the performance of this kind of additives in a real organic solar cell, and study the conditions for performance optimization, as well as the reasons behind the observed improvements in the J_{SC} and thus in the solar cell efficiency.

3.2 Additive Design

The envisioned additive would act as a surfactant in-between the **rr-P3HT/PC$_n$BM** phases. The proposed additive would then be a polymer with two distinct sides: one bearing aromatic functional groups that would improve interaction with the **PC$_n$BM** phase and that

would place a dipole at this interface, and the other one unfunctionalized and capable of interacting with the **P3HT** phase (Figure 3.6).

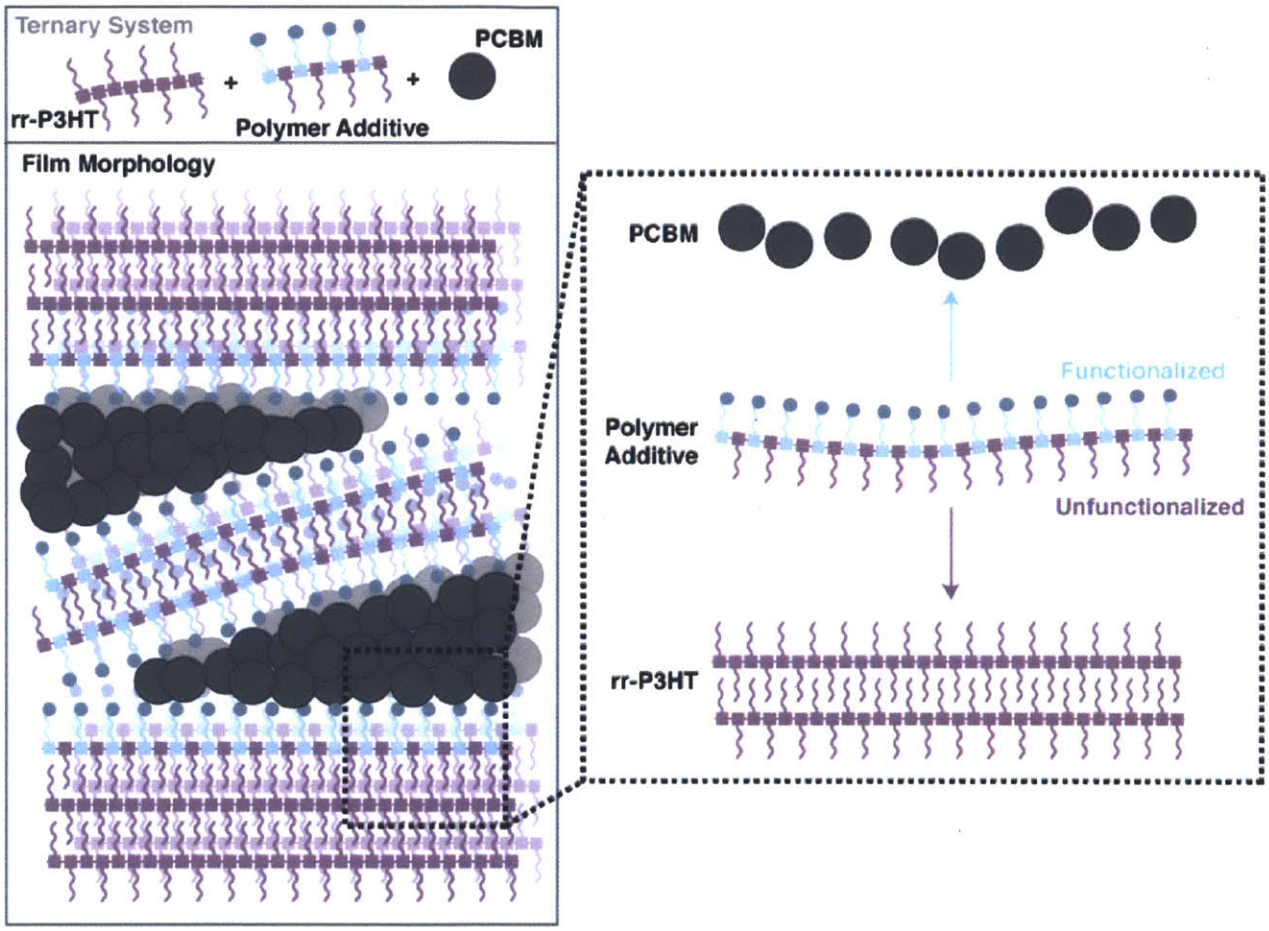

Figure 3.6. Polymer additive design

This could be easily achieved with a regioregular AB alternating polythiophene, in which every other alternating repeat unit would be the bearer of an aromatic moiety (Figure 3.7). Given the side-chain distribution of **rr-P3HT** in the solid state described in the previous section of this chapter, it was postulated that this specific kind of polymer would behave as a surfactant giving the desired effect, since functionalization in every other repeat unit (AB alternating copolymer) for a regioregular polythiophene would mean that in the solid state one side of the polymer

would be tailored with functional groups, while the other one could still take part in the interdigitation of alkyl functional chains with the **rr-P3HT** phase.

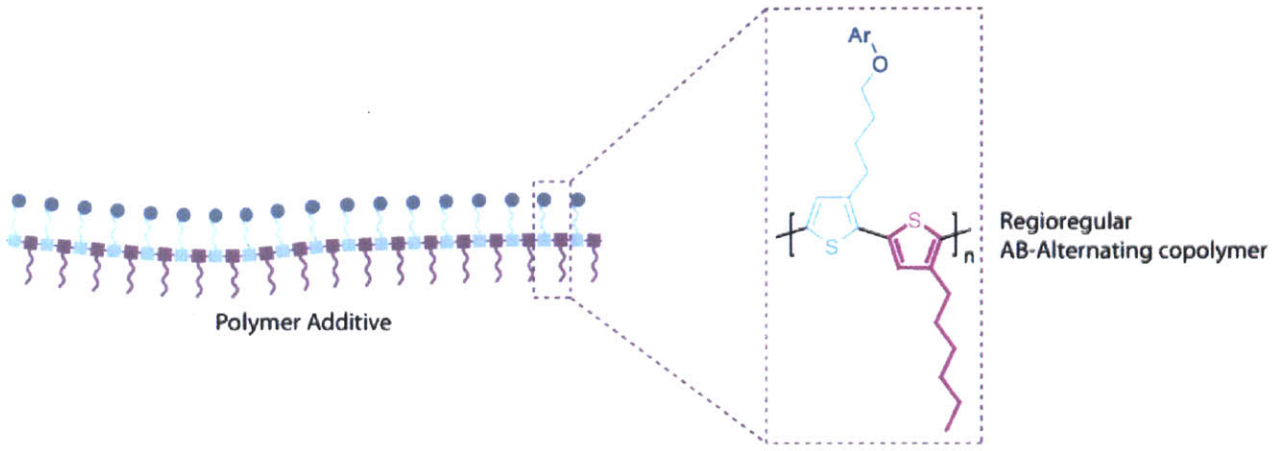

Figure 3.7. Chemical structure of the polymer additive

3.3 Side-chain Functionalized Polythiophene Synthesis

3.3.1 Proposed Polymer Additives

Six different AB-alternating side-chain functionalized polythiophene additives bearing aromatic moieties (**P1-P6**, Figure 3.8) are proposed as additives to the **P3HT/PC$_n$BM** system.

Polythiophene **P1** contains a non-conjugated phenyl moiety in its side chain in order to elucidate the effects of introducing structural complexity at side-chain termini in a benchmark polymeric donor material. To further elaborate on this concept, polymers **P2-P6** are also explored as additives: the effects of steric bulk or congestion can be revealed by **P2**, **P4** and **P5**, while the effects of having weak, isolated dipoles at side-chain termini can be investigated using **P3** (which contains electron-rich anisole moieties) and **P6** (which contains electron-deficient perfluorophenyl moieties). Triptycene-containing polymer **P5** is also chosen because triptycene

has been reported to be capable of interacting with fullerene analogues and forming highly-ordered arrays in the solid state.[34]

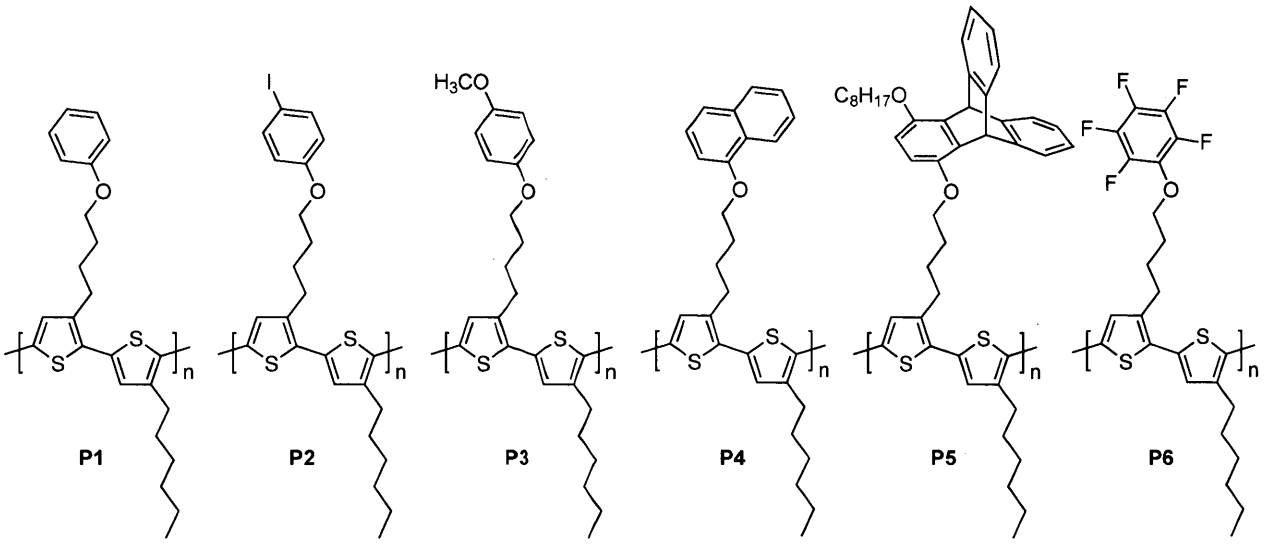

Figure 3.8. Chemical structure of the polymer additives **P1-P6**

Furthermore, all of these additives will be having a dipole in the side chain, since these aromatic moieties have a dipole different from zero. The calculated dipoles (B3LYP 6-31G*, vapor phase, in the absence of any intermolecular interactions) of the six side-chain moieties found in the repeat units of additives **P1-P6**, are shown on Figure 3.9. The green arrow shown in the wireframe representation of the appropriate structure denotes the direction of the calculated dipole.

The resulting dipole of every repeat unit was calculated in the same way, and depicted on Figure 3.10. All of the repeat units have a resulting dipole, so the corresponding polymer will have a resulting dipole as well, proportional to the magnitude of the dipole on the side-chain.

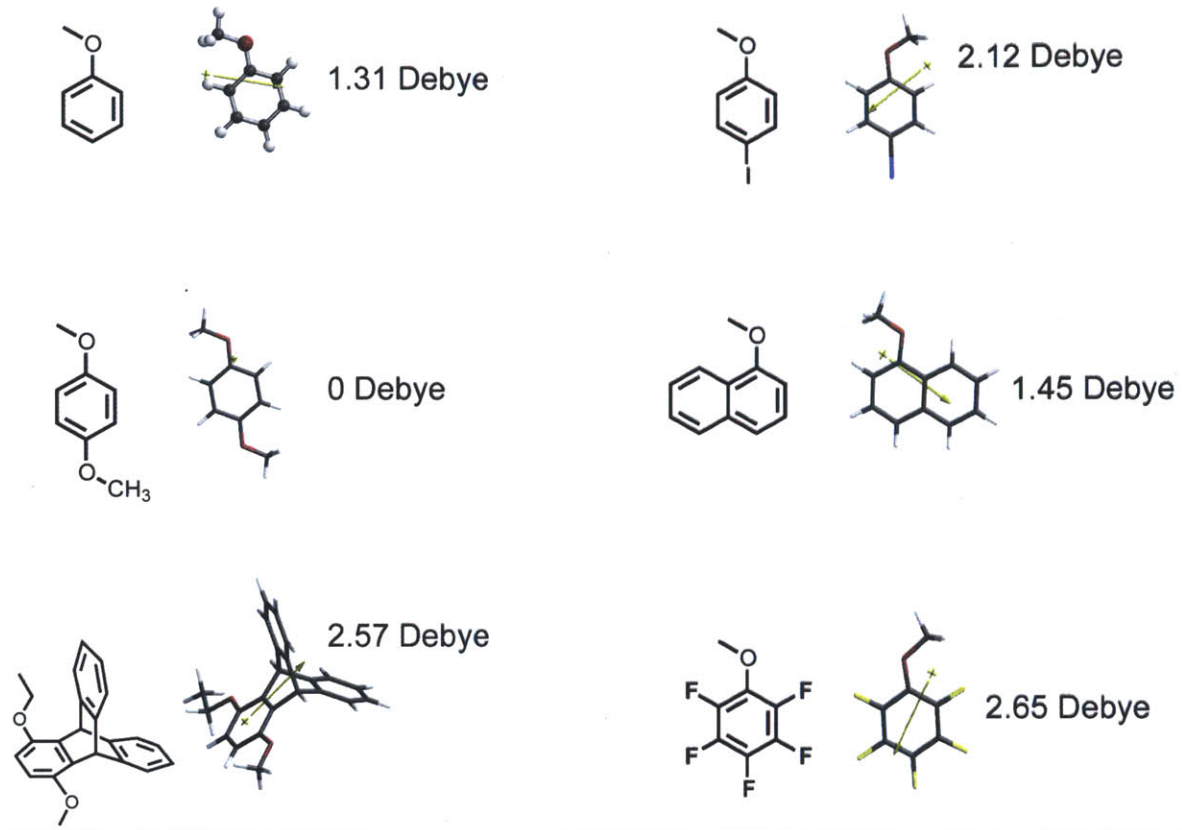

Figure 3.9. Calculated dipoles (B3LYP 6-31G*) of the six side-chain moieties found in the repeat units of additives **P1-P6**, respectively. The green arrow denotes the direction of the calculated dipole

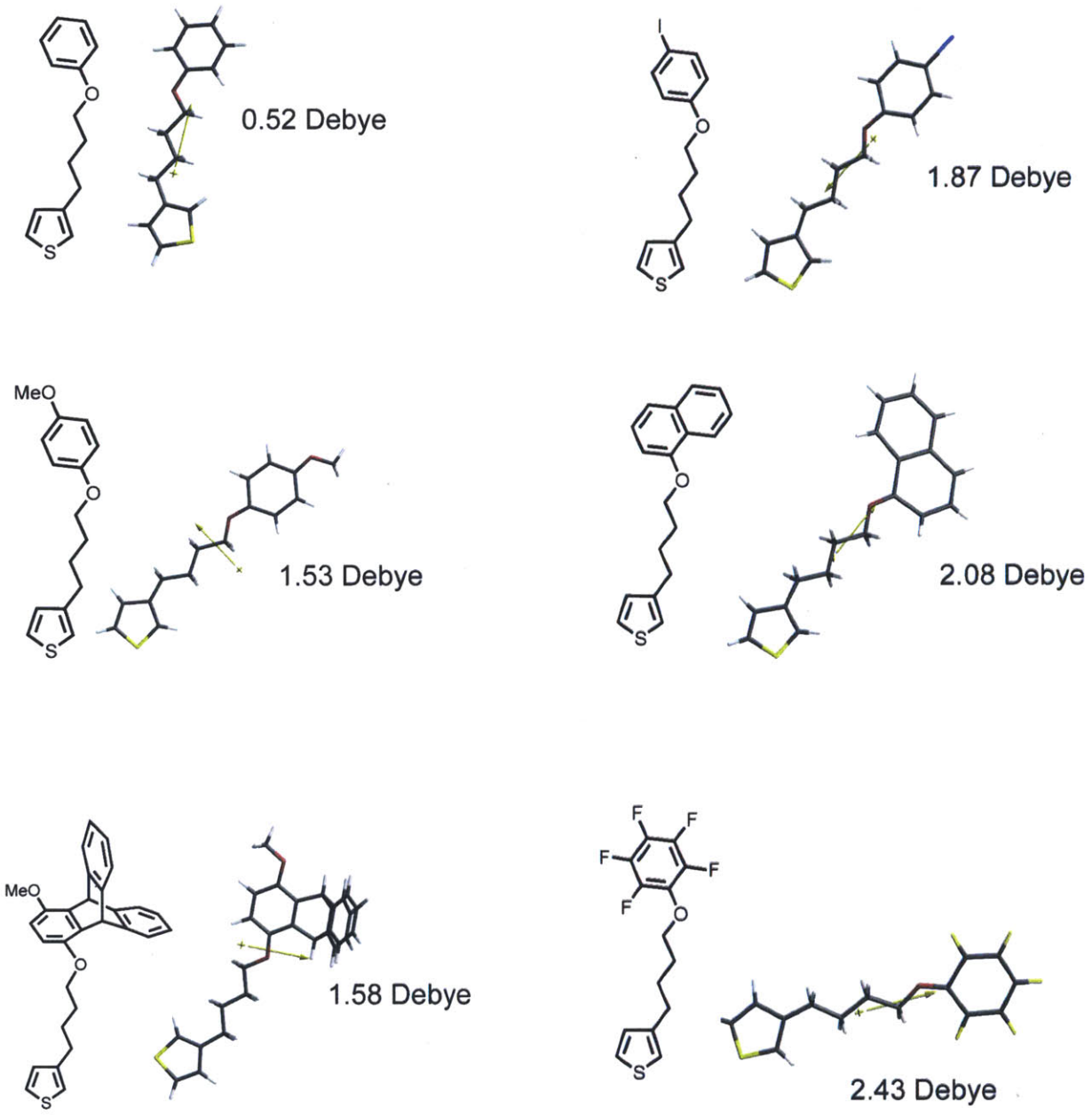

Figure 3.10. Calculated dipoles (B3LYP 6-31G*) of six side-chain functionalized thiophene monomers, such as those found in the repeat units of additives **P1-P6**, respectively. The green arrow shown in the wireframe representation of the appropriate structure denotes the direction of the calculated dipole.

3.3.2 Synthetic Approach

The Grignard metathesis (GRIM) polymerization[35,36,37] method described by McCullough et al. is one of the most straightforward ways to gain access to regioregular polythiophenes starting with the corresponding dibrominated thiophene monomer or dibrominated bithiophene species (Scheme 3.1).[38]

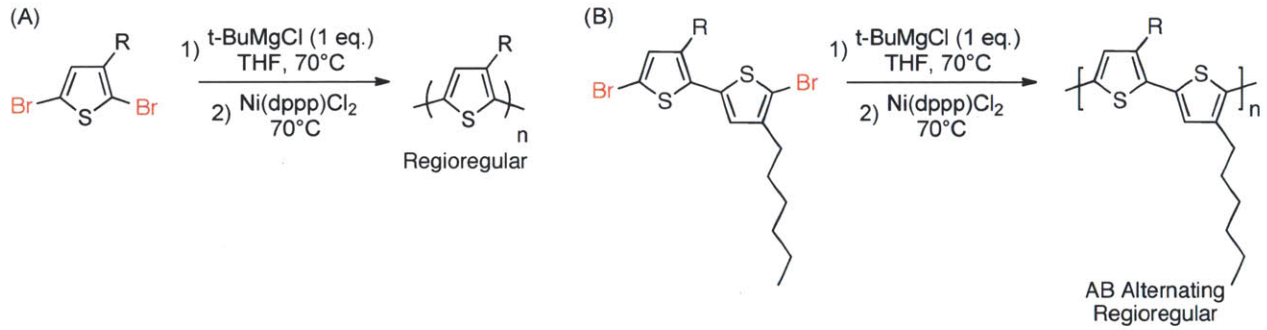

Scheme 3.1. The Grignard metathesis (GRIM) polymerization of (A) 2,5-dibromo-3-alkylthiophenes and (B) 5,5'-dibromo-3-alkyl-4'-alkyl'-2,2'-bithiophenes

In this polymerization method, the dibrominated heterocycle is transformed into the corresponding mono-Grignard reagent by virtue of a transmetalation reaction. The Grigard reagent is mostly formed in the least hindered position of the thiophene/bisthiophene. Subsequent cross-coupling using a nickel (Ni) catalyst yields a a regioregular polythiophene with mostly head to tail (HT) connections (steps shown on Scheme 3.2). The polythiophenes obtained this way usually have moderately good molecular weights (15-35 KDa) and relatively low polydispersities (1.1-1.7).

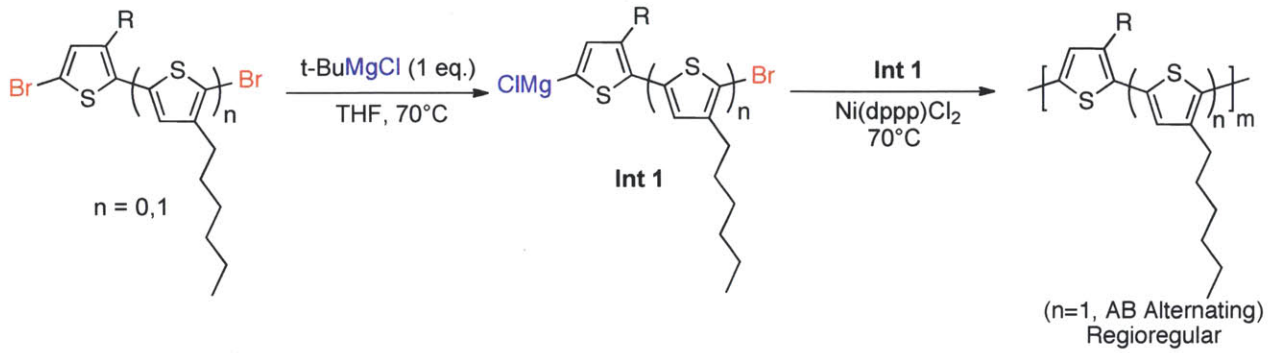

Scheme 3.2. Mechanism of the GRIM polymerization

The synthetic scheme to access the desired polythiophene additives is detailed in Schemes 3.3 and 3.4. First, a parent monomer (**M0**) is synthesized (Scheme 3.3) in which the HT connection in between the functionalized/unfunctionalized repeat units is fixed prior to polymerization. This parent monomer can be tailored with an aromatic moiety via an S_N2 reaction prior to polymerization, and then the dibrominated monomer (**M1**, **M3-M6**) is polymerized using GRIM polymerization methods (Scheme 3.4a). In order to attach functionalities not compatible with the polymerization conditions, an alternative synthetic route was used in which the parent monomer **M0** was first polymerized using GRIM conditions and then functionalized via post-polymerization modification (Scheme 3.4b).

Parent monomer bithiophene derivative **M0** was obtained from the cross-coupling of 2-bromo-2-bromo-3-(4-bromobutyl)thiophene (**2**) and 2-(4-hexylthiophen-2-yl)-5,5-dimethyl-1,3,2-dioxaborinane (**3**) and dibromination using N-bromosuccinimide (NBS). Compounds **2** and **3** were accessed using modified lithiation and bromination procedures previously reported in the literature starting with 3-bromothiophene and 3-hexylthiophene respectively (Scheme 3.3).

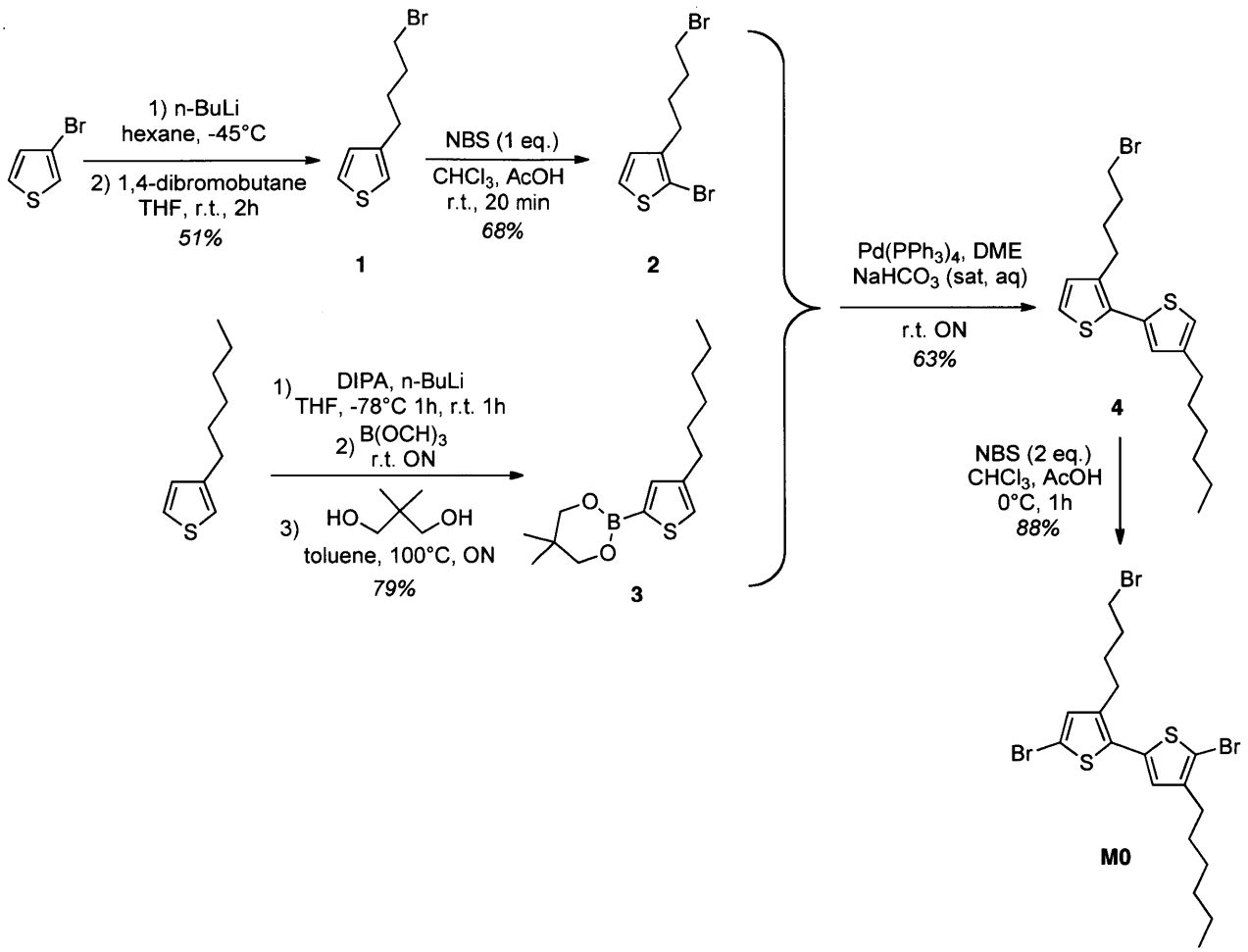

Scheme 3.3. Synthesis of parent monomer **M0**

Monomers **M1** and **M3-M6** are accessed in good yield by subjecting compound **M0** to Williamson ether synthesis conditions with the corresponding phenol. Subsequent nickel-catalyzed Grignard metathesis (GRIM) polymerization[35, 36, 37] of **M1** and **M3-M6** yields **P1** and **P3-P6** in high yields (Scheme 3.4a). Considering that an iodophenyl moiety could be competitively metallated under standard GRIM polymerization conditions and introduce unwanted side reactions, polymer **P2** is synthesized following Route 2 (Scheme 3.4b). Bromobutane-containing polymer **P7** is synthesized by GRIM polymerization of **M0**, and

subsequent post-polymerization functionalization with 4-iodophenol yields **P2** in moderate yield and with a high degree of substitution (99%) on the side-chain.

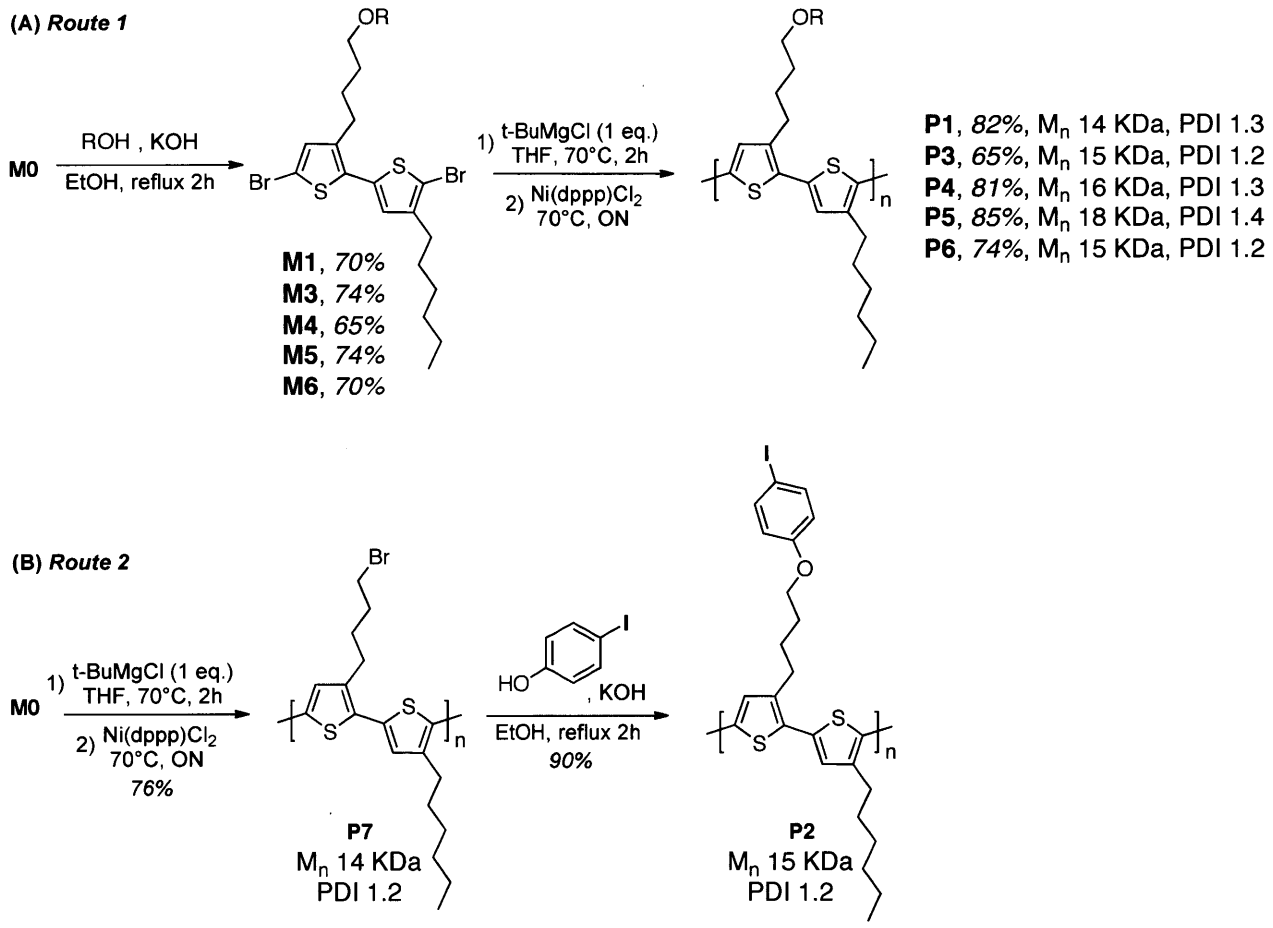

Scheme 3.4. (A) Synthesis of monomers **M1**, **M3-M6** via Williamson ether synthesis and polymerization to obtain **P1**, **P3-P6**. (B) GRIM polymerization of **M0** and post-polymerization modification to yield polymer additive **P2**

The polythiophene additives thus obtained have number-averaged molecular weights (M_ns) of 16 ± 2 KDa and polydispersities (PDIs) of 1.3 ± 0.1. In comparison, the commercial **rr-P3HT** used as the majority donor material in BHJ OPVs has a Mn of 45 KDa and a PDI of 1.7.

3.4 Side-chain Functionalized Polythiophene Characterization

3.4.1 Additive Regioregularity

The regioregularity of polymers **P1-P7** was studied using ^{1}H-NMR techniques.[39] The degree of regioregularity can be traced to the relative intensity of the signal for the HT-HT triad in the aromatic region of the ^{1}H-NMR spectrum (δ 6.98, blue protons, a, in Figure 3.11) vs. the intensity of the TT-HT (δ 7.00), HT-HH (δ 7.03), and TT-HH (δ 7.05).

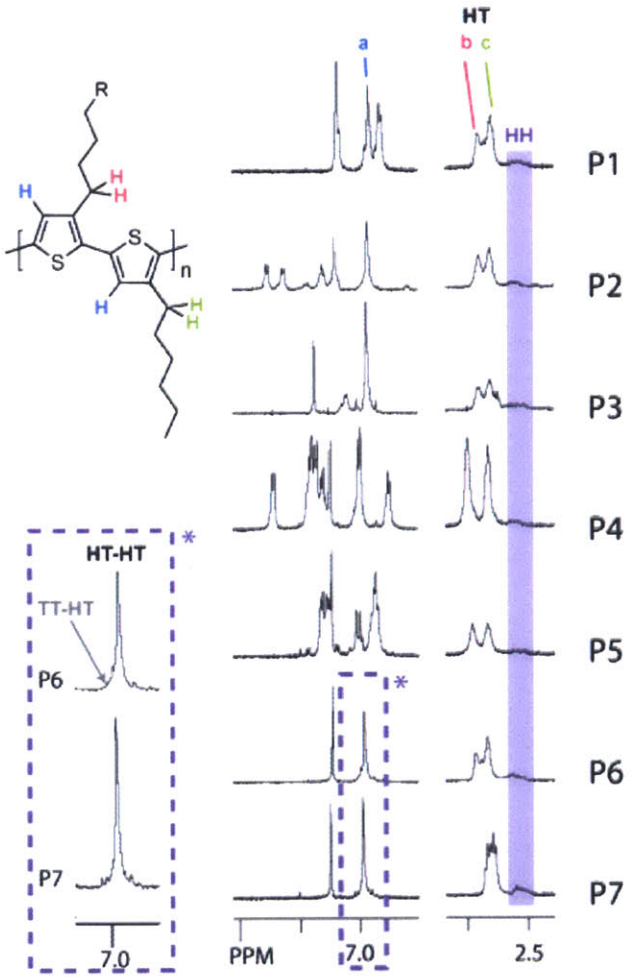

Figure 3.11. ^{1}H-NMR ($CDCl_3$) spectra for polymers **P1-P7** showing the connectivity of the polymer repeat units

For situations in which this region of the ^{1}H-NMR spectra was masked due to overlapping signals from the side-chain moiety, the diad signals in the alkyl region are used (red and blue, b and c respecitvely, Figure 3.11): HT (δ 2.81) and HH (δ 2.61).

Of all the synthesized polymers, only **P6** and **P7** had no overlapping signals in the aromatic region, and these polymers show no evidence of regioisomers other than the HT-HT kind. In order to determine the regioregularity of the remaining polymers, the δ 2.0-3.0 region of the spectrum was used. Here it is also confirmed that primarly HT connections were formed through the polymerization, with only very weak signals for the HH connections present.

3.4.2 Photophysical Properties of Additives

The UV-visible and emission spectra of the polymers give information about the optical band-gap of the polymer, the wavelengths at which the conjugated polymer absorbs light and how the side-chains affect the structure of the conjugated polymer backbone.

The absorption and emission spectra of **P1-P6** (Figure 3.12) and their corresponding peak maxima in dilute chloroform solutions are both similar to those of **rr-P3HT** (data summarized on Table 3.1). Additionally, the solution quantum yields and excited state lifetimes of **P1-P6** are also identical to those of commercial **rr-P3HT** (within the error of each measurement). These results indicate that side-chain functionalization does not alter the effective conjugation length of the polythiophenes, and thus their optoelectronic properties. This is expected, since the additional side-chain moiety is not directly conjugated to the polymer backbone and it is far enough from the backbone to prevent the creation of an additional torque in the backbone due to steric hindrance.

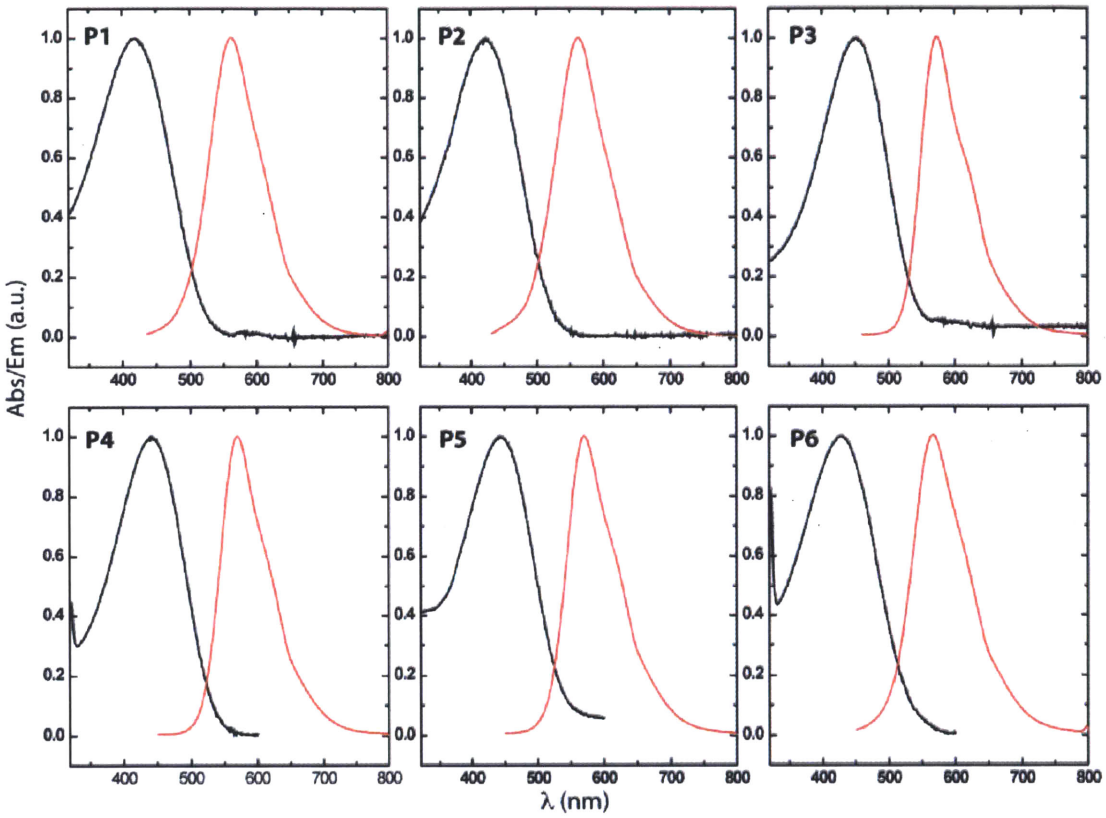

Figure 3.12. Normalized absorbance (black) and emission (red) spectra for polymers **P1-P6**

	λ_{abs} (nm)	λ_{em} ($CHCl_3$, nm)	$^{b}\Phi_F$	τ ($CHCl_3$, ns)
rr-P3HT	452 ($CHCl_3$) 545 (film)[a]	573	0.20	0.58
P1	450 ($CHCl_3$) 550 (film)[a]	570	0.22	0.64
P2	447 ($CHCl_3$) 545 (film)[a]	571	0.12	0.57
P3	455 ($CHCl_3$) 552 (film)[a]	573	0.22	0.62
P4	440 ($CHCl_3$) 548 (film)[a]	570	0.22	0.61
P5	445 ($CHCl_3$) 540 (film)[a]	570	0.18	0.57
P6	442 ($CHCl_3$) 545 (film)[a]	575	0.20	0.60

Table 3.1. Photophysical properties of polymers **P1-P6.** [a] 40 ± 5 nm-thick films spun-cast from 1,2-dichlorobenzene. [b] Fluorescence quantum yields are determined against perylene in EtOH (Φ 0.94). The measurement error is 0.03

Spun-cast, annealed thin films of **P1-P6** (40 nm) displayed red-shifted absorption maxima and weak luminescence at room temperature, similar to **rr-P3HT**. However, unlike films of **rr-P3HT**, a characteristic "order peak" at 600 nm is not observed to evolve in the absorption spectra of neat thin films of **P1-P6**. This optical "order peak" is assigned to interplane interactions in highly-ordered crystalline regions of **rr-P3HT**;[40] therefore, the lack of an "order peak" in films of **P1-P6** indicates that side-chain functionalization of polythiophenes hinders crystallization of polymer chains.

3.4.3 Solid State Ordering of Additives

In order to study the ordering in the solid state, we conducted X-Ray Diffraction (XRD) measurements. For **rr-P3HT**, which has both crystalline lamellar regions as well as amorphous regions in the solid state, the characteristic XRD spectrum shows three characteristic peaks, which correspond to the three dimensions of the unit cell of the lamellae present in the crystalline regions of **rr-P3HT** (see figure 3.5).

X-Ray diffractograms of spun-cast and annealed films of **P1-P6** do not contain sharp diffraction signals and indicate that these neat polymer films are amorphous (Figure 3.13A). This observation is consistent with the aforementioned absence of an "order peak" in the absorption spectra of thin films of **P1-P6**. However, diffractograms of **rr-P3HT/PC_{61}BM** thin films containing up to 10 wt% of **P1-P6** reveal that the presence of up to 10 wt% of the additives does not hinder lamella formation within the **rr-P3HT** phase of the bulk film (Figure 3.13B). Thus, we infer that the lower molecular-weight additives do not disturb crystalline domain formation in the **rr-P3HT** phase, and predominantly localize in amorphous regions within the **rr-**

P3HT/$PC_{61}BM$ BHJ, which is also the region where interpenetration between the **rr-P3HT/$PC_{61}BM$** phases occur.

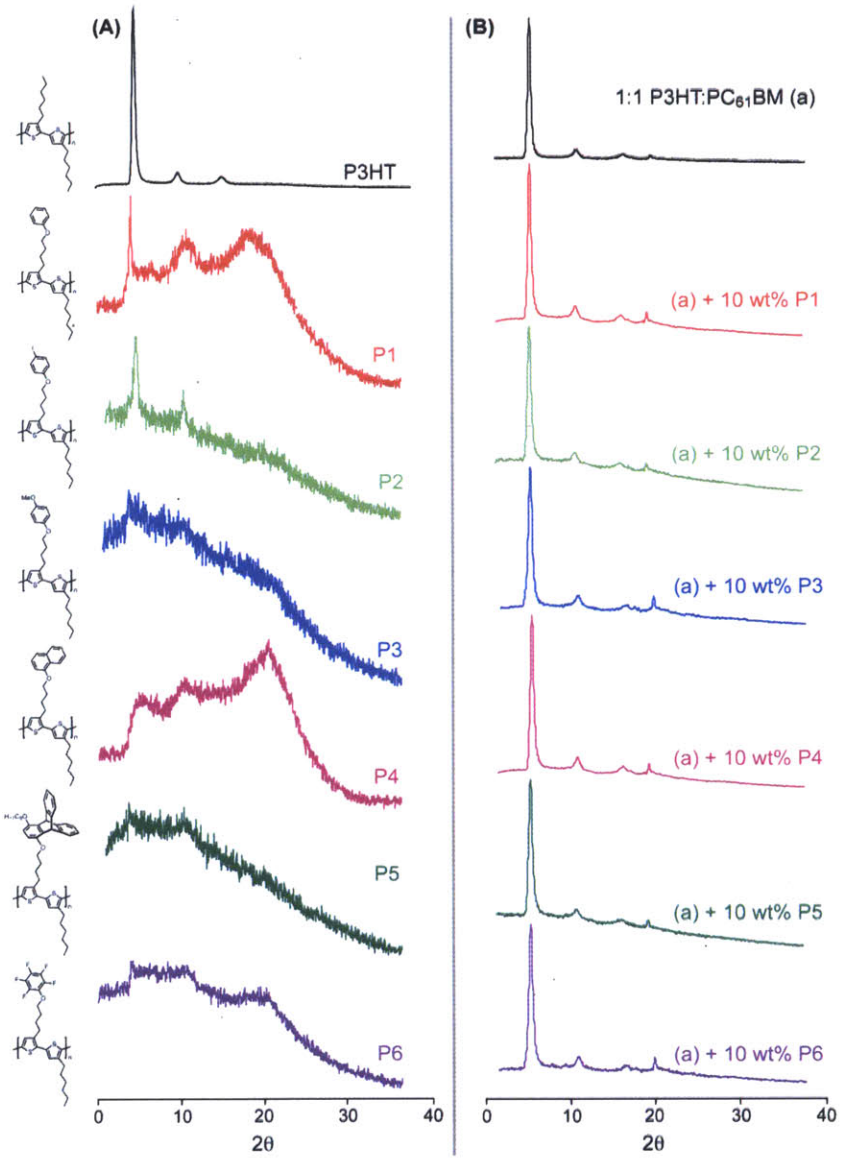

Figure 3.13. XRD spectra of (A) 40 nm-thick neat films of **rr-P3HT** and **P1-P6** and (B) 75 nm-thick films containing ternary mixtures of **rr-P3HT**, **$PC_{61}BM$** and 10 wt% **P1-P6**. The films shown in both (A) and (B) were annealed at 150 °C for one hour

3.4.4 Quenching Studies

In order to study the variations in the interaction among the polythiophene additives and **$PC_{61}BM$**, Stern-Volmer fluorescence quenching studies were carried out.

The fluorescence quenching properties were investigated by measuring the fluorescence intensity changes of the polymer solutions with the addition of **$PC_{61}BM$**. **$PC_{61}BM$** was dissolved in a polymer solution with the same concentration as the initial solution, so that the polymer concentration remained constant throughout the experiment. No new emission bands were observed during the quenching studies. There is competitive absorption of **$PC_{61}BM$** at the excitation and emission wavelengths of the studied polythiophenes. To account for this effect, the measured fluorescence was corrected by the equation shown on Figure 3.14.

$$F = F_{em} \times \frac{1 - e^{-\varepsilon_1 C_1 l}}{\varepsilon_1 C_1 l} \times \frac{\varepsilon_1 C_1 l + \varepsilon_2 C_2 l}{1 - e^{-(\varepsilon_1 C_1 + \varepsilon_1 C_1) l}} \times \frac{\varepsilon_3 C_2 l}{1 - e^{-\varepsilon_3 C_2 l}}$$

Figure 3.14. Formula for the corrected fluorescence for polymers **P1-P6** in Stern-Volmer quenching studies

In this equation, F_{em} denotes the experimental fluorescence intensity, F denotes the corrected fluorescence intensity, C_1 is the molar concentration of polythiophene, C_2 is the molar concentration of **$PC_{61}BM$**, ε_1 is the molar extinction coefficient of a polythiophene at its excitation wavelength (452 nm for **P3HT**), ε_2 is the molar extinction coefficient of **$PC_{61}BM$** at the excitation wavelength of the polymer (452 nm for **P3HT**), ε_3 is the molar extinction coefficient of **$PC_{61}BM$** at the emission maxima of the polymer (573 nm for **P3HT**), and l is the optical pathlength in cm.

Steady-state fluorescence quenching studies of **P1-P6** with **$PC_{61}BM$** in chloroform solutions (Figure 3.15) reveal larger Stern-Volmer quenching constants (K_{sv}) for the additives compared to **rr-P3HT** (Table 3.2): for example, K_{sv} values of 4.1×10^3 and 3.6×10^3 M^{-1} are measured in $CHCl_3$ for **P1** and **P4**, respectively, compared to 2.4×10^3 M^{-1} for **rr-P3HT**. Lifetime Stern-Volmer measurements reveal that the excited state lifetimes of the polymers do not change significantly with increasing fullerene concentration, indicating the dominance of a static quenching mechanism. In this case, a higher value of K_{sv} can be correlated with a larger binding affinity between the fluorophore and quencher, thus indicating that the side-chain functionalized polythiophene additives **P1-P6** have a higher binding affinity for **$PC_{61}BM$** than **rr-P3HT**. We note that a slight increase in the excited state lifetime of **P5** was observed in the presence of **$PC_{61}BM$**, which we ascribe to conformational changes in the polymer backbone induced by a triptycene-fullerene binding interaction.

	rr-P3HT	**P1**	**P2**	**P3**	**P4**	**P5**	**P6**
K_{sv} $(M^{-1})/10^3$	2.4	4.1	3.3	2.4	3.6	3.0	2.8

Table 3.2. Stern-Volmer constants for polymers **P1-P6** (Steady-state quenching constant for each polymer with **$PC_{61}BM$** in $CHCl_3$)

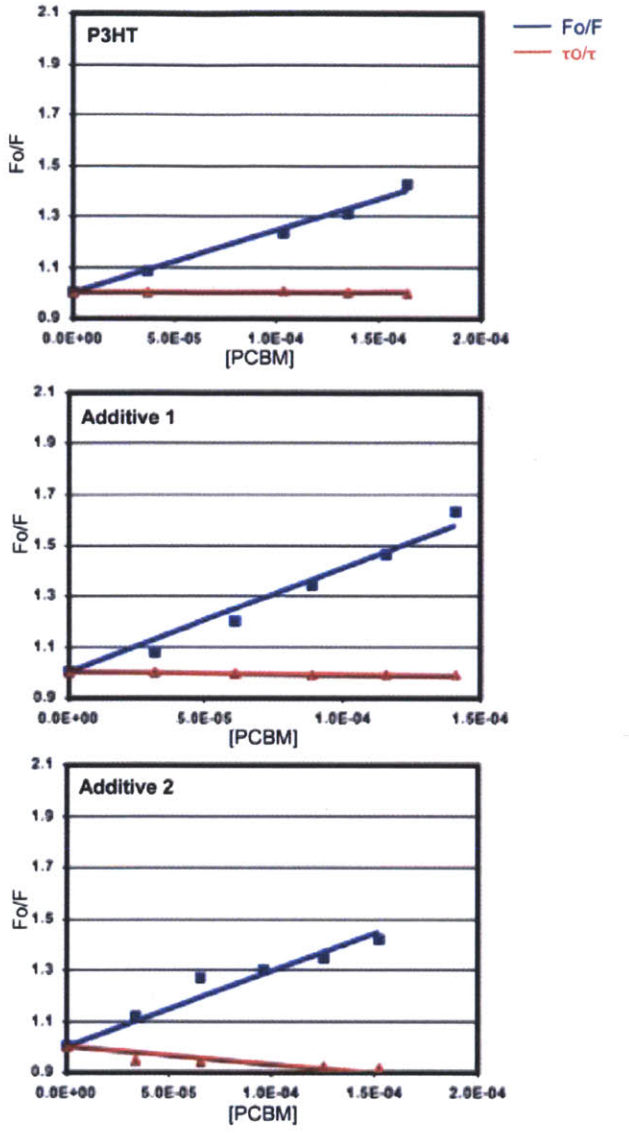

Figure 3.15. Stern-Volmer plots of the quenching response of **P3HT**, polymer **P1** and polymer **P5** to **$PC_{61}BM$** in dilute $CHCl_3$ solutions. Blue squares depict the change in intensity of the corresponding emission maximum (λ_{em}) with added fullerene. F_0 and τ_0 correspond to the emission intensity (at λ_{em}) and polymer lifetime, respectively, in the absence of fullerene. Red triangles depict the change in fluorescence lifetime with added fullerene. The solid lines are linear fits to the data. Polymer lifetimes are not observed to change with added fullerene, thus indicating a static quenching process

3.5 Conclusions

In summary, in this chapter the synthesis of a new class of regioregular AB alternating side-chain functionalized polythiophenes (**P1-P6**) has been described. The polymers can be accessed using GRIM polymerization conditions on a functionalized bithiophene monomer, or by post-polymerization modification reaction of a polymer also obtained via the GRIM polymerization.

The polymers described are regioregular, and the presence of functional moieties in the side-chain does not alter their optoelectronic properties. The ordering in the solid-state of these new polythiophenes is different from that of unfunctionalized **rr-P3HT**, probably due to the steric hindrance of the functional groups on the side-chain. However, addition of these new polythiophenes on to the **rr-P3HT/PC_{61}PBM** does not prevent formation of crystalline-domains in the **rr-P3HT** phase, which means the additives locate themselves in the amorphous regions of **rr-P3HT**. Stern-Volmer quenching studies in solution reveal that the binding constants between polymer additives **P1-P6** and **PC_{61}PBM** is greater than that of unfunctionalized **rr-P3HT** and **PC_{61}PBM**, which is a good sign for improvement of interactions in the solid state.

3.6 Experimental Section

Materials: Unless otherwise noted, all reactions were performed in flame-dried glassware, and under an oxygen-free atmosphere of argon using standard Schlenk techniques. Anhydrous solvents were obtained using a solvent purification solvent (Innovative Technologies). All other chemicals were of reagent grade from Sigma-Aldrich and were used as received. Regioregular P3HT for XRD and spectroscopic studies was purchased from Aldrich (electronic grade, 99.995% trace metals basis, average Mn 30,000-60,000).

NMR Spectroscopy: NMR spectra were obtained on a Bruker Avance (400 MHz). NMR chemical shifts are given in ppm referenced to $CHCl_3$/TMS (7.24 ppm for ^1H, 77.24 ppm for ^{13}C)

Mass Spectrometry: High-resolution mass spectra (HRMS) were obtained on a Bruker Daltonics APEXII 3 Tesla Fourier Transform Mass Spectrometer at the MIT Department of Chemistry Instrumentation Facility (DCIF).

Molecular Weight Determination: Polymer molecular weights were determined at room temperature on a HP series 1100 GPC system in THF at 1.0 mL/min (1 mg/mL sample concentrations), approximate molecular weights were estimated using a polystyrene calibration standard.

X-Ray Diffractometry: X-Ray data was collected using an Inel CPS 120 position sensitive detector using an XRG 3000 generator (Cu Kα).

UV-Vis/Fluorimetry: UV-Vis spectra were recorded with an Agilent 8453 diode-array or Cary 50 UV-Vis spectrophotometer, corrected for baseline with a solvent-filled cuvette. Emission spectra were acquired on a SPEX Fluorolog-τ3 fluorimeter. The spectra were obtained at room temperature using a quartz cuvette with a path length of 1cm at right angle detection. The absorbance of all samples used for fluorescence studies was equal or below 0.1.

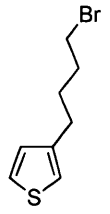

3-(4-bromobutyl)thiophene (1).[41] 3-bromothiophene (9 ml, 96 mmol) was dissolved in 120 ml dry hexanes. The solution was cooled down to -45°C, and 60 ml n-BuLi (60 ml 1.6M, 96 mmol) was added dropwise. The solution was stirred at -45°C for 10 min, after which the lithium salt was precipitated by addition of 6 mL dry THF. After stirring at -45°C for 1h, the solution was warmed up to -10°C, and an excess of 1,4-dibromobutane (44 ml, 368 mmol) was added. After stirring at room temperature for 2h, the solution was extracted with ether, washed with water, brine, dried over magnesium sulfate, and the solvent was removed. Excess 1,4-dibromobutane was removed under vacuum. Filtration of the residue through a silica plug (hexanes), and solvent removal afforded product **1** (10.7 g, 51% yield) as a colorless oil. ^{1}H-NMR ($CDCl_3$): 1.75-1.81 (2H, m), 1.86-1.91 (2H, m), 2.67 (2H, t, J=7.32 Hz), 3.44 (2H, t, J=7.32 Hz), 6.92-6.94 (2H, m), 7.25-7.26 (1H, m). ^{13}C-NMR ($CDCl_3$): 29.2, 29.5, 32.4, 33.8, 120.4, 125.6, 128.3, 142.3. m/z (HRMS) found: 218.9843 $(M+H)^+$, theoretical: 218.9838.

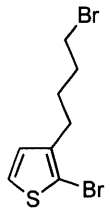

2-bromo-3-(4-bromobutyl)thiophene (2).[42] Compound **1** (8 g, 36.5 mmol) was dissolved in 250 ml $CHCl_3$, and glacial acetic acid (250 ml) was added in the dark. NBS (6.5 g, 36.5 mmol) was added, and the mixture was stirred for 20 minutes at room temperature in the dark. The reaction mixture was washed with water, saturated $NaHCO_3$, dried over magnesium sulfate and the

solvent was removed under vacuum. Purification by column chromatography afforded compound **S2** (7.4 g, 68% yield) as a light yellow oil. ^{1}H-NMR ($CDCl_3$): 1.71-1.77 (2H, m), 1.85-1.89 (2H, m), 2.6 (2H, t, J=7.44 Hz), 3.43 (2H, t, J=7.32 Hz), 6.78 (1H, d, J=5.6 Hz), 7.19 (1H, d, J=5.6 Hz). ^{13}C-NMR ($CDCl_3$): 27.5, 29.4, 32.9, 33.9, 109.2, 125.5, 128.4, 141.8. m/z (GC-MS) found: 295.89, calculated: 295.89.

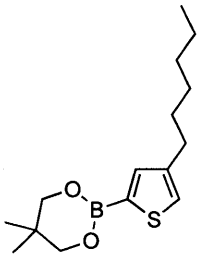

2-(4-hexylthiophen-2-yl)-5,5-dimethyl-1,3,2-dioxaborinane (3).[42] Diisopropylamine (7 ml, 50 mmol) was dissolved in dry THF (200 ml). The mixture was cooled down to 0°C and n-BuLi (31 ml 1.6 M, 50 mmol) was added. After stirring at 0°C for 30 min, the mixture was cooled down to -78°C and 3-hexylthiophene (8.1 ml, 45 mmol) was added dropwise. After stirring at -78°C for 1h the reaction was warmed up to room temperature, and the mixture was stirred for 1 h. Then, the reaction was cooled down to -78°C, and trimethylborate (15 ml, 134 mmol) was added. After 10 min, the reaction was warmed up to room temperature, and stirred over night. Quenching with 10% aqueous HCl (40 ml) followed, and the aqueous layer was extracted with ether. The ether phase was washed with water, brine, dried over magnesium sulfate and the solvent was removed under vacuum. 250 ml toluene was added to the remaining oil, followed by neopentyl glycol (7.02 g, 67.4 mmol). The mixture was sparged with argon, and heated up to 100°C. After 24 h, the solvent was removed under reduced pressure. Hexanes were added to the remaining residue, and the hexanes phase was purified by column chromatography (99:1 to 97:3

hexanes:acetone). The product **3** was obtained as a colorless oil (9.9 g, 79% yield). ^{1}H-NMR ($CDCl_3$): 0.85 (3H, t, J=6.24 Hz), 1.00 (6H, s), 1.22-1.33 (6H, m), 1.59 (2H, m), 2.59 (2H, t, J=7.76 Hz), 3.73 (4H, s), 7.13 (1H, s), 7.38 (1H, s). ^{13}C-NMR ($CDCl_3$), 14.1, 21.9, 22.6, 29.0, 30.1, 30.6, 31.7, 32.0, 72.4, 122.9, 126.5, 137.0, 144.5. m/z (HRMS) found: 218.1742 $(M+H)^+$, calculated: 218.1753.

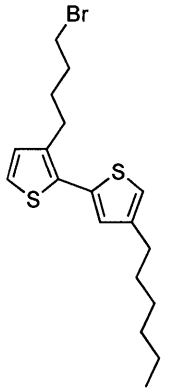

3-(4-bromobutyl)-4'-hexyl-2,2'-bithiophene (4). A mixture of a saturated solution of $NaHCO_3$ (115 ml) and DME (230 ml) was sparged with argon for 45 minutes. Compounds **2** (10.4 g, 35 mmol) and **3** (9.9 g, 35 mmol) were added, followed by addition of $Pd(PPh_3)_4$. After warming up to 80°C, the mixture became first bright yellow, and then dark orange. After stirring at 80°C for 18 h, a saturated solution of NH_4Cl (aq, 210 ml) was added, and the mixture was extracted with ether. The organic phase was washed with water, a saturated solution of $NaHCO_3$ and brine. After drying over magnesium sulfate and solvent removal, the dark orange oil was purified by colum chromatography using hexanes as the eluent. The product (6.07 g, 45% yield) was isolated as a pale yellow oil and used without further purification. ^{1}H-NMR ($CDCl_3$): 0.87 (3H, t, J=6.96 Hz), 1.25-1.36 (6H, m), 1.61 (2H, m), 1.76 (2H, m), 1.88 (2H, m), 2.58 (2H, t, J=8.52 Hz), 2.76 (2H, t, J=7.56 Hz), 3.38 (2H, t, J=6.72 Hz), 6.86-6.93 (3H, m), 7.14 (1H, d, J=5.2 Hz). ^{13}C-NMR

($CDCl_3$): 14.1, 21.2, 22.3, 29.0, 29.2, 30.5, 30.7, 31.0, 31.1, 31.8, 121.2, 123.6, 128.1, 129.8, 132.0, 135.5, 137.1. m/z (HRMS) found: 385.06, $(M+H)^+$, calculated: 385.06.

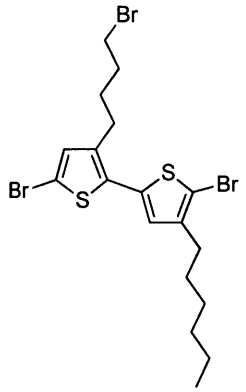

5,5'-dibromo-3-(4-bromobutyl)-4'-hexyl-2,2'-bithiophene (M0). Compound **4** (5.4 g, 14 mmol) was dissolved in 100 ml CHCl3, and glacial acetic acid (100 ml) was added in the dark. The mixture was cooled down to 0°C, and NBS (4.94 g, 27.75 mmol) was added stepwise. The mixture was stirred for 1 h at 0°C in the dark. The reaction mixture was washed with water, saturated $NaHCO_3$, brine, dried over magnesium sulfate and the solvent was removed under vacuum. Purification by column chromatography (hexanes) afforded compound **M0** (6.99 g, 92% yield) as a light yellow oil. ^{1}H-NMR ($CDCl_3$): 0.86 (3H, t, J=7 Hz), 1.22-1.35 (6H, m), 1.53-1.60 (2H, m), 1.67-1.76 (2H, m), 1.83-1.91 (2H, m), 2.52 (2H, t, J=7.8 Hz), 2.65 (2H, t, J=7.72 Hz), 3.38 (2H, t, J=6.6 Hz), 6.72 (1H, s), 6.86 (1H, s). ^{13}C-NMR ($CDCl_3$): 14.3, 22.8, 28.3, 29.1, 29.2, 29.7, 29.8, 32.4, 33.5, 34.9, 109.6, 111.3, 125.7, 127.8, 132.5, 134.2, 139.7, 142.9. m/z (HRMS) found: 540.8888 $(M+H)^+$, calculated: 540.8864.

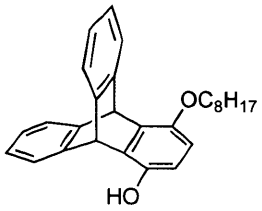

9,10[1',2']-benzene-9,10-dihydro-4-hydroxy-1-octyloxyanthracene.[43] To a solution of triptycene hydroquinone (35.8g, 125 mmol) in 500ml DMF under Ar was added K_2CO_3. 1-bromooctane (25 ml, 125 mmol) was added dropwise over 1.5 hr. The solution was then heated to 50°C for 24 hours. The solution was then cooled to room temperature and quenched by pouring into dilute aqueous NH_4Cl. The product was extracted with Et_2O, the combined organic layers washed with dilute aqueous NH_4Cl and brine. The organic layer was then dried over $MgSO_4$, filtered and solvent removed in vacuo to yield a mixture of mono- and dialkylated triptycenes. This mixture was added to 1M NaOH in a 50/50 mixture of EtOH and water. The resulting dark solution was filtered and the residual solids rinsed with additional 1M NaOH to yield a white powder (dialkylated, 27.7g, 43%). The filtrate was acidified with 5% HCl to precipitate the monoalkylated product as a tan powder, which was filtered, washed with copious amount of water and dried to yield the title compound (25.4 g, 51% yield). ^{1}H-NMR ($CDCl_3$): 0.91 (3H, t, J = 6.8 Hz), 1.54-1.30 (10H, m), 1.82 (2H, m), 3.91 (2H, t, J = 6.2 Hz), 4,44 (1H, s), 5.79(1H, s), 5.87 (1H, s), 6.37 (1H, d, J = 8.5 Hz), 6.42 (1H, d, J = 8.5 Hz), 6.98 (4H, m), 7.40 (4H, m). ^{13}C-NMR ($CDCl_3$): 14.3, 22.9, 26.4, 29.6 (3 peaks), 32.1, 47.5, 47.8, 70.0, 111.4, 113.1, 123.8, 123.9, 124.0, 124.1, 125.1, 125.3, 133.3, 136.1, 144.6, 145.7, 145.8, 148.7. m/z (HRMS) found: 399.2323 $(M+H)^+$, calculated: 399.2319.

General procedure for monomer (M) synthesis. To a solution of an appropriate phenol (1.5 eq) in EtOH was added KOH (1.7 eq) and the mixture stirred for 10 minutes. Compound **M0** and a spatula tip-full of NaI was added and the reaction subsequently refluxed under argon for 2 h.

After addition of H_2O, the reaction was extracted with ether (3x, 50 mL), and the combined organic phases were washed with water (2x, 50mL), brine and dried over magnesium sulfate. After solvent removal, the resulting oil was purified by column chromatography.

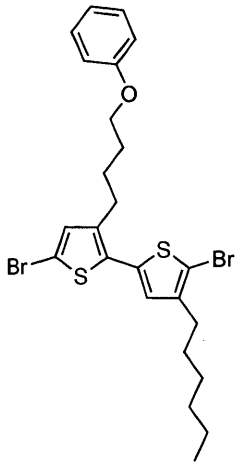

Monomer M1. Synthesized with **M0** and phenol and purified by column chromatography (hexanes:ethyl acetate, 99:1) to afford compound **M1** as a yellow oil (70% yield). ^{1}H-NMR ($CDCl_3$): 0.89 (3H, t, J=6.8 Hz), 1.27-1.38 (6H, m), 1.53-1.62 (2H, m), 1.74-1.85 (4H, m), 2.52 (2H, t, J=6.8 Hz), 2.73 (2H, t, J=7 Hz), 3.94 (2H, t, J=6 Hz), 6.74 (1H, s), 6.84-6.97 (4H, m), 7.24-7.30 (2H, m). ^{13}C-NMR ($CDCl_3$): 14.3, 27.3, 28.8, 29.0, 29.0, 29.7, 29.8, 31.8, 67.5, 109.4, 111.1, 114.6, 120.8, 125.6, 127.6, 129.6, 132.7, 134.3, 140.4, 142.8, 159.1. m/z (HRMS) found: 578.9839 $(M+Na)^+$, calculated: 578.9829.

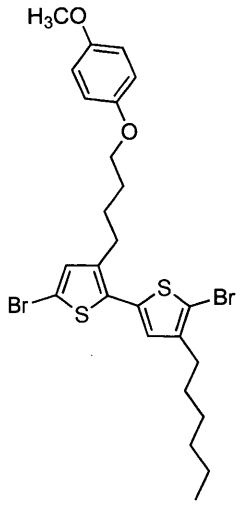

Monomer M3. Synthesized with **M0** and *p*-hydroxyanisole and purified by column chromatography (hexanes: toluene, 3:1) to afford compound **M3** as a yellow oil (74% yield). ^{1}H-NMR ($CDCl_3$): 0.88 (3H, t, J=6.4 Hz), 1.26-1.42 (6H, m), 1.56 (2H, m), 1.77 (4H, m), 2.52 (2H, t, J=7.6 Hz), 2.71 (2H, t, J=7.2 Hz), 3.75 (3H, s), 3.88 (2H, t, J=5.7 Hz), 6.72 (1H, s), 6.80 (4H, d, J=1.36 Hz), 6.88 (1H, s). ^{13}C-NMR ($CDCl_3$): 14.3, 22.8, 27.3, 28.8, 29.1, 29.1, 29.7, 29.8, 31.8, 55.9, 68.3, 109.4, 111.1, 114.8, 115.6, 127.6, 132.0, 132.6, 134.3, 140.1, 142.8, 153.3, 154.0. m/z (HRMS) found: 587.0129 $(M+H)^+$, calculated: 587.0115.

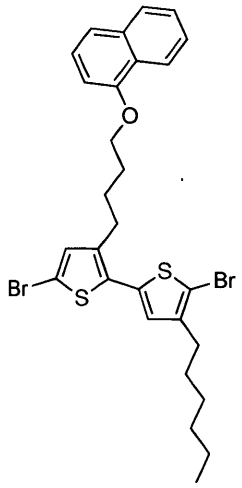

Monomer M4. Synthesized with **M0** and α-naphthol and purified by column chromatography (hexanes) to afford compound **M4** as a yellow oil (65% yield). ^{1}H-NMR ($CDCl_3$): 0.92 (3H, t, J=8 Hz), 1.27-1.36 (6H, b), 1.56 (2H, m), 1.85-1.99 (4H, m), 2.51 (2H, t, J=7.6 Hz), 2.79 (2H, t, J=7.6 Hz), 4.12 (2H, t, J=5.8 Hz), 6.76 (1H, s), 6.77 (1H, d, J=6.8 Hz), 6.93 (1H, s), 7.37 (1H, t, J=8 Hz), 7.43 (1H, d, J=8 Hz), 7.45 (2H, m), 7.81 (1H, m), 8.28 (1H, m). ^{13}C-NMR ($CDCl_3$): 14.3, 22.8, 27.5, 28.9, 29.0, 29.1, 29.7, 29.8, 31.8, 67.7, 104.7, 109.5, 111.2, 120.3, 122.2, 125.4, 125.9, 126.1, 126.6, 127.7, 128.4, 132.0, 132.6, 134.3, 134.7, 140.1, 142.8, 154.9. m/z (HRMS) found: 607.0170 $(M+H)^+$, calculated: 601.0167.

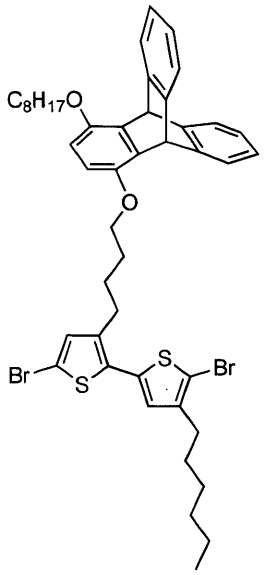

Monomer M5. Synthesized with **M0** and 9,10[1',2']-benzene-9,10-dihydro-4-hydroxy-1-octyloxyanthracene and purified by column chromatography (hexanes:toluene, 3:1 to 1:1) to afford compound **M5** as a yellow oil (65% yield). ^{1}H-NMR ($CDCl_3$), 0.88-1.01 (6H, m), 1.30-1.45 (16H, m), 1.52-1.65 (2H, m), 1.88 (6H, m), 2.54 (2H, 7, J-7.8 Hz), 2.82 (2H, t, J=6.84 Hz), 3.96 (4H, t, J=6.2 Hz), 5.88 (1H, s), 5.92 (1H, s), 6.49 (2H, m), 6.80 (1H, s), 6.92 (1H, s), 7.0 (4H, m), 7.40 (4H, m). ^{13}C-NMR ($CDCl_3$), 14.3, 14.4, 22.8, 23.0, 26.5, 27.4, 28.9, 29.1, 29.2, 29.6, 29.6, 29.7, 29.7, 29.8, 31.8, 32.1, 47.7, 47.7, 69.1, 69.8, 109.5, 110.5, 110.8, 111.1, 123.9, 125.1, 125.1, 127.6, 128.4, 129.2, 131.4, 132.1, 132.7, 134.4, 135.8, 135.9, 140.2, 142.8, 145.9, 146.0, 146.0, 148.4. m/z (HRMS) found: 883.1674 $(M+Na)^+$, calculated: 883.1663.

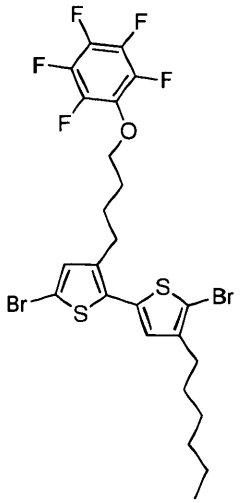

Monomer M6. Synthesized with **M0** and pentafluorophenol and purified by column chromatography (hexanes:acetone, 99:1) to afford compound **M6** as a yellow oil (70% yield). ^{1}H-NMR ($CDCl_3$): 0.86 (3H, t, J=6 Hz), 1.24-1.34 (6H, m), 1.56 (2H, t, J=7.2 Hz), 1.77 (4H, m), 2.51 (2H, t, J=7.6 Hz), 2.70 (2H, t, J=6 Hz), 4.12 (2H, t, J=6 Hz), 6.72 (1H, s), 6.87 (1H, s). ^{13}C-NMR ($CDCl_3$): 14.3, 22.8, 26.8, 28.7, 29.1, 29.6, 29.7, 29.8, 31.8, 75.4, 109.5, 111.3, 127.8, 132.1, 132.5, 134.2, 137.0, 139.4, 139.8, 140.8, 142.8, 143.2. ^{19}F NMR ($CDCl_3$): -163.8, -163.5, -157.1. m/z (HRMS) found: 646.9538 $(M+H)^+$, calculated: 646.9539.

General procedure for Polymer Additive (P) synthesis (Route 1). To a solution of the appropriate monomer **M** (1 eq) in dry THF was added *t*-BuMgCl (1.0 M in THF, 1 eq) at room temperature and the reaction subsequently heated to 70°C. After stirring for 2h, $NidpppCl_2$ (1.4 mol%) dispersed in 1ml dry THF was added via cannula. The reaction was observed to immediately turn deep orange and fluorescent yellow. After stirring for 10 h, excess methanol was added to the reaction mixture to precipitate the polymer. The resulting dark purple solid was reprecipitated twice with $CHCl_3$/MeOH, subjected to Soxhlet extraction with MeOH and acetone and subsequently extracted with $CHCl_3$ to isolate the desired polymer sample.

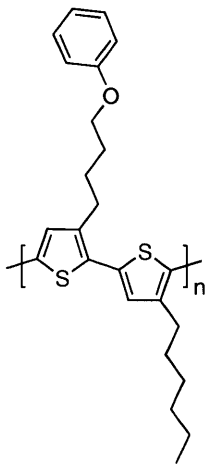

Polymer Additive P1. (82% yield). M_n = 14 KDa, PDI= 1.3. ^{1}H-NMR ($CDCl_3$): 0.88 (3H, b), 1.24-1.50 (6H, mb), 1.61-1.77 (2H, b), 1.77-2.09 (4H, b), 2.7-2.92 (4H, b), 3.98 (2H, b), 6.81-7.02 (5H, m), 7.20-7.25 (2H, b). ^{13}C-NMR ($CDCl_3$): 14.4, 22.9, 27.3, 29.3, 29.5, 29.7, 30.8, 31.9, 32.7, 67.7, 114.7, 120.8, 128.6, 129.1, 129.7, 130.7, 131.4, 133.8, 134.2, 139.4, 140.3, 159.2.

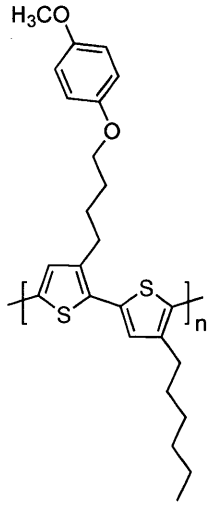

Polymer Additive P3. (65% yield). M_n = 15 KDa, PDI= 1.2. ^{1}H-NMR ($CDCl_3$): 1.03 (3H, b), 1.28-1.63 (6H, mb), 1.63-2.10 (6H, b), 2.80-3.01 (4H, b), 3.87 (3H, b), 4.08 (2H, b), 6.95 (4H, m), 7.40 (2H, b). ^{13}C-NMR ($CDCl_3$): 14.4, 22.9, 27.3, 29.1, 29.5, 29.9, 30.8, 31.9, 55.9, 56.0, 68.5, 114.8, 115.6, 128.7, 129.0, 133.8, 134.0, 136.7, 136.9, 142.9, 143.3, 153.4, 153.9.

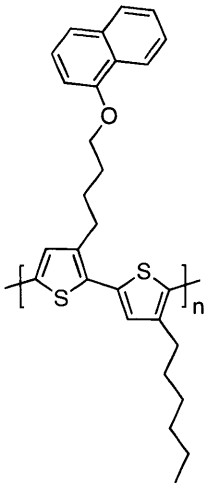

Polymer Additive P4. (81% yield). M_n = 16 KDa, PDI= 1.3. ^{1}H-NMR ($CDCl_3$): 0.85 (3H, b), 1.14-1.44 (6H, b), 1.52-1.72 (2H, b), 1.99 (4H, b), 2.74 (2H, b), 2.92 (2H, b), 4.11 (2H, b), 6.72 (1H, db), 6.98 (2H, b), 7.26-7.47 (4H, b), 7.73 (1H, db), 8.25 (1H, db). ^{13}C-NMR ($CDCl_3$): 14.4, 22.9, 27.4, 29.3, 29.3, 29.5, 29.7, 30.7, 31.9, 67.9, 104.7, 120.3, 122.3, 125.3, 125.9, 126.1, 126.5, 127.6, 128.7, 129.1, 130.8, 131.1, 133.8, 134.2, 134.7, 139.5, 140.3, 155.0.

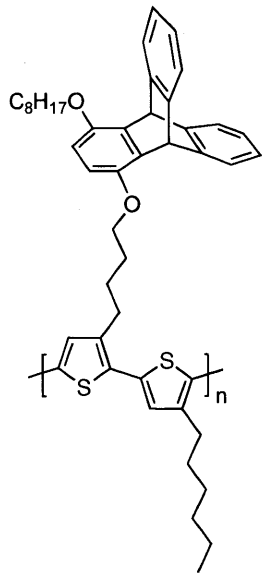

Polymer Additive P5. (85% yield). M_n = 18 KDa, PDI= 1.4. ^{1}H-NMR ($CDCl_3$): 0.78-0.93 (6H, m), 1.20-1.53 (16H, m), 1.57-1.72 (2H, mb), 1.72-1.95 (6H, m), 2.76 (2H, sb), 2.89 (2H, sb),

3.80-3.93 (4H, m), 5.81 (2H, sb), 6.40 (2H, sb), 6.80-6.94 (4H, m), 6.96-7.48 (2H, m), 7.25-7.36 (4H, m). ^{13}C-NMR ($CDCl_3$): 14.4, 14.4, 22.9, 23.0, 26.4, 27.4, 29.2, 29.3, 29.4, 29.5, 29.6, 29.6, 29.7, 30.8, 31.2, 32.1, 47.7, 47.7, 69.4, 69.8, 110.7, 110.8, 123.9, 123.9, 125.1, 128.0, 128.4, 129.0, 130.8, 131.3, 133.7, 134.3, 135.0, 135.9, 136.0, 139.0, 140.2, 145.9, 145.9, 146.0, 148.5, 148.7.

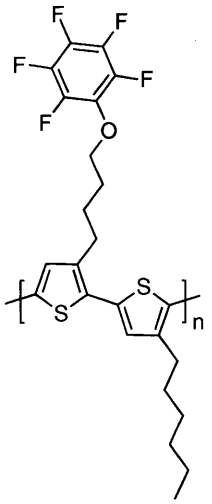

Polymer Additive P6. (74% yield). M_n = 15 KDa, PDI= 1.2. ^{1}H-NMR ($CDCl_3$): 0.87 (3H, b), 1.08-1.48 (6H, mb), 1.48-1.96 (6H, b), 1.77-2.09 (4H, b), 2.68-2.92 (4H, b), 4.18 (2H, b), 6.98 (2H, s). ^{13}C-NMR ($CDCl_3$): 14.4, 22.9, 26.7, 27.5, 29.0, 29.3, 29.7, 30.7, 31.9, 75.7, 128.5, 129.3, 130.6, 131.8, 135.4, 136.4, 139.1, 140.2. ^{19}F-NMR ($CDCl_3$): -163.9, -163.6, -157.0.

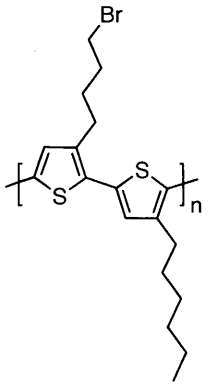

Polymer P7 (Route 2). (76% yield). M_n = 14 K Da, PDI= 1.2. ^{1}H-NMR ($CDCl_3$): 0.90 (3H, b), 1.24-1.47 (6H, mb), 1.61-1.76 (2H, mb), 1.79-1.91 (2H, mb), 1.91-2.03 (2H, mb), 2.71-2.88 (4H, mb), 3.45 (2H, mb), 6.97 (2H, s). ^{13}C-NMR ($CDCl_3$): 14.4, 22.9, 28.7, 29.2, 29.5, 29.7, 30.8, 31.9, 32.7, 33.8, 128.6, 129.1, 130.7, 131.1, 133.6, 134.2, 139.0, 140.4.

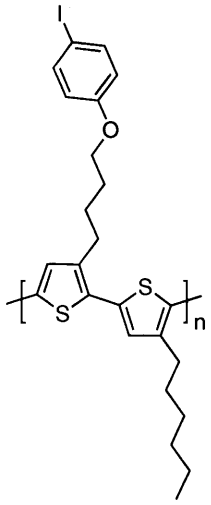

Polymer Additive P2 (R = *p*-iodophenyl). Synthesized following the general procedure for monomer synthesis, using **P7** instead of compound **M0**. The extent of side-chain substitution was monitored by ^{1}H-NMR and ^{13}C-NMR spectroscopy. The resulting polymer was purified twice by reprecipitation from methanol. The side-chain substitution reaction was found to proceed in ca. 99% yield based on ^{1}H-NMR signals, specifically those arising from the CH_2

moiety *alpha* to the bromo or *p*-iodophenol functional group (90% yield of polymer after reprecipitation). M_n = 15 KDa, PDI= 1.2. ^{1}H-NMR ($CDCl_3$): 0.88 (3H, b), 1.13-1.46 (6H, mb), 1.61-2.04 (6H, b), 2.66-2.91 (4H, b), 3.37 (2H, b), 6.98 (2H, s), 7.68 (2H, d), 7.81 (2H, d). ^{13}C-NMR ($CDCl_3$): 14.4, 22.9, 23.7, 27.0, 29.2, 29.5, 29.9, 30.7, 31.9, 33.5, 77.4, 121.2, 128.5, 129.3, 130.6, 131.3, 133.7, 134.5, 139.1, 140.3, 153.5, 167.3.

3.7 References and Notes

(1) (a) O'Regan, B.; Grätzel, M. *Nature* **1991**, *353*, 737-740. (b) Bach, U.; Lupo, D.; Comte, P.; Moser, J. E.; Weissörtel, F.; Salbeck, J.; Spreitzer, H.; Grätzel, M. *Nature* **1998**, *395*, 583-585. (c) Graetzel, M.; *Nature* **2001**, *414*, 338-344.

(2) Yella, A.; Lee, H. W.; Tsao, H. N.; Yi, C.; Chandiran, A. K.; Nazeeruddin, M. K.; Diau, E. W. G.; Yeh, C. Y.; Zakeeruddin, S. M.; Gratzel, M. *Science* **2011**, *334*, 629–634.

(3) Venkataraman, D.; Yurt, S.; Venkatraman, B. H.; Gavvalapalli, N. J. *Phys. Chem. Lett.*, **2010**, *1*, 947-958.

(4) (a) Sacriciftci, N. S., Smilowitz, L.; Heeger A. J.; Wudl, F. *Science*, **1992**, *258*, 1474-1476. (b) Yu, G.; Gao, J.; Hummelen, J. C.; Wudl F.; Heeger, A. J. *Science*, **1995**, *270*, 1789-1791. (c) Mayer, A. C.; Toney, M. F.; Scully, S. R.; Rivnay, J.; Brabec, C. J.; Scharber, M.; Koppe, M.; Heeney, M.; McCulloch, I.; McGehee, M. D. *Adv. Funct. Mater.* **2009**, *19*, 1173-1179.

(5) Plexcore PV 1000 Ink System; Technical Bulletin for Sigma-Aldrich AL-256:Milwaukee, WI, July 2009.

(6) Jørgensen, M.; Norrman, K.; Gevorgyan, S. A.; Tromholt, T.; Andreasen, B.; Krebs F. C. *Adv. Mater.* **2012**, *24*, 580-612.

(7) Barr, M. C.; Rowehl, J. A.; Lunt, R. R.; Xu, J.; Wang, A.; Boyce, C. M.; Im, S. G.; Bulović, V.; Gleason, K. K. *Adv. Mater.* **2011**, *23*, 3500-3505.

(8) Coakley, K. M.; McGehee, M. D. *Chem. Mater.* **2004**, *16*, 4533-4542.

(9) Forrest, S. R. *MRS Bull.* **2005**, *30*, 28-32.

(10) Wu, F.-C.; Huang, Y.-C.; Cheng, H.-L.; Chou, W.-Y.; Tang, F.-C. *J. Phys. Chem. C* **2011**, *115*, 15057-15066.

(11) Yin, W.; Dadmun, M. *ACS Nano* **2011**, *5*, 4756-4768.

(12) Hopkinson, P. E.; Staniec, P. A.; Pearson, A. J.; Dunbar, A. D. F.; Wang, T.; Ryan, A. J.; Jones, R. A. L.; Lidzey, D. G.; Donald, A. M. *Macromolecules* **2011**, *44*, 2908-2917.

(13) Kozub, D. R.; Vakhshouri, K.; Orme, L. M.; Wang, C.; Hexemer, A.; Gomez, E. D. *Macromolecules* **2011**, *44*, 5722-5726.

(14) Kiel, J. W.; Mackay, M. E.; Kirby, B. J.; Maranville, B. B.; Majkrzak, C. F. *J. Chem. Phys.* **2010**, *133*, 074902.

(15) (a) Scharber, M. C.; Mühlbacher, D.; Koppe, M.; Denk, P.; Waldauf, C.; Heeger, A. J.; Brabec, C. J. *Adv. Mater.* **2006**, *18*, 789-794. (b) Chen, H.-Y.; Hou, J.; Zhang, S.; Liang, Y.; Yang, G.; Yang, Y.; Yu, L.; Wu, Y.; Li G. *Nature Photon.* **2009**, *3*, 649-653. (c) Huo, L.; Hou, J.; Chen, H.-Y.; Zhang, S.; Jiang, Y.; Chen T. L.; Yang, Y. *Macromolecules* **2009**, *42*, 6564-6571. (d) Zhu, Z.; Waller, D.; Brabec, C. J. *New Construction of Low-Bandgap Conducting Polymers. In Organic Photovoltaics*; Brabec, C., Dyakonov, V, Scherf, U., Eds.; Wiley-VCH: Weinheim, 2008; pp.129-151.

(16) (a) Padinger, F.; Rittberger, R. S.; Sariciftci, N. S. *Adv. Funct. Mater.* **2003**, *13*, 85-88. (b) Hoppe, H.; Saricitfci, N. S. *J. Mater. Chem.* **2006**, *16*, 45-61. (c) Woo, C. H.; Thompson, B. C.; Kim, B. J.; Toney M. F.; Fréchet, J. M. J. *J. Am. Chem. Soc.* **2008**, *130*, 16324-16329.

(17) Brabec, C. J.; Gowrisanker, S.; Halls, J. J. M.; Laird, D.; Jia, S.; Williams, S. P. *Adv. Mater.* **2010**, *22*, 3839-3856 and references therein.

(18) Brinkmann, M.; Rannou, P. *Adv. Funct. Mater.* **2007**, *17*, 101–108.

(19) Lee, J. K.; Ma, W. L.; Brabec, C. J.; Yuen, J.; Moon, J. S.; Kim, J. Y.; Lee, K.; Bazan, G. C.; Heeger, A. J. *J. Am. Chem. Soc.* **2008**, *130*, 3619-3623.

(20) Tsai, J.-H.; Lai, Y.-C; Higashihara, T.; Lin, C.-J.; Ueda, M.; Chen, W.-C. *Macromolecules* **2010**, *43*, 6085-6091.

(21) Sivula, K.; Ball, Z. T.; Watanabe, N.; Fréchet, J. M. J. *Adv. Mater.* **2006**, *18*, 206-210.

(22) Yang, C.; Lee, J. K.; Heeger, A. J.; Wudl, F. *J. Mater. Chem.* **2009**, *19*, 5416-5423.

(23) Campoy-Quiles, M.; Kanai, Y.; El-Basaty, A.; Sakai H.; Murata, H. *Org. Elect.* **2009**, *10*, 1120-1132.

(24) Nguyen, L. H.; Hoppe, H.; Erb, T.; Günes, S.; Gobsch, G.; Sariciftci, N. S. *Adv. Funct. Mater.* **2007**, *17*, 1071-1078.

(25) Wu, P.-T.; Ren, G.; Jenekhe, S. A. *Macromolecules* **2010**, *43*, 3306-3313.

(26) Mondal, R.; Ko, S.; Verploegen, E.; Becerril, H. A.; Toney, M. F.; Bao, Z. *J. Mater. Chem.* **2011**, *21*, 1537-1543.

(27) Thompson, B. C.; Kim, B. J.; Kavulak, D. F.; Sivula, K.; Mauldin, C.; Fréchet, J. M. J. *Macromolecules* **2007**, *40*, 7425-7428.

(28) Moulé, A. J.; Allard, S.; Kronenberg, N. M.; Tsami, A.; Scherf, U.; Meerholz, K. *J. Phys. Chem. C* **2008**, *112*, 12583-12589.

(29) Mayer, A. C.; Toney, M. F.; Scully, S. R.; Rivnay, J.; Brabec, C. J.; Scharber, M.; Koppe, M.; Heeney, M.; McCulloch, I.; McGehee, M. D. *Adv. Funct. Mater.* **2009**, *19*, 1173-1179.

(30) Ohshimizu, K.; Takahashi, A.; Rho, Y.; Higa-shihara, T.; Ree, M.; Ueda, M. *Macromolecules* **2011**, *44*, 719-727.

(31) Stokes, K. K.; Heuzé, K.; McCullough, R. D. *Macromolecules* **2003**, *36*, 7114-7118.

(32) Bjørnholm, T.; Greve, D. R.; Reitzel, N.; Has-senkam, T.; Kjaer, K.; Howes, P. B.; Larsen, N. B.; Bøgelund, J.; Jayaraman, M.; Ewbank, P. C.; McCullough, R. D. *J. Am. Chem. Soc.* **1998**, *120*, 7643-7644.

(33) Wang, F.; Yang, Y.; Swager, T. M. *Angew. Chem. Int. Ed.* **2008**, *47*, 8394-8396.

(34) Veen, E. M.; Postma, P. M.; Jonkman, H. T.; Spek, A. L.; Feringa. *Chem. Commun.* **1999**, 1709-1710.

(35) McCullough, R. D.; Lowe, R. D. *Chem. Commun.* **1992**, 70-72.

(36) Loewe, R. S.; Khersonsky, S. M.; McCullough, R. D. *Adv. Mater.* **1999**, *11*, 250-253.

(37) Loewe, R. S.; Ewbank, P. C.; Liu, J.; Zhai, L.; McCullough, R. D. *Macromolecules* **2001**, *34*, 4324-4333.

(38) For examples of GRIM polymerizations used to obtain alternating AB copolymers from the corresponding 5,5′-dibromo-2,2′-bithiophene monomer, see: (a) Wang, B.; Watt, S.; Hong, M.; Domercq, B.; Sun, R.; Kippelen, B.; Collard, D. M. *Macromolecules* **2008**, *41*, 5156-5165. (b) Benanti, T. L.; Kalaydjian, A.; Venkataraman, D. *Macromolecules* **2008**, *41*, 8312-8315 (c) Hong, X. M.; Tyson, J. C.; Collard, D. M. *Macromolecules* **2000**, *33*, 3502-3504.

(39) Wang, Q.; Takita, R.; Kikuzaki, Y.; Ozawa, F. *J. Am. Chem. Soc.* **2010**, *132*, 11420–11421.

(40) Kim, Y.; Cook, S.; Tuladhar, S. M.; Choulis, S. A.; Nelson, J.; Durrant, J. R.; Bradley, D. D. C.; Giles, M.; McCulloch, I.; Ha, C.-S.; Ree, M. *Nature Materials* **2006**, *5*, 197-203.

(41) Adapted from Stokes, K. K.; Heuzé, K.; McCullough, R. D. *Macromolecules* **2003**, *36*, 7114-7118.

(42) Benanti, T. L.; Kalaydjian, A.; Venkataraman, D. *Macromolecules*, **2008**, *41*, 8312-8315.

(43) Long, T. M.; Swager. T. M. *J. Am. Chem. Soc.* **2002**, *124*, 3826-3827.

CHAPTER 4

Side-Chain Functionalized Polythiophene Additives: Photovoltaic Cell Performance and Optimization

Adapted and reprinted in part with permission from:

Lobez, J. M.; Andrew, T. L.; Bulović, V.; Swager, T. M. "Improving the Performance of P3HT-Fullerene Bulk Heterojunction Solar Cells with Side-Chain Functionalized Polythiophene Additives: A New Paradigm for Polymer Design" *ACS Nano* **2012** DOI: 10.1021/nn204589u

4.1 Introduction

In this chapter, the fabrication of solar cells containing the polymer additives introduced in chapter 3 (Figure 4.1) is described, and their performance is evaluated. The origin of their influence in the solar cell efficiency is also studied in this chapter.

An example of the resulting solar cells is shown in Figure 4.2. There are many factors that have an effect in the final solar cell performance such as the exact formulation of the active layer (ratio of donor to acceptor and additive loading) and the active layer thickness and those aspects are explored in this chapter as well. Finally, the exact influence of the regioregularity, alternance and degree of substitution on additive performance is also described.

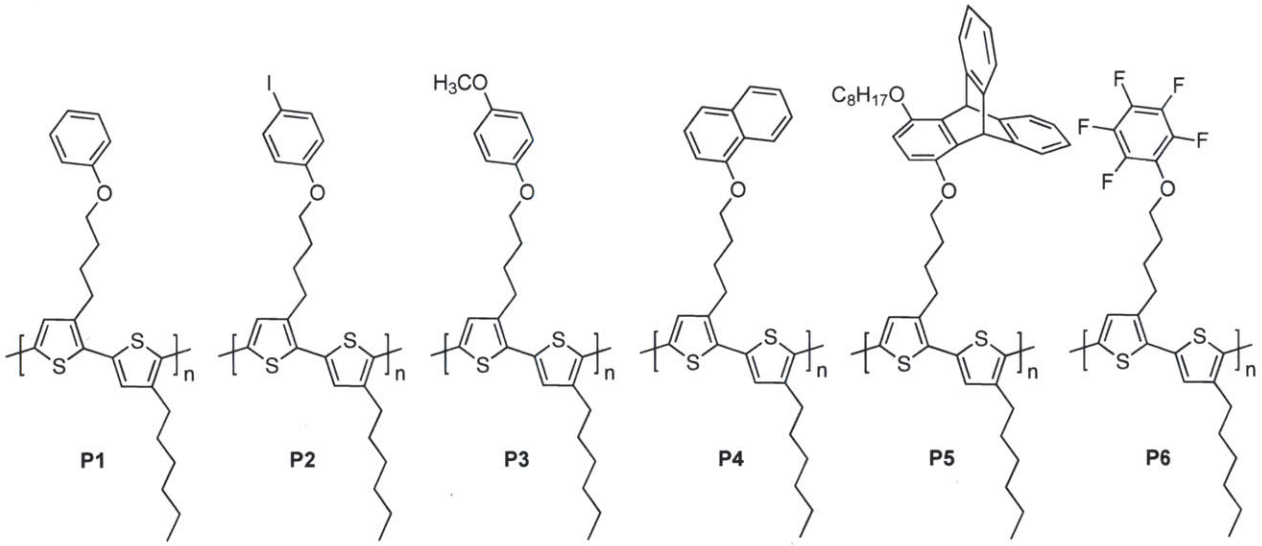

Figure 4.1. Polymer Additives **P1-P6**

Figure 4.2. Size comparison of a coupon containing 8 solar cells on it and a 5 cent coin

4.2 Photovoltaic Cell Performance of Bulk Heterojunctions Including Polythiophene Additives

The motivation of this study is to determine if small amounts of designer polymers placed at the bulk heterojunction (BHJ) interface can influence the performance of an OPV device. In order to investigate the effect of side-chain functionalization on solar cell efficiency, solar cells containing **P1-P6** in the active layer were fabricated. Considering the disordered solid-state packing structure demonstrated by neat films of **P1-P6** described in the previous chapter of this thesis, we expected that these polymers would not perform well as majority donor materials in a solar cell; indeed, solar cells containing binary mixtures of **P1-P6** and phenyl-C_{61}-cetylbutyric acid methyl ester (**$PC_{61}BM$**) displayed poor power conversion efficiencies and diode rectification. Therefore, to test the performance of **P1-P6** as designer additives, we investigated OPVs containing ternary mixtures of regioregular poly (3-hexylthiophene) (**rr-P3HT**), **P1-P6** and a fullerene.

4.2.1 J/V Curves under Illumination

The current density-voltage (J-V) curves under illumination (averaged over eight devices) for solar cells fabricated with 1:1 **P3HT**:**$PC_{61}BM$** and 0.25 wt% **P1-P6** are shown in Figure 4.3. Table 4.1 provides a summary of pertinent device metrics (short circuit current J_{SC}, open circuit voltage V_{OC}, fill factor FF, series resistance R_s and shunt resistance R_{sh}).

The J-V curve for an average **P3HT/$PC_{61}BM$** solar cell without an additive is provided in black in Figure 4.3B. In our hands, these reference devices (with an active layer thickness of 75 ± 5 nm) display open circuit voltage (V_{OC}) values of 0.59 ± 0.01 V, short circuit current (J_{SC}) values of 9.3 ± 0.2 mA/cm^2 and fill factors (FFs) of 0.52 ± 0.03. As can be seen in Figure 4.3B

and Table 4.1, the addition of small amounts of **P1-P6** to the **P3HT/$PC_{61}BM$** BHJ leads to an increase in the J_{SC} of the solar cells, while the V_{OC} and FF remain approximately the same.

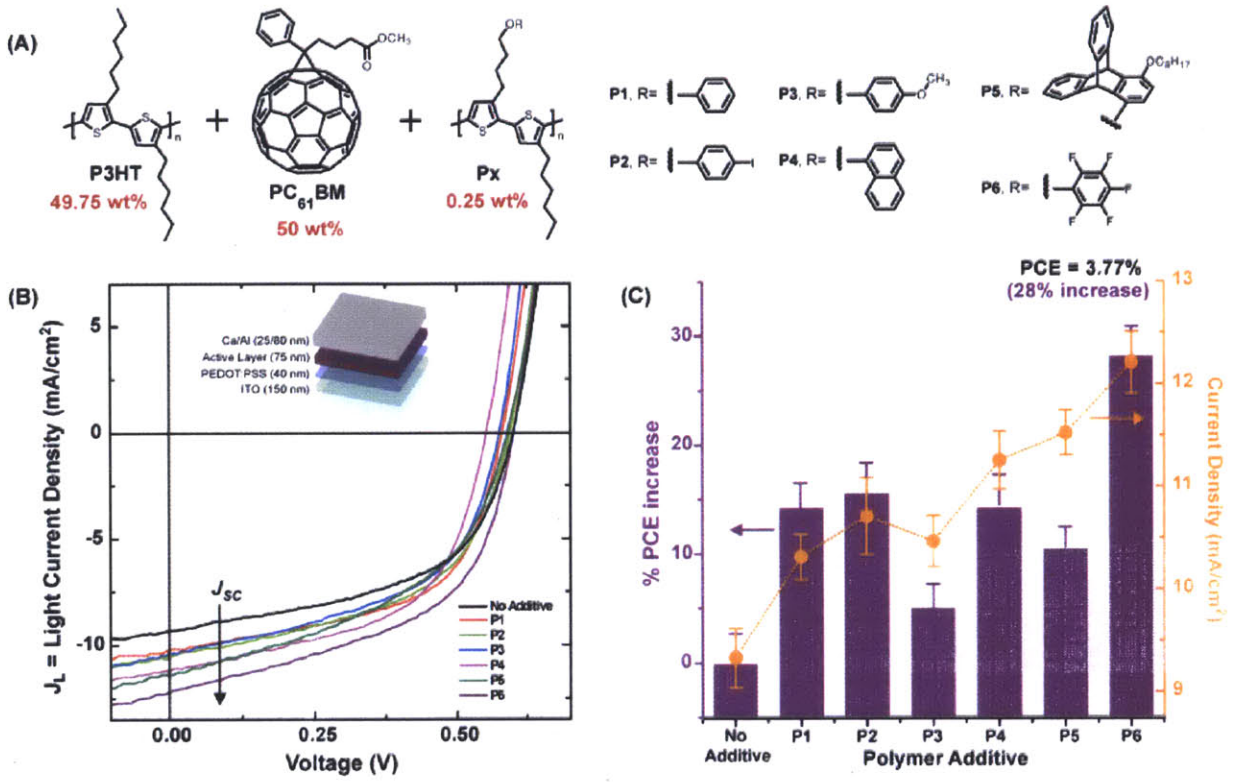

Figure 4.3. Performance of devices containing ternary mixtures of **P3HT**, **P1-P6** and fullerene. (A) Composition of active layer – 1:1 ratio of total polymer (**P3HT** + 0.25 wt% **P1-P6**) to **$PC_{61}BM$**. (B) J-V curves (average over 8 different devices) under 1 sun for solar cells containing the active layer shown in (A). Inset: device architecture. (C) PCE increase (purple bars, left Y-Axis, % versus a solar cell with no additive) upon incorporation of 0.25 wt% **P1-P6**. The variation of J_{SC} with different additives is superposed (orange, right Y-Axis)

Notably, adding a polythiophene with phenyl moieties at side-chain termini (**P1**) to the **P3HT/$PC_{61}BM$** BHJ increases the observed J_{SC} by 11% ± 3%. The comparatively bulky p-iodophenyl analog **P2** and the electron-rich analog **P3** perform similar to **P1**. Naphthyl moieties

(**P4**) lead to higher observed J_{SC} than phenyl moieties (**P1**), but significantly decrease the V_{OC} of the devices. If fullerene-binding triptycene moieties (**P5**) are introduced instead of simple phenyl groups (**P1**), the J_{SC} increases by 23% ± 4%; however, **P5** decreases the FF of the resulting device. Pentafluorophenol-containing additive **P6** leads to the highest increase in overall PCE (28% ± 4%) by increasing the J_{SC} by 25% ± 3% while leaving the V_{OC} unchanged.

	J_{SC} (mA/cm^2)	V_{OC} (V)	FF
P3HT/PC$_{61}$BM	9.32	0.59	0.52
+ 0.25 wt% **P1**	10.3	0.58	0.57
+ 0.25 wt% **P2**	10.7	0.60	0.53
+ 0.25 wt% **P3**	10.4	0.57	0.52
+ 0.25 wt% **P4**	11.2	0.55	0.54
+ 0.25 wt% **P5**	11.5	0.59	0.48
+ 0.25 wt% **P6**	12.2	0.60	0.53

Table 4.1. Summary of device metrics for solar cells containing ternary mixtures of **P3HT**, 0.25 wt% **P1-P6** and **PC$_{61}$BM** (1 sun illumination)

4.2.2 Dark J/V Curves

The series resistance (R_s) and the shunt resistance of the devices (R_{sh}) can be obtained from the dark J-V curves (Figure 4.4, values tabulated on Table 4.2). In these curves, the built-in voltage, V_{BI}, is subtracted from the applied bias, V, to provide the corrected voltage. V_{BI} is taken as a compensation voltage $V_0 \approx V_{OC} + 0.05$ V. R_s is defined as the slope of the dark J-V curves at 0.6 V, and R_{sh} can be defined as dV/dJ of the dark J-V curve at V = -0.1 – 0 V.

R_s is lower in cells containing **P1-P6** compared to the reference **P3HT/PC$_{61}$BM** device. This can be seen more clearly in the log-log representation of the dark J-V curves (Figure 4.4, inset), where higher dark injection currents are observed for devices containing **P1-P6** compared

to **P3HT/PC$_{61}$BM**. It is also evident from semilog plots of the dark J-V curves that the side-chain functionalized additives yield higher rectifying values compared to reference cells.

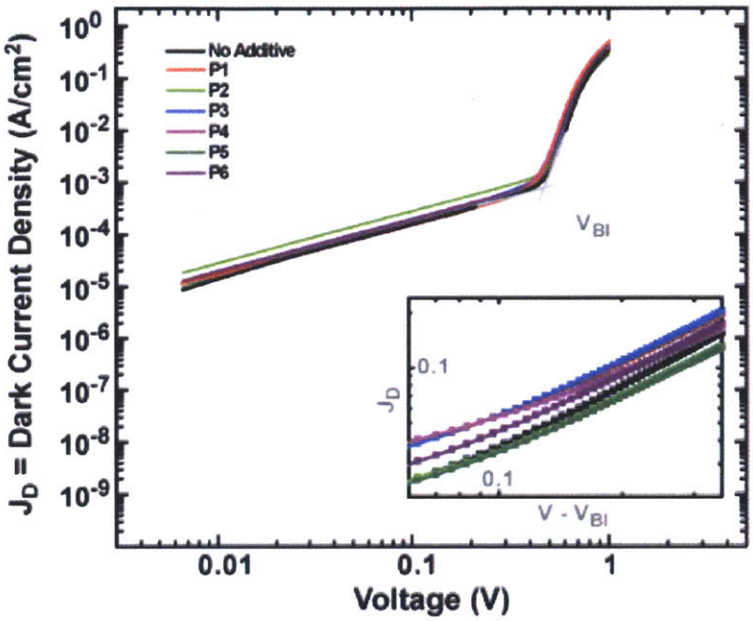

Figure 4.4. Log-Log plot of dark J-V curves for solar cells containing the active layer shown in Figure 4.2A. The inset is a plot of the dark current density, J_D, versus corrected voltage values

	R_S (Ωcm^2)	R_{Sh} (Ωcm^2)
P3HT/PC$_{61}$BM	13.5	1280
+ 0.25 wt% **P1**	7.3	1460
+ 0.25 wt% **P2**	12.1	909
+ 0.25 wt% **P3**	7.7	1055
+ 0.25 wt% **P4**	5.8	1081
+ 0.25 wt% **P5**	12.8	1397
+ 0.25 wt% **P6**	10.7	1043

Table 4.2. Summary of resistance values for device containing ternary mixtures of **P3HT**, 0.25 wt% **P1-P6** and **PC$_{61}$BM**

4.2.3 External Quantum Efficiencies

The increase in the J_{SC} upon adding 0.25 wt% side-chain functionalized polythiophenes is also manifested as an increase in the external quantum efficiency (EQE) of the devices containing **P1-P6** (see Figure 4.5). The increase in EQE cannot simply be attributed to an increase in light absorption because the absorption spectra and optical densities of 75 nm-thick films of **P3HT/PC$_{61}$BM** with or without 0.25 wt% **P1-P6** are nearly identical (see Figure 4.6). Therefore, this effect possibly originates from a decrease in the amount of charge recombination at the polymer-fullerene heterointerface.

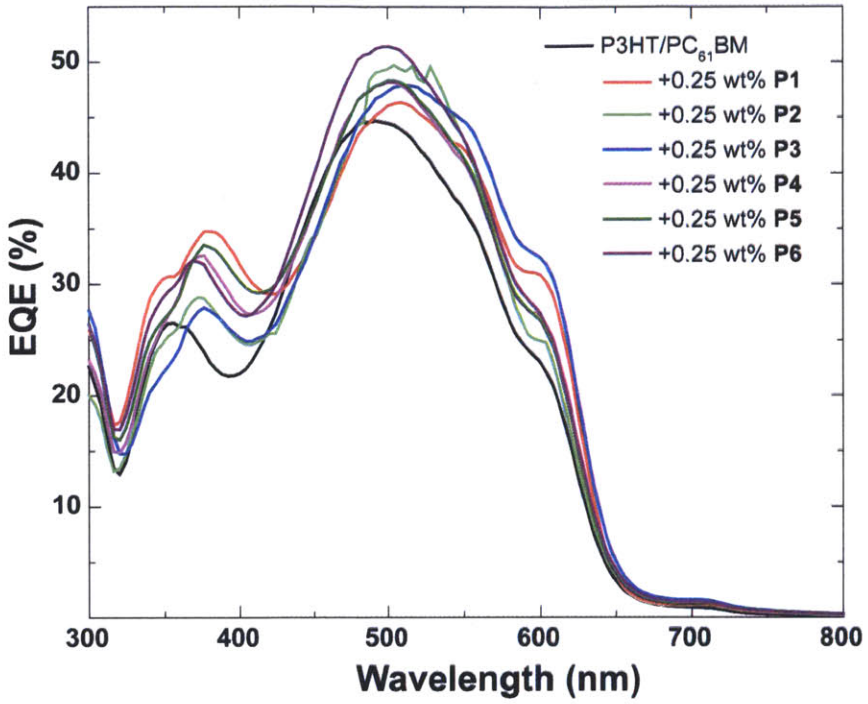

Figure 4.5. EQEs of solar cells fabricated with 1:1 **P3HT**:**PC$_{61}$BM** and 0.25 wt% **P1-P6**

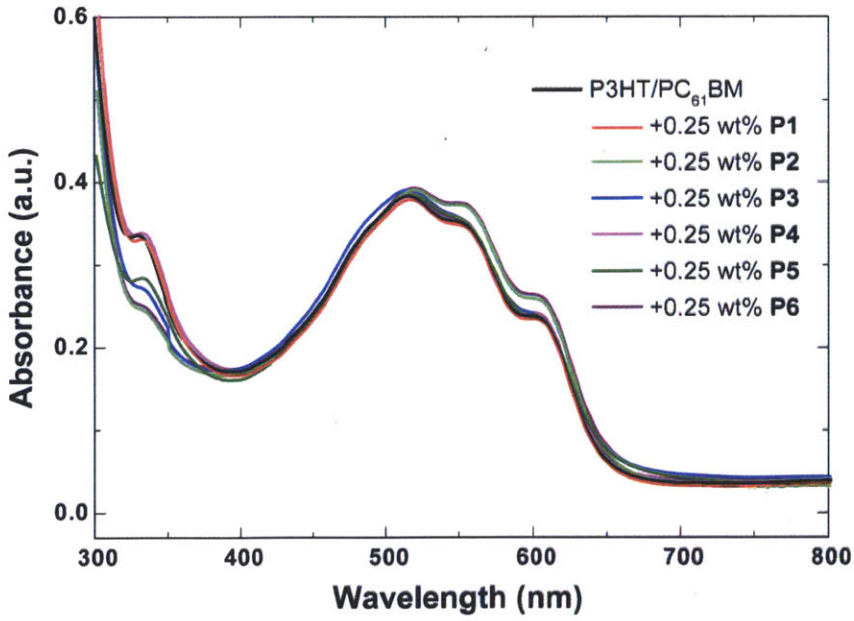

Figure 4.6. Absorption spectra (transmission mode) of the solar cell active layers from Figure 4.2 (1:1 **P3HT**:**PC$_{61}$BM** with added 0.25 wt% **P1-P6**). All films are 75 nm-thick and are spun-cast on glass

4.2.4 Photocurrent Measurements

Figure 4.7 shows the experimental photocurrent J_{ph} as a function of effective applied voltage ($V_{eff} = V_0 - V$) for solar cells containing 0.25 wt% of **P1-P6**. The photocurrent ($J_{ph} = J_L - J_D$) is the measured current under illumination (J_L) corrected for the dark current (J_D), whereas the compensation voltage V_0 is defined as the voltage at which the photocurrent J_{ph} is zero. At voltages close to the compensation voltage ($V_0 - V < 0.1$ V), the photocurrent is observed to increase linearly with voltage.

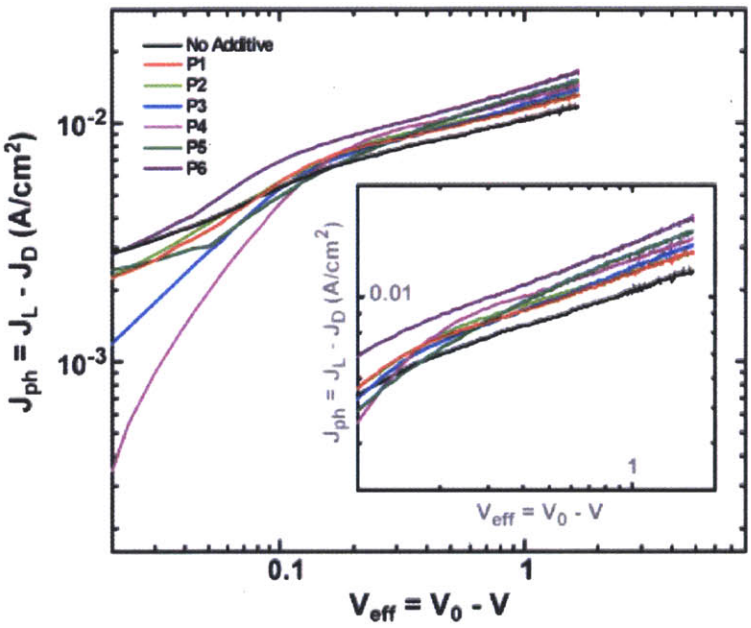

Figure 4.7. Experimental photocurrent as a function of effective applied voltage, $V_{eff} = V_0 - V$, for solar cells containing the active layer shown in (A). V0 represents the compensation voltage for which the photocurrent $J_{ph} = J_L - J_D = 0$. The inset zooms-in on the region where $V_{eff} > 0.1$ and the photocurrent displays a square root dependence on voltage

For $V_0 - V > 0.1V$, the photocurrent enters a regime where a square root dependence on the effective voltage is observed. Similar behavior has been characterized in multiple conjugated polymer-fullerene BHJ OPVs, where the decrease in photocurrent for $V_0 - V > 0.1V$ is attributed to recombination effects.[1,2] Specifically, the low mobilities or short lifetimes of free carriers (due to either recombination or trapping) are believed to limit the observed photocurrent in polymer solar cells. As seen in Figure 4.7, polymer additives **P1-P6** consistently yield higher photocurrents in the square root regime ($V_0 - V > 0.1V$) compared to **P3HT/PC$_{61}$BM** reference cells, thus suggesting that these side-chain functionalized additives decrease charge recombination.

4.3 Transient Open Circuit Voltage Measurements

To directly probe charge recombination in solar cells containing **P1-P6** in the active layer, small-perturbation transient open-circuit voltage decay measurements[3,4] were performed. In this measurement, a device is illuminated with 100 mW/cm^2 white light (1 sun) to create open circuit conditions while, simultaneously, a low-intensity pulsed 635 nm laser is used to induce a small perturbation to the V_{OC} by transiently generating additional electrons and holes. The resulting additional transient photovoltage, ΔV, will then decay with a lifetime that is determined by the recombination rate constant of the electrons and holes. Bias illumination was 100 mW/cm^2 white light giving V_{OC} values of: 0.59 V for no additive (**P3HT/PC$_{61}$BM**); 0.58 V for additive **P1**; 0.60 V for additive **P2**; 0.57 V for additive **P3**; 0.55 V for additive **P4**; 0.59 V for additive **P5**; and 0.60 V for additive **P6**. The secondary pulse was from a 635 nm laser, length 5s.

Figure 4.8 shows representative photovoltage transients for cells with or without **P1-P6**. The transients were taken at V_{OC} for each device with 1 sun bias light. The signals have been normalized to the same height at time zero. The actual voltage peak of all transients was <3 mV.

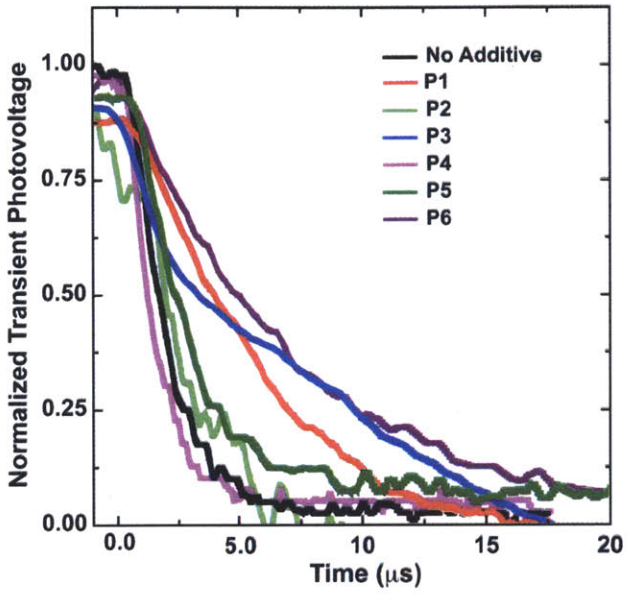

Figure 4.8. Normalized transient photovoltage curves at V_{OC} for solar cells containing a 1:1 ratio of total polymer (**P3HT** + 0.25 wt% **P1-P6**) to **$PC_{61}BM$**. The J-V curves under 1 sun for these devices are shown in Figure 4.2

With the exception of **P4**, additive incorporation caused a slower decay in transient photovoltage, which indicates an increase in charge carrier lifetime. As seen in the J-V curve in Figure 4.3, the presence of 0.25 wt% **P4** leads to a significant decrease in the V_{OC} of the resulting solar cell and, therefore, the minimal, off-trend decrease in transient V_{OC} lifetime observed in the presence of **P4** is expected. Blends containing additive **P3**, with electron-rich p-anisyl moieties at side-chain termini, display multi-exponential decay, thus suggesting the presence of multiple charge trapping or recombination mechanisms in this device. Blends containing **P6** that have the

highest J_{SC} values also demonstrate the slowest decay in transient photovoltage. This result can be interpreted as a decrease in the recombination rate across the polymer-fullerene heterointerface in the presence of **P6**.

4.4 Additive Loading Optimization

Figure 4.9 shows the J-V curves of devices containing varying amounts of **P1-P6** in the active layer. Appropriate metrics for the various devices examined in Figure 4.9 are tabulated in Table 4.3).

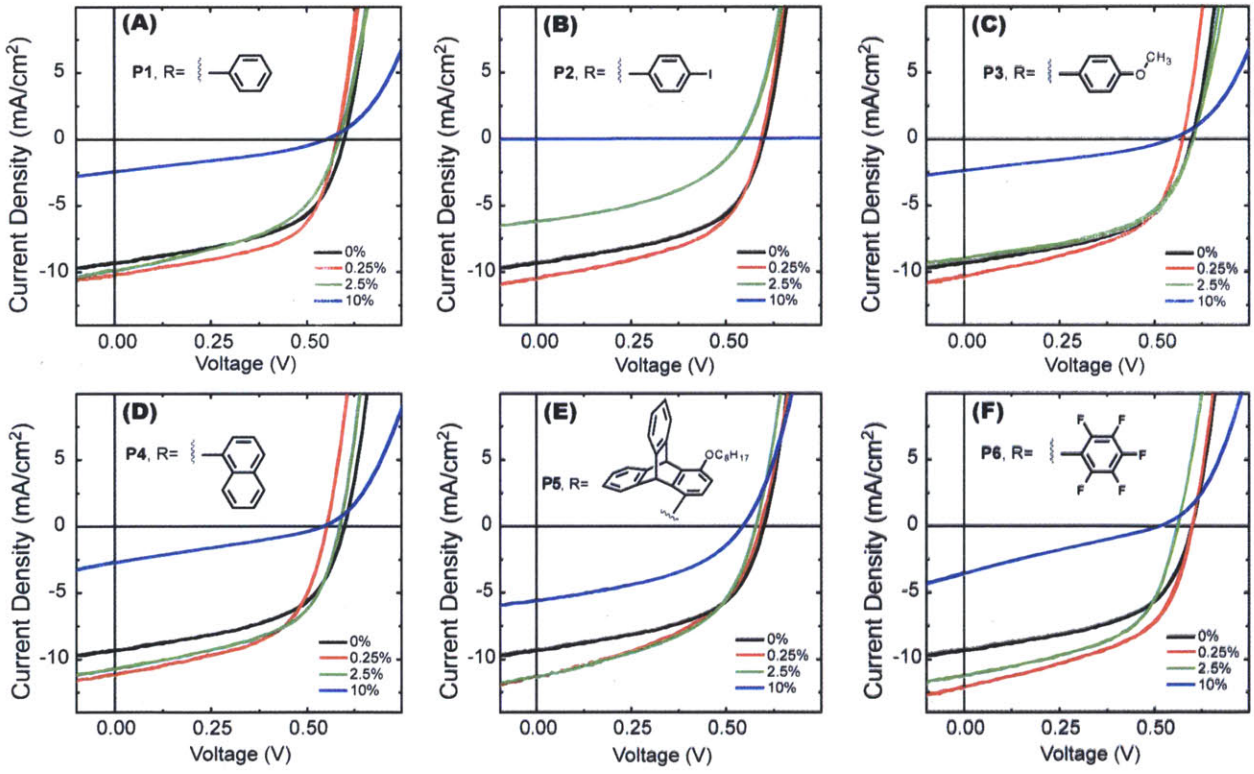

Figure 4.9. J-V curves under 1 sun for solar cells containing 50/50 total polymer/**$PC_{61}BM$** with varying amounts (0% black, 0.25% red, 2.5% green, 10% blue) of **P1-P6**. The average J-V curves from eight different devices are shown in each case. Panels **A-F** correspond to additives **P1-P6**, respectively. The insets show the structure of the functional group attached to the side-chain of the corresponding additive

In general, when additives **P1-P6** are present in 0.25 wt%, higher PCEs are observed compared to a **P3HT/PC$_{61}$BM** control. However, if greater than ca. 5 wt% of **P1-P6** is used, a decrease in the PCE is observed for all additives due to increased series resistances, which manifests as a decrease in both J_{SC} and FF values. Similar observations of reduced performance have been noted for other macromolecular additives,[5] and are attributed to a decrease in the carrier mobilities caused by phase segregation and significant disruptions of the BHJ morphology. Indeed, for higher doping concentrations an expected increase in the series resistance can be observed, consistent with reduced carrier mobilities.

	J_{SC} (mA/cm^2)	V_{OC} (V)	FF	PCE
P3HT/$PC_{61}BM$	9.32 ± 0.20	0.59 ± 0.01	0.52 ± 0.03	2.9 ± 0.2%
+ P1				
10 wt%	2.45 ± 0.30	0.55 ± 0.01	0.34 ± 0.02	0.42 ± 0.2%
2.5 wt%	9.93 ± 0.20	0.59 ± 0.02	0.48 ± 0.03	2.8 ± 0.2%
0.25 wt%	10.3 ± 0.1	0.58 ± 0.01	0.57 ± 0.03	3.4 ± 0.1%
+ P2				
10 wt%	0.0365 ± 0.008	0.50 ± 0.01	0.17 ± 0.02	0.003 ± 0.001%
2.5 wt%	6.22 ± 0.30	0.54 ± 0.01	0.43 ± 0.02	1.4 ± 0.2%
0.25 wt%	10.7 ± 0.3	0.60 ± 0.01	0.53 ± 0.05	3.4 ± 0.4%
+ P3				
10 wt%	2.38 ± 0.20	0.55 ± 0.02	0.37 ± 0.03	0.48 ± 0.2%
2.5 wt%	9.07 ± 0.30	0.60 ± 0.01	0.52 ± 0.02	2.8 ± 0.2%
0.25 wt%	10.4 ± 0.2	0.57 ± 0.01	0.52 ± 0.03	3.1 ± 0.2%
+ P4				
10 wt%	2.73 ± 0.30	0.55 ± 0.01	0.29 ± 0.02	0.43 ± 0.12%
2.5 wt%	10.8 ± 0.30	0.59 ± 0.01	0.53 ± 0.02	3.4 ± 0.2%
0.25 wt%	11.2 ± 0.2	0.55 ± 0.01	0.54 ± 0.03	3.3 ± 0.2%
+ P5				
10 wt%	5.61 ± 0.20	0.54 ± 0.04	0.43 ± 0.04	1.3 ± 0.4%
2.5 wt%	11.4 ± 0.2	0.58 ± 0.02	0.49 ± 0.03	3.2 ± 0.3%
0.25 wt%	11.5 ± 0.1	0.59 ± 0.01	0.48 ± 0.03	3.2 ± 0.1%
+ P6				
10 wt%	3.62 ± 0.20	0.52 ± 0.01	0.25 ± 0.03	0.47 ± 0.05%
2.5 wt%	11.3 ± 0.30	0.56 ± 0.01	0.53 ± 0.02	3.4 ± 0.2%
0.25 wt%	12.2 ± 0.2	0.60 ± 0.01	0.53 ± 0.02	3.8 ± 0.2%

Table 4.3. Summary of device metrics for solar cells containing 50/50 total polymer/**$PC_{61}BM$** with varying amounts (0.25 wt%, 2.5 wt%, 10 wt%) of **P1-P6** (1 sun illumination)

4.5 Photovoltaic Cell Morphology Characterization

The nanoscale morphologies of the polymer-**$PC_{61}BM$** films were studied using tapping-mode atomic force microscopy (AFM)[6] and the resulting measurements are depicted in Figure 4.10. Surface topography (left) and phase images (right) were taken for films containing 0 wt%, 0.25 wt% and 2.5 wt% **P6**. Average surface roughness values measured from the topography images of three different 5 μm × 5 μm regions of each film are as follows: 1.51 ± 0.02 nm for 0 wt% **P6**; 3.00 ± 0.01 nm for 0.25 wt% **P6**; and 2.98 ± 0.02 nm for 2.5 wt% **P6**.

With **P6** loadings as low as 0.25 wt%, the average surface roughness is double that of **P3HT/$PC_{61}BM$** films, therefore suggesting that aromatic moieties present at side-chain termini are capable of significantly affecting the morphology of polymer-fullerene blends. Very different morphologies are indeed observed for the three different blends in their phase images (Figure 4.10, right panels). Bicontinuous networks of nanoscale fibrillar features are apparent in Figure 10A and 10B for films containing 0 wt% and 0.25 wt% **P6**, respectively. However, the phase images of films containing 2.5 wt% **P6** reveal the presence of isolated clusters with relatively large domain widths (up to 30 nm). These observations are consistent with the loading-dependent J-V curves shown in Figure 4.9, wherein higher **P6** loadings lead to decreased V_{OC} and J_{SC} values and increased series resistances.

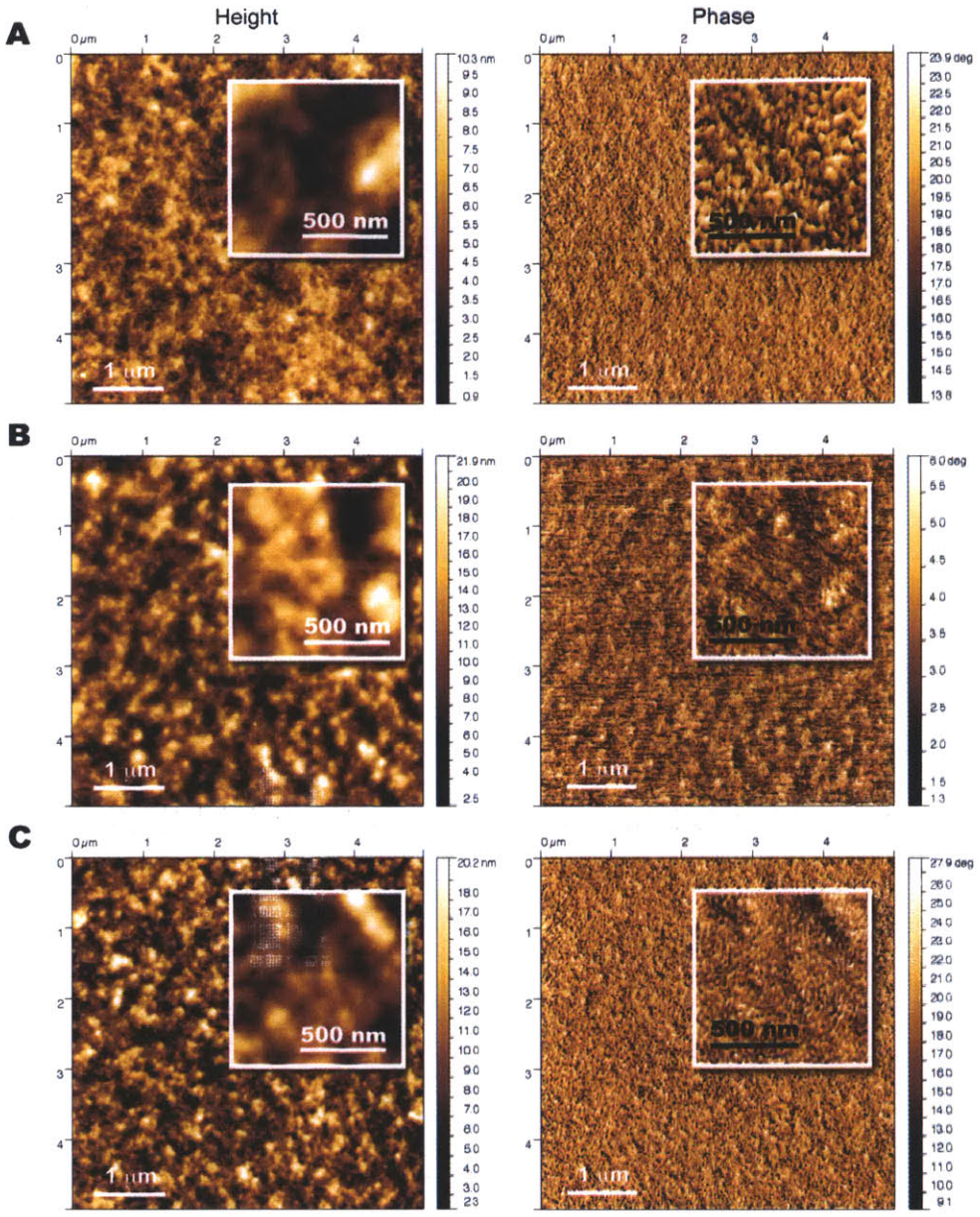

Figure 4.10. Tapping-mode atomic force microscopy images of a 5 µm × 5 µm region of three films used in making devices shown in Figure 4.9F. (**A**) 1:1 **P3HT** : **$PC_{61}BM$**. (**B**) 1:1 (**P3HT** + 0.25 wt% **P6**) to **$PC_{61}BM$**. (**C**) 1:1 (**P3HT** + 2.5 wt% **P6**) to **$PC_{61}BM$**. (**A-C**) The topography of each film is shown in the left panels and the corresponding phase images in the right panels. Insets show the topography and corresponding phase images for a smaller scan area (1 µm × 1 µm) of the same films

4.6 Layered Photovoltaic Cells

In order to further characterize the effects of the side-chain functionalized additives on device performance in the absence of morphological factors, layered solar cells were fabricated. Specifically, devices containing discrete layers of **P3HT**, fullerene and a side-chain functionalized polythiophene were studied to ascertain whether the side-chain moiety can introduce a dipole at the polymer-fullerene interface and thus increase the observed V_{OC}.[7,8] The device structure is as follows: ITO / PEDOT:PSS / **P3HT** / additive / C_{60} / Ca / Al (Figure 4.11).

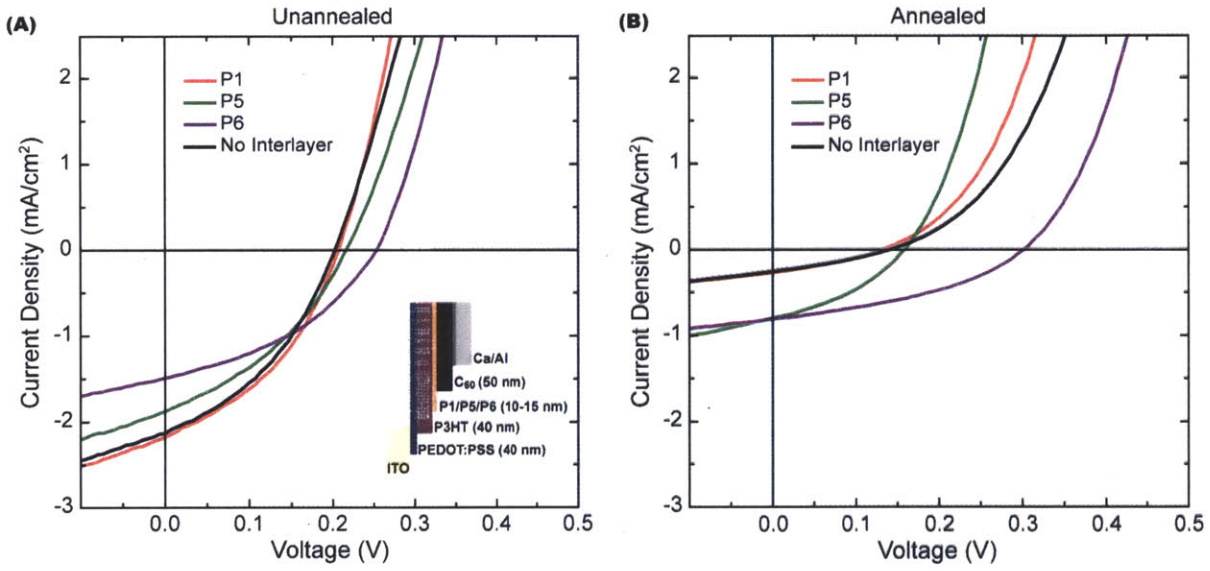

Figure 4.11. Devices containing discrete layers of **P3HT**, side-chain functionalized polythiophenes and C_{60}. A reference **P3HT**/C_{60} device lacking a layer of the side-chain functionalized additive is shown in black. (A) J-V curves under illumination of as-deposited, planar devices. The inset depicts the layered device architecture, with the thickness of each layer provided. (B) J-V curves under illumination of the same devices as in (A) after annealing at 150°C under nitrogen for 1 hour to create a planar-mixed heterojunction

Discrete layers of **P3HT** and **P1**, **P5**, or **P6** are obtained by first spin-casting a layer of **P3HT** from 1,2-dichlorobenzene and annealing it at 150°C, then spin-casting a layer of the appropriate additive from dichloromethane (DCM) solutions. The procedure of using DCM as an orthogonal solvent for high molecular **rr-P3HT** has been previously reported.[9] The high molecular weight **rr-P3HT** used in this study is insoluble in DCM; however polymer additives **P1-P6** are solubilized by DCM, thus allowing for their deposition onto **rr-P3HT** with minimal layer mixing. A 50 nm-thick layer of C_{60}, followed by layers of calcium (25 nm) and aluminum (80 nm) are then deposited by thermal evaporation under high vacuum.

Appropriate metrics for the devices examined in Figure 4.11 are tabulated in Table 4.4. Indeed, when a thin layer (15 ± 5 nm) of **P1**, **P5** or **P6** is introduced between layers of **P3HT** (40 nm) and C_{60} (50 nm), a 3 mV, 13 mV and 51 mV increase, respectively, in the V_{OC} of the solar cell is observed compared to **P3HT**/C_{60} devices lacking an interlayer (Figure 4.11). Furthermore, this increase in V_{OC} is preserved upon thermally annealing the layered device, which encourages the formation of a planar-mixed heterojunction.[10,11] In the case of the planar-mixed heterojunctions thus formed, higher J_{SC} and FF values, in addition to increased V_{OC} values, are observed in the presence of **P5** and **P6**, similar to previous observations in ternary **P3HT**/**$PC_{61}BM$** devices.

The calculated dipole moments (B3LYP 6-31G*) of the six *isolated* side-chain moieties found in **P1-P6** were provided in the previous chapter of this thesis (Figure 3.9), as well as the calculated dipole moments of the six side-chain functionalized *thiophene repeat units* found in **P1-P6** (Figure 3.10). The dipole moments of the side-chain functionalized repeat units contained in **P1**, **P5** and **P6** are calculated to be 0.52, 1.58 and 2.43 Debye, respectively. Therefore, the trend in the strength of the dipole moments within this family of additives qualitatively concurs

with the trend in the V_{OC} increase observed with additive interlayers. Additive **P6** contains pentafluorophenyl ether side-chain moieties that display the largest isolated dipole moments and, correspondingly, leads to the largest observed increase in V_{OC} in layered devices.

	J_{SC} (mA/cm^2)	V_{OC} (V)	FF	PCE
Unannealed (Planar Heterojunction)				
P3HT / C_{60}	2.12 ± 0.10	0.202 ± 0.005	0.38 ± 0.02	0.163% ± 0.010%
P3HT/**P1 (15 ± 5 nm)** / C_{60}	2.18 ± 0.20	0.205 ± 0.003	0.39 ± 0.02	0.173% ± 0.009%
P3HT/**P5 (15 ± 5 nm)** / C_{60}	1.88 ± 0.20	0.215 ± 0.005	0.36 ± 0.02	0.150% ± 0.008%
P3HT/**P6 (15 ± 5 nm)** / C_{60}	1.52 ± 0.20	0.253 ± 0.005	0.40 ± 0.02	0.152% ± 0.009%
P3HT/**P6 (25 ± 5 nm)** / C_{60}	0.351 ± 0.050	0.268 ± 0.003	0.31 ± 0.03	0.029% ± 0.008%
P3HT/**P6 (35 ± 5 nm)** / C_{60}	0.091 ± 0.008	0.272 ± 0.002	0.25 ± 0.03	0.006% ± 0.005%
Annealed (Planar-Mixed Heterojunction)				
P3HT / C_{60}	0.255 ± 0.050	0.141 ± 0.008	0.31 ± 0.02	0.011% ± 0.005%
P3HT/**P1 (15 ± 5 nm)** / C_{60}	0.282 ± 0.050	0.134 ± 0.005	0.32 ± 0.02	0.012% ± 0.006%
P3HT/**P5 (15 ± 5 nm)** / C_{60}	0.804 ± 0.080	0.158 ± 0.005	0.37 ± 0.02	0.047% ± 0.005%
P3HT/**P6 (15 ± 5 nm)** / C_{60}	0.819 ± 0.080	0.301 ± 0.007	0.39 ± 0.02	0.096% ± 0.005%

Table 4.4. Summary of device metrics for layered solar cells containing discrete layers of **P3HT**, side-chain functionalized polythiophenes and C_{60}

4.7 Fullerene Loading Optimization

The J_{SC} values for solar cells containing 0.25 wt% **P6** with varying ratios of polymer to either $PC_{61}BM$ or $PC_{71}BM$ are shown in Figure 4.12 and the device metrics are summarized in Figure 4.18.

Notable increases in J_{SC} in the presence of **P6** are only obtained for polymer:fullerene ratios of 1:1, for both **$PC_{61}BM$** and **$PC_{71}BM$**. Previous studies have shown that for high molecular-weight, regioregular P3HT, a polymer fullerene ratio of 1:1 leads to optimal PCEs,[12,13] consistent with the data presented in Figure 4.11.

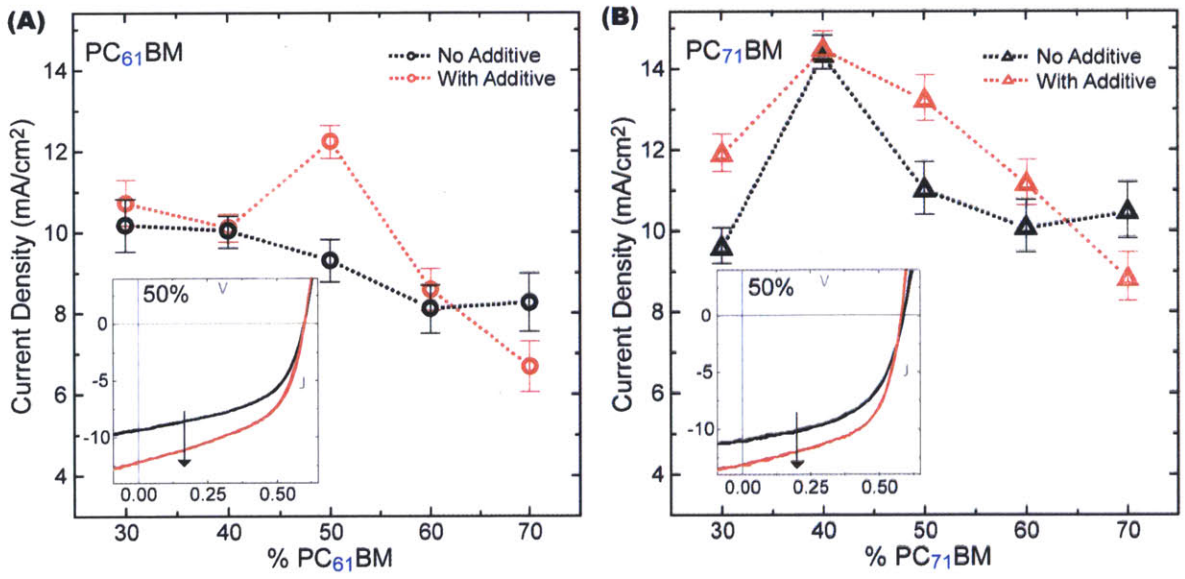

Figure 4.12. Study of the influence of fullerene structure and loading. J_{SC} for solar cells containing 0.25 wt% of pentafluorophenol additive **P6** with varying ratios of total polymer/**PC_nBM** compared to reference devices for $PC_{61}BM$ (**A**, circles) and $PC_{71}BM$ (**B**, triangles). J_{SC} for solar cells of the same composition with no additive are shown in black. The inset shows the J-V curves under 1 sun for solar cells containing 50/50 total polymer/PC_nBM with (red) and without (black) **P6**. Average J_{SC} values from eight different devices are reported

4.8 Active Layer Thickness Optimization

In order to investigate the effects of the best-performing additive, **P6**, on solar cells containing a thicker active layer, devices containing a 220 nm-thick bulk heterojunction are fabricated (see Figure 4.13). It has been demonstrated that the **P3HT/PCBM** bulk heterojunction solar cells should be approximately 220 nm-thick to achieve an optimal PCE of 4.5% – 5%.[2] Using an active layer compostion of 49.75 wt% P3HT, 0.25 wt% **P6** and 50 wt% **$PC_{61}BM$** (which yields the maximal PCE increase in 75 nm-thick devices according to the aforementioned experiments), a PCE of upto 5.3% is achieved with 220 nm-thick solar cells (30% PCE increase over a control device lacking **P6**, see Table 4.5).

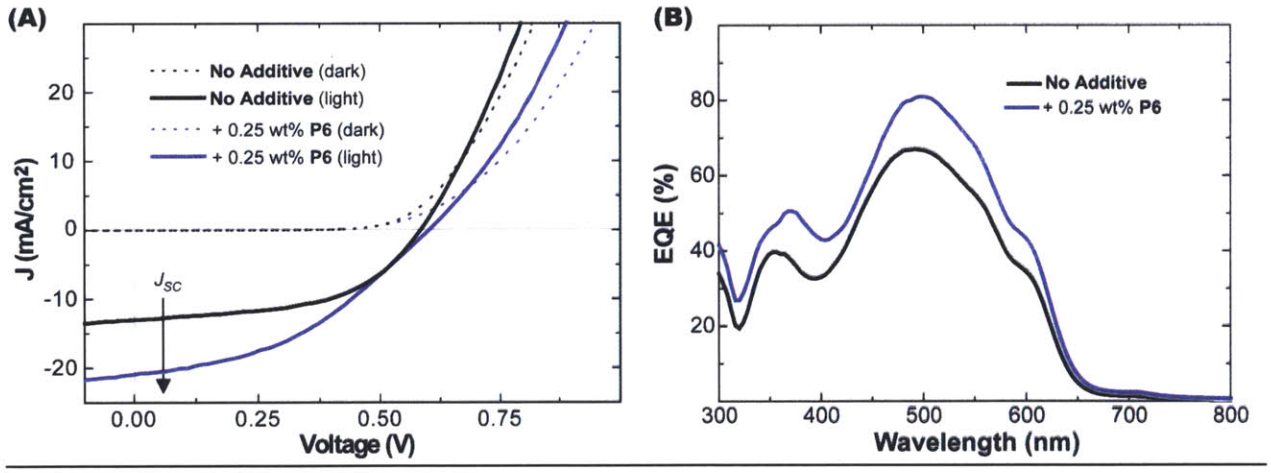

Figure 4.13. (A) J-V curves of a 220 nm-thick **P3HT**:**$PC_{61}BM$** solar cell (black) and a solar cell fabricated with 49.75 wt% **P3HT**, 0.25 wt% **P6** and 50 wt% **$PC_{61}BM$** (purple). The dark J-V curves are shown as dotted lines and the light curve (1 sun illumination) is a bold line. (B) EQEs of the 220 nm-thick devices from (A)

	J_{SC} (mA/cm^2)	V_{OC} (V)	FF	PCE
P3HT/$PC_{61}BM$	13.0 ± 0.20	0.58 ± 0.02	0.52 ± 0.03	3.9 ± 0.2%
+ 0.25 wt% **P6**	21.0 ± 0.30	0.59 ± 0.01	0.42 ± 0.02	5.1 ± 0.2%

Table 4.5. Summary of device metrics for 220 nm-thick solar cells

4.9 Influence of Additive Regioregularity and Alternance in the Photovoltaic Cell Performance

In the additive design introduced in the previous chapter of this thesis, the importance of having a regioregular, AB alternating system was highlighted. In order to test the exact influence of these parameters in additive performance, variations in the structure of the best performing additive (**P6**) were carried out, both in the degree of regioregularity and alternance.

4.9.1 Synthesis

The following polymers were synthesized: a random (not AB alternating) but regioregular copolymer, **P6a**; a homopolymer (functionalized on all side-chains, not just alternating) regioregular **P6b**; and a random (not AB alternating), regiorandom copolymer **P6c** (Figure 4.14).

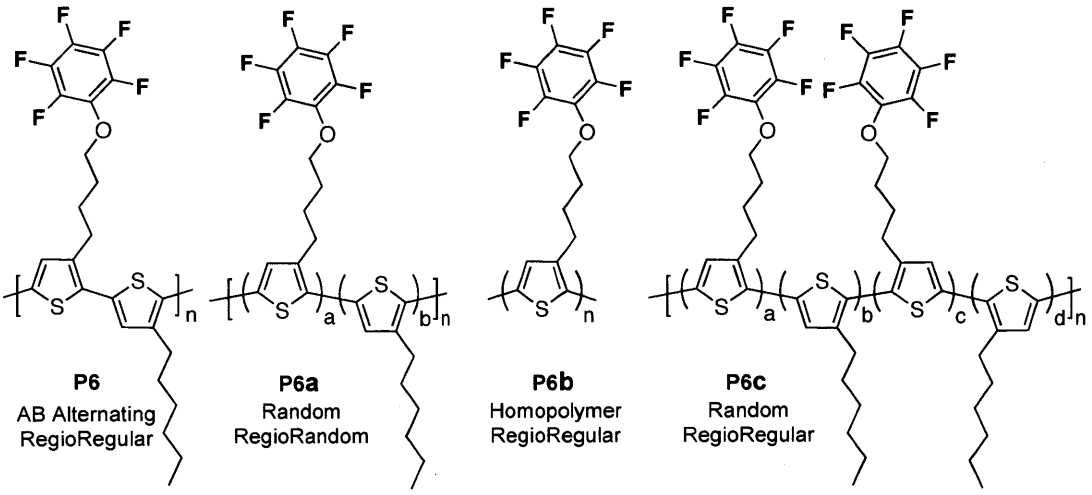

Figure 4.14. Structures of the analogues of polymer additive **P6**

The synthetic schemes to obtain these three polymers are summarized on Scheme 4.1. In order to access **P6a**, thiophene **1** was dibrominated using bromine yielding 2,5-dibromo-3-(4-bromohexyl)-thiophene **2** and then functionalized in the side-chain with a pentafluorophenoxy moiety via a Williamson ether synthesis to yield **3**. Copolymerization with 2,5-dibromo-3-hexylthiophene in a one to one ratio using standard Grignard metathesis (GRIM) polymerization conditions afforded polymer **P6a**. The homopolymerization of **3** using GRIM conditions yielded polymer **P6b**. In order to obtain regiorandom polymer **P6b**, polymerization conditions in which the positions 2 and 5 of 2 different 3-substituted thiophenes could react at random were chosen: compound **4,** obtained from the Williamson ether synthesis of **1**, and 3-hexylthiophene were polymerized using oxidative coupling conditions ($FeCl_3$). Polymer **P6c**, in which not only the alternance of the repeat units was random, but also the connectivity between contiguous thiophene repeat units was obtained in good yields using this strategy.

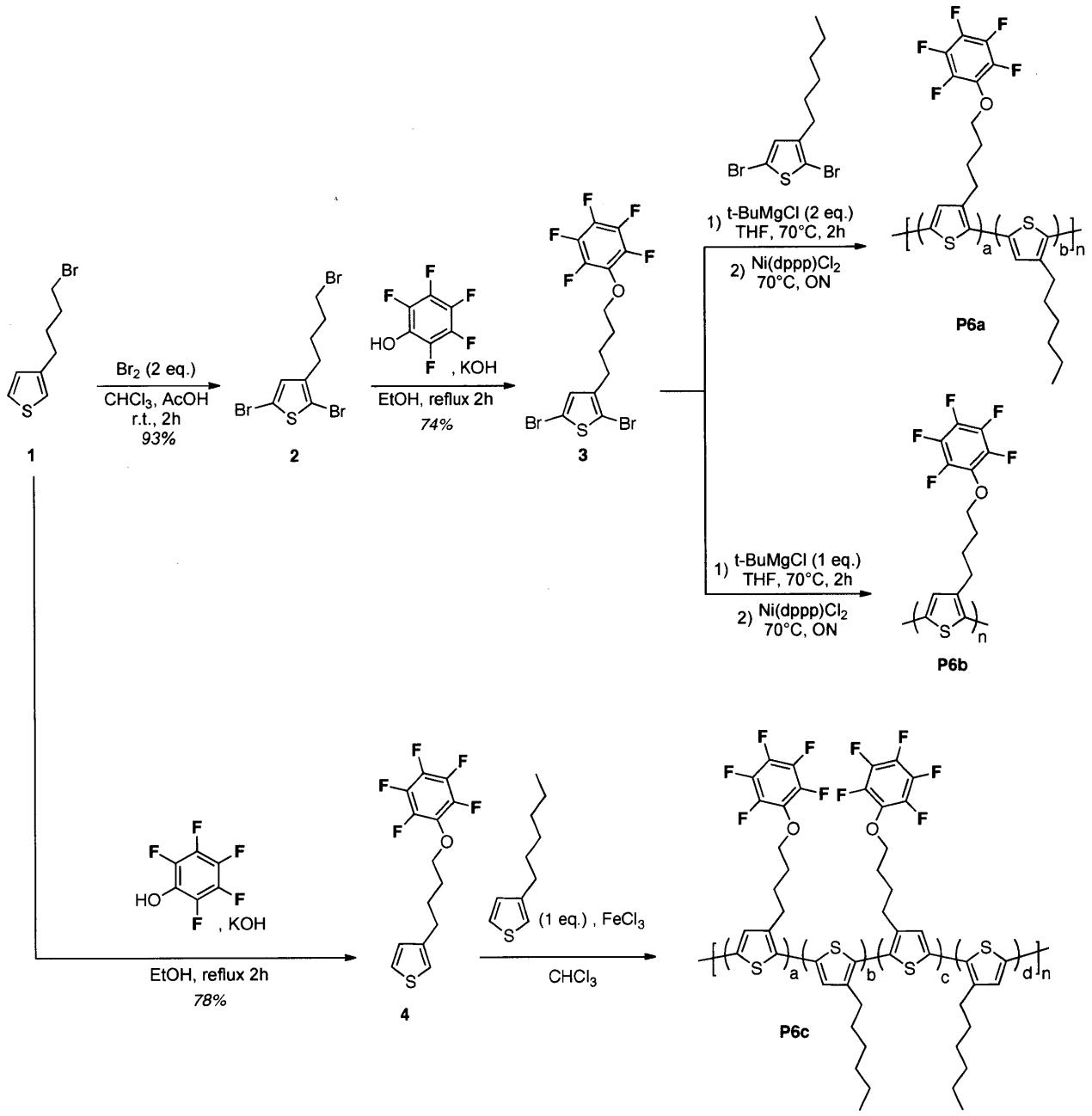

Scheme 4.1. Synthesis of polymers **P6a**, **P6b** and **P6c**

The ^{1}H NMR signals of additives **P6** and **P6a-c** in the diagnostic aromatic region are shown in Figure 4.15: as expected, increasing disorder in the polymer backbone leads to broadening of the aromatic signal at 6.9 ppm (HT-HT diad). ^{1}H NMR signals of **P6** and **P6a-c** in

the aromatic region showing very sharp signals for the H in the 4-position of the polymer backbone for regioregular polymers (**P6**, **P6a**, **P6b**). Regiorandom **P6c** shows an additional shoulder at 7.0 ppm corresponding to TT-HT connectivity.

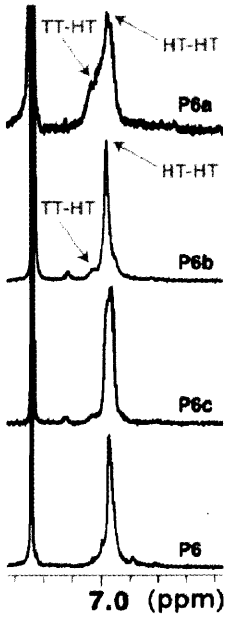

Figure 4.15. ^{1}H-NMR spectra of polymer additives **P6**, **P6a**, **P6b** and **P6c**

4.9.2 Photovoltaic Cell Performance

Varying the regioregularity and the degree of substitution of the best-performing additive **P6** significantly diminishes its ability to yield higher J_{SC} values.

PVs containing the random, regioregular copolymer **P6a** display lower J_{SC} values compared to those containing the AB-alternating regioregular polymer **P6** (averaged over eight devices, Figure 4.16). The device metrics are summarized in Table 4.6. In the case of a regiorandom random copolymer, **P6c**, little effect on J_{SC} values is observed with ternary mixtures

relative to a P3HT/$PC_{61}BM$ control. The effects of homopolymer **P6b** fall inbetween those of **P6a** and **P6c**.

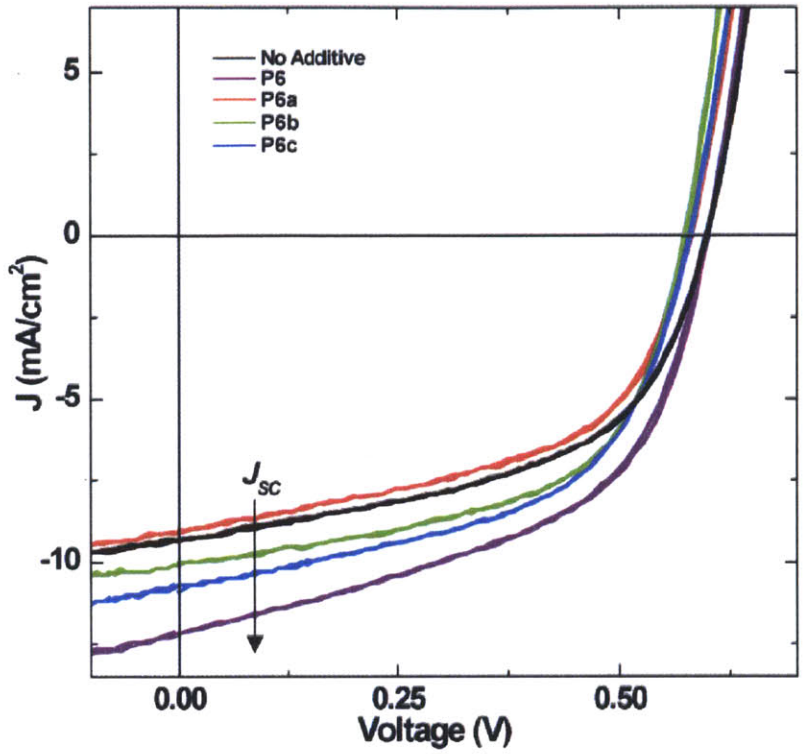

Figure 4.16. J-V curves under 1 sun for solar cells containing a 1:1 ratio of total polymer (**P3HT** + 0.25 wt% **P6a-c**) to $PC_{61}BM$, and for a reference device with no additive (black). Average J-V curves for eight different devices are shown

	J_{SC} (mA/cm^2)	V_{OC} (V)	FF	PCE
P3HT/$PC_{61}BM$	9.32 ± 0.20	0.59 ± 0.01	0.52 ± 0.03	2.9 ± 0.2%
+ 0.25 wt% **P6**	12.2 ± 0.2	0.60 ± 0.01	0.53 ± 0.02	3.8 ± 0.2%
+ 0.25 wt% **P6a**	10.8 ± 0.2	0.58 ± 0.01	0.54 ± 0.03	3.4 ± 0.2%
+ 0.25 wt% **P6b**	10.1 ± 0.2	0.57 ± 0.02	0.57 ± 0.03	3.3 ± 0.2%
+ 0.25 wt% **P6c**	9.07 ± 0.30	0.58 ± 0.01	0.53 ± 0.02	2.8 ± 0.2%

Table 4.6. Summary of device metrics for the solar cells of Figure 4.15

4.9.3 Transient Open Circuit Voltage Measurements

Small-perturbation transient open-circuit voltage decay measurements of charge carrier lifetime in the presence of these disordered additives reveal that only the AB-alternating regioregular polymer **P6** results in increased charge carrier lifetimes compared to a reference cell (Figure 4.17).

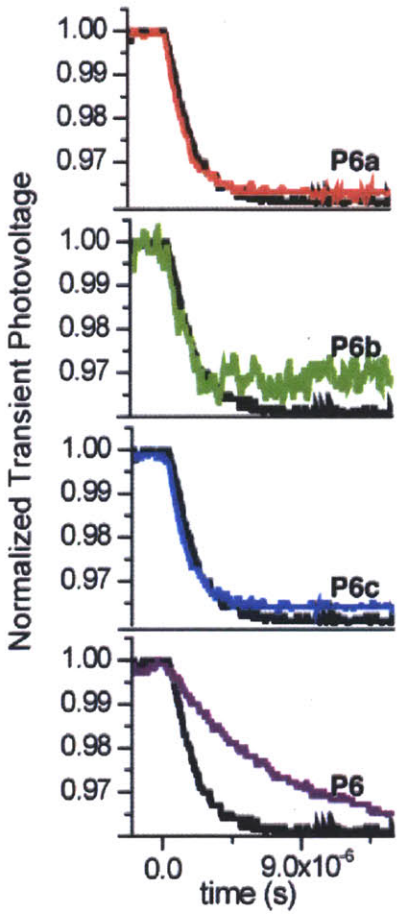

Figure 4.17. Normalized transient photovoltage decay curves at V_{OC} for the same devices as in (C). Bias illumination was 100 mW/cm^2 white light giving V_{OC} values of: 0.59 V for P3HT/$PC_{61}BM$; 0.60 V for additive **P6**; 0.58 for additives **P6a** and **P6c**; and 0.57 V for additive **P6b**. The secondary pulse was from a 635 nm laser, length 5 s

4.10 Conclusions

BHJ solar cells containing ternary mixtures of **rr-P3HT**, PC_nBM (n = 61, 71) and varying weight ratios of additives **P1-P6** were fabricated and characterized. At low loadings (0.25 wt%), the presence of **P1-P6** consistently increases the short circuit current (J_{SC}) and decreases the series resistance (R_s) of the corresponding photovoltaic cells, leading to an increase in the power conversion efficiency (PCE) compared to reference **P3HT/PC_{61}BM** cells.

Given the marked difference in steady-state quenching responses and solar cell performance metrics between polymers **P1-P6**, we infer that aromatic moieties present at side-chain termini interact with fullerenes and that the exact nature and identity of the side-chain aromatic moieties influences the degree of this interaction. Since the presence of a side-chain functionalized polythiophene layer leads to increased V_{OC} values in layered devices, we conclude that aromatic moieties at side-chain termini are capable of inducing a dipole at the polymer-fullerene interface. Moreover, we believe that this induced dipole is responsible for the increased charge carrier lifetimes and higher photocurrents observed in bulk heterojunctions containing side-chain functionalized polythiophenes.

Small-perturbation transient open-circuit voltage decay measurements reveal that, at 0.25 wt% incorporation, additives **P1-P6** increase charge carrier lifetimes in **P3HT/PC_{61}BM** solar cells. Higher additive loadings (>5 wt%) lead to detrimental nanoscale phase separation within the active layer blend and produce solar cells with high series resistances and low overall PCEs.

Perfluorophenoxy-containing polymer **P6** is the most effective side-chain functionalized additive and yields a 28% increase in PCE when incorporated into the **rr-P3HT/PC_{61}BM** BHJ at a 0.25 wt% loading. Moreover, the regioregularity and copolymer composition of the side-chain functionalized poly(thiophene)s is found to significantly affect their efficacy as additives in solar

cells, with only the regioregular AB-alternating copolymer **P6** yielding a large increase in PCE. Devices with 220 nm-thick BHJs containing 0.25 wt% **P6** are fabricated and display PCE values of upto 5.3% (30% PCE increase over a control device lacking **P6**).

We propose that the regioregular additives **P1-P6** selectively localize at the interface between **rr-P3HT** and **PC_nBM** such that the functional groups at side-chain termini interact with the fullerene phase. We believe that these side-chain aromatic moieties introduce a dipole at the polymer-fullerene interface, which decreases the rate of bimolecular recombination and, therefore, improves charge collection across the active layer in a bulk heterojunction polymer solar cell. A proposed model of the nanoscale organization within ternary blends of **P1-P6**, **rr-P3HT** and **PC_nBM** is depicted in Figure 3.6. Based on the combined observations that additives **P1-P6** do not disrupt the crystallinity of the **P3HT** phase in ternary blends and that only AB-alternating regioregular analogs improve the performance of OPV devices, we propose that the side-chain functionalized additives selectively localize at the **rr-P3HT**-fullerene interface, likely in the amorphous region of **P3HT** where the **P3HT** domains contain approximately 20% (in volume) of **PC_nBM**.

Based on the results presented herein, we suggest that side-chain functionalization is an as-of-yet under-explored strategy to design polymeric additives that improve the power conversion efficiencies of polymer solar cells by fine-tuning charge transfer phenomena at the polymer-fullerene interface.

4.11 Experimental Section

Materials: Unless otherwise noted, all reactions were performed in flame-dried glassware, and under an oxygen-free atmosphere of argon using standard Schlenk techniques. Anhydrous solvents were obtained using a solvent purification solvent (Innovative Technologies). The synthesis for compound **1** was described in the previous chapter of this paper. All other chemicals were of reagent grade from Sigma-Aldrich and were used as received. Regioregular P3HT for photovoltaic studies was purchased from Aldrich (electronic grade, 99.995% trace metals basis, average Mn 30,000-60,000).

NMR Spectroscopy: NMR spectra were obtained on a Bruker Avance (400 MHz). NMR chemical shifts are given in ppm referenced to $CHCl_3$/TMS (7.24 ppm for ^{1}H, 77.24 ppm for ^{13}C) or $CFCl_3$ (0 ppm for ^{19}F).

Mass Spectrometry: High-resolution mass spectra (HRMS) were obtained on a Bruker Daltonics APEXII 3 Tesla Fourier Transform Mass Spectrometer at the MIT Department of Chemistry Instrumentation Facility (DCIF).

Molecular Weight Determination: Polymer molecular weights were determined at room temperature on a HP series 1100 GPC system in THF at 1.0 mL/min (1 mg/mL sample concentrations), approximate molecular weights were estimated using a polystyrene calibration standard.

Device Fabrication: Pre-patterned indium tin oxide (ITO)-coated glass substrates (Thin Film Devices, Inc.) were sonicated in acetone (30 min) and isopropanol (30 min) and oxygen plasma-cleaned (3 min) immediately prior to deposition of the PEDOT:PSS layer. PEDOT:PSS (2-5 wt% in water, Aldrich) was spin-coated in a nitrogen atmosphere at 4000 rpm and annealed at 150°C (using a hotplate) for 15 min under nitrogen. A 40 nm PEDOT layer was thus obtained.

Film thickness was determined by ellipsometry measurements on separate films prepared on silicon substrates. For the active layer, a 10 mg/mL solution of 1:1 total polymer:**PC_nBM** in 1,2-dichlorobenzene (DCB) was employed (in a representative example, 1.9 mg **P3HT**, 0.1 mg P1, and 2 mg **$PC_{61}BM$** were dissolved in 0.2 mL DCB). 60 μL of this solution was then spin-coated onto the PEDOT layer at 1000 rpm under nitrogen. The substrate was taken from the spin chuck and immediately placed under an inverted Petri dish inside the glovebox for 10 minutes to encourage solvent annealing from the small amount of residual DCB on the substrate. Next, the solar cells were placed on a 150 °C hotplate and annealed for 45 min under nitrogen. A 75 ± 5 nm active layer was thus obtained. A 220 nm-thick active layer was obtained following the same procedure, with the exception of using a 30 mg/mL solution of 1:1 total polymer:**PC_nBM** in DCB. Following this deposition procedure, the top electrode was deposited by thermal evaporation of a 25 nm thick film of Ca followed by 80 nm thick film of Al. The device area, as defined by the anode-cathode overlap, is 1.21 mm^2.

Device Characterization: Current density-voltage (J-V) measurements were recorded by a Keithley 6487 picoammeter both in the dark and under illumination. The devices were illuminated through the glass substrate using an Oriel 91191 150 W full spectrum solar simulator. The illumination intensity was calibrated to 100 mW/cm^2 using an NREL-certified silicon photodiode. Spectral mismatch was not corrected for in these measurements. For measurement of external quantum efficiencies, the sample was illuminated with optically-chopped broadband light from a 1000 W Xe lamp focused into an Acton Spectrapro 300i monochromator that underfilled the device area. A calibrated silicon photodetector was used to measure the optical power of the output, which was subsequently focused onto the device under

study. A SRS-830 lock-in amplifier provided with the reference signal from the optical chopper (45 Hz) was used to extract a measurement of the AC photocurrent.

Transient Open Circuit Voltage Measurements: For the small-perturbation transient photovoltage measurement, a Newport LQD laser diode (λ 635 nm) driven by an Agilent 33220A function generator (11 Hz, 50% duty cycle) was used as a second light source to provide square wave modulated illumination. This illumination was filtered through a neutral density filter before reaching the device to ensure a small (<5 %) illumination perturbation. V_{OC} decay transients were recorded on a Tektronix TDS 3054B digital oscilloscope with a Tektronix ADA440A high impedance differential preamplifier.

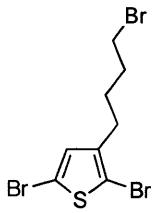

2,5-dibromo-3-(4-bromobutyl)thiophene (2). Compound **1** (5 g, 23 mmol) was dissolved in 100 ml $CHCl_3$, and glacial acetic acid (100 ml) was added in the dark. The mixture was cooled down to 0°C, and Br_2 (2.36 ml, 46 mmol) was added dropwise. The mixture was warmed up to room temperature and stirred for 2 h in the dark. The reaction mixture was washed with water, saturated $NaHCO_3$, brine, dried over magnesium sulfate and the solvent was removed under vacuum. Purification by column chromatography (hexanes) afforded compound **2** (8.1 g, 93% yield) as a light yellow oil. ^{1}H NMR (ppm, $CDCl_3$): 1.69 (2H, m), 1.86 (2H, m), 2.53 (2H, t, J=7.7 Hz), 3.4 (2H, t, J=5.6 Hz), 6.76 (1H, s). ^{13}C NMR (ppm, $CDCl_3$): 28.2, 28.7, 32.1, 33.5, 108.6, 110.9, 130.9, 142.1. HRMS (ESI) (m/z) found: 378.7945 [M+H], calculated: 378.7932.

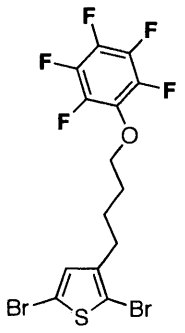

2,5-dibromo-3-(4-(perfluorophenoxy)butyl)thiophene (3). Perfluorophenol (700mg, 3.8 mmol) was dissolved in 15 ml EtOH. After addition of KOH (242 mg, 4.3 mmol) and stirring for 10 minutes, **2** (940 mg, 2.5 mmol) was added. After adding a spatula tip of NaI, the reaction was brought to reflux, and stirred for 2 h. After addition of H_2O, ether, the mixture was extracted with ether and the combined organic phases were washed with water, brine, dried over magnesium sulfate. After solvent removal, the resulting oil was purified by column chromatography (hexanes) to afford compound **3** as a yellow oil (888 mg, 74% yield). ^{1}H NMR (ppm, $CDCl_3$): 1.70-1.85 (4H, m), 2.58 (2H, t, 7.4 Hz), 4.14 (2H, t, J=5.3 Hz), 6.78 (1H, s). ^{13}C NMR (ppm, $CDCl_3$): 25.8, 29.1, 29.4, 75.5, 108.6, 110.9, 131.0, 134.2, 137.2, 140.9, 142.3, 143.5. ^{19}F NMR (ppm, $CDCl_3$): -163.7, -163.5, -157.1. HRMS (ESI) (m/z): found: 480.8719 [M+H], calculated: 480.8719.

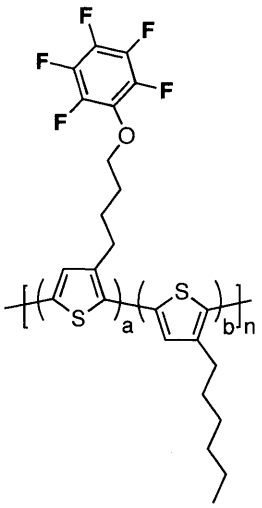

Polymer Additive P6a (Random Copolymer, RegioRegular) The same general procedure for polymer additive synthesis described in the previous chapter of this thesis (Route 1) was used for this polymerization, with a ratio of **3** to 2,5-dibromo-3-hexylthiophene of 1:1 (85% yield). M_n = 15K, PDI= 1.3. ^{1}H NMR (ppm, $CDCl_3$): 0.88 (3H, b), 1.20-1.49 (6H, mb), 1.53-2.03 (6H, b), 2.72-2.92 (4H, mb), 4.17 (2H, b), 6.98 (2H, s). ^{13}C NMR (ppm, $CDCl_3$): 14.3, 22.9, 26.7, 29.1, 29.5, 29.7, 29.8, 30.7, 31.9, 75.6, 128.3, 129.3, 130.1, 130.7, 131.2, 133.8, 134.1, 135.6, 137.0, 140.1, 140.8, 143.1. ^{19}F NMR (ppm, $CDCl_3$): -163.9, -163.6, -157.1.

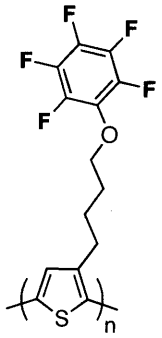

Polymer Additive P6b (Homopolymer, RegioRegular). The same general procedure for polymer additive synthesis described above (Route 1) was used to polymerize compound **S7**

(90% yield). M_n = 15K, PDI= 1.3. ^{1}H NMR (ppm, $CDCl_3$): 1.88 (4H, b), 2.88 (2H, b), 4.17 (2H, b), 6.98 (1H, s). ^{13}C NMR (ppm, $CDCl_3$): 26.7, 29.0, 29.7, 75.6, 129.0, 131.2, 134.0, 136.2, 136.9, 139.6, 140.1, 143.3. ^{19}F NMR (ppm, $CDCl_3$): -163.8, -163.7, -157.1.

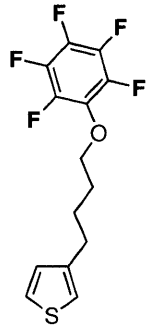

3-(4-(perfluorophenoxy)butyl)thiophene (4). Perfluorophenol (745mg, 4.0 mmol) was dissolved in 15 ml EtOH. After addition of KOH (258 mg, 4.6 mmol) and stirring for 10 minutes, **1** (600mg, 2.7 mmol) was added. After adding a spatula tip of NaI, the reaction was brought to reflux, and stirred for 2 h. After addition of H_2O, ether, the mixture was extracted with ether and the combined organic phases were washed with water, brine, dried over magnesium sulfate. After solvent removal, the resulting oil was purified by column chromatography (hexanes:toluene, 1:0 to 3:1) to afford compound **4** as a yellow oil (610 mg, 78% yield). ^{1}H NMR (ppm, $CDCl_3$): 1.76-1.83 (4H, m), 2.69 (2H, t, 6.7 Hz), 4.15 (2H, t, J=6 Hz), 6.92 (2H, m), 7.24 (1H, m). ^{13}C NMR (ppm, $CDCl_3$): 26.5, 29.6, 30.1, 75.3, 120.4, 125.6, 128.3, 136.4, 137.0, 141.0, 142.5, 143.3. ^{19}F NMR (ppm, $CDCl_3$): -164.1, -163.7, -157.2. HRMS (ESI) (m/z): found: 323.0529 [M+H], calculated: 323.0524.

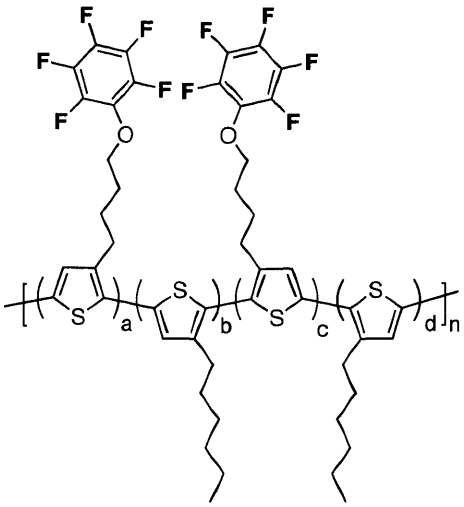

Polymer Additive P6c (Random Copolymer, RegioRandom). Compound **4** (323 mg, 1 mmol) and 3-hexylthiophene (0.18 ml, 1 mmol) were dissolved in 6 ml $CHCl_3$. $FeCl_3$ (1 g, 6.4 mmol) was added, and the mixture was sonicated for 2 hours, followed by stirring at room temperature for 24 hours. The mixture was poured into MeOH, and the precipitate was collected, redissolved in $CHCl_3$, and washed with a saturated solution of ammonium chloride. The solvent was removed under vacuum, and the resulting solid was reprecipitated from MeOH (90% yield). M_n = 15K, PDI= 1.5. ^{1}H NMR (ppm, $CDCl_3$): 0.88 (3H, b), 1.20-2.01 (12H, mb), 2.52-3.02 (4H, mb), 4.02-4.30 (2H, mb), 6.98-7.05 (2H, mb). ^{19}F NMR (ppm, $CDCl_3$): -163.9, -163.6, -157.0.

4.12 Additional Figures

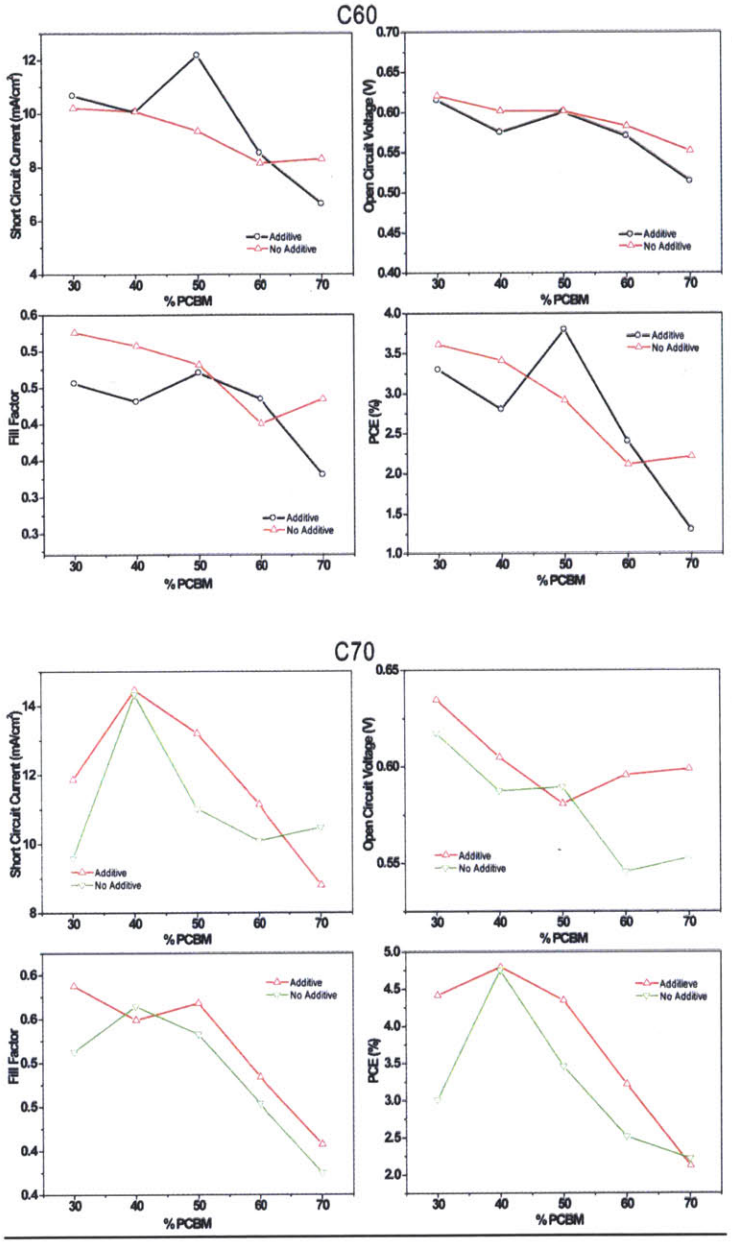

Figure 4.18. Study of the influence of fullerene structure and loading. Shown are device metrics for BHJ solar cells fabricated with varying ratios of either PC61BM or PC71BM and with or without 0.24 wt% of P6. Average values over eight devices are shown. Typical standard deviations were <5% of the values plotted. This figure is an expansion of Figure 4.12

4.13 References and Notes

(1) Lenes, M.; Morana, M.; Brabec, C. J.; Blom, P. W. M. *Adv. Funct. Mater.* **2009**, *19*, 1106-1111.

(2) Mihailetchi, V. D.; Koster, L. J. A.; Blom, P. W. M.; Melzer, C.; de Boer, B.; van Duren, J. K. J.; Janssen, R. A. J. *Adv. Funct. Mater.* **2005**, *15*, 795-801.

(3) O'Regan, B. C.; Scully, S.; Mayer, A. C.; Palomares, E.; Durrant, J. R. *J. Phys. Chem. B* **2005**, *109*, 4616-4623.

(4) Zhao, N.; Osedach, T. P.; Chang, L.-Y.; Geyer, S. M.; Wanger, D.; Binda, M. T.; Arango, A. C.; Bawendi, M. G.; Bulović, V. *ACS Nano* **2010**, *4*, 3743-3752.

(5) (a) Lee, J. K.; Ma, W. L.; Brabec, C. J.; Yuen, J.; Moon, J. S.; Kim, J. Y.; Lee, K.; Bazan, G. C.; Heeger, A. J *J. Am. Chem. Soc.* **2008**, *130*, 3619-3623. (b) Tsai, J.-H.; Lai, Y.-C; Higashihara, T.; Lin, C.-J.; Ueda, M.; Chen, W.-C. *Macromolecules* **2010**, *43*, 6085-6091. (c) Sivula, K.; Ball, Z. T.; Watanabe, N.; Fréchet, J. M. J. *Adv. Mater.* **2006**, *18*, 206-210. (d) Yang, C.; Lee, J. K.; Heeger, A. J.; Wudl, F. *J. Mater. Chem.* **2009**, *19*, 5416-5423. (e) Campoy-Quiles, M.; Kanai, Y.; El-Basaty, A.; Sakai H.; Murata, H. *Org. Elect.* **2009**, *10*, 1120-1132. (f) Nguyen, L. H.; Hoppe, H.; Erb, T.; Günes, S.; Gobsch, G.; Sariciftci, N. S. *Adv. Funct. Mater.* **2007**, *17*, 1071-1078.

(6) For an example of using topography and phase AFM images to study the nanoscale morphology of polymer/fullerene blends, see: Verploegen, E.; Mondal, R.; Bettinger, C. J.; Sok, S.; Toney, M. F.; Bao, Z. *Adv. Funct. Mater.* **2010**, *20*, 3519-3529.

(7) For an example of the effects of interface modification on photovoltaic performance, see: Goh, C.; Scully, S. R.; McGehee, M. D. *J. Appl. Phys.* **2007**, *101*, 114503.

(8) For a second example of the effects of interface modification on photovoltaic performance, see: Tada, A.; Geng, Y.; Wei, Q.; Hashimoto, K.; Tajima, K. *Nature Materials* **2011**, *10*, 450-455.

(9) Ayzner, A. L.; Tassone, C. J.; Tolbert, S. H.; Schwartz, B. J. *J. Phys. Chem. C* **2009**, *113*, 20050-20055.

(10) For an example of forming a planar-mixed heterojunction between P3HT and $PC_{61}BM$ by thermally annealing a bilayer, see: Treat, N. D.; Brady, M. A.; Smith, G.; Toney, M. F.; Kramer, E. J.; Hawker, C. J.; Chabinyc, M. L. *Adv. Energy Mater.* **2011**, *1*, 82-85.

(11) For a second example of forming a planar-mixed heterojunction between P3HT and $PC_{61}BM$ by thermally annealing a bilayer, see: Gevaerts, V. S.; Koster, L. J. A.; Wienk, M. M.; Janssen, R. A. J. *ACS Appl. Mater. Interfaces* **2011**, *3*, 3252-3256.

(12) Sanyal, M.; Schmidt-Hansberg, B.; Klein, M. F. G.; Munuera, C.; Vorobiev, A.; Colsman, A.; Scharfer, P.; Lemmer, U.; Schabel, W.; Dosch, H.; Barrena, E. *Macromolecules* **2011**, *44*, 3795-3800.

(13) Nicolet, C.; Deribew, D.; Renaud, C.; Fleury, G.; Brochon, C.; Cloutet, E.; Vignau, L.; Wantz, G.; Cramail, H.; Geoghegan, M.; Hadziioannou, G. *J. Phys. Chem. B* **2011**, *115*, 12717-12727.

CHAPTER 5

Side-Chain Functionalized Liquid-Crystalline Polymers: 3D Macroscopic Assemblies

The work described in this chapter was carried out in the labs of Prof. Takuzo Aida at the University of Tokyo / RIKEN

5.1 Introduction

Systems capable of displaying stable long-range 3D macroscopic ordering are interesting not only because of their unique supramolecular properties but also for their potential application in materials and devices.[1] The understanding of factors that control morphology and ordering on the nanoscale is crucial for the rational design of nanostructures necessary for the advancement of many different fields, such as biochemistry[2] and organic photovoltaics.[3] However, the mechanisms that govern long-range ordering are not well understood.

Liquid crystals are compounds that exhibit two distinct melting points (first-order thermal transitions) and a mesophase in between those melting points.[4] The liquid crystal is fluid in the mesophase between these two transitions, but still retains some ordering from the solid state and shows birefringence under illumination when using crossed polarizers in a polarized optical microscope. Many examples of liquid crystals have been reported, including both small molecules and polymers (main-chain,[5] side-chain[6] and block-copolymer),[7] as well as liquid crystals bearing metals (metallomesogens).[8] In recent years liquid crystals have found application in optoelectronic devices, displays, semiconductors, laser writeable devices, non-linear optics devices, sensors and actuators.[9] Variations in the structure of polymer liquid crystals have been reported to attain different nanomorphologies.[10] However, it is hard to preserve the ordering obtained in the mesophase to achieve self-standing and processable solid-state films with controlled nanomorphologies. Were this level of design achievable, it would have implications for the fabrication of organic active layers in solar cells where the morphology at the nanoscale is paramount.[3]

Previously, there have been numerous reports on both liquid crystalline polymers and the use of azobenzene units for photoactive stimuli-responsive materials,[11] and how cross-linked

elastomeric liquid crystals can show actuation.[12] However, it was not until recently that the first example was reported on a method to process liquid crystalline polymer brushes to yield films that were macroscopically ordered and capable of displaying macroscopic actuation without the need for cross-linking the liquid crystalline polymer into an elastomer.[13] These polymer brushes were highly substituted polymers containing several azobenzene mesogenic units in the side chain (Figure 5.1). The polymer brushes were processed by hot pressing a powder sample of liquid crystalline polymer at the mesophase temperature of the liquid crystalline polymer brush using Teflon sheets containing alignment grooves. The self-standing films obtained this way were extremely ordered and aligned. Additionally, the films displayed a macroscopic and reversible actuation, originated due to a photomechanical response triggered by irradiation at the appropriate wavelength.

The specific system used in this study was a polymer brush that could self-assemble into nanoscopic cylindrical structures in a bimorph state (Figure 5.1c). In this bimorph state, the polymer backbone was aligned homeotropically, while the bulky side chains were directed perpendicular to the polymer backbone (Figure 5.1d). The length of the functional side chains was crucial in order to observe supramolecular ordering. Another prerequisite for ordering and macroscopic actuation in the thin film was that the polymer brush had to exhibit a liquid crystalline behavior. The processing conditions (alignment films used, processing temperature, and orientation grooves of the Teflon films) also played a pivotal role in obtaining the desired architecture for a photomechanic response.

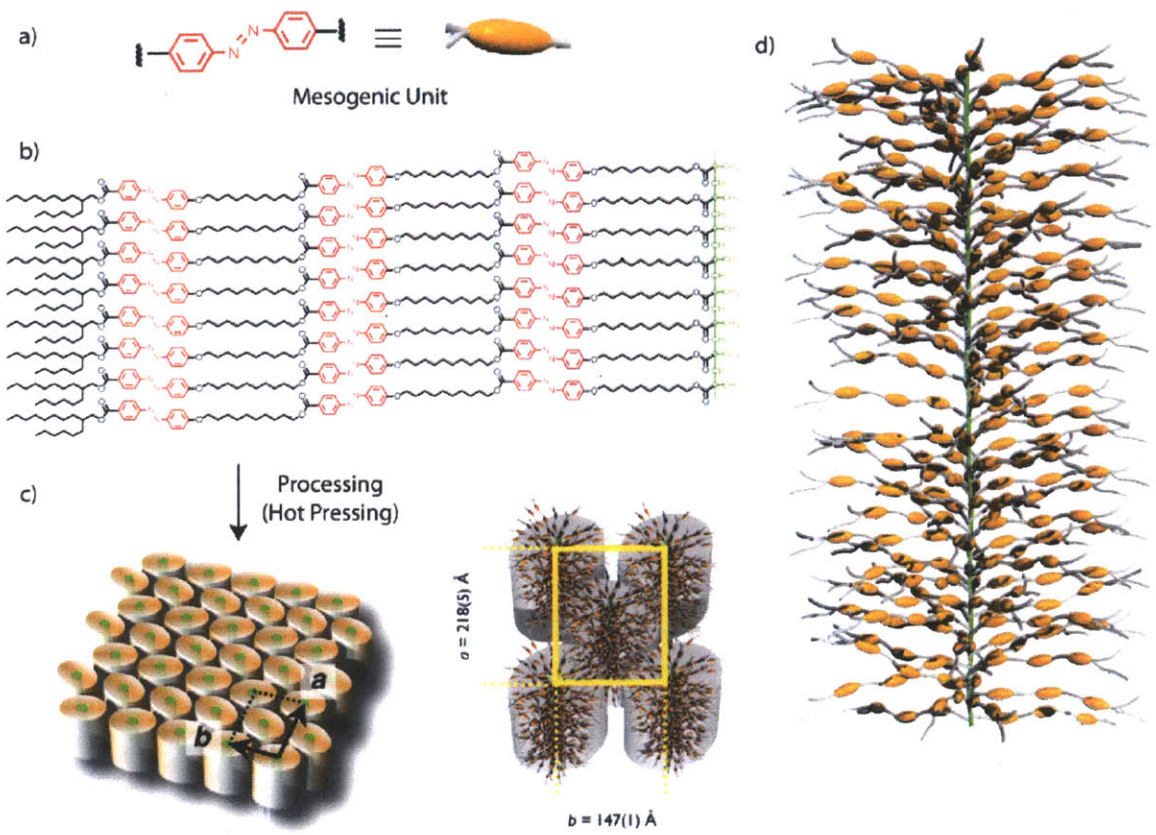

Figure 5.1. Previously reported polymer brushes a) Azobenzene mesogenic unit b) Chemical structure of the polymer brushes c) Homeotropic arrangement of cylindrical structures obtained after hot pressing using Teflon films d) Distribution of the long mesogenic side-chains in the solid state after hot-pressing

If these side-chain functionalized polymer brushes can be used to obtain other long range macroscopically-ordered structures, a system such as this could find use as a supramolecular scaffold in photovoltaic applications, where control of the morphology at the nanoscale is crucial for performance.[3] Liquid crystalline organic molecules with conducting properties and potential for use in photovoltaic devices have been reported in the literature, but no self-standing thin films with useful morphologies have been demonstrated.[14]

For application in organic photovoltaics, a different kind of photoactive aromatic moieties would have to be incorporated into the side chain. One could imagine that if both donor and acceptor photoactive mesogenic aromatic groups are used, an ideal structure with concentric cylinders of donor and acceptor molecules could be obtained (Figure 5.2). If a perfectly ordered array of such cylinders is obtained after processing, or any other kind of morphology with a very high degree of ordering, the resulting film would have the ideal morphology for hole and electron transport after light absorption, exciton generation, diffusion and charge separation has ocurred. This would be of great interest, since rational control of the nanomorphology in organic solar cells is still an unresolved problem, and most research discoveries on the factors affecting assembly are still empirical or merely fortuitous at best, with no rational molecular design involved.

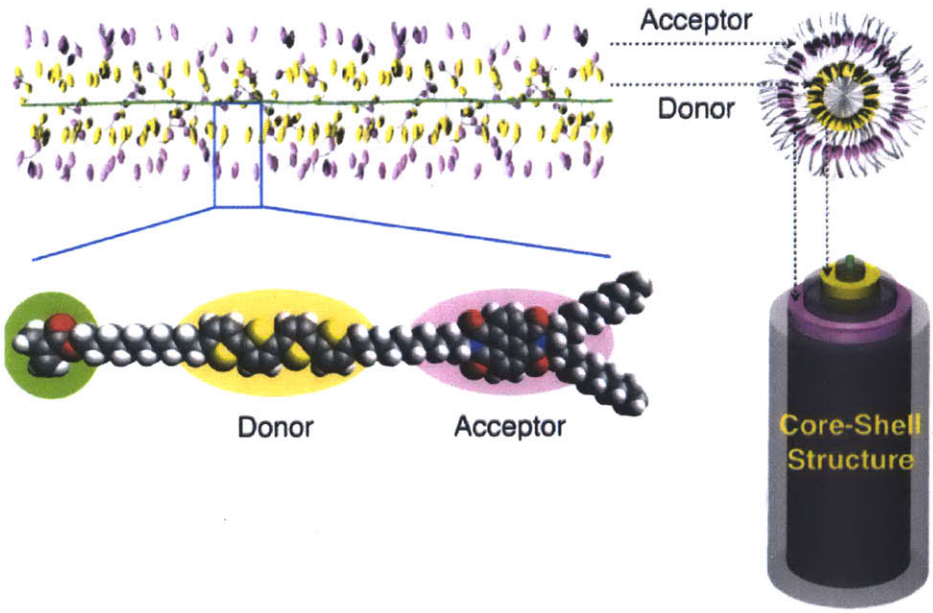

Figure 5.2. Diagram showing the structure of an ideal polymer brush to be used for organic photovoltaic applications

However, the generality of using polymer brushes to obtain very ordered supramolecular assemblies under the right processing conditions has not yet been shown. Furthermore, the influence of the nature of the aromatic mesogenic unit in the side-chains is still mostly unexplored. For this reason, before synthesizing these ideal target polymers, there is a need to study the many factors potentially influencing the mesophase formation, ordering, alignment and morphology. Namely, one could think of changing the end-group, nature and number of the mesogenic units, alkyl spacer, nature and length of the polymer backbone, and polydispersity and use of copolymers (Figure 5.3).

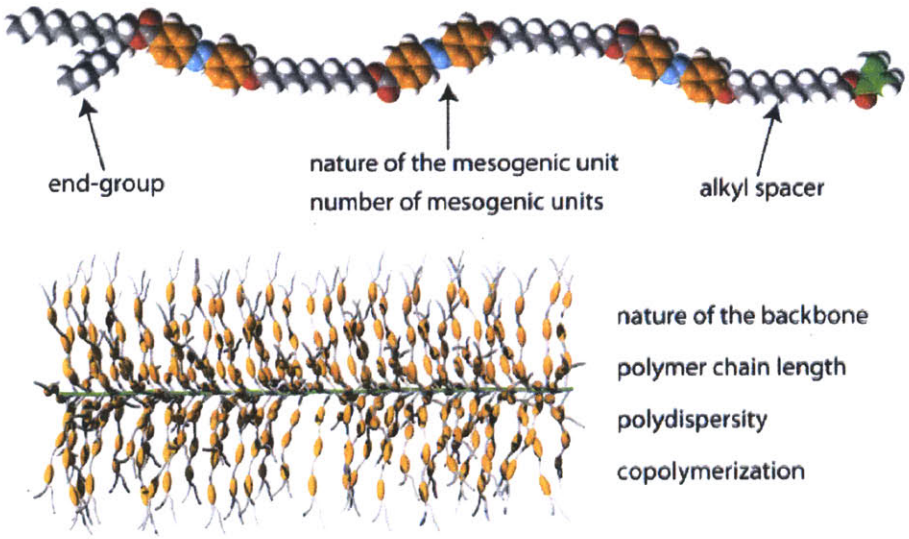

Figure 5.3. Some of the factors potentially affecting mesophase formation, ordering, alignment and morphology of polymer brush thin films

The purpose of the study described in this chapter is to understand how some of the aforementioned factors affect liquid crystalline behavior, ordering and alignment and nanomorphology in the thin film. We propose the substitution of the azobenzene units by shorter, less sterically demanding biphenyl units (Figure 5.4a), to study how this variation affects the

supramolecular assembly properties of the film. We will also study how varying the number of functional mesogenic units on the side-chain and thus the monomer length can affect the properties exhibited by these systems (Figure 5.4b), and how polymer processing conditions translate into different properties for films made out of these polymers.

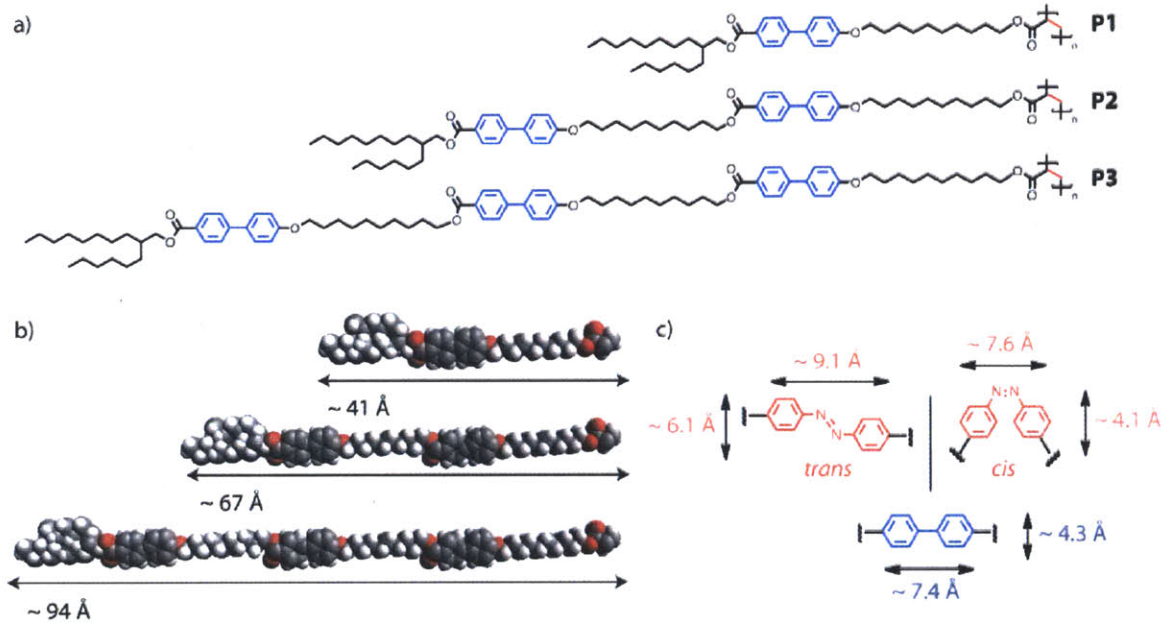

Figure 5.4. a) Target polymers b) Corresponding monomers with varying length and number of mesogenic units c) Dimensions of the mesogenic unit

To fulfill this goal, polymers **P1**, **P2**, **P3** were synthesized from the corresponding monomers (Figure 5.4). The structure of the obtained polymers, monomers and monomer precursors was characterized in detail. The liquid crystalline properties of these polymers, and supramolecular assembly under processing conditions using a hot press was investigated by DSC, POM and XRD techniques. Once a suitable polymer was identified for assembly into

polymer films, the effect of the polymer molecular weight on the mesophase and thin film alignment was also studied.

This study also illustrates the difference between monomer and polymer properties, and how modification of the functional side-chain of polymers can be used to influence the properties exhibited by these polymers.

5.2 Monomer Synthesis and Characterization

5.2.1 Monomer Synthesis

The synthesis of monomers **1**, **2**, **3** is detailed in Schemes 5.1, 5.2 and 5.3 respectively, and it makes use of standard protection/deprotection and saponification/esterification chemistry. Commercially available 10-bromodecan-1-ol was protected with TBDMS and then subjected to nucleophilic substitution with ethyl 4'-hydroxy-[1,1'-biphenyl]-4-carboxylate to obtain monomer precursor **6**. Saponification followed by re-esterification to attach a hexadecyl end-group yielded compound **8,** using 4-(dimethylamino)pyridinium-4-Toluenesulfonate (DPTS) as an esterification agent.[15] Compound **8** was then deprotected and end-capped with the polymerizable acrylate moiety by *via* reaction with acrylic acid chloride to yield monomer **1**.

Starting from compound **7** and using a different alcohol (**9**) for the esterification step, the precursor to monomer **2**, compound **10**, was obtained. After deprotection with TBAF and esterification with acrylic acid chloride, monomer **2** was obtained. Monomer **3** was obtained following a similar strategy as used with monomer **2** but starting from compound **7** and alcohol **11**.

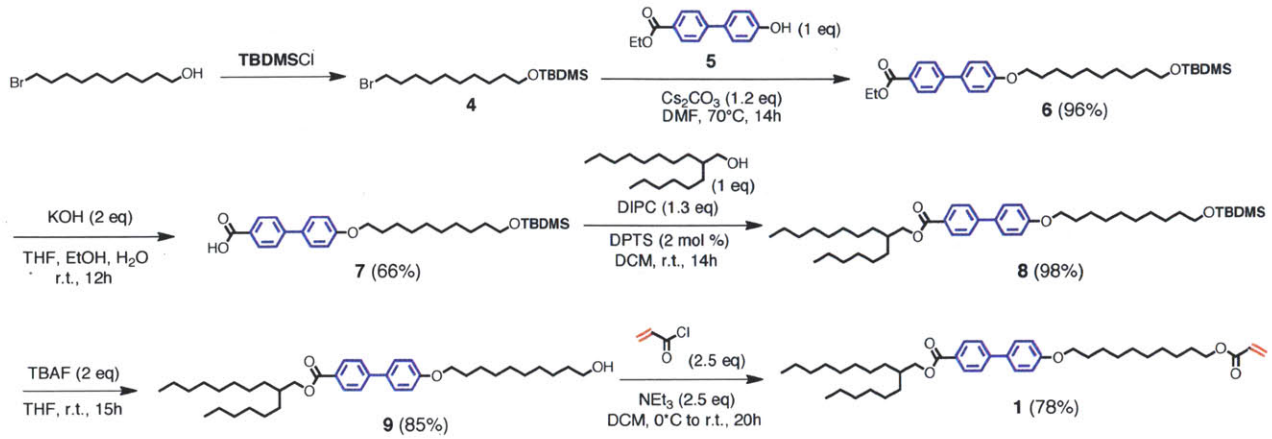

Scheme 5.1. Synthetic pathway for monomer **1**

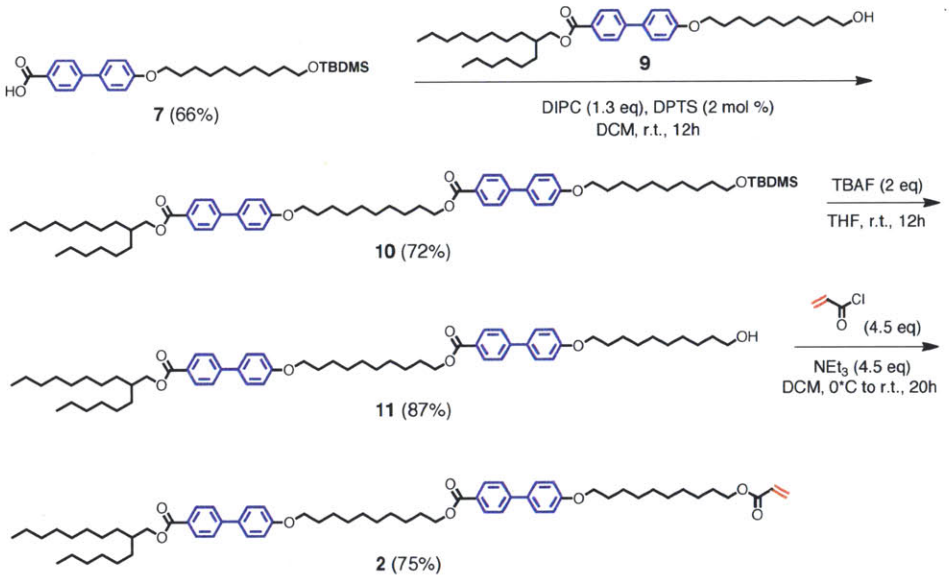

Scheme 5.2. Synthetic pathway for monomer **2**

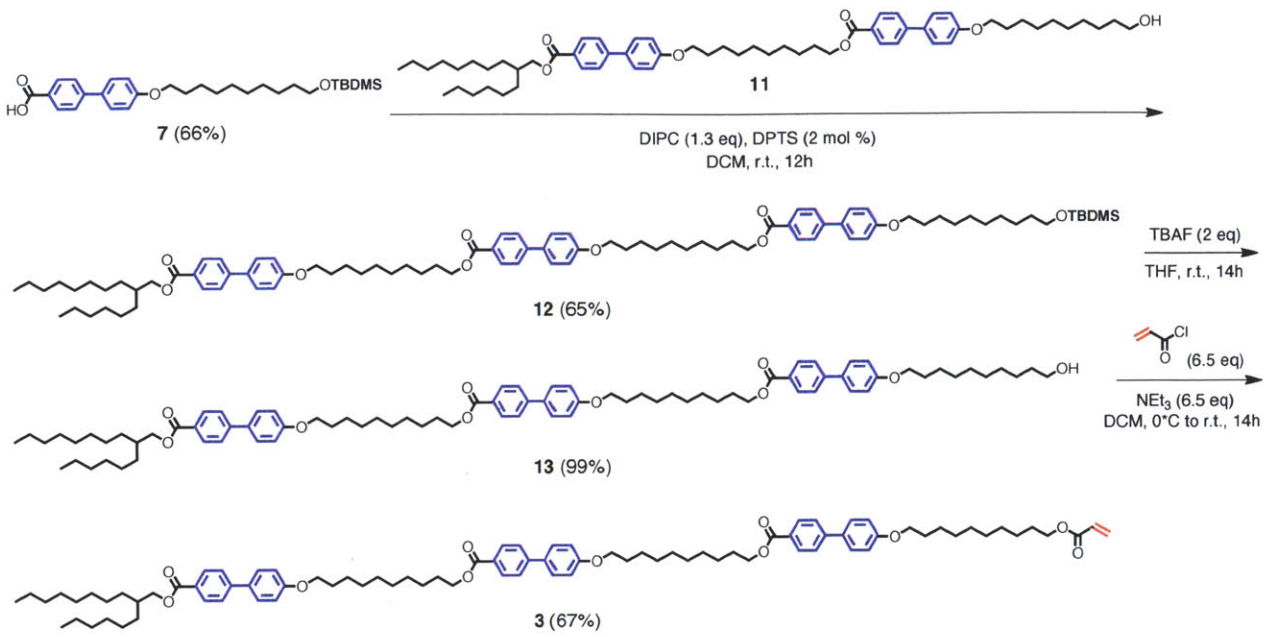

Scheme 5.3. Synthetic pathway for monomer **3**

5.2.2 DSC/POM Characterization

In comparing the differential scanning calorimetry (DSC) traces (second heating curves) of monomers **1**, **2** and **3** (Figure 5.5) it is clear that by increasing the number of mesogenic units (and thus the chain length), the melting point in the series also increases, as expected: from 9.09°C for **1**, to 49.72°C for **2** and 90.77°C for **3**. The variation in the series is very regular, and it corresponds to an increase of about 40°C for every incorporated mesogenic unit and decyl alkyl spacer.

Another important piece of information that can be inferred from the DSC data is the fact that when we compare the shorter **1**, which is a liquid at room temperature, to its longer versions **2** and **3** an additional phase transition of first order appears in the DSC signal, as evidenced by the presence of a very small peak. This second melting point may indicate the presence of a mesophase.

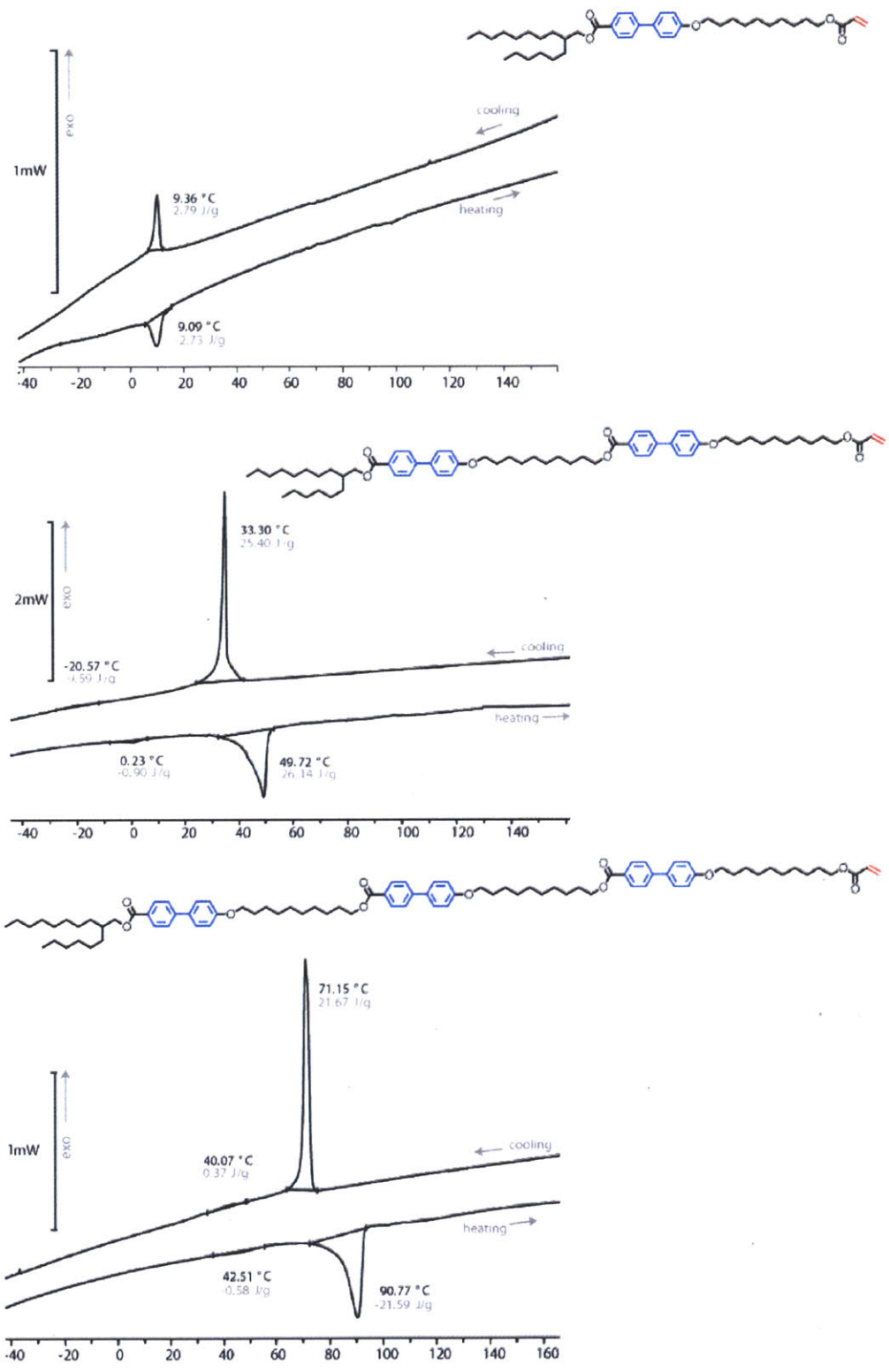

Figure 5.5. Second heating DSC traces (5°C/min) of monomers **1** (top), **2** (middle), **3** (bottom)

It should be noted that from a more rigorous and purist point of view the compounds described in Figure 5.5 should not be considered as liquid crystals, but plastic crystals. This is owing to the relative size of the melting points, which should have inverted relative intensities in the case of a true liquid crystal. For the sake of clarity and consistency with the previously reported data by Hosono et al. these compounds will be designated as liquid crystals throughout the rest of this thesis chapter.

To confirm the presence of a mesophase, samples of these compounds were sandwiched between a microscope slide and a microscope slide cover and heated/cooled across a wide range of temperatures, while analyzing changes in the morphology with a Polarized Optical Microscope (POM) under crossed polarizers. It is clear from the pictures shown in Figure 5.6 that when going from an isotropic state (liquid, 60°C for **2** and 100°C for **3**) to a second state an ordered mesophase can be observed, which can be seen from the colored textures exhibited by **2** and **3** at 30°C and 66°C, respectively.

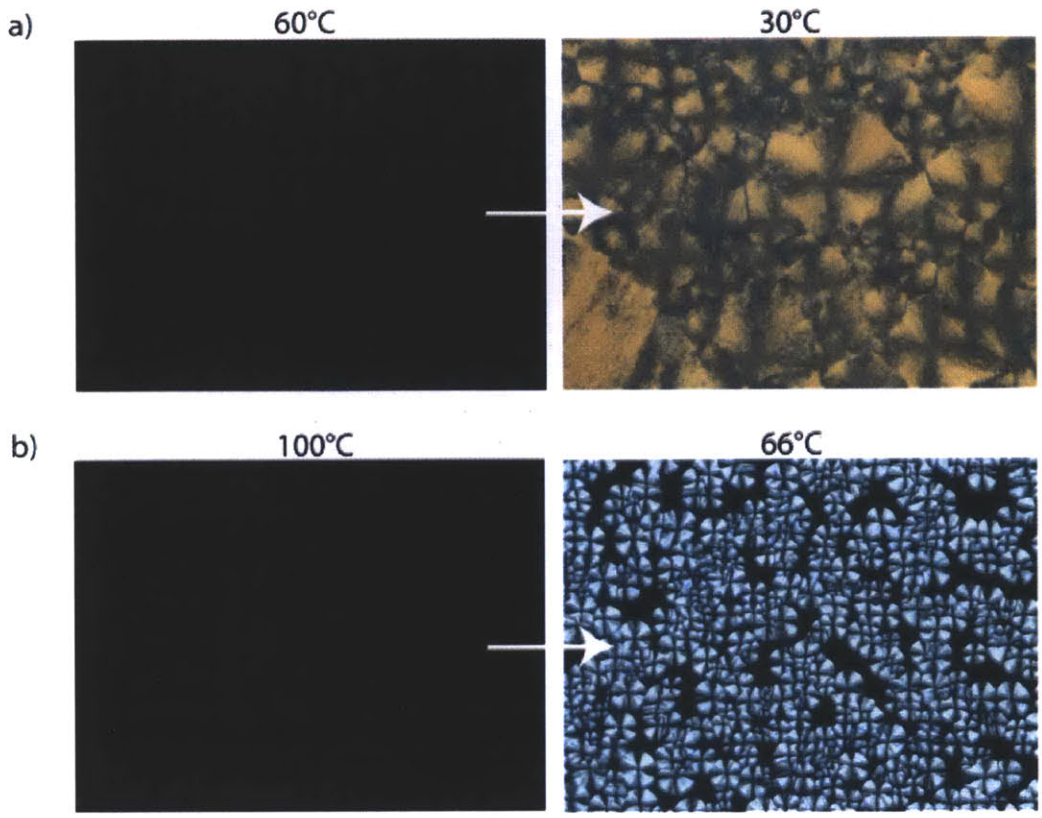

Figure 5.6. POM micrographs for compounds a) **2** and b) **3** at an isotropic liquid state (left) and after cooling to below the first phase transition observed in the DSC (right)

In order to study whether the end-capping moiety has an effect on the mesophase properties exhibited by these kind of oligomeric liquid crystals, the precursors to monomers **2** and **3** (alcohols **11** and **13** respectively) where studied using DSC and POM.

The DSC traces for **11** and **13** are shown in Figure 5.7 and, as expected, the melting point increases from 67.39°C for **11** (2 mesogenic units) to 101.25°C for **13** (3 mesogenic units). These values are higher than those corresponding to monomers **2** and **3** (49.72°C and 90.77°C, respectively). The increase in melting point can be attributed to the stronger interactions induced by the polar alcohol end groups in **11** and **13**. It is also interesting to observe that the alcohol precursors show a comparable range of temperatures for their mesophase (a range spanning

45.35°C and 31.8°C for **11** and **13** compared to a range spanning 49.49°C and 48.26°C for **2** and **3** for the second heating), but with a more pronounced second melting point when comparing **3** (0.58 J/g) and its alcohol precursor, **13** (6.64 J/g), while **2** and its alcohol precursor **11** are within the same order of magnitude (0.90 J/g and 0.75 J/g, respectively).

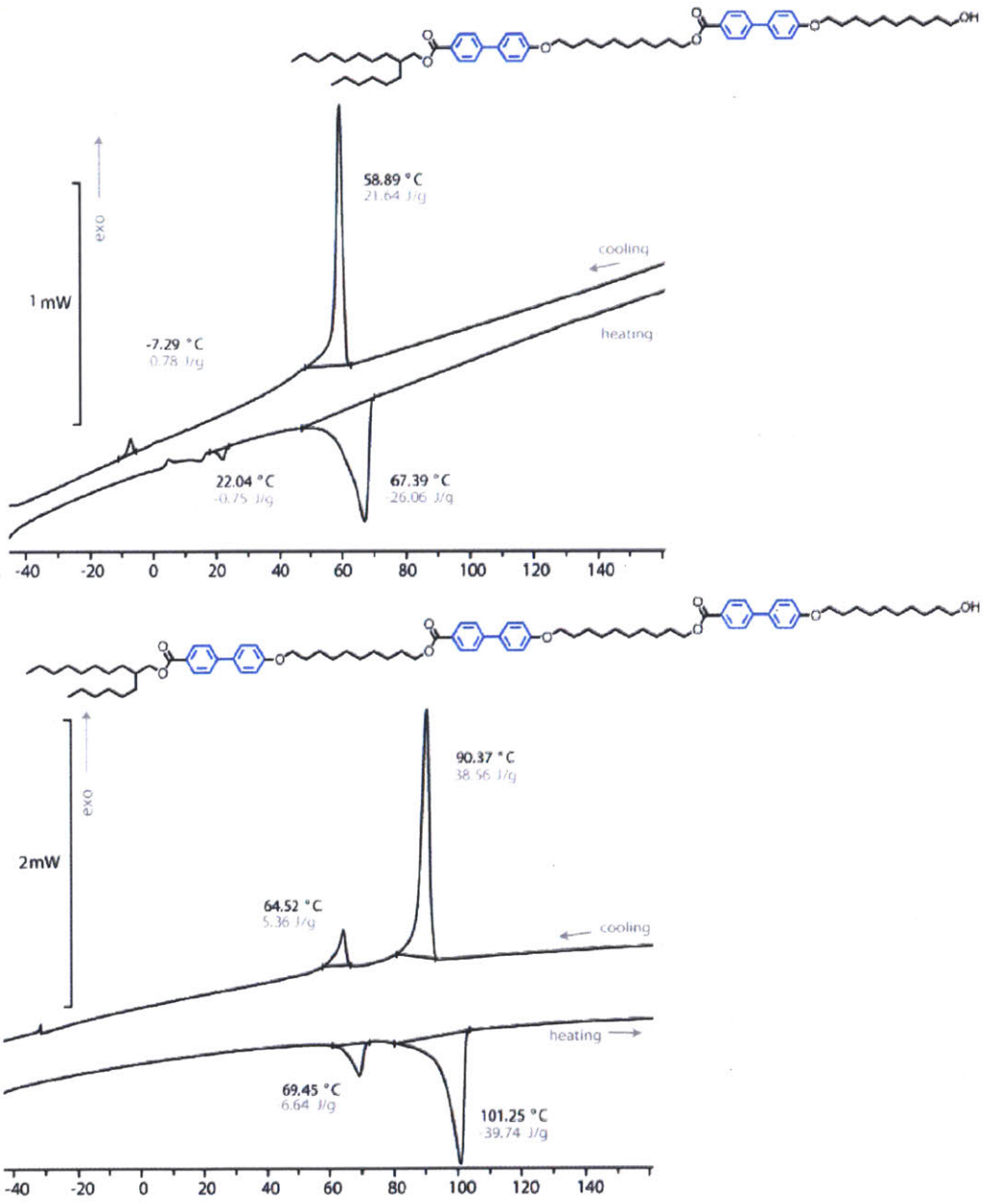

Figure 5.7. Second heating DSC traces (5°C/min) of monomer precursors **11** (top) and **13** (bottom)

The textures observed with the POM for compounds **11** and **13** are also notably different from those of monomers **2** and **3** (Figure 5.8). While compound **13** showed similar features to those of monomer **3**, the domain size of the features was notably smaller. The color and shapes observed in the texture of monomer precursor **11** were completely different from those observed for monomer **2**, and were closer to the texture observed for compound **13**.

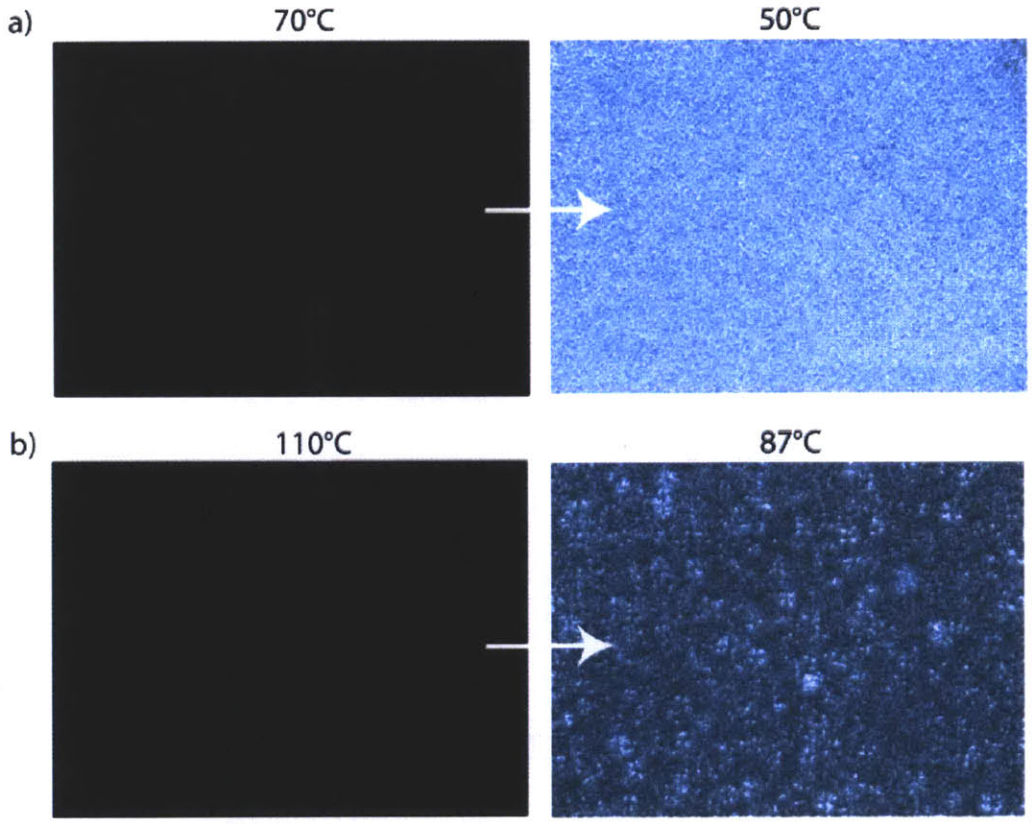

Figure 5.8. POM micrographs for monomer precursors a) **11** and b) **13** at an isotropic liquid state (left) and after cooling to below the first phase transition observed in the DSC (right).

5.2.3 XRD Studies

In order to elucidate the structures in the mesophase and solid state of the compounds mentioned above, the variable temperature X-Ray diffraction spectra of powder samples of

compounds **2** and **3** were measured using a synchrotron as the irradiation source (SPring-8 synchrotron) using both Small Angle (SAXS) and Wide Angle (WAXS) detectors, and they were compared to the spectra of compounds **11** and **13** obtained under analogous conditions.

When cooling monomer **2** (2 mesogenic units, Figure 5.9, top) from an isotropic liquid state, the reflections characteristic of a lamellar structure (Figure 5.10, top) could be observed in the SAXS spectrum, with interlayer spacing on the order of magnitude of the monomer length. Signals corresponding to pi-pi stacking interactions were evident from the WAXS spectrum. The distance measured in this X-Ray experiment was slightly shorter than that of the monomer length, which can likely be explained by a slightly interdigitated lamella. On the other hand, monomer **3** (3 mesogenic units, Figure 5.9, bottom) similarly showed signals corresponding to pi-pi stacking interactions in the WAXS spectrum. However, the main signal from the SAXS spectrum was much broader, and there was only one reflection detected, which may be an indication of lamellar packing in which the lamellae are irregularly distributed (Figure 5.10, bottom).

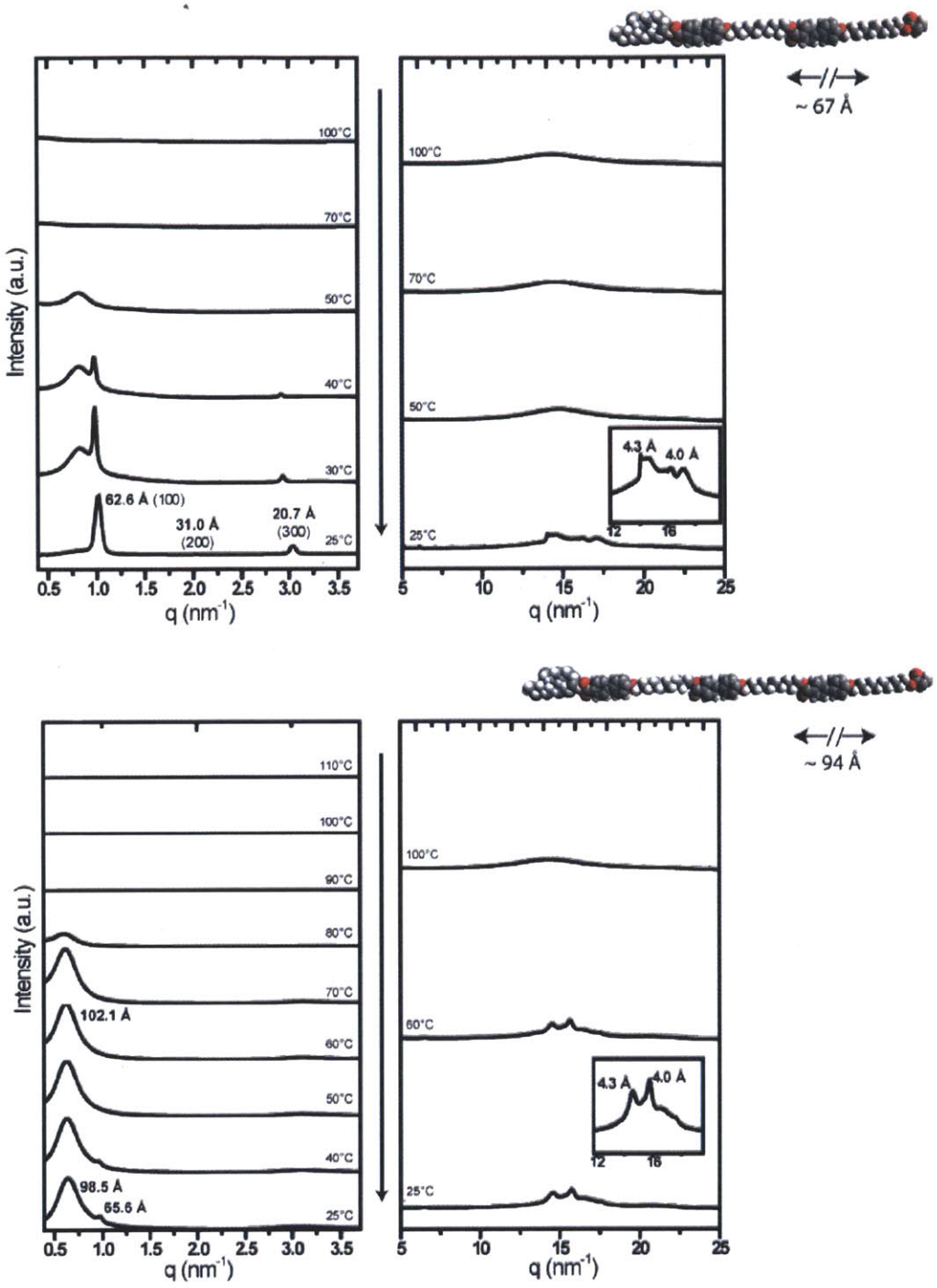

Figure 5.9. Small Angle X-Ray Scattering (SAXS, left) and Wide Angle X-Ray Scattering (WAXS, right) for monomer **2** (upper) and monomer **3** (lower), cooling from an isotropic liquid state (top) to a mesophase state (bottom)

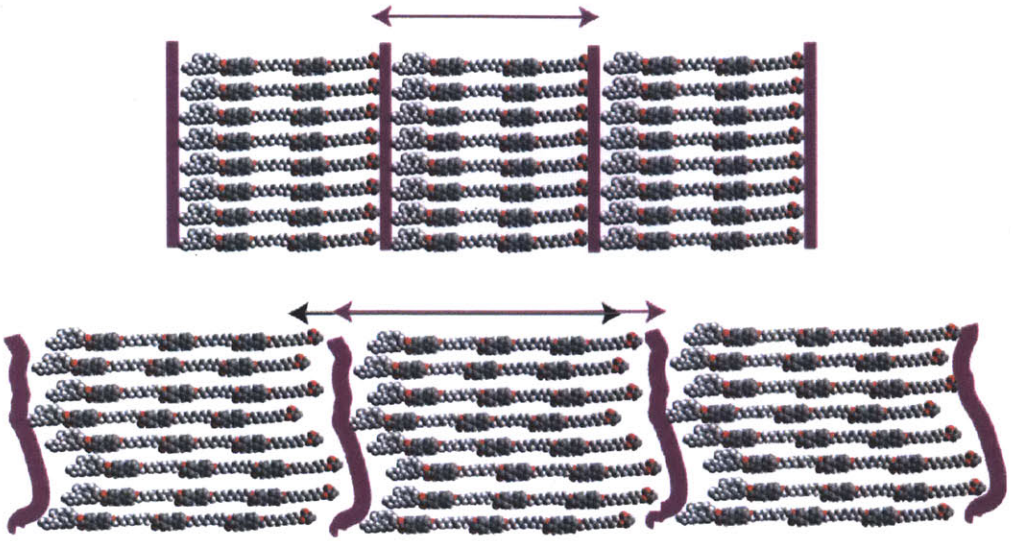

Figure 5.10. Model of a lamellar assembly of **2** (upper) and irregular lamellae of **3** (lower)

For the case of monomer precursors **11** and **13** (Figure 5.11), a lamellar structure was also observed, albeit with some differences. For the case of compound **11**, some unidentified extra peaks were observed when cooling down from an isotropic state, and the spacing of the lamellae was twice the length of compound **11**. This is probably due to the very different nature of each end of the molecule. While one end is terminated in an alcohol and is, thus, hydrophilic, the other end is terminated in a long, branched alkyl chain and is very hydrophobic. When the molecules are cooled down to the mesophase, they probably order themselves so that the hydrophilic ends interact with each other and hydrophobic ends interact with each other, thus generating a double lamellae ordering (Figure 5.12, top). For the case of compound **13**, the molecule is longer and this hydrophobic/hydrophilic effect has less significance, yielding the regular lamellae structure that was also observed for monomers **2** and **3**.

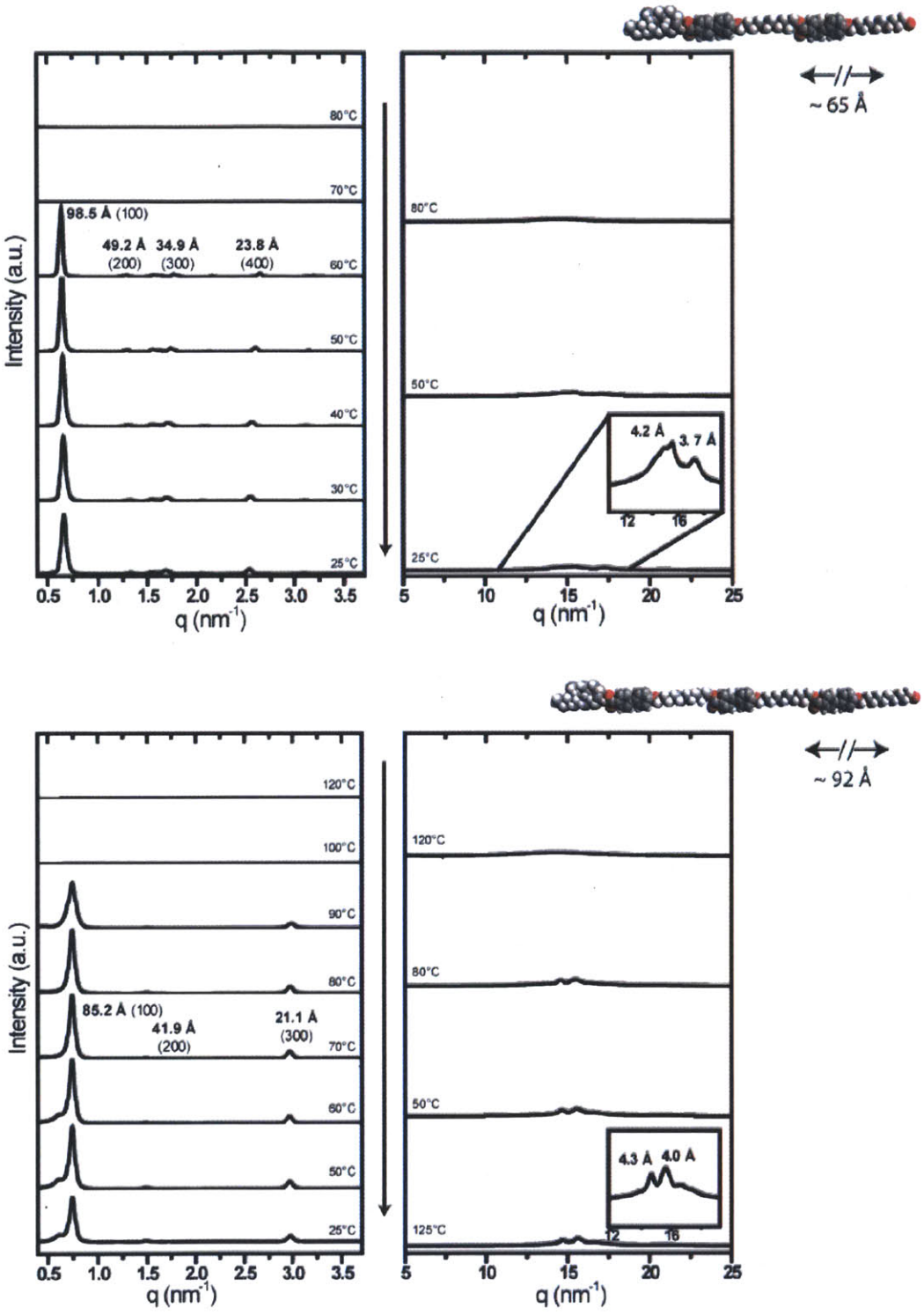

Figure 5.11. Small Angle X-Ray Scattering (SAXS, left) and Wide Angle X-Ray Scattering (WAXS, right) for monomer precursor **11** (upper) and monomer precursor **13** (lower) cooling from an isotropic liquid state (top) to a mesophase state (bottom)

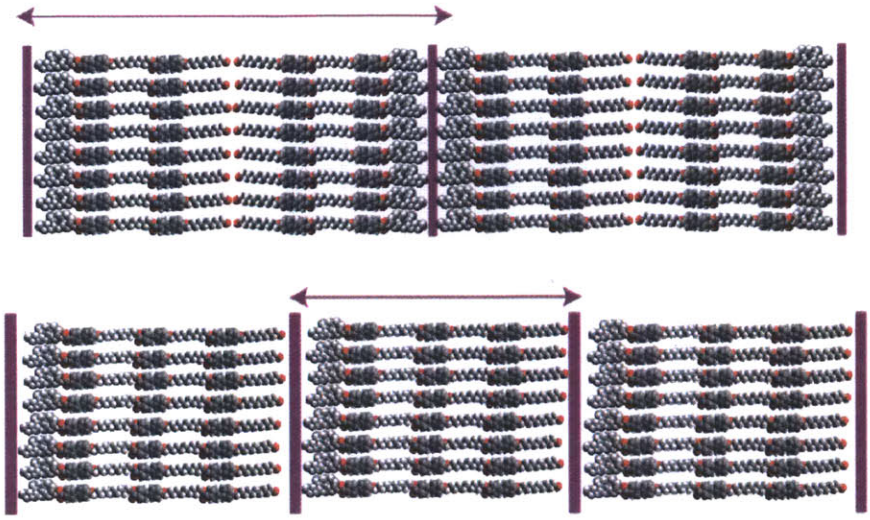

Figure 5.12. Model of a double lamellar assembly of **2** (top) and irregular lamellae of **3** (bottom)

From the DSC, POM and XRD data of monomers **2**, **3** and their precursors, it is clear that the end group in these kind of liquid crystals affects the melting point, liquid crystalline behavior and morphology obtained, as has been reported for other families of liquid crystalline compounds.

5.3 Polymer Synthesis and Characterization

5.3.1 Polymer Synthesis

The polymers of monomers **1**, **2** and **3** were obtained via free radical polymerization under inert atmosphere in benzene, using AIBN as the initiator. The exact polymerization conditions are detailed in Table 5.1. The polymerizations proceeded in reasonably good yields to give **P1** as a sticky oil, and **P2** and **P3** as white powders. The degree of polymerization corresponded relatively well with the initial mix ratio of monomer to initiator.

Polymer	[M]	M / I	T	time	Mn	DP
P1	1M	50 / 1	70°C	36h	33K	57
P2	0.6M	50 / 1	70°C	48h	55K	55
P3	0.45M	50 / 1	70°C	36h	69K	48

Table 5.1. Polymerization conditions for polymers **P1**, **P2**, **P3**

5.3.2 DSC/POM Characterization

The DSC curves of polymers **P1**, **P2**, and **P3** (Figure 5.13) show the polymer melting points increase after the polymerization, when comparing them to the corresponding monomer melting points (for the second heating curves: 9.09°C to 20.12°C from monomer **1** to polymer **P1**, 49.72°C to 61.70°C from monomer **2** to polymer **P2**, 90.77°C to 93.25°C from monomer **3** to polymer **P3**). The melting point for polymer **P1** is below room temperature, and its physical appearance is that of a sticky oil. While monomer **2** displayed a mesophase on its DSC curve, the second melting point is not present in the DSC for the corresponding polymer, which does not show any liquid crystalline behavior. While monomer **3** also displayed a very clear mesophase in the DSC on a range of temperatures spanning over 40°C, the two peaks presumably corresponding to the phase transitions liquid (isotropic) to mesophase and mesophase to solid are practically overlapping in this case.

When analyzing **P2** and **P3** under the POM using crossed polarizers, we can observe birefringence for both cases when cooling down from an isotropic melt (Figure 5.14). While only for the case of **P3** this can be attributed to a liquid crystalline phase (**P2** only displayed a melting point in the DSC), it is clear that for both cases there is some degree of ordering when the polymer is cooled. Since only polymer **P3** displays a mesophase, we decided to explore the dependence of mesophase ordering, thin film ordering, alignment and morphology of **P3** on molecular weight.

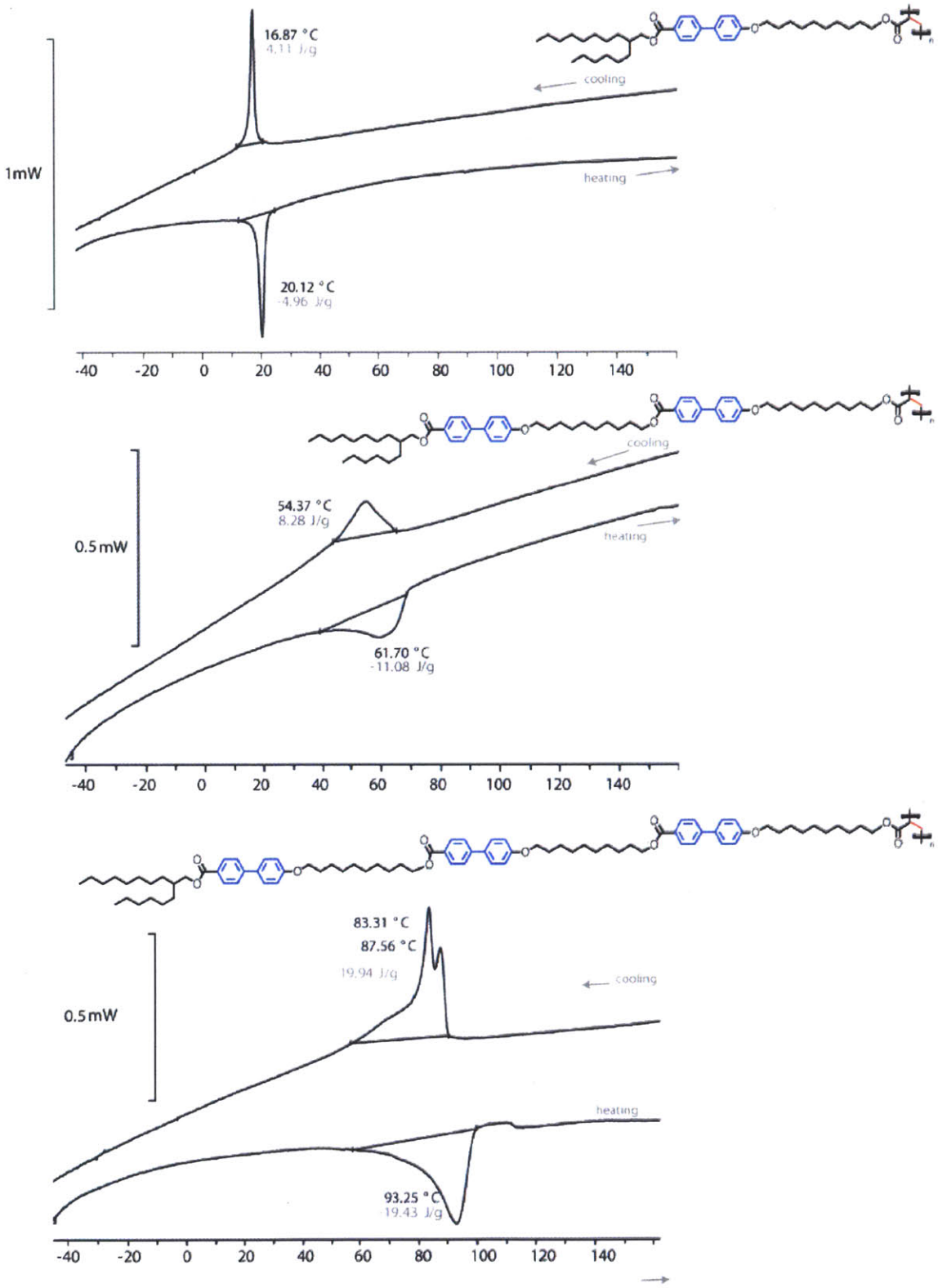

Figure 5.13. Second heating DSC traces (5°C/min) of polymers **P1**, **P2**, **P3**

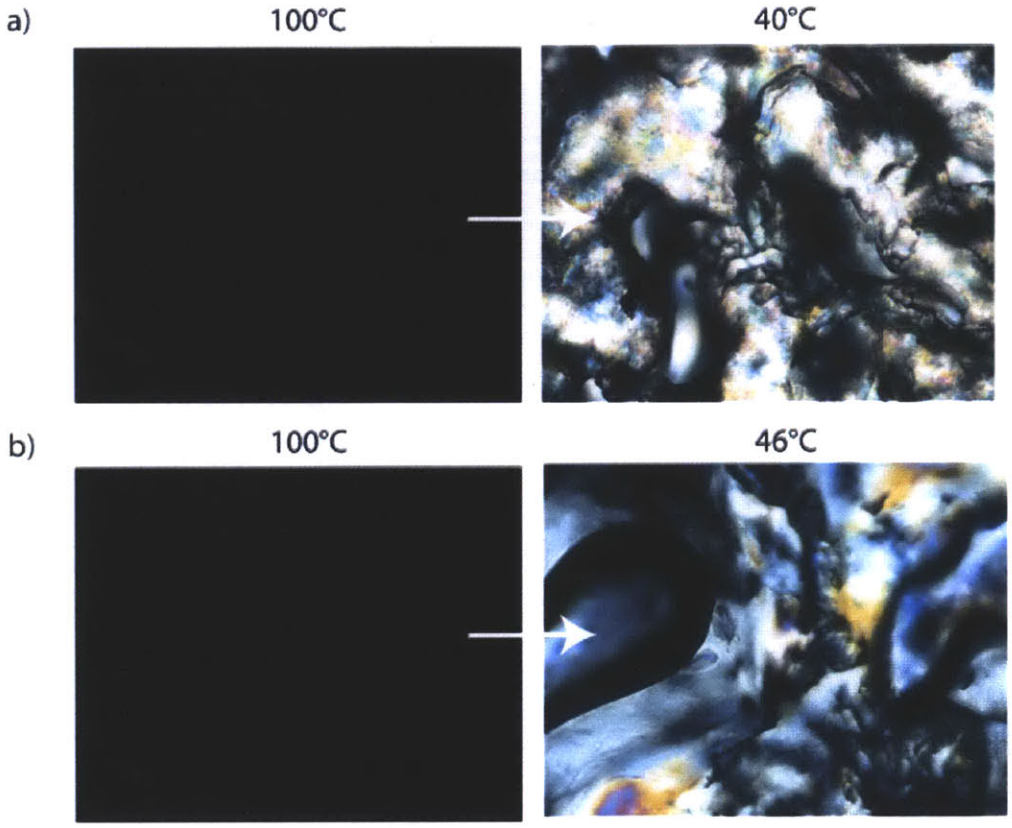

Figure 5.14. POM micrographs for polymers a) **P2** and b) **P3** at an isotropic liquid state (left) and after cooling down below the first phase transition observed in the DSC (right)

5.4 Influence of Polymer Molecular Weight in Polymer Properties (P3)

5.4.1 Polymer Synthesis

The free radical polymerization of monomer **3** was performed under different conditions in order to vary the molecular weight. The goal of this study was to gain a better understanding of the influence of the length of the polymer backbone on the solid state ordering of this family of polymer brushes. The polymerization conditions are described in Table 5.2. When a low ratio of initiator was used (100/1 of monomer/initiator ratio), long chain polymers were only obtained when the concentration of monomer was high enough (compare entries for polymers **P3a** and

P3b). When a very high concentration of **3** was used in combination with a low loading of initiator (as for the case of polymer **P3c**) a monolithic insoluble sample was obtained as a result of the polymerization. One could argue that this insolubility is due to the fact that the polymer chains are extremely long. However, the fact that the polymer melts only partially (see next section for detailed discussion) seems to indicate that thermal cross-linking of some sort occurred in the solid state. When a larger amount of initiator was used together with a lower monomer concentration (as for the case of **P3b**), a polymer of intermediate molecular weight was obtained.

Polymer	[M]	M / I	T	time	Mn
P3a	0.3M	100 / 1	70°C	36h	29K
P3b	0.45M	50 / 1	70°C	36h	69K
P3c	0.6M	100 / 1	70°C	72h	cross-linked

Table 5.2. Polymerization conditions for polymers **P3a**, **P3b**, **P3c**

5.4.2 DSC/POM Characterization

Only **P3b** displayed a homotropic liquid crystalline phase in its DSC curve. Its shorter version **P3a**, and crosslinked analogue **P3c** only showed a single melting point on the DSC (Figure 5.15). The shorter polymer **P3a** did not show any birefringence in the POM either, whereas both **P3b** and cross-linked **P3c** showed birefringence when cooling down from an isotropic state (Figure 5.16)

It has been shown that the molecular weight of the polymer backbone has an effect in mesophase stability, and that the range of temperatures at which the mesophase occurs can be influenced both by the nature of the polymer backbone and its length.[16] Given the experimental

results for the system under study, one could postulate that when the backbone of the polymer is too short (as in the case of **P3a**), no ordering of the polymer brushes occurrs upon cooling (the polymer is just amorphous in the solid state). In this case, the polymer backbone prevents the mesogenic units from arranging themselves in a more close-packed arrangement. When the polymer is crosslinked (**P3c**), even though the melting and subsequent packing of the side chains gives rise to an ordered phase (and thus a texture in the POM), since the backbones are cross-linked there is not enough freedom for the polymer chains to reptate and adopt an ordered mesophase, thus explaining the lack of a second first order phase change peak. It is only when the polymer backbone is long enough that several adjacent side-chain mesogenic units can interact with each other that a mesophase can occur, albeit in a very short range of temperatures for this case.

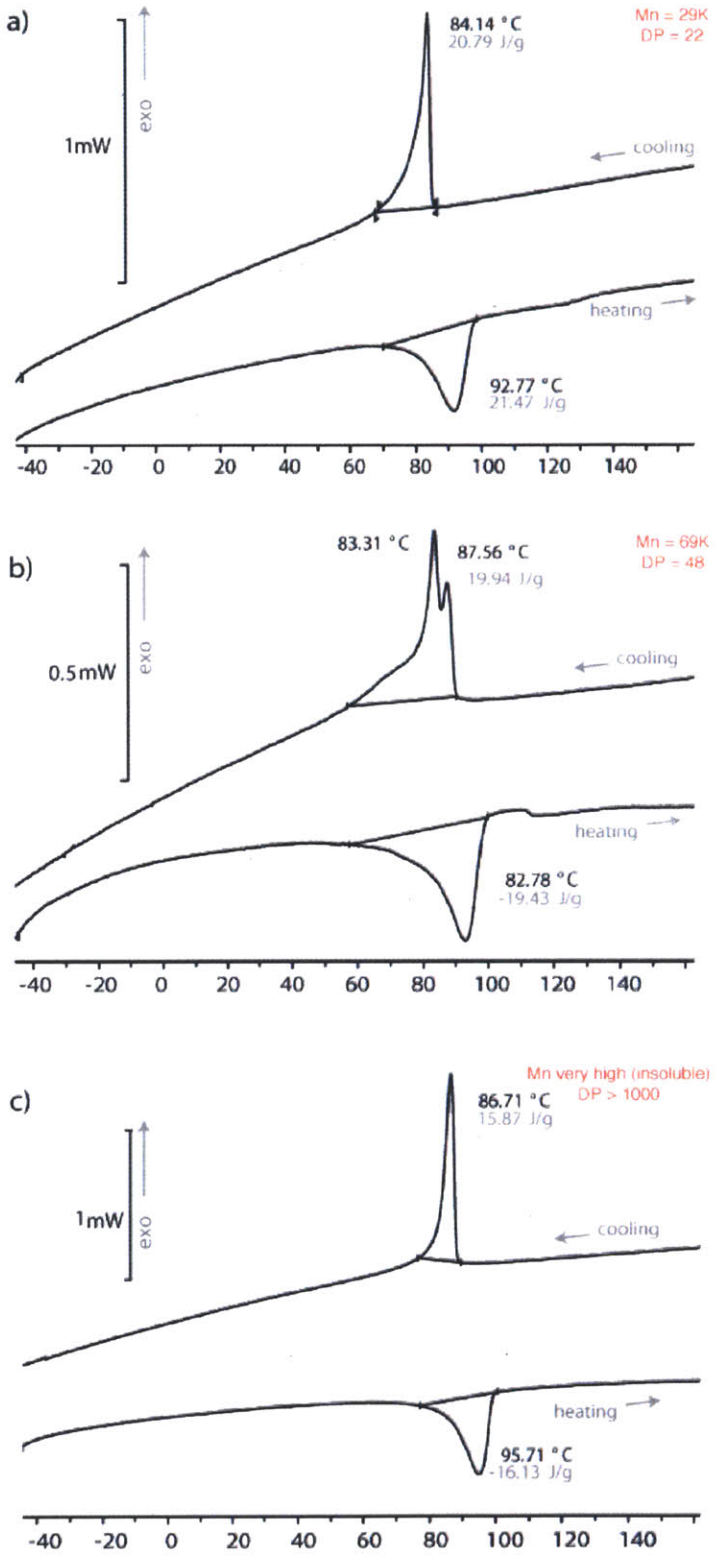

Figure 5.15. Second heating DSC traces (5°C/min) of polymers **P3a** (top, Mn=29K), **P3b** (middle, Mn=69K), **P3c** (bottom, cross-linked)

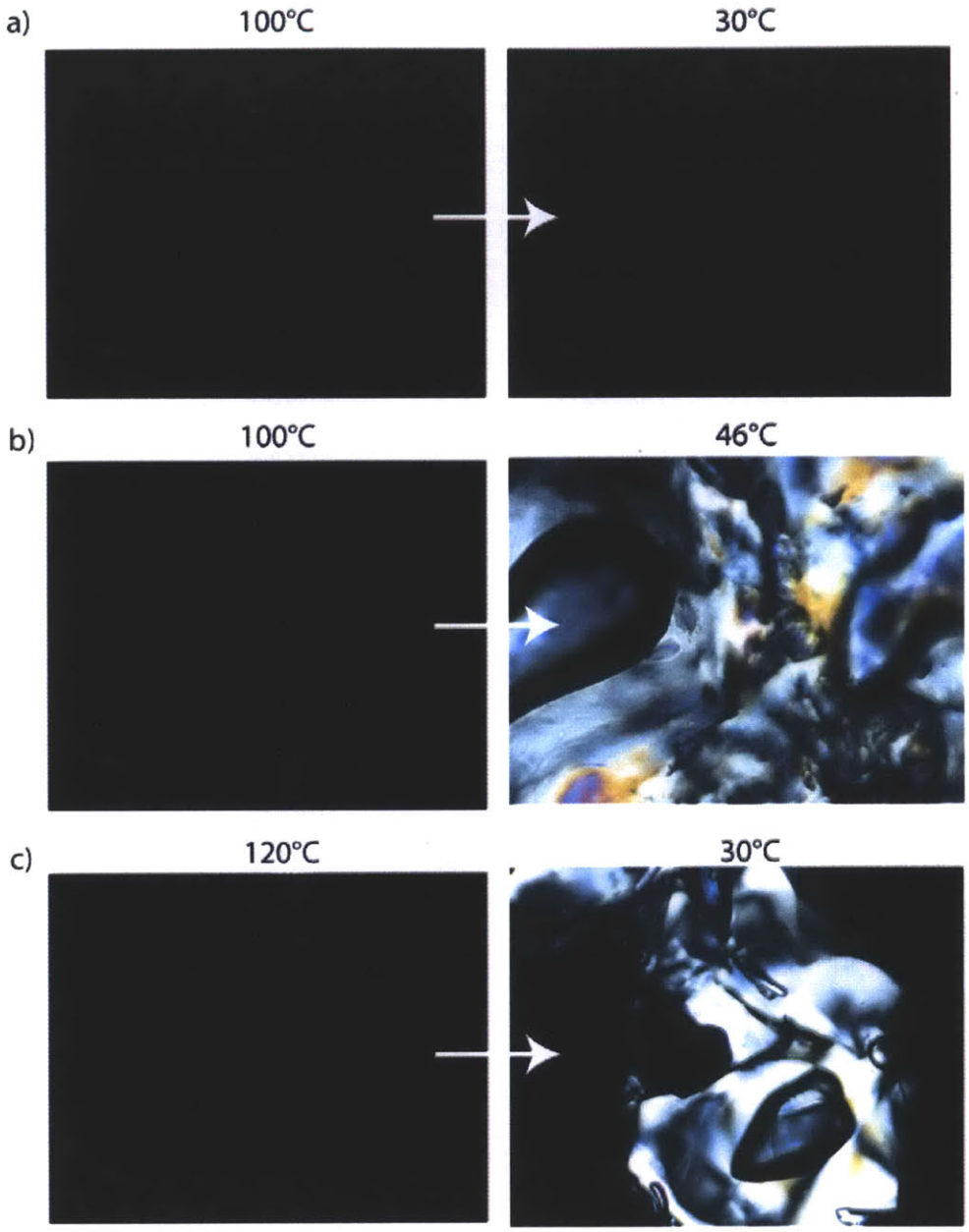

Figure 5.16. POM micrographs for polymers a) **P3a** b) **P3b** and c) **P3c** at an isotropic liquid state (left) and after cooling down below the first phase transition observed in the DSC (right)

5.4.3 XRD Studies

In order to investigate the structures of **P3a**, **P3b** and **P3c** when cooling from an isotropic (liquid) state the variable temperature X-Ray diffraction spectra of powder samples of polymers **P3a**, **P3b** and **P3c** were measured using both Small Angle (SAXS) and Wide Angle (WAXS) detectors (Figure 5.17). All 3 polymers showed signals corresponding to pi-pi stacking interactions in the WAXS spectrum. As for the spectrum in the small-angle region, a single broad signal was observed. This is an indication of ordering which is not so regular. This single reflection is on the order of magnitude of the length of monomer **3**, which as for the case of monomer **3**, can be an indication of a lamellar packing were the lamellae are irregularly distributed.

This result contrasts with the observations of Hosono *et al.* for similar systems in which the mesogenic unit was an azobenzene moiety, and the polymer backbone was a poly (methylmethacrylate) instead of a poly (acrylate). For the system in this study, the morphology is that of an irregular lamella, instead of a homeotropic arrangement of cylinders, and the degree of ordering is much lower. Intrigued by this new morphology, we decided to study the alignment capabilities of these polymers (**P3a**, **P3b** and **P3c**) in the thin film under hot pressing processing conditions.

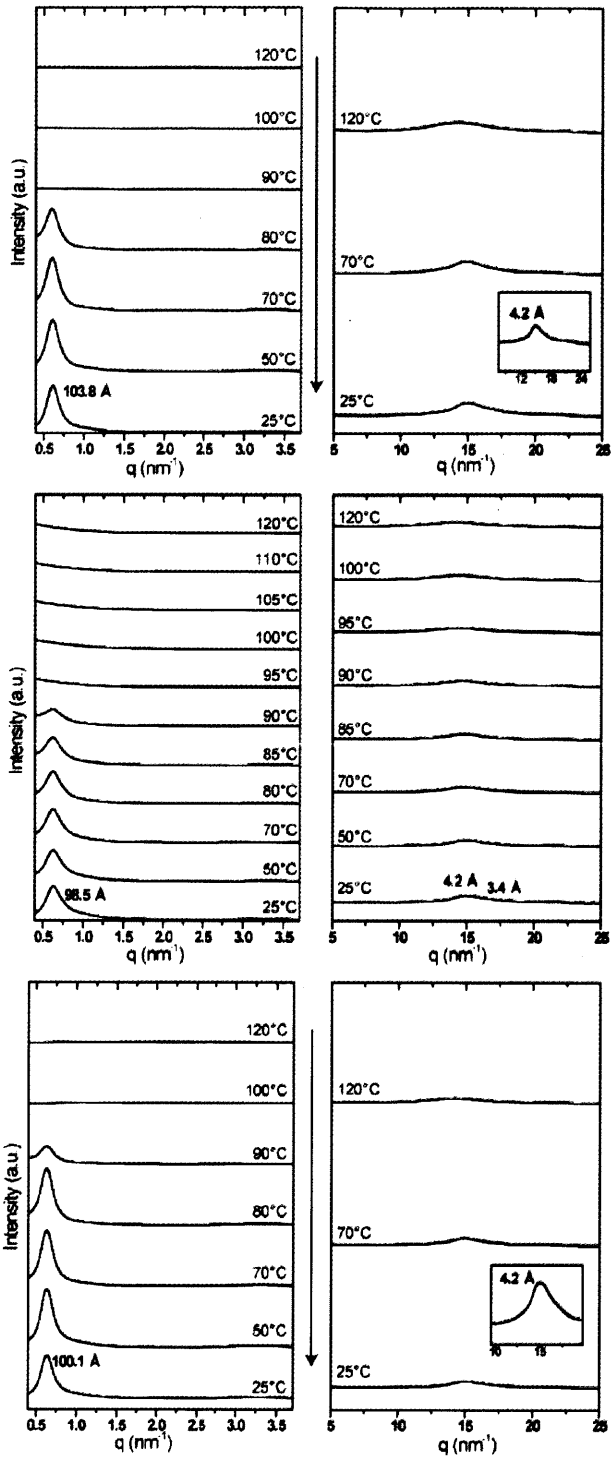

Figure 5.17. Small Angle X-Ray Scattering (SAXS, left) and Wide Angle X-Ray Scattering (WAXS, right) for polymer **P3a** (top), polymer **P3b** (middle) and polymer **P3c** (bottom) cooling from an isotropic state

5.5 Influence of Polymer Molecular Weight in Film Ordering and Alignment

5.5.1 Hot Pressing of Polymers

Conditions similar to those reported by Hosono *et al.* were used for the processing of polymer thin films by hot pressing (Figure 5.18). A powder sample of the corresponding polymer was placed in between two sheets of Teflon with alignment grooves oriented in a parallel fashion. The sandwiched polymer sample was hot pressed above the melting temperature of the polymer for 5 minutes and then cooled to a temperature within the mesophase range of the polymer and annealed for one hour. After annealing, the system was slowly brought back to room temperature. By performing this operation on a liquid crystalline polymer, the polymer chains can be organized in a 3D macroscopically ordered morphology, with alignment induced by the action of the Teflon sheets.

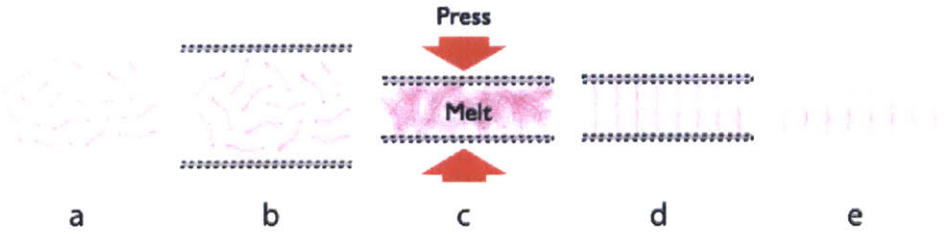

Figure 5.18. Polymer brush thin film processing by hot pressing a) Polymer brush b) Polymer brush sandwiched between Teflon sheets c) Pressure and heat are applied to the polymer d) Hometotropic alignment of the polymer brushes e) Aligning Teflon sheets removal

For this particular case, the polymer sample was heated to an isotropic state, and then cooled down and annealed at the polymer melting temperature for polymers **P3a** and **P3c**, and to a temperature in between the two almost overlapping melting points for the case of polymer **P3b**.

Self-standing films of **P3b**, **P3c** were prepared this way. Films of **P3a** were not self-standing, probably owing to the low molecular weight of the polymer. Thin film measurements for polymer **P3a** were performed over one of the Teflon alignment sheets.

5.5.2 Thin Film Characterization (SAXS, POM) and Alignment Evaluation

If there is ordering in the solid state, the polymer thin films processed by the hot pressing method described above would show a signal in the SAXS. Additionally, if the alignment has been successful then a preferred orientation should be shown by a directional increase in brightness in the two-dimensional (2D) SAXS. This preferred alignment can also be seen with a POM using crossed polarizers, where a contrast would be seen every 45° on rotation, with a dark image when the azimuthal angles between the polarizing direction of the incident light and drawing direction of the Teflon sheets is 0° and 90°.

Thin films of short polymer **P3a** showed no preferential alignment on its 2D SAXS signal, whereas longer polymer **P3b** did show a preferential alignment, indicated by the stronger signals on the drawing direction (highlighted by white circles in Figure 5.19). Cross-linked polymer **P3c** showed some alignment, but it was weaker than that of **P3b**.

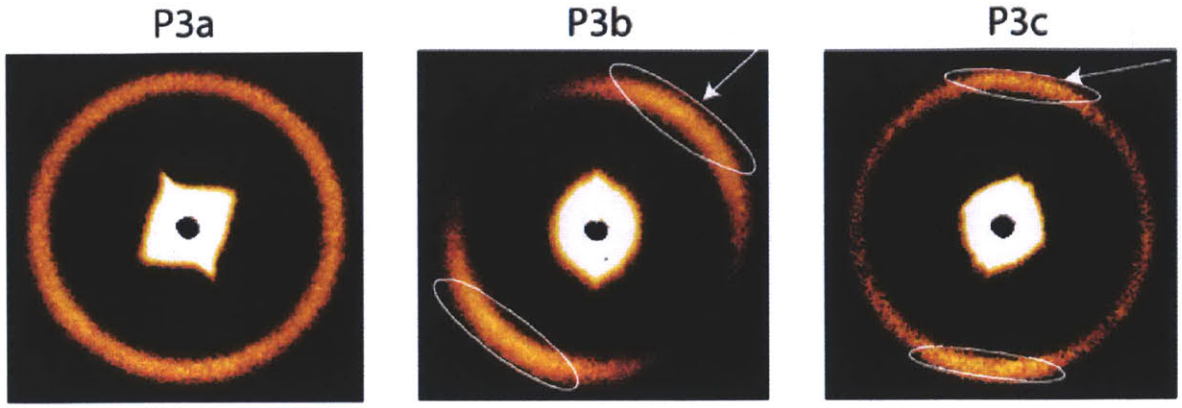

Figure 5.19. 2D Small Angle X-Ray Scattering (SAXS) for hot pressed thin film samples of polymers **P3a, P3b** and **P3c**

POM analysis of thin films of polymer **P3** with varying molecular weights (Figure 5.20) showed that for the case of the shortest polymer **P3a,** only dark images were obtained, as expected, since bulk samples of the same polymer did not show any birefringence. On the other hand, the longer polymer **P3b** did show an angle dependence on its analysis by POM, an indication of good alignment, in accordance with the data obtained from 2D SAXS measurements. For the case of polymer **P3c**, the Teflon films succeeded in aligning the mesogenic units, since the brightness of the textures varied with the angle of the sample, being the brightest at 45°C. However, the texture did not become completely dark at 0°C and 90°C, indicating that the alignment is not perfectly homogeneous across the surface of the sample, and that different domains are present in the sample. This multi-domain morphology probably originates from the fact that this cross-linked sample did not melt completely under the film processing conditions, making it impossible for the side-chains of the polymer brushes to efficiently align with the action of the Teflon sheets.

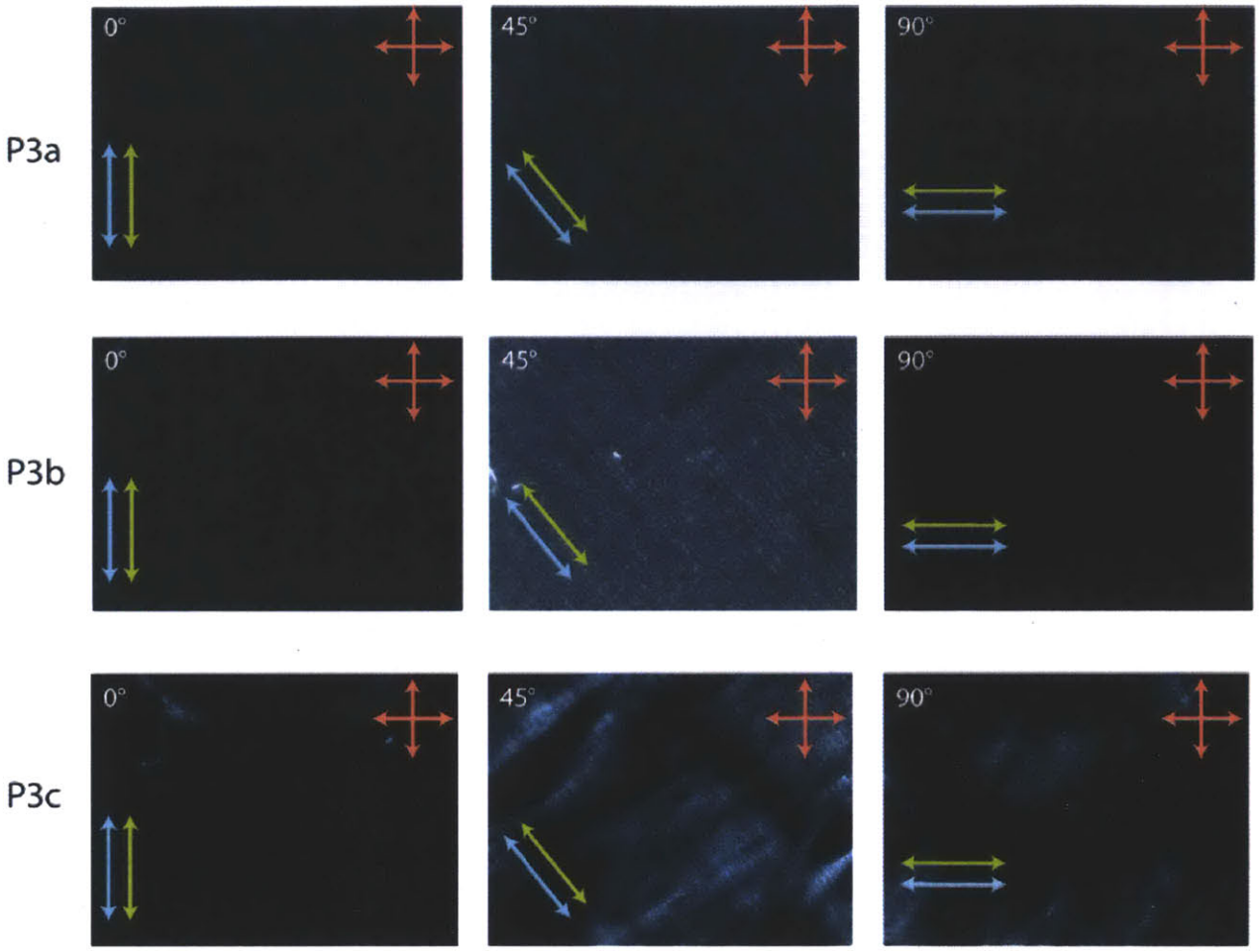

Figure 5.20. POM for hot pressed thin film samples of (A) polymer **P3a,** (B) polymer **P3b** and (C) polymer **P3c**. The blue and green arrows indicate the direction of orientation of the grooves in the Teflon films, whereas the red arrows indicate the directions of alignment of the crossed polarizers in the microscope. A change in the texture brightness indicates a preferred orientation of the mesogenic units

These results stress the importance of the polymer molecular weight on the alignment capabilities, and how only when polymers with the right molecular weight are obtained, a good alignment can be achieved.

5.6 Conclusions

As described in the study carried out by Hosono *et al.*, changing the number of mesogenic units in both the monomeric and polymeric molecules greatly influenced the physical properties. When both monomers and polymers contained more mesogenic units, an increase in the melting point as measured by DSC was observed. By increasing the number of mesogenic units, molecules were also more prone to exhibit liquid crystalline behavior. In fact, none of the studied molecules containing only one mesogenic unit displayed a mesophase.

The end group in monomers also had a great effect on the melting point, mesophase formation, and texture observed in the POM. While the molecules end-capped with an alcohol moiety displayed clear mesophases in the DSC, the acrylate-capped analogues had a much less pronounced additional melting point. The phases displayed were also different, as evidenced by the XRD studies.

Polymers had higher melting points than the monomeric analogues, as has been described many times in the literature. By changing the number of mesogenic units in the side chain of these polymer brushes, one can tune their physical properties. For instance, only the polymer containing three mesogenic units in the side chain showed a liquid crystalline phase.

The morphology of biphenyl-containing polymer brushes was that of an irregular lamella, very different from the cylindrical arrangements observed by Hosono *et al.* This can be explained partly by the fact that biphenyl mesogenic units are less sterically demanding than the analogous azobenzene. Consequently, the steric repulsion that drove the side chains of the polymer brush to the axial direction perpendicular to the polymer backbone is diminished. The range of temperatures in which biphenyl-containing polymers displayed a mesophase was much shorter, a fact that can be attributed to the lower-melting point backbone used in this study. A

deeper analysis as to the exact role the backbone plays in assembly is necessary, to which purpose more rigid, higher melting point polymer backbones should be used

It was also evidenced that the molecular weight of the polymers can influence liquid crystalline behavior. Only when the polymer brushes are of sufficient length can a mesophase be observed. However, when cross-linking of the polymer chains occurs, no mesophase is detected in the DSC. The length of the polymer chains is also important from the point of view of alignment in the thin film, with only sufficiently long polymers showing alignment from hot pressing conditions. Cross-linking proved to be detrimental for alignment by hot pressing, as smaller domains of oriented polymer brushes were obtained in this case.

In summary, this study shows a new kind of polymer brush with functionalized side-chains composed of oligomeric liquid crystals, and illustrates how the properties of these polymers can be affected by chemical tuning of these side-chains, specifically the nature and number of mesogenic units. The polymer properties were also greatly affected by changing the length of the polymer backbone. Both the structure of the side-chains and the polymer length affect the solid-state morphology of thin films, as well as the ordering and alignment properties of these polymer brushes. It was also shown that cross-linking of the polymer brushes was detrimental for alignment to obtain large-area ordered domains in the thin film. It was also described how the nature of the end group for certain kinds of oligomeric liquid crystals has a huge effect on the physical properties displayed by this type of liquid crystals.

The lamellar assemblies described here are different from those obtained when using azobenzene units in the side-chain, but 3D macroscopic alignment can also be induced under the right processing conditions. This particular morphology is also interesting from the point of view of future photovoltaic applications, since lamellae can provide optimal hole and electron

conducting pathways. A broader variety of mesogenic units should be explored to find out what other structures can be obtained. To this effect, useful photoactive mesogenic units could be employed that would provide a photovoltaic response. The use of a conducting polymer as the polymer backbone could also be advantageous for this purpose. Conjugated polymers with a degree of polymerization similar to the those of polymer brushes reported here should be easily accessible with current conjugated polymer synthesis techniques.

5.7 Experimental Section

Materials: Unless otherwise noted, all reactions were performed in flame-dried glassware, and under an oxygen-free atmosphere of argon using standard Schlenk techniques. Reagents were used as received from Aldrich Chemical [2-hexyl-1-decanol (97%) and acrylic acid chloride], Tokyo Chemical Industry (TCI) [tert-butyldimethylchlorosilane (TBDMSCl, 98%), and tetrabutylammonium fluoride (TBAF, 1 M in tetrahydrofuran (THF))], and Wako Pure Chemical Industries [N,N'-diisopropylcarbodiimide (DIPC, 99%), triethylamine (99%), 2,2'-azobisisobutyronitrile (AIBN, 98%), $NaHCO_3$ (> 99%), Cs_2CO_3 (> 95%), and KOH (85%)]. 4-(dimethylamino)pyridinium 4-toluenesulfonate (DPTS), compounds **4** and **5** were prepared following previous reports from the literature.[17] Dry THF was obtained from a solvent purification system. Other dehydrated solvents were used as received from Wako Pure Chemical Industries or Kanto Chemicals. Uniaxially stretched polytetrafluoroethylene (PTFE, TeflonTM) sheets (300 mm x 10 m x 0.1 mm) were purchased from Flon Industry and cut into a proper size before use. Column chromatography was carried out with Wakogel silica C-200 (particle size: 75–150 μm).

NMR Spectroscopy: ^1H and ^{13}C NMR spectra were recorded at 25 °C on a 500 MHz JEOL model JNM-ECA500 spectrometer, and chemical shifts (δ in ppm) are given relative to $CHCl_3$ (7.24 ppm and 77.24 ppm for ^1H and ^{13}C) unless otherwise noted.

Mass Spectrometry: Matrix-assisted laser desorption ionization time-of-flight (MALDI-TOF) mass spectrometry was performed on an Applied Biosystems model MDS SCIEX 4800 Plus MALDI TOF/TOFTM Analyzer using dithranol as a matrix.

Molecular Weight Determination: Analytical GPC was performed at 40 °C on a TOSOH model HLC-8220 GPC system equipped with a refractive index (RI) detector, using $CHCl_3$ as an eluent

at a flow rate of 0.35 mL/min. The estimated molecular weights were obtained using a calibration curve of polystyrene standards.

Differential scanning calorimetry: DSC was performed on a Mettler–Toledo model DSC 1 differential scanning calorimeter, where temperature and enthalpy were calibrated with In (430 K, 3.3 J/mol) and Zn (692.7 K, 12 J/mol) standard samples using sealed Al sample pans. Cooling and heating profiles were recorded and analyzed using the Mettler–Toledo STARe software system.

Polarized optical microscopy: POM was performed on a Nikon model Eclipse LV100POL optical polarizing microscope equipped with a Mettler–Toledo model FP90 controller attached to a FP82HT hot stage.

Thin Film Fabrication: Hot press was performed on an Imoto Machinery model IMC-180C compact press. Film thicknesses were measured using a Mitutoyo model MDQ-30M micrometer.

XRD Measurements: Small-angle X-ray scattering (SAXS) and wide-angle X-ray scattering (WAXS) experiments were carried out at BL45XU in SPring-8 (Hyogo, Japan) with an imaging plate area detector, a R-AXIS IV++ (Rigaku). The scattering vector, $q = 4\pi\sin\theta/\lambda$, and the position of incident X-ray on the detector were calibrated using several orders of layer reflections from silver behenate (d = 58.380 Å), where 2θ and λ are scattering angle and wavelength of X-ray (0.90 A), respectively. The sample-to-detector distances for SAXS and WAXS measurements were 2.5 and 0.5 m, respectively. The scattering/diffraction images recorded were integrated along the Debye-Scherrer ring, affording one-dimensional intensity data using the FIT2D software. The cell parameters were refined using the CellCalc ver. 2.10 software. Powder samples were measured by placing an aliquot into a 1.0 mm-φ glass capillary in a temperature-controlled heating block and once heated to melting

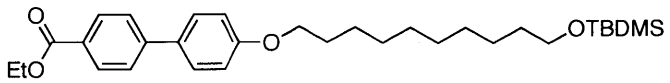

Ethyl 4'-((10-((tert-butyldimethylsilyl)oxy)decyl)oxy)-[1,1'-biphenyl]-4-carboxylate (6). 17.5 g of compound **4** (50 mmol) were dissolved in 40 ml DMF under argon. Compound **5** (12 g, 50 mmol) was added to the mixture, followed by addition of Cs_2CO_3 (19.5 g, 60 mmol). The resulting mixture was heated up to 70 °C and stirred for 14h, after which the solution turned yellow. After cooling to room temperature, the solid formed was filtered and washed thoroughly with DCM. The filtrate was washed with a saturated solution of ammonium chloride, water, and brine. After drying over magnesium sulfate, the solvent was removed *in vacuo*. The resulting crude was washed with a minimum amount of ethanol, and dried under vacuum to yield 24.4 g of compound **6** (96% yield) as a pale yellow powder. ^{1}H-NMR (ppm, $CDCl_3$): 0.00 (6H, s), 0.85 (9H, s), 1.23 – 1.31 (12H, m), 1.36 (3H, t, J=5.95 Hz), 1.39 – 1.47 (2H, m), 1.76 (2H, m), 3.55 (2H, t, J=6.75 Hz), 3.95 (2H, t, J=6.75 Hz), 4.34 (2H, q, J=5.95 Hz), 6.93 (2H, d, J=8.55 Hz), 7.51 (2H, d, J=6.70 Hz), 7.56 (2H, d, J=6.70 Hz), 8.02 (2H, d, J=8.55 Hz). ^{13}C-NMR (ppm, $CDCl_3$) -5.0, 14.6, 18.6, 26.0, 26.2, 26.3, 29.5, 29.6, 29.6, 29.7, 29.8, 33.1, 61.1, 63.5, 68.4, 115.1, 126.6, 128.5, 128.8, 130.4, 132.4, 145.4, 159.6, 166.8. MALDI-TOF (m/z) found: 513.35 [M+H], calculated: 513.33.

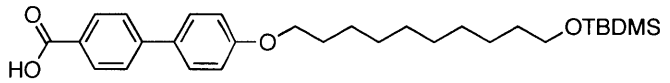

4'-((10-((tert-butyldimethylsilyl)oxy)decyl)oxy)-[1,1'-biphenyl]-4-carboxylic acid (7). 15 g of compound **6** (29 mmol) was dissolved in 400 ml of dry THF under argon atmosphere. Then 120 ml of ethanol and 60 ml of a 1M solution of KOH (aq.) was added, and the resulting mixture was stirred at 50 °C for 12 h. The solvent was removed *in vacuo*, and the crude mixture was taken up

in ethyl acetate. Owing to the low solubility of the product, the resulting solution was separated in several fractions to perform the necessary washing operations. These fractions were washed with ammonium chloride, water and brine. After solvent removal and drying, the combined fractions were collected as a white powder, which was identified as compound **7** (9.25 g, 66% yield). ^{1}H-NMR (ppm, DMSO-d^{6}): 0.65 (6H, s), 0.19 (9H, s), 0.56-0.82 (12H, m), 1.06 (2H, m), 1.82 (2H, m), 2.90 (2H, t, J=6.1 Hz), 3.56 (2H, q, J=6.1 Hz), 6.36 (2H, d, J=7.9 Hz), 6.98 (2H, d, J=8.55 Hz), 7.06 (2H, d, J=8.55 Hz), 7.30 (2H, d, J=7.9 Hz). ^{13}C-NMR (ppm, DMSO-d^{6}) -11.1, 12.2, 19.4, 19.7, 20.0, 22.8, 22.9, 22.9, 23.1, 23.1, 26.4, 56.6, 61.7, 109.2, 117.6, 120.3, 122.3, 124.1, 125.3, 149.21, 153,.2, 163.0. MALDI-TOF (m/z) found: 485.31 [M+H], calculated: 485.30.

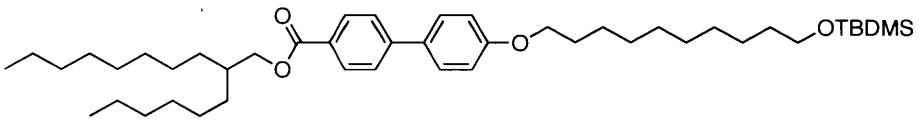

2-hexyldecyl 4'-((10-((tert-butyldimethylsilyl)oxy)decyl)oxy)-[1,1'-biphenyl]-4-carboxylate (8). 4 g of compound **7** (8.25 mmol) was dispersed in 50 ml of DCM, and DPTS (479 mg) and DIPC (1.73 ml, 11.12 mmol) were added. After stirring at room temperature for 35 min, the reaction mixture became a homogeneous solution, to which the alcohol 2-hexyldecan-1-ol (2.4 ml, 8.27 mmol) was added. After stirring at room temperature over night, the reaction mixture was poured over water. After extracting with DCM, the combined organics were washed with water, brine, dried over magnesium sulfate and the solvent was removed *in vacuo*. The residue was purified by column chromatography using $CHCl_3$ as the eluent to obtain compound **8** as a colorless oil (5.7 g, 98%). ^{1}H-NMR (ppm, $CDCl_3$): 0.03 (6H, s), 0.84-0.87 (15H, m), 1.10 – 1.54 (37H, m), 1.74 – 1.77 (4H, m), 3.58 (2H, t, J=6.7 Hz), 3.98 (2H, t, J=6.77 Hz), 4.22 (2H, d, J=5.5

Hz), 6.96 (2H, d, J=8.55 Hz), 7.53 (2H, d, J=8.55 Hz), 7.59 (2H, d, J=8.55 Hz), 8.04 (2H, d, J=8.55 Hz). ^{13}C-NMR (ppm, $CDCl_3$) -5.0, 14.3, 18.6, 22.9, 22.9, 26.0, 26.2, 26.3, 27.0, 29.5, 29.5, 29.6, 29.7, 29.7, 29.8, 29.9, 30.2, 31.7, 32.0, 32.1, 33.1, 37,7, 63.6, 67.9, 68.4, 115.2, 126.6, 128.8, 129.3, 130.3, 132.4, 145.5, 159.6, 167.0. MALDI-TOF (m/z) found: 709.55 [M+H], calculated: 709.55.

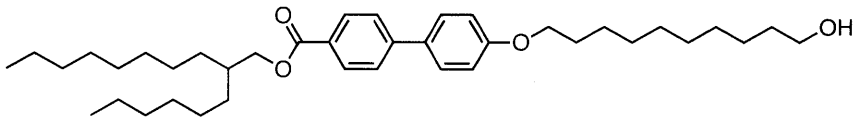

2-hexyldecyl 4'-((10-hydroxydecyl)oxy)-[1,1'-biphenyl]-4-carboxylate (9). Compound **8** (5.7 g, 8.1 mmol) was dissolved in 22 ml dry THF under an argon atmosphere, and 17 ml of a 1M solution of TBAF (THF) was added. After stirring at room temperature for 15 h, the solvent was removed and the remaining crude residue was dissolved in a mixture of DCM and a saturated solution of ammonium chloride (aq.). The mixture was extracted with DCM, and the combined organic phases were washed with water and brine. After drying over magnesium sulfate and removing the solvent *in vacuo*, the residue was purified by column chromatography using $CHCl_3$ as the eluent to obtain compound **9** as a colorless oil (4.1 g, 85%). ^{1}H-NMR (ppm, $CDCl_3$): 0.84-0.86 (6H, m), 1.16 – 1.51 (38H, m), 1.74 – 1.81 (4H, m), 3.63 (2H, tb), 3.99 (2H, t, J=6.77 Hz), 4.22 (2H, d, J=5.5 Hz), 6.97 (2H, d, J=8.55 Hz), 7.53 (2H, d, J=8.55 Hz), 7.59 (2H, d, J=8.55 Hz), 8.04 (2H, d, J=8.55 Hz). ^{13}C-NMR (ppm, $CDCl_3$) 14.3, 14.3, 22.9, 22.9, 26.0, 26.3, 27.0, 27.0, 29.5, 29.5, 29.6, 29.6, 29.7, 29.8, 29.8, 29.9, 30.2, 31.7, 32.1, 32.1, 33.0, 37,7, 63.3, 67.9, 68.4, 115.2, 126.6, 128.5, 130.1, 130.3, 132.5, 145.5, 159.6, 167.3. MALDI-TOF (m/z) found: 595.47 [M+H], calculated: 595.46.

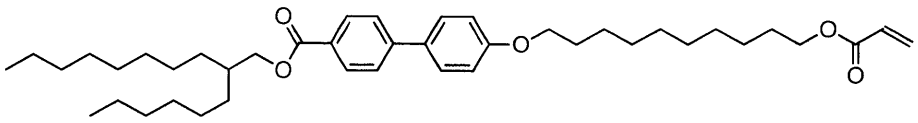

Monomer 1. Compound **9** (1 g, 1.7 mmol) was dissolved in 70 ml DCM and cooled down to 0 °C. 2.5 equivalents of triethylamine (0.6 ml, 4.3 mmol) was added in one fraction, after which acrylic acid chloride (0.35 ml, 4.3 mmol) dissolved in 10 ml of DCM was added dropwise over a period of 30 minutes *via* an addition funnel. After the addition was complete, the mixture was warmed to room temperature, and stirred for 20 h. The solvent was removed and the crude residue was dissolved in a mixture of DCM and a saturated solution of ammonium chloride (aq.). The mixture was extracted with DCM, and the combined organic phases were washed with water and brine. After drying over magnesium sulfate and removing the solvent *in vacuo*, the residue was purified by column chromatography using $CHCl_3$ as the eluent to obtain monomer **1** as a colorless oil (860 mg, 78%). ^{1}H-NMR (ppm, $CDCl_3$): 0.81-0.89 (6H, m), 1.19 – 1.49 (37H, m), 1.61 – 1.68 (2H, m), 1.74 – 1.82 (2H, m), 3.98 (2H, t, J=6.3 Hz), 4.13 (2H, t, J=6.9 Hz), 4.22 (2H, d, J=5.7 Hz), 5.79 (1H, dd, J=1.75, 10.9 Hz), 6.11 (1H, dd, J=10.9, 17.75 Hz), 6.37 (1H, dd, J=1.75, 17.75 Hz), 6.96 (2H, d, J=8.55 Hz), 7.53 (2H, d, J=8.55 Hz), 7.59 (2H, d, J=8.55 Hz), 8.04 (2H, d, J=8.55 Hz). ^{13}C-NMR (ppm, $CDCl_3$) 14.3, 22.9, 22.9, 26.1, 26.3, 27.0, 27.0, 28.8, 29.5, 29.5, 29.5, 29.6, 29.6, 29.7, 29.8, 29.9, 30.2, 31.7, 32.0, 32.1, 37.7, 64.9, 67.9, 68.4, 115.2, 126.6, 128.5, 128.9, 128.9, 130.3, 130.7, 132.5, 145.4, 159.3, 166.6, 166.7. MALDI-TOF (m/z) found: 649.49 [M+H], calculated: 649.48.

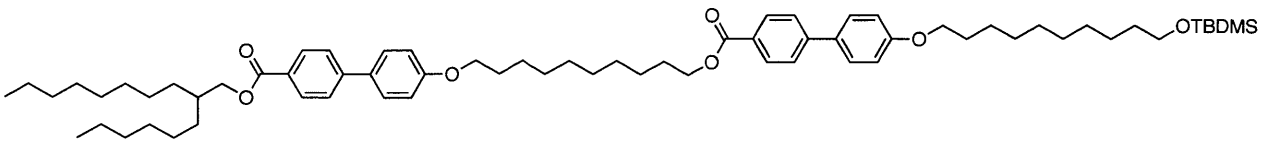

2-hexyldecyl 4'-((10-((4'-((10-((tert-butyldimethylsilyl)oxy)decyl)oxy)- [1,1'-biphenyl]-4-carbonyl)oxy)decyl)oxy)-[1,1'-biphenyl]-4-carboxylate (10). Compound **7** (2.28 g, 4.7 mmol) was dispersed in 30 ml DCM. DPTS (275 mg), and DIPC (0.93 ml, 6.1 mmol) were added. After stirring at room temperature for 35 min, the reaction mixture became a homogeneous solution, to which compound **9** (2.8 g, 4.7 mmol) was added. After stirring at room temperature for 14 h, the reaction mixture was poured over water, DCM and extracted with DCM. The combined organics were washed with water, brine, dried over magnesium sulfate and the solvent was removed *in vacuo*. The residue was purified by column chromatography using $CHCl_3$ as the eluent to obtain compound **10** as a colorless oil (3.6 g, 72%). ^{1}H-NMR (ppm, $CDCl_3$): 0.02 (6H, s), 0.83-0.89 (15H, m), 1.20 – 1.77 (57H, m), 3.58 (2H, t, J= 6.9 Hz), 3.98 (4H, m), 4.22 (2H, d, J=5.7 Hz), 4.31 (2H, t, J=6.9 Hz), 6.96 (4H, d, J=8.55 Hz), 7.53 (4H, d, J=8.55 Hz), 7.59 (4H, d, J=8.55 Hz), 8.04 (4H, d, J=8.55 Hz). ^{13}C-NMR (ppm, $CDCl_3$) -5.0, 14.3, 18.6, 22.9, 22.9, 26.0, 26.2, 26.3, 27.0, 27.0, 29.0, 29.5, 29.5, 29.6, 29.6, 29.6, 29.7, 29.8, 29.8, 29.9, 30.2, 31.7, 32.0, 32.1, 33.1, 37.7, 63.6, 65.2, 67.9, 68.4, 115.2, 126.7, 128.5, 128.5, 129.0, 130.3, 132.5, 145.4, 159.7, 166.9, 167.0. MALDI-TOF (m/z) found: 1061.77 [M+H], calculated: 1061.76.

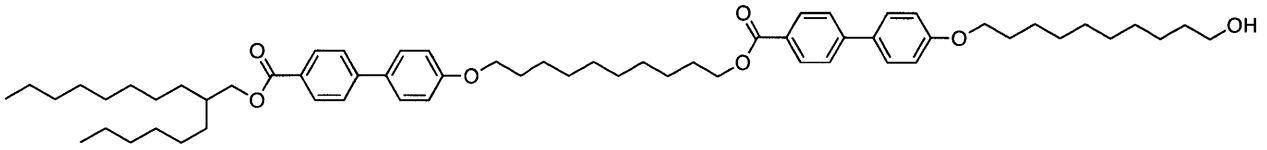

2-hexyldecyl 4'-((10-((4'-((10-hydroxydecyl)oxy)-[1,1'-biphenyl]-4-carbonyl)oxy)decyl)oxy)-[1,1'-biphenyl]-4-carboxylate (11). Compound **10** (3.6 g, 3.4 mmol) was dissolved in 10 ml dry THF under an argon atmosphere, and 7.13 ml of a 1M solution of TBAF (THF) was added. After

stirring at room temperature for 12 h, the solvent was removed and the remaining crude residue was dissolved in a mixture of DCM and a saturated solution of ammonium chloride (aq.). The mixture was extracted with DCM, and the combined organic phases were washed with water and brine. After drying over magnesium sulfate and removing the solvent *in vacuo*, the residue was purified by column chromatography using $CHCl_3$ as the eluent to obtain compound **9** as a white solid (2.7 g, 87%). ^{1}H-NMR (ppm, $CDCl_3$): 0.83-0.89 (6H, m), 1.20 – 1.77 (57H, m), 3.63 (2H, t, J= 6.9 Hz), 3.98 (4H, m), 4.22 (2H, d, J=5.7 Hz), 4.31 (2H, t, J=6.9 Hz), 6.96 (4H, d, J=8.55 Hz), 7.53 (4H, d, J=8.55 Hz), 7.60 (4H, d, J=8.55 Hz), 8.05 (4H, d, J=8.55 Hz). ^{13}C-NMR (ppm, $CDCl_3$) 14.3, 22.9, 22.9, 25.9, 26.0, 26.3, 27.0, 27.0, 29.0, 29.5, 29.6, 29.6, 29.6, 29.7, 29.7, 29.7, 29.8, 29.8, 29.9, 30.2, 31.7, 32.0, 32.1, 33.0, 37.7, 63.3, 65.3, 67.9, 68.4, 115.2, 126.6, 126.7, 128.5, 128.8, 130.3, 132.5, 145.4, 159.7, 166.5, 167.0. MALDI-TOF (m/z) found: 947.68 [M+H], calculated: 947.67.

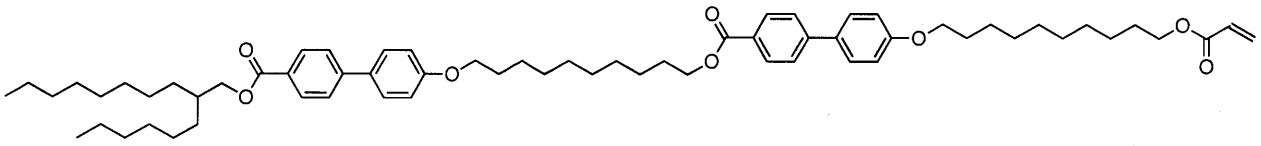

Monomer 2. Compound **11** (500 mg, 0.53 mmol) was dissolved in 20 ml DCM and cooled down to 0 °C. Triethylamine (0.33 ml, 2.4 mmol) was added in one fraction, after which acrylic acid chloride (0.19 ml, 2.4 mmol) dissolved in 10 ml of DCM was added dropwise over a period of 30 minutes *via* an addition funnel. After the addition was complete, the mixture was warmed to room temperature, and stirred for 20 h. The solvent was removed and the remaining crude residue was dissolved in a mixture of DCM and a saturated solution of ammonium chloride (aq.). The mixture was extracted with DCM, and the combined organic phases were washed with water and brine. After drying over magnesium sulfate and removing the solvent *in vacuo*, the residue

was purified by column chromatography using $CHCl_3$ as the eluent to obtain monomer **2** as white solid (397 mg, 75%). ^{1}H-NMR (ppm, $CDCl_3$): 0.83-0.89 (6H, m), 1.20 – 1.77 (56H, m), 3.97 (4H, m), 4.13 (2H, t, J= 6.9 Hz), 4.22 (2H, d, J=5.7 Hz), 4.31 (2H, t, J=5.7 Hz), 5.79 (1H, dd, J=1.75, 10.9 Hz), 6.11 (1H, dd, J=10.9, 17.75 Hz), 6.37 (1H, dd, J=1.75, 17.75 Hz), 6.96 (4H, d, J=8.55 Hz), 7.53 (4H, d, J=8.55 Hz), 7.60 (4H, d, J=8.55 Hz), 8.05 (4H, d, J=8.55 Hz). ^{13}C-NMR (ppm, $CDCl_3$) 14.3, 22.9, 22.9, 26.1, 26.3, 27.0, 28.8, 29.5, 29.5, 29.5, 29.6, 29.7, 29.7, 29.7, 29.8, 29.9, 30.2, 31.7, 32.0, 32.1, 37.7, 64.9, 66.0, 67.9, 68.4, 115.2, 126.6, 126.7, 128.5, 128.9, 130.3, 130.6, 132.0, 138.1, 145.4, 159.6, 166.2, 167.0. MALDI-TOF (m/z) found: 1001.68 [M+H], calculated: 1001.68.

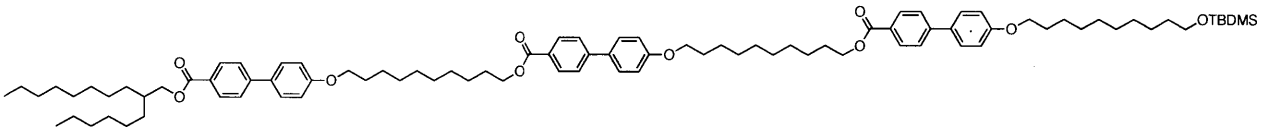

2-hexyldecyl 4'-((10-((4'-((10-((4'-((10-((tert-butyldimethylsilyl)oxy)decyl)oxy)- [1,1'-biphenyl]-4-carbonyl)oxy)decyl)oxy)- [1,1'-biphenyl]-4-carbonyl)oxy)decyl)oxy)- [1,1'-biphenyl]-4-carboxylate (12). Compound **7** (870 g, 1.8 mmol) was dispersed in 12 ml DCM. DPTS (112 mg), and DIPC (0.37 ml, 2.4 mmol) were added. After stirring at room temperature for 35 min, the reaction mixture became a homogeneous solution, to which compound 11 (1.7 g, 1.8 mmol) was added. After stirring at room temperature for 14 h, the reaction mixture was poured over water, DCM and extracted with DCM. The combined organics were washed with water, brine, dried over magnesium sulfate and the solvent was removed *in vacuo*. The residue was purified by column chromatography using $CHCl_3$ as the eluent to obtain compound **12** as a white solid (1.65 g, 65%). ^{1}H-NMR (ppm, $CDCl_3$): 0.02 (6H, s), 0.83-0.89 (15H, m), 1.20 – 1.53 (63H, m), 1.72 – 1.82 (10H, m) 3.58 (2H, t, J=6.3 Hz), 3.97 (6H, m), 4.22 (2H, d, J=5.7 Hz),

4.31 (4H, t, J=5.7 Hz), 6.96 (6H, d, J=8.55 Hz), 7.53 (6H, d, J=8.55 Hz), 7.60 (6H, d, J=8.55 Hz), 8.05 (6H, d, J=8.55 Hz). ^{13}C-NMR (ppm, $CDCl_3$) -5.0, 14.3, 18.6, 22.9, 22.9, 26.0, 26.2, 26.3, 27.0, 29.0, 29.5, 29.5, 29.5, 29.6, 29.6, 29.7, 29.7, 29.7, 29.8, 29.9, 30.2, 31.7, 32.0, 33.1, 37.7, 63.5, 65.3, 67.9, 68.4, 115.2, 126.6, 126.7, 128.5, 128.8, 130.3, 132.4, 145.4, 159.6, 166.9, 167.0. MALDI-TOF (m/z) found: 1413.96 [M+H], calculated: 1413.96.

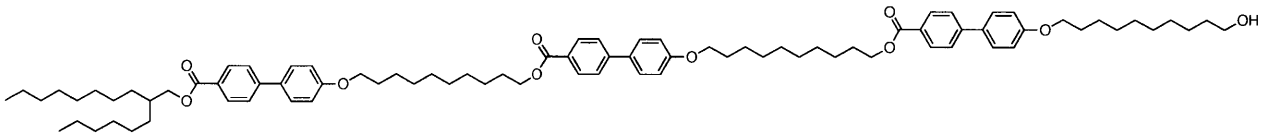

2-hexyldecyl 4'-((10-((4'-((10-((4'-((10-hydroxydecyl)oxy)-[1,1'-biphenyl]-4-carbonyl)oxy)decyl)oxy)-[1,1'-biphenyl]-4-carbonyl)oxy)decyl)oxy)-[1,1'-biphenyl]-4-carboxylate (13). Compound **12** (2.2 g, 1.6 mmol) was dissolved in 6 ml dry THF under an argon atmosphere, and 3.27 ml of a 1M solution of TBAF (THF) was added. After stirring at room temperature for 14 h, the solvent was removed and the remaining crude residue was dissolved in a mixture of DCM and a saturated solution of ammonium chloride (aq.). The mixture was extracted with DCM, and the combined organic phases were washed with water and brine. After drying over magnesium sulfate and removing the solvent *in vacuo*, the residue was purified by column chromatography using $CHCl_3$ as the eluent to obtain compound **13** as a white solid (2.0 g, 99%). ^{1}H-NMR (ppm, $CDCl_3$): 0.83-0.89 (6H, m), 1.25 – 1.53 (64H, m), 1.72 – 1.82 (10H, m), 3.62 (2H, t, J=6.3 Hz), 3.97 (6H, m), 4.22 (2H, d, J=5.7 Hz), 4.31 (4H, t, J=5.7 Hz), 6.96 (6H, d, J=8.55 Hz), 7.53 (6H, d, J=8.55 Hz), 7.60 (6H, d, J=8.55 Hz), 8.05 (6H, d, J=8.55 Hz). ^{13}C-NMR (ppm, $CDCl_3$) 14.3, 22.9, 22.9, 25.9, 26.3, 27.0, 27.0, 29.0, 29.5, 29.5, 29.5, 29.6, 29.7, 29.7, 29.7, 29.8, 29.8, 29.9, 30.2, 31.7, 32.0, 32.1, 33.0, 37.7, 63.3, 65.3, 67.9, 68.3, 115.2,

126.6, 126.6, 128.5, 128.8, 130.3, 132.4, 145.4, 159.6, 166.9, 167.0. MALDI-TOF (m/z) found: 1321.80 [M+Na], calculated: 1321.86.

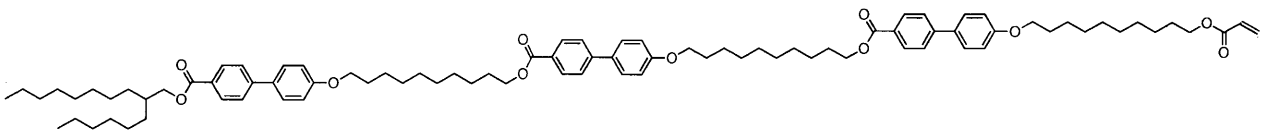

Monomer 3. Compound **13** (1 g, 0.77 mmol) was dissolved in 30 ml DCM and cooled down to 0 °C. Triethylamine (0.64 ml, 4.6 mmol) was added in one fraction, after which acrylic acid chloride (0.38 ml, 4.6 mmol) dissolved in 10 ml of DCM was added dropwise over a period of 30 minutes *via* an addition funnel. After the addition was complete, the mixture was warmed up to room temperature, and stirred for 14 h. The solvent was removed and the remaining crude residue was dissolved in a mixture of DCM and a saturated solution of ammonium chloride (aq.). The mixture was extracted with DCM, and the combined organic phases were washed with water and brine. After drying over magnesium sulfate and removing the solvent *in vacuo*, the residue was purified by column chromatography using $CHCl_3$ as the eluent to obtain monomer **3** as white solid (698 mg, 67%). ^{1}H-NMR (ppm, $CDCl_3$): 0.81-0.85 (6H, m), 1.25 – 1.53 (63H, m), 1.74 – 1.78 (10H, m), 3.94 (6H, m), 4.10 (2H, t, J=6.8 Hz), 4.19 (2H, d, J=5.7 Hz), 4.28 (4H, t, J=5.7 Hz), 5.75 (1H, dd, J=1.75, 10.9 Hz), 6.07 (1H, dd, J=10.9, 17.75 Hz), 6.34 (1H, dd, J=1.75, 17.75 Hz), 6.92 (6H, d, J=8.55 Hz), 7.53 (6H, d, J=8.55 Hz), 7.60 (6H, d, J=8.55 Hz), 8.05 (6H, d, J=8.55 Hz). ^{13}C-NMR (ppm, $CDCl_3$) 14.3, 22.9, 22.9, 26.1, 26.3, 27.0, 27.0, 28.9, 29.0, 29.5, 29.5, 29.5, 29.6, 29.7, 29.7, 29.8, 29.9, 31.7, 32.0, 32.1, 37.7, 64.9, 65.3, 67.9, 68.4, 115.2, 126.3, 126.6, 128.5, 128.9, 130.3, 130.6, 132.0, 138.1, 145.4, 159.6, 166.9, 166.9. MALDI-TOF (m/z) found: 1375.82 [M+Na], calculated: 1375.87.

Polymerization conditions. In a standard polymerization, the monomer was placed in a previously flame-dried and argon purged Schlenk flask. A stock solution of recrystallized AIBN in anhydrous benzene was degassed by freeze-pump-thaw cycles of 30 minutes (five times). The desired amount of this stock solution was transferred into the reaction flask via syringe, and the mixture was warmed to 70°C and stirred at this temperature. The reaction mixture was then poured into MeOH and the polymer precipitate formed was collected by filtration and reprecipitated twice from MeOH.

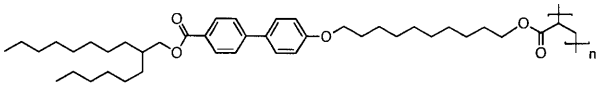

Polymer 1. ^{1}H-NMR (ppm, $CDCl_3$): 0.81-0.89 (6H, bm), 1.19 – 1.49 (39H, bm), 1.61 – 1.82 (4H, bm), 3.47 (1H, b), 3.72 (2H, b), 3.80-3.90 (2H, bm), 4.17 (2H, b), 6.86 (2H, b), 7.47-7.51 (4H, bm), 7.99 (2H, b).

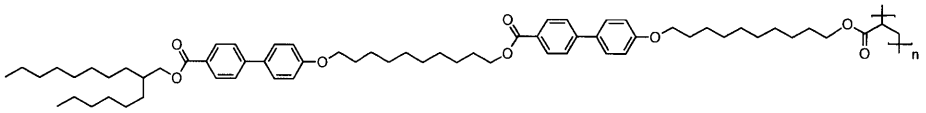

Polymer 2. ^{1}H-NMR (ppm, $CDCl_3$): 0.86 (6H, b), 1.20 – 1.77 (58H, m), 3.97 (5H, m), 4.13 (2H, b), 4.22 (2H, b), 4.31 (2H, b), 6.96 (4H, b), 7.53 (4H, b), 7.60 (4H, b), 8.03 (4H, b).

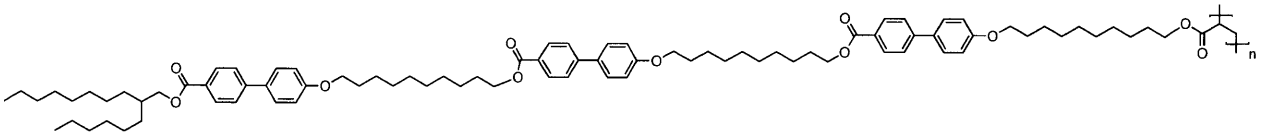

Polymer 3. ^{1}H-NMR (ppm, $CDCl_3$): 0.86 (6H, b), 1.25 – 1.53 (65H, bm), 1.74 – 1.78 (10H, bm), 3.94 (7H, bm), 4.10-4.20 (4H, b), 4.28 (4H, b), 6.94 (6H, b), 7.51-7.59 (12H, b), 8.03 (6H, b).

5.8 References and Notes

(1) Whitesides, G. M.; Grzybowski, B. *Science* **2002**, *295*, 2418-2421.

(2) (a) Anfinsen, C. B. *Science* **1973**, *181*, 223-230. (b) Luque, I.; Leavitt, S. A.; Freire, E. *Annu. Rev. Biophys. Biomol. Struct.* **2002**, *31*, 235-256.

(3) (a) Charvet, R.; Yamamoto, Y.; Sasaki, T.; Kim, J.; Kato, K.; Takata, M.; Saeki, A.; Seki, S.; Aida, T. *J. Am. Chem. Soc.* **2012**. (b) Günes, S.; Neugebauer, H.; Sariciftci, N. S. *Chem. Rev.* **2007**, *107*, 1324-1338. (c) Thompson, B. C.; Fréchet, J. M. J. *Angew. Chem. Int. Ed.* **2008**, *47*, 58-77. (d) Pisula, W.; Kastler, M.; Wasserfallen, D.; Robertson, J. W. F.; Nolde, F.; Kohl, C.; Müllen, K. *Angew. Chem., Int. Ed.* **2006**, *45*, 819-823. (e) Wei, Z.; Jin, W.; Fukushima, T.; Saeki, A.; Seki, S.; Aida, T. *Science* **2011**, 334, 340-343.

(4) Reinitzer, F. *Monatshefte für Chemie* **1888,** *9*, 421-441.

(5) (a) Vorländer, D. *Z. Phys Chem.* **1923**, *105*, 211-254. (b) Bruce, D. W.; Heyns, K.; Vill, V. C. R. *Acad. Sci. Paris* **1975**, 281, 101-103.

(6) (a) Finkelmann, H.; Happ, M.; Portugall, M.; Ringsdorf, H. *Makromol. Chem.* **1978**, *179*, 2541-2544. (b) Dubois, J. C.; LeBarny, P.; Mauzac, M.; Noel, C.; Demus, D.; Goodby, J. W.; Gray, G. W.; Spiess, H. W.; Vill, V. *Handbook of Liquid Crystals*; VCH: Weinheim, Germany, 1998; Vol. 3, p 207.

(7) (a) Anthamatten, M.; Hammond, P. T. *Macromolecules* **1999**, *32*, 8066-8076. (b) Moment, A.; Hammond, P. T. *Polymer* **2001**, *42*, 6945-6959. (c) Gabert, A. J.; Verploegen, E.; Hammond, P. T.; Schrock, R. R. *Macromolecules* **2006**, *39*, 3993–4000. (d) Singh, R.; Verploegen, E.; Hammond, P. T.; Schrock, R. R. *Macromolecules* **2006**, *39*, 8241–8249.

(8) (a) Serrette, A. G.; Carroll, P. J.; Swager, T. M. *J. Am. Chem. Soc.* **1992**, *114*, 1887-1888. (b) Zheng, H.; Carroll, P. J.; Swager, T. M. **1993**, 14, 1421-1429. (c) Zheng, H.; Xu, B.; Swager, T. M. *Chem. Mater.* **1996**, *8*, 907-911.

(9) (a) Donald, A. M.; Windle, A. H.; Hana, S. *Liquid Crystalline Polymers*; Cambridge University Press: Cambridge, 2006. (b) Long, T. M.; Swager, T. M. *Adv. Mater.* **2001**, *13*, 601-604.

(10) (a) Verploegen, E.; Boone, D., Jr.; Hammond, P. T. *J. Polym. Sci. B Polym. Phys.* **2007**, *45*, 3263-3266. (b) Verploegen, E.; Zhang, T.; Murlo, N.; Hammond, P. T. *Soft Matter* **2008**, *4*, 1279-1287. (c) Verploegen, E.; Zhang, T.; Jung, Y. S.; Ross, C.; Hammond, P. T. *Nano Lett.* **2008**, *8*, 3434-3440.

(11) (a) Petr, M.; Hammond, P. T. *Macromolecules* **2011**, *44*, 8880-8885. (b) Bléger, D.; Yu, Z.; Hecht, S. *Chem. Commun.* **2011**, *47*, 12260-12266.

(12) (a) Yu, Y.; Nakano, M.; Ikeda, T. *Nature* **2003,** *425*, 145-156. (b) Ikeda, T.; Mamiya, J.; Yu, Y. *Angew. Chem. Int. Ed.* **2007,** *46*, 506-528.

(13) Hosono, N.; Kajitani, T.; Fukushima, T.; Ito, K.; Sasaki, S.; Takata, M.; Aida, T. *Science* **2010**, *330*, 808-811.

(14) (a) Culligan, S. W.; Geng, Y.; Chen, S. H.; Klubek, K.; Vaeth, K. M.; Tang, C. W. *Adv. Mater.* **2003**, *15*, 1176-1180. (b) Leroy, J.; Levin, J.; Sergeyev, S.; Geerts, Y. *Chem. Lett.* **2006**, *35*, 166-167. (c) Nishizawa, T.; Lim, H. K.; Tajima, K.; Hashimoto, K. *J. Am. Chem. Soc.* **2009**, *131*, 2464-2465. (d) Kim, D. H.; Lee, B.-L.; Moon, H.; Kang, H. M.; Jeong, E. J.; Park, J.-I.; Han, K.-M.; Lee, S.; Yoo, B. W.; Koo, B. W.; Kim, J. Y.; Lee, W. H.; Cho, K.; Becerril, H. A.; Bao, Z. *J. Am. Chem. Soc.* **2009**, *131*, 6124-6132.

(15) Moore, J. S.; Stupp, S. I. *Macromolecules* **1990**, *23*, 65-70.

(16) (a) Finkelman, H.; Rehage G. *Adv. Polym. Sci.* **1984**, *60-61*, 97-172. (b) Percec, V.; Pugh, C. *Side Chain Liquid Crystal Polymers*; C. B. McArdle, pp. 30-105.

(17) Moore, J. S.; Stupp, S. I. *Macromolecules* **1990**, *23*, 65-70.

APPENDIX 1

NMR Spectra for Chapter 1

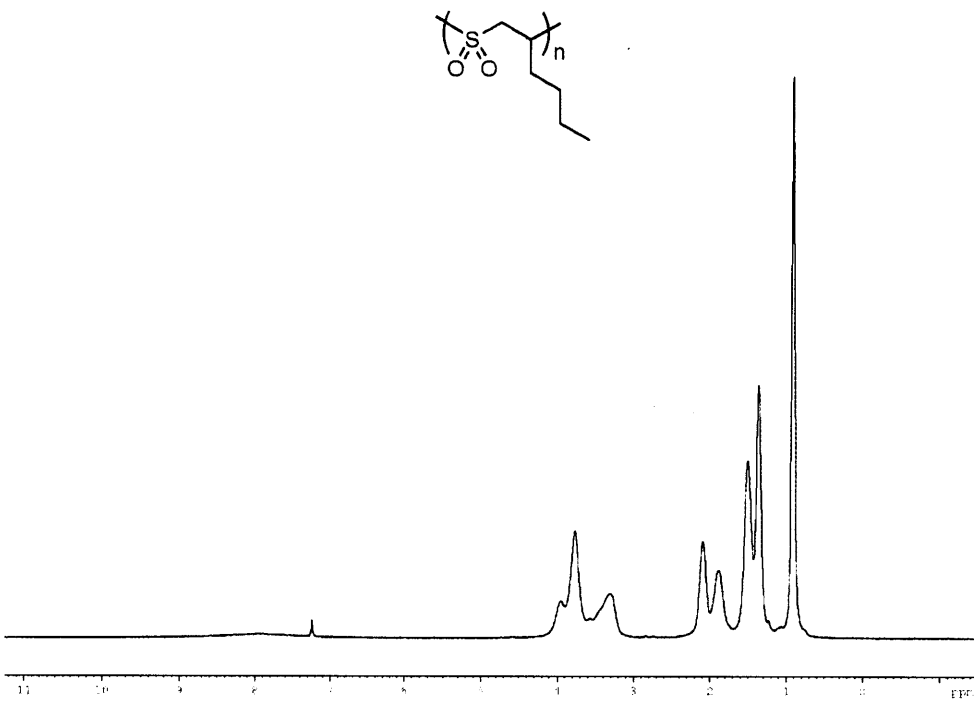

^{1}H-NMR spectrum ($CDCl_3$) of **P1HS**

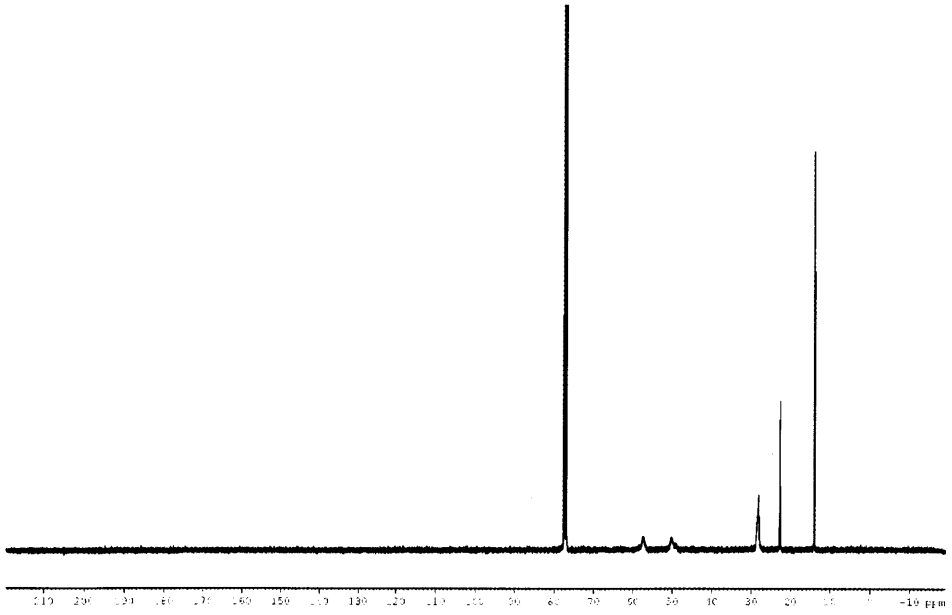

^{13}C-NMR spectrum ($CDCl_3$) of **P1HS**

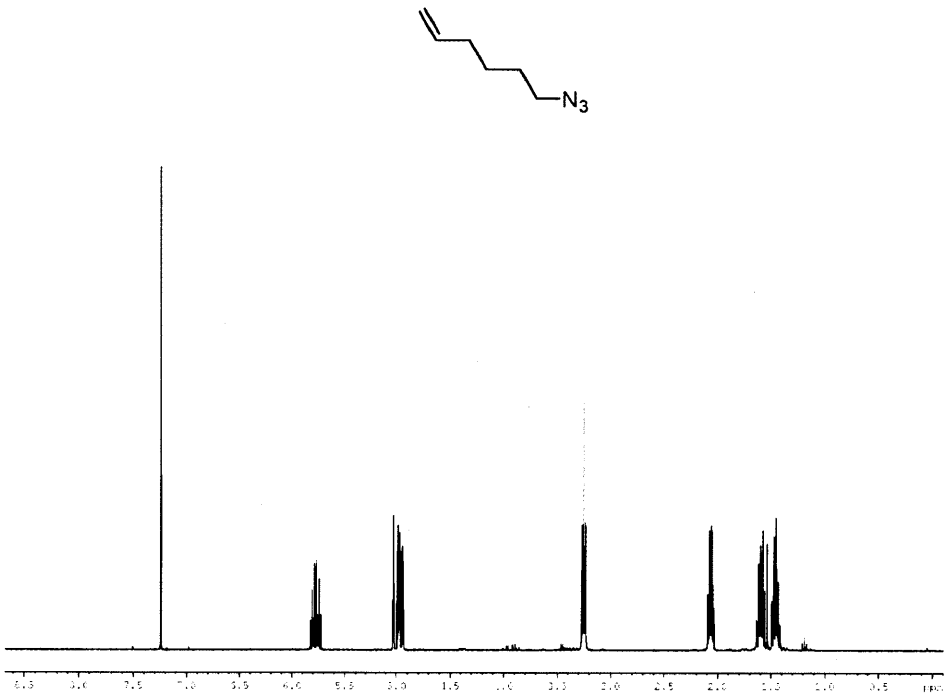

^{1}H-NMR spectrum ($CDCl_3$) of **6-azido-1-hexene**

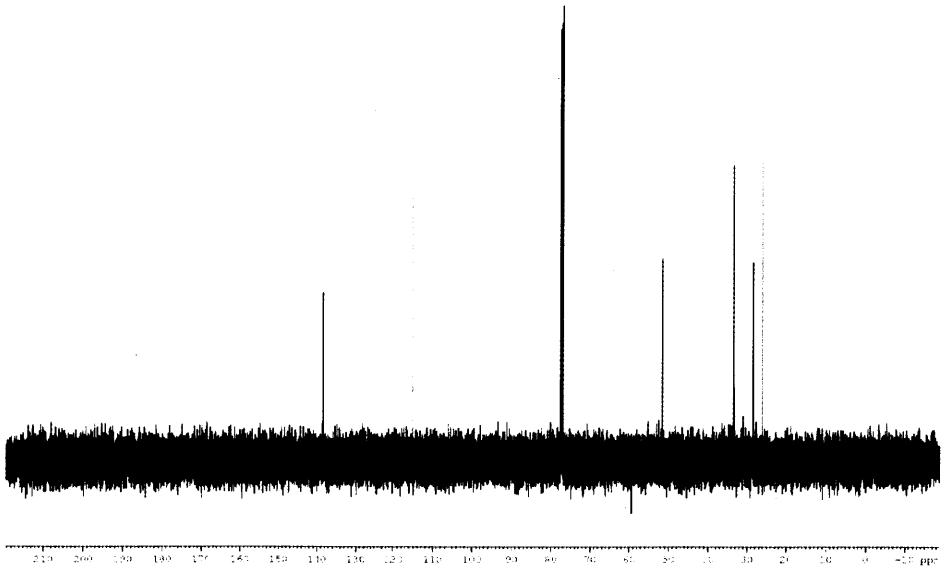

^{13}C-NMR spectrum ($CDCl_3$) of **6-azido-1-hexene**

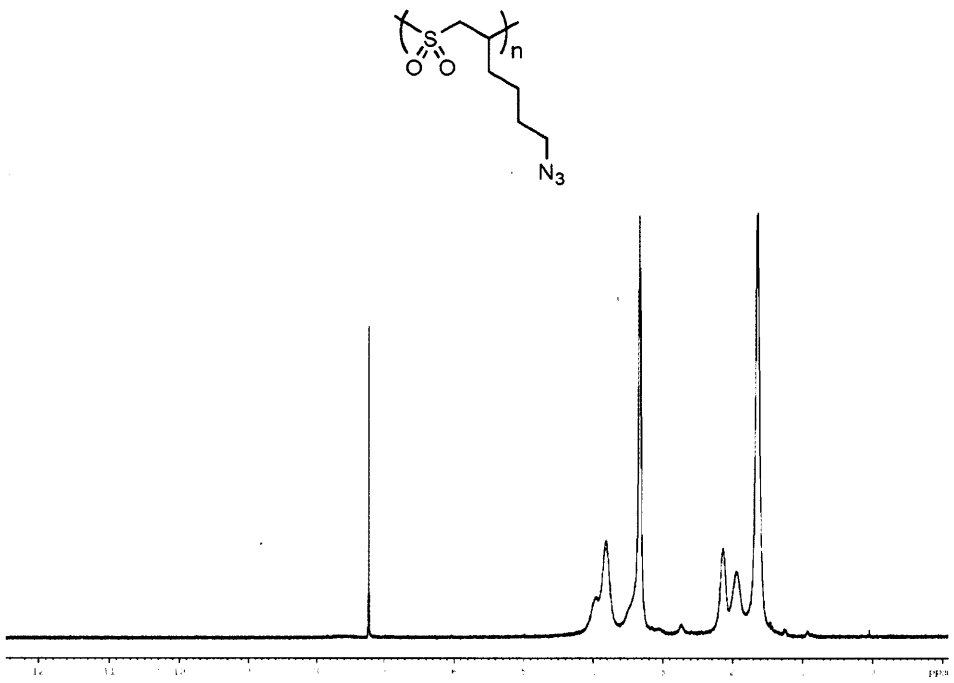

^{1}H-NMR spectrum ($CDCl_3$) of **poly (6-azido-1-hexene sulfone)**

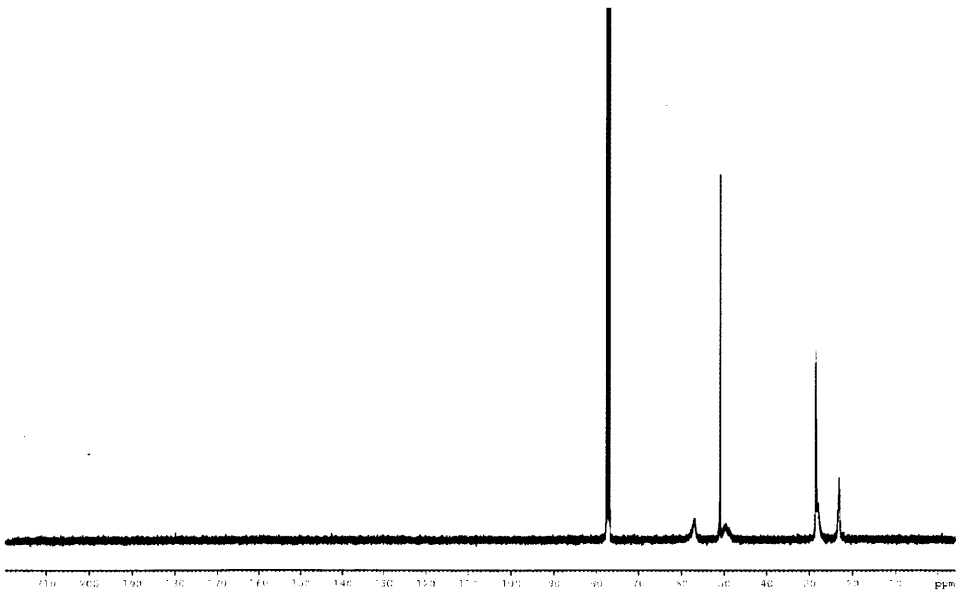

^{13}C-NMR spectrum ($CDCl_3$) of **poly (6-azido-1-hexene sulfone)**

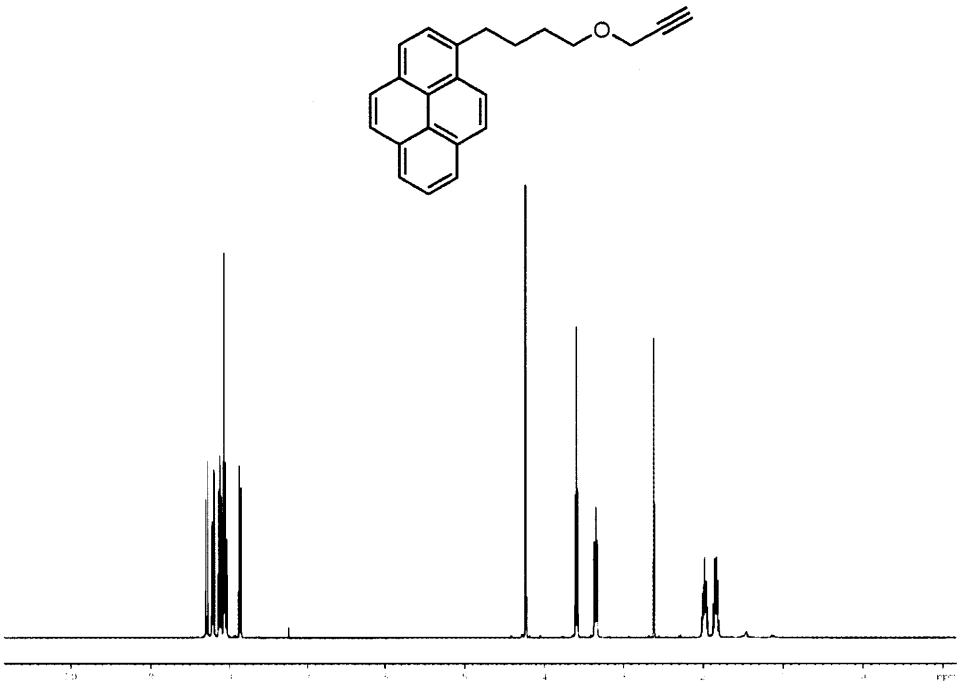

^{1}H-NMR spectrum ($CDCl_3$) of **1**

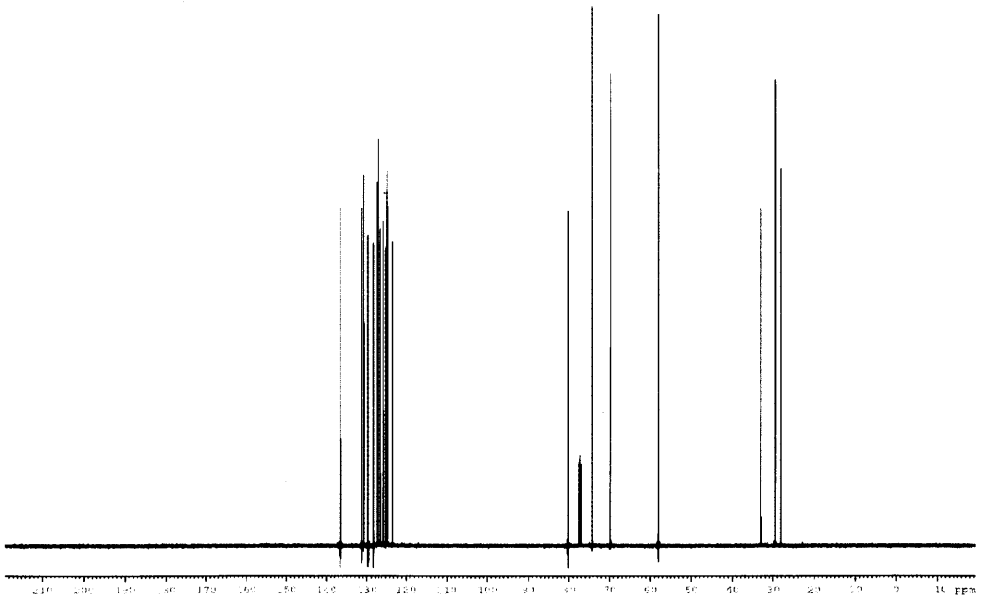

^{13}C-NMR spectrum ($CDCl_3$) of **1**

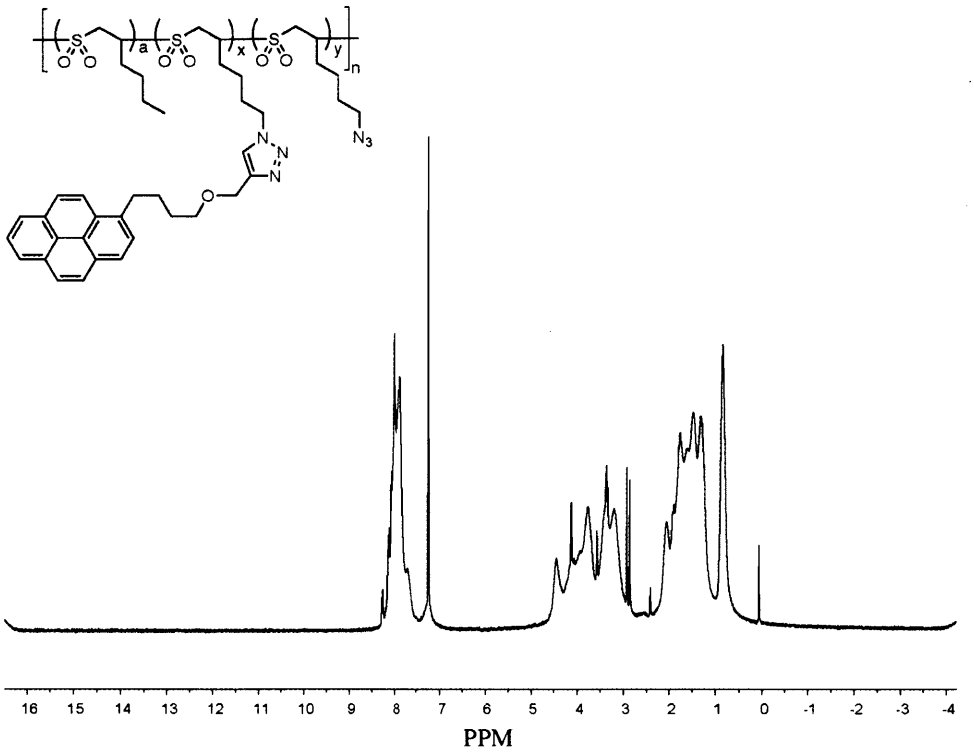

^{1}H-NMR spectrum ($CDCl_3$) of **2**

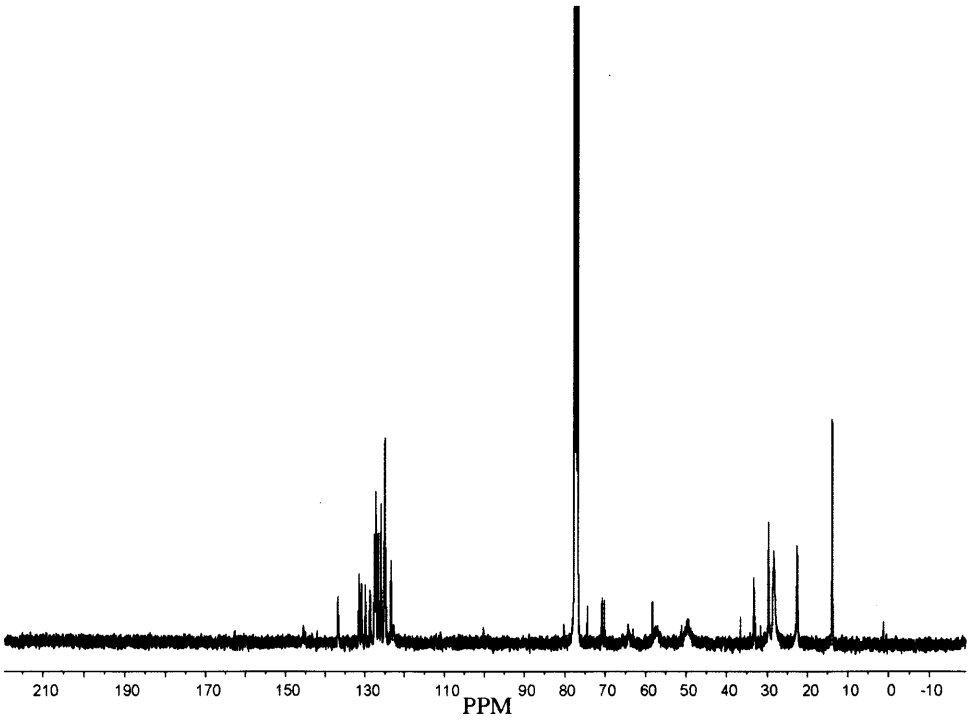

^{13}C-NMR spectrum ($CDCl_3$) of **2**

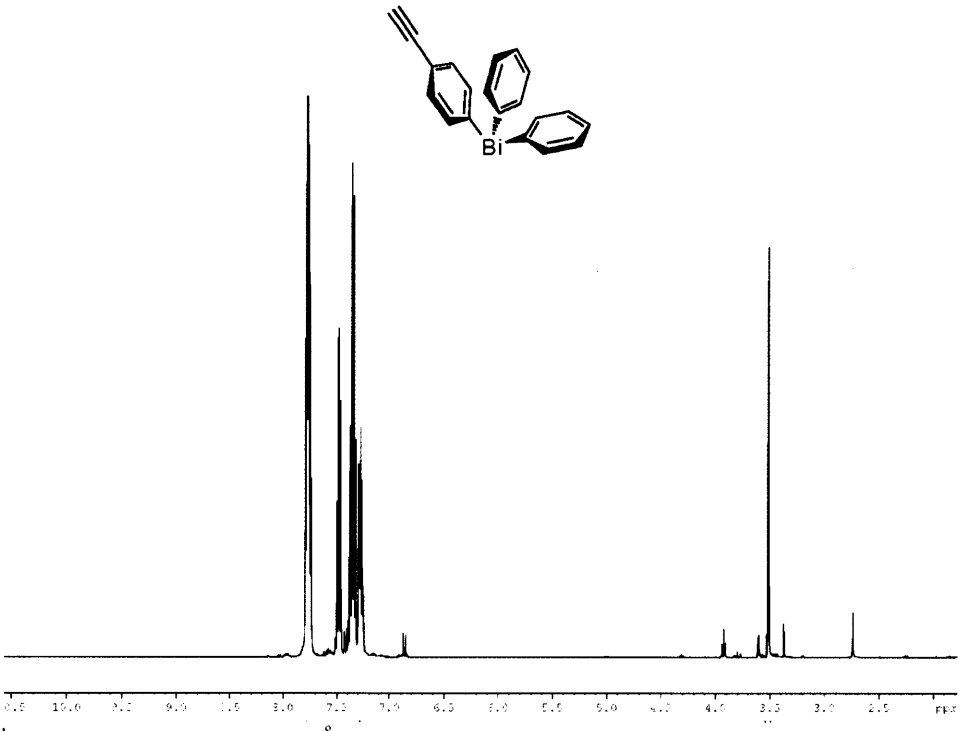

^{1}H-NMR spectrum (THF-d^{8}) of **4**

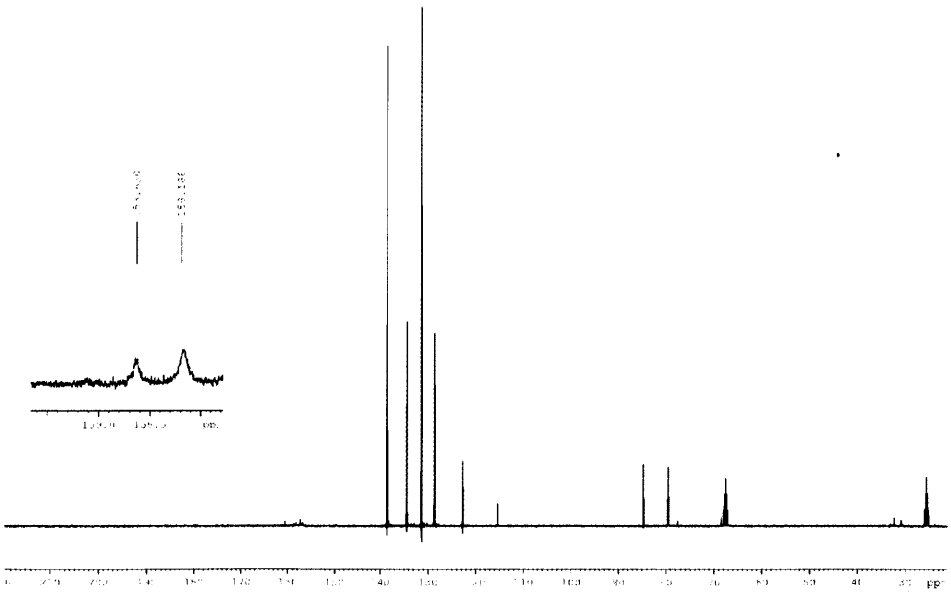

^{13}C-NMR spectrum (THF-d^{8}) of **4**

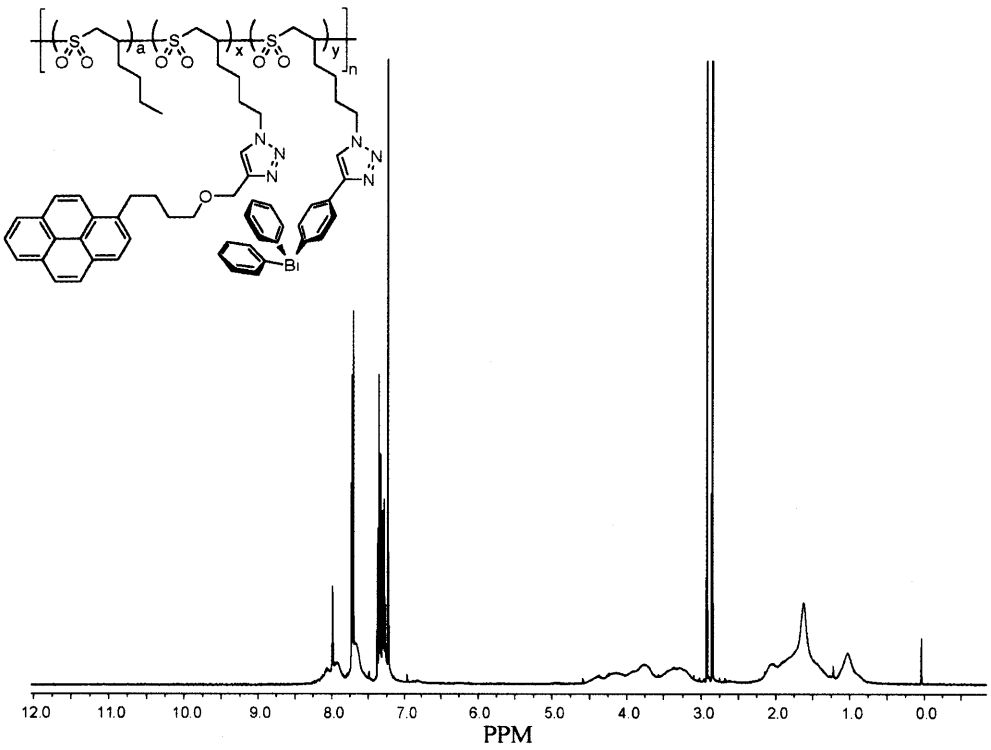

^{1}H-NMR spectrum (DMF-d^{7}) of **5**

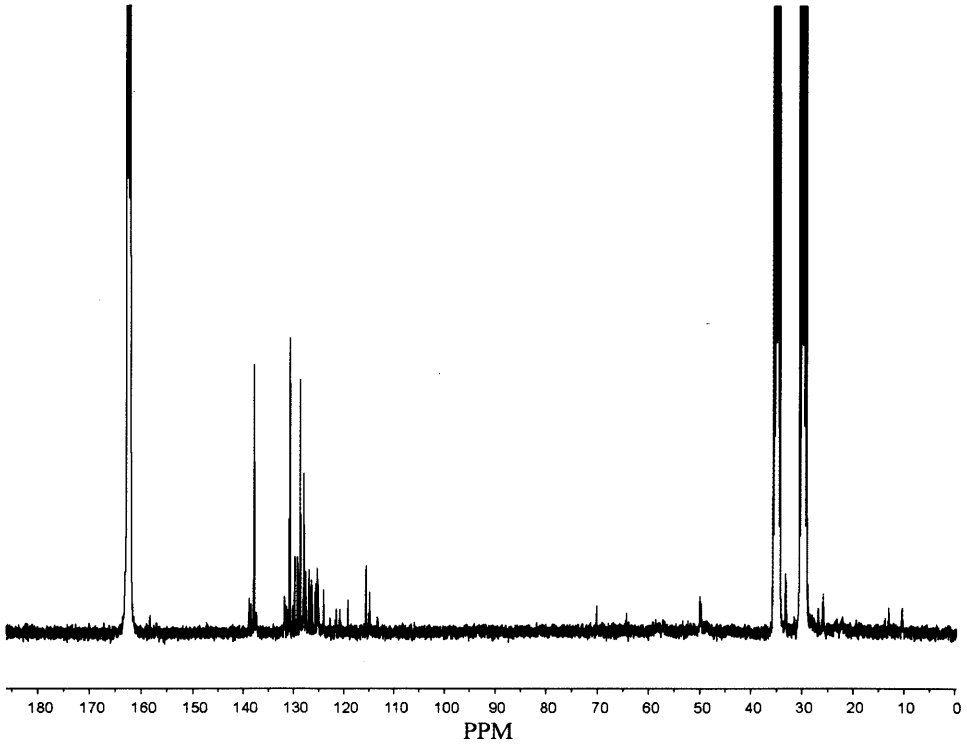

^{13}C-NMR spectrum (DMF-d^{7}) of **5**

APPENDIX 2

NMR Spectra for Chapter 2

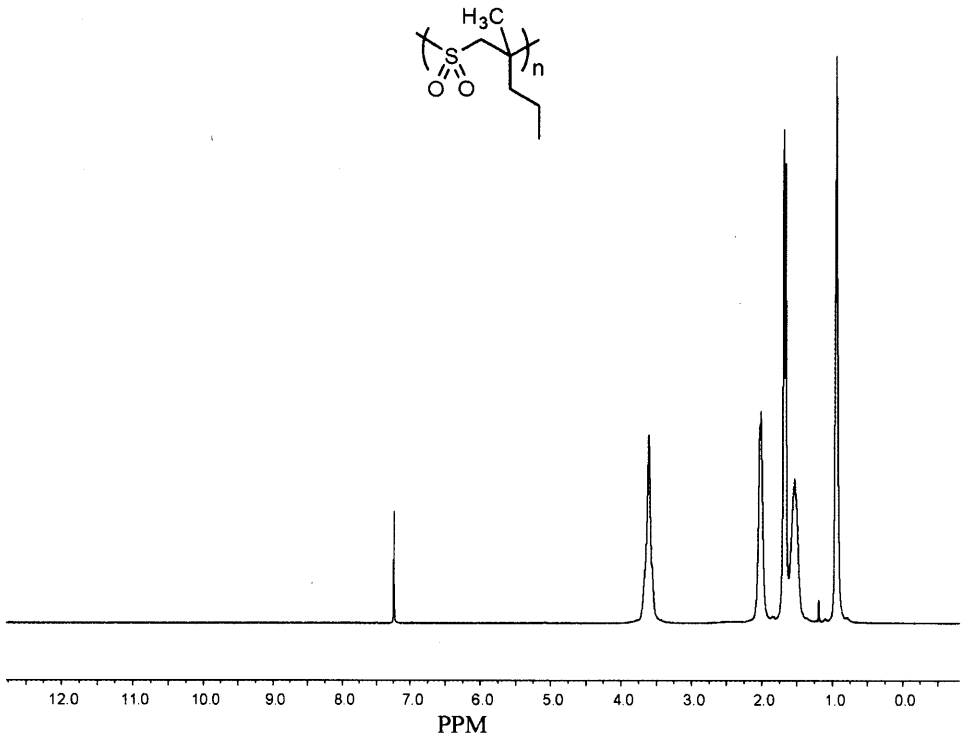

^{1}H-NMR spectrum ($CDCl_3$) of **P2MPS**

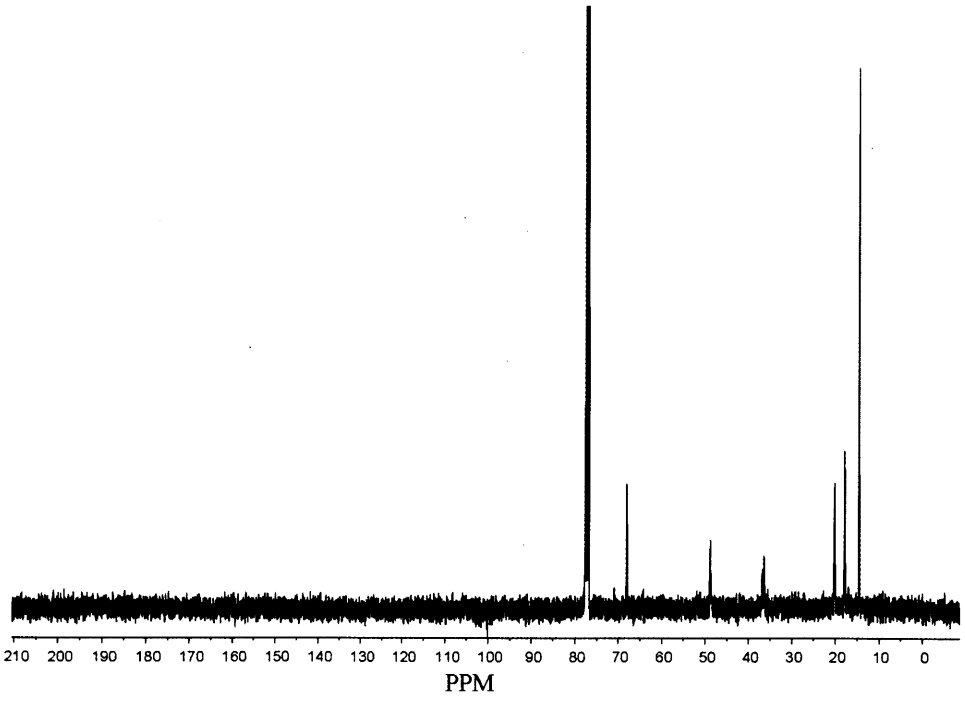

^{13}C-NMR spectrum ($CDCl_3$) of **P2MPS**

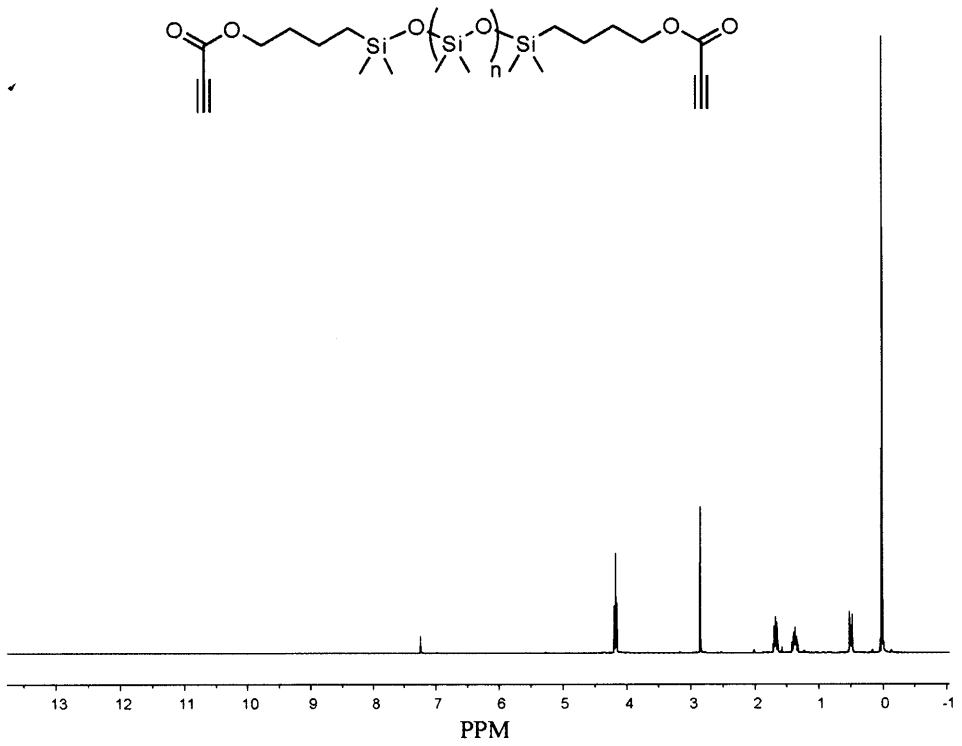

^{1}H-NMR spectrum ($CDCl_3$) of **2**

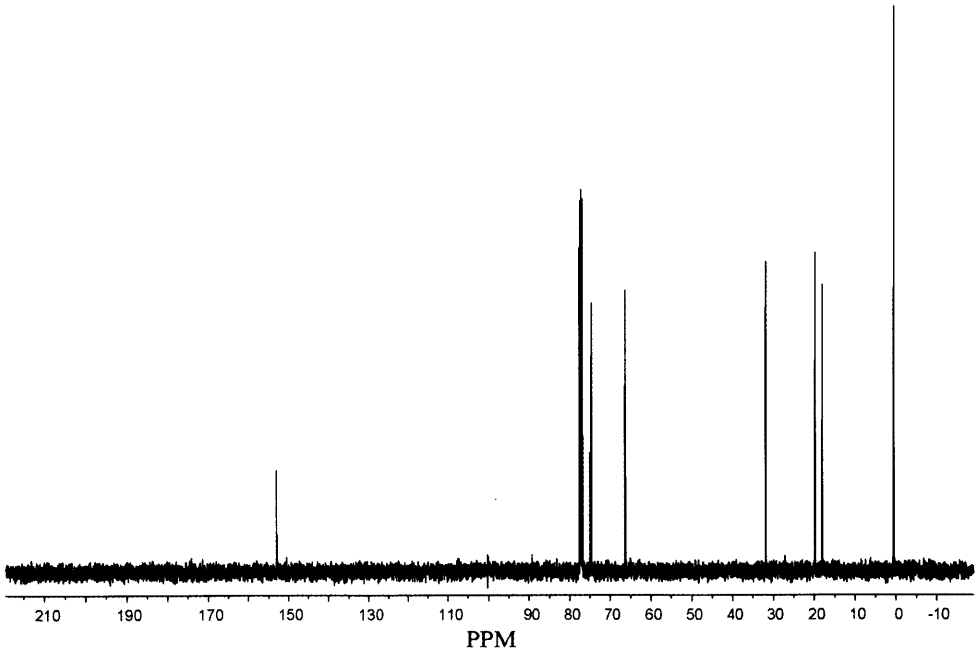

^{13}C-NMR spectrum ($CDCl_3$) of **2**

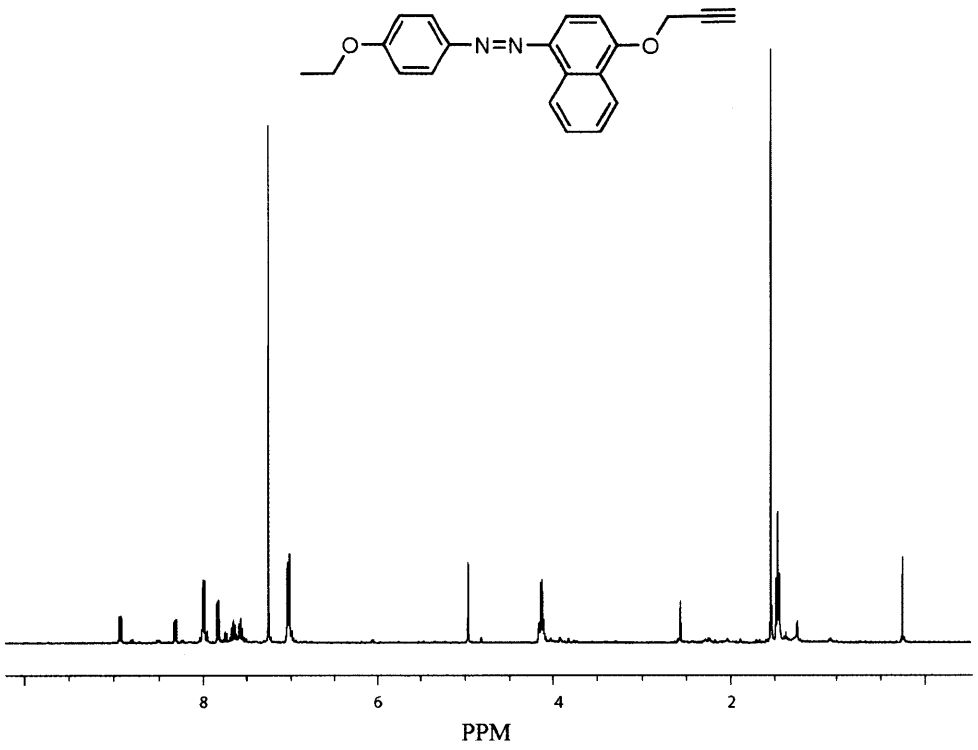

^{1}H-NMR spectrum ($CDCl_3$) of **3**

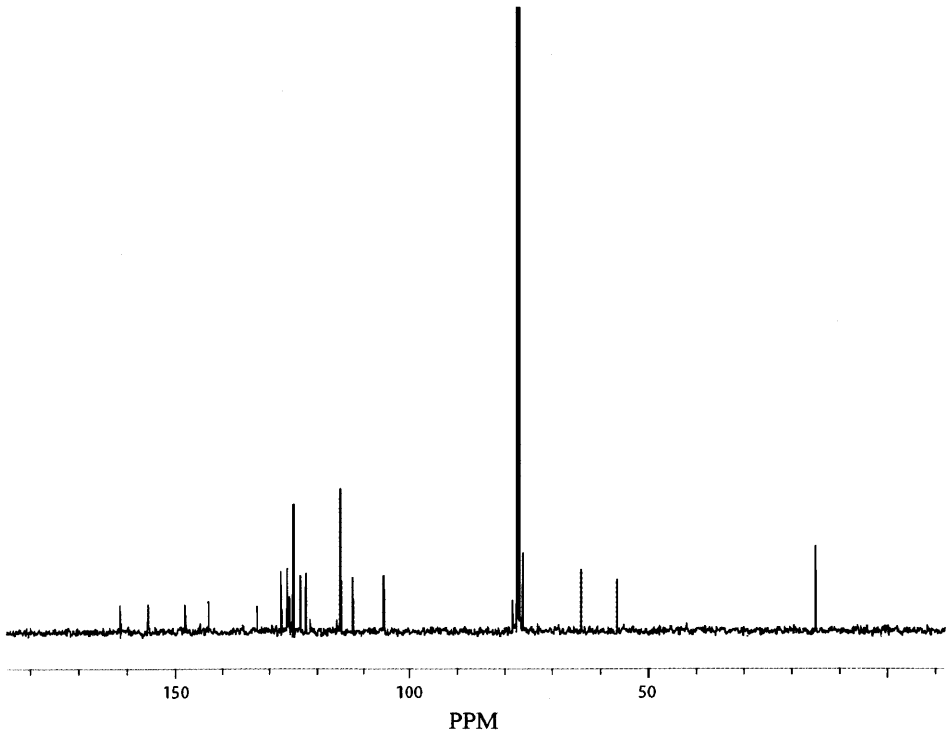

^{13}C-NMR spectrum ($CDCl_3$) of **3**

APPENDIX 3

NMR Spectra for Chapter 3

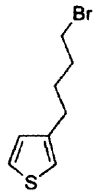

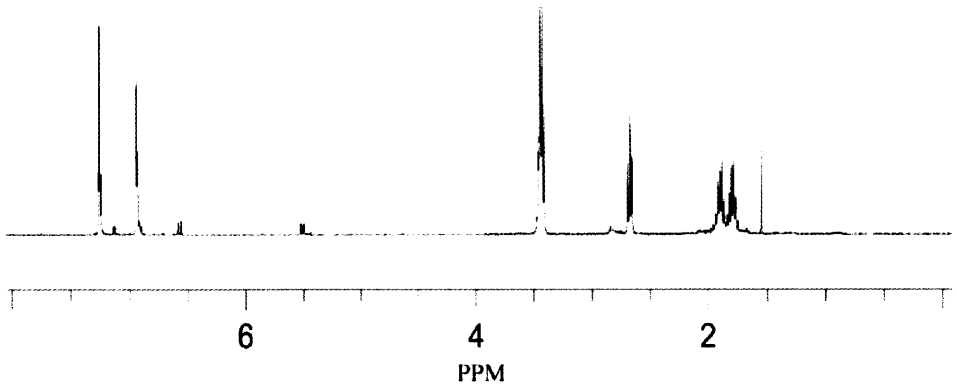

^{1}H-NMR spectrum ($CDCl_3$) of **1**

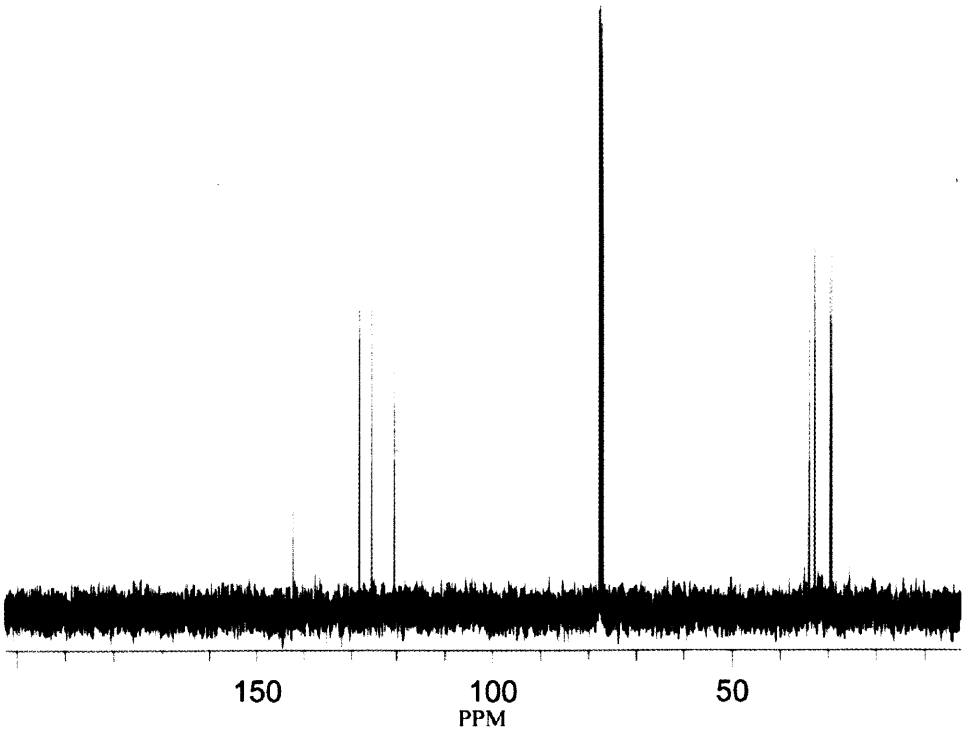

^{13}C-NMR spectrum ($CDCl_3$) of **1**

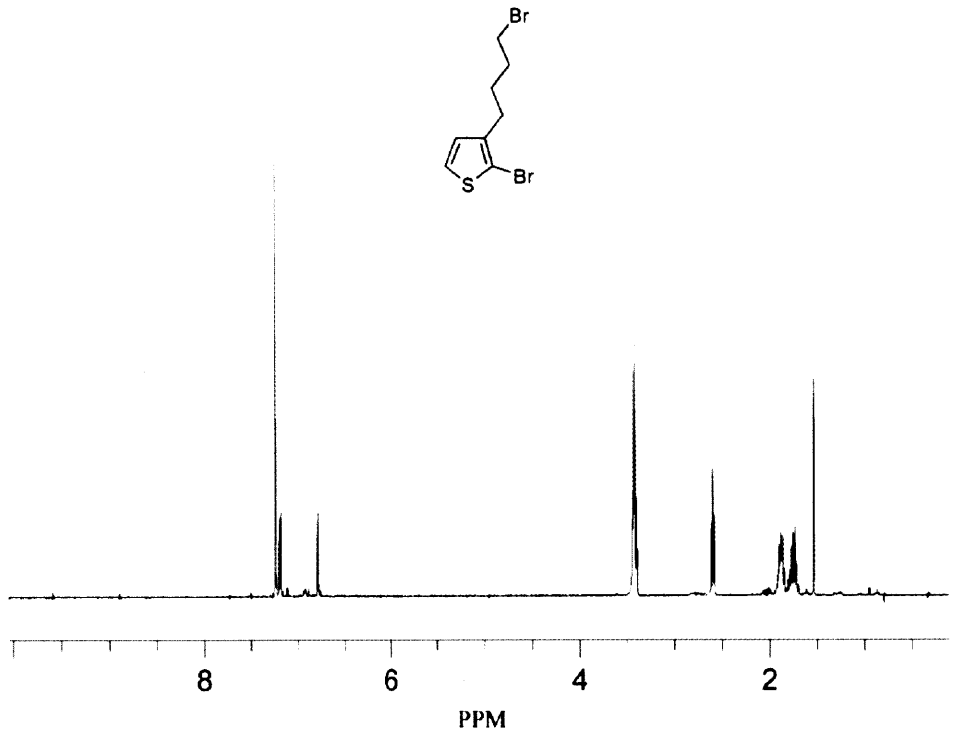

^{1}H-NMR spectrum ($CDCl_3$) of **2**

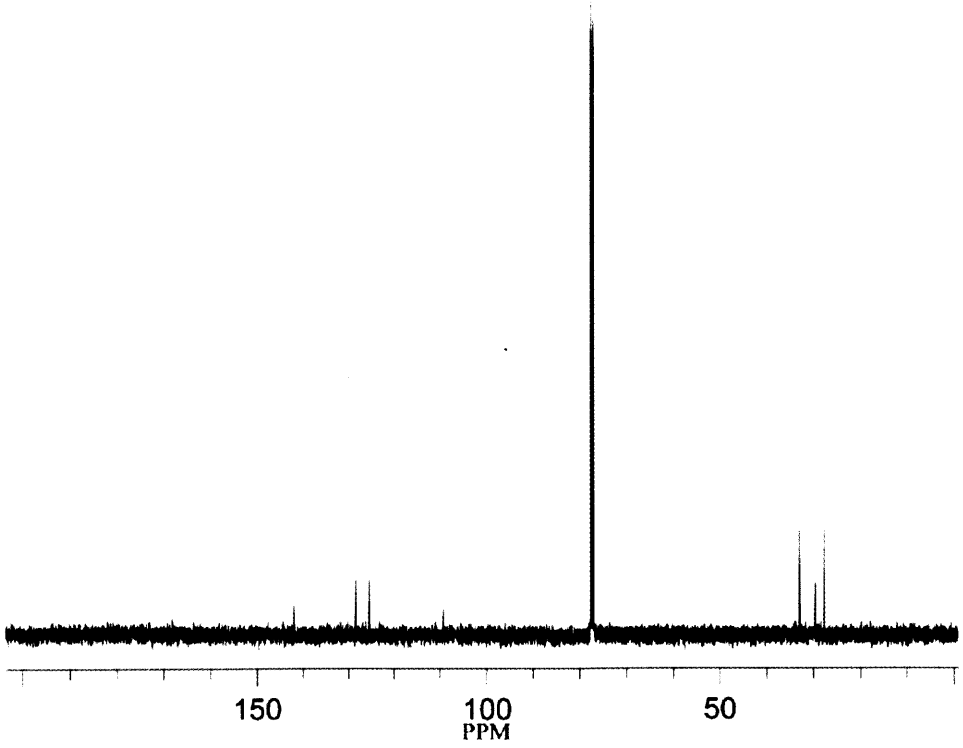

^{13}C-NMR spectrum ($CDCl_3$) of **2**

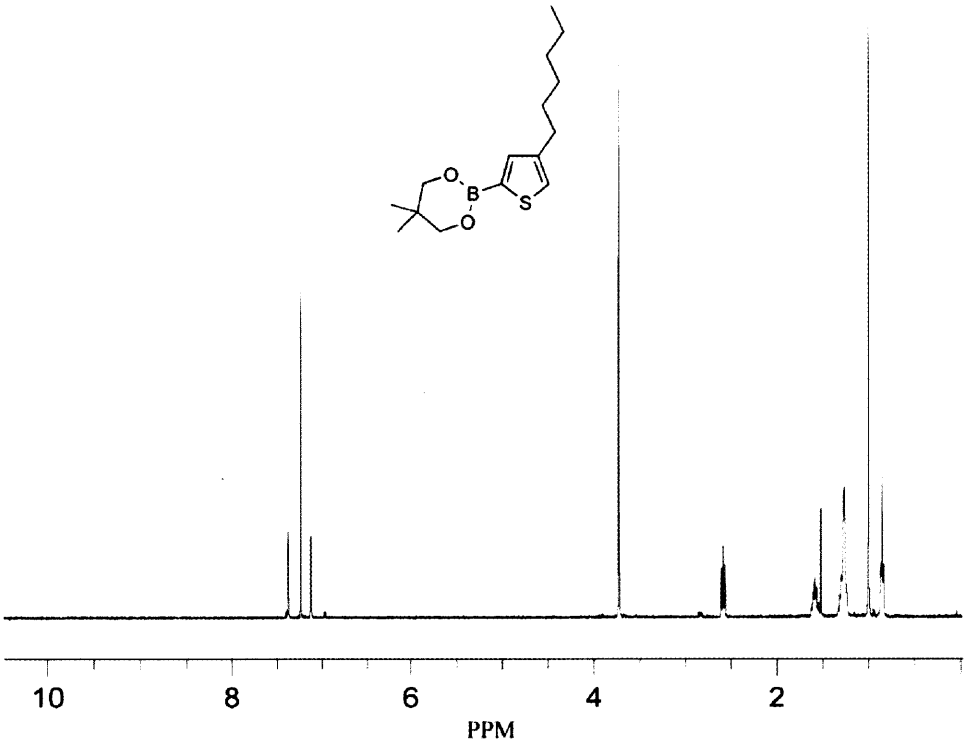

^{1}H-NMR spectrum ($CDCl_3$) of **3**

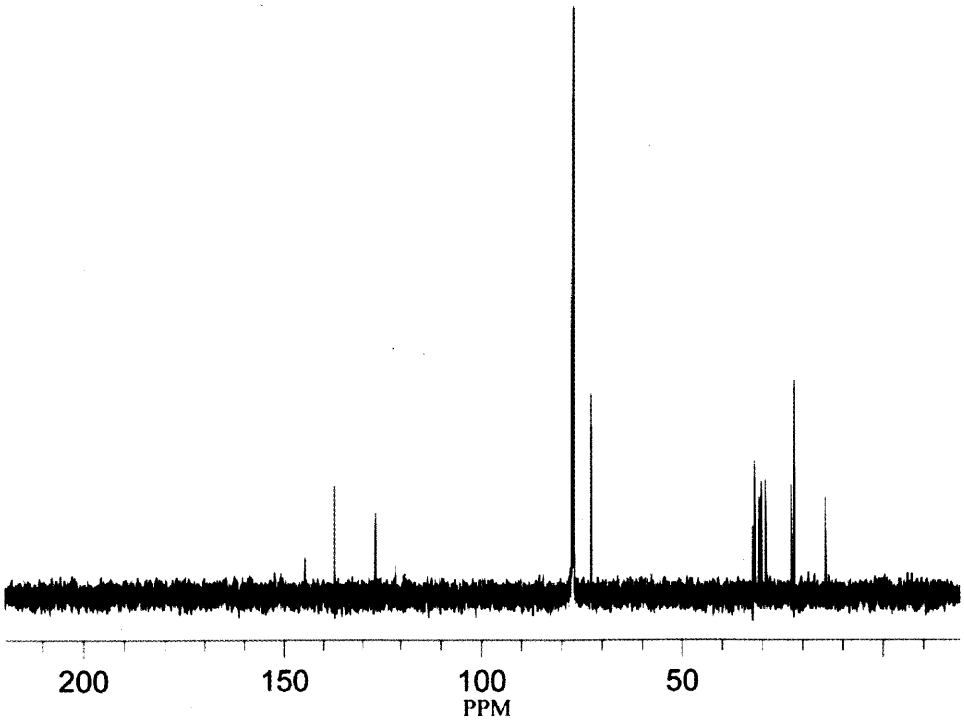

^{13}C-NMR spectrum ($CDCl_3$) of **3**

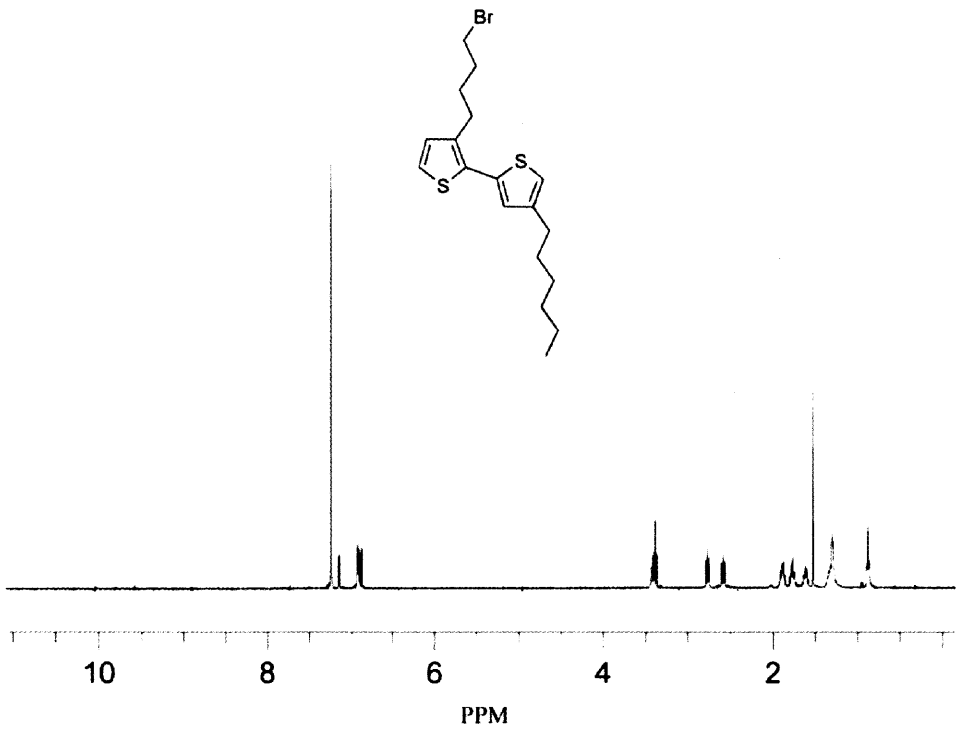

^{1}H-NMR spectrum ($CDCl_3$) of **4**

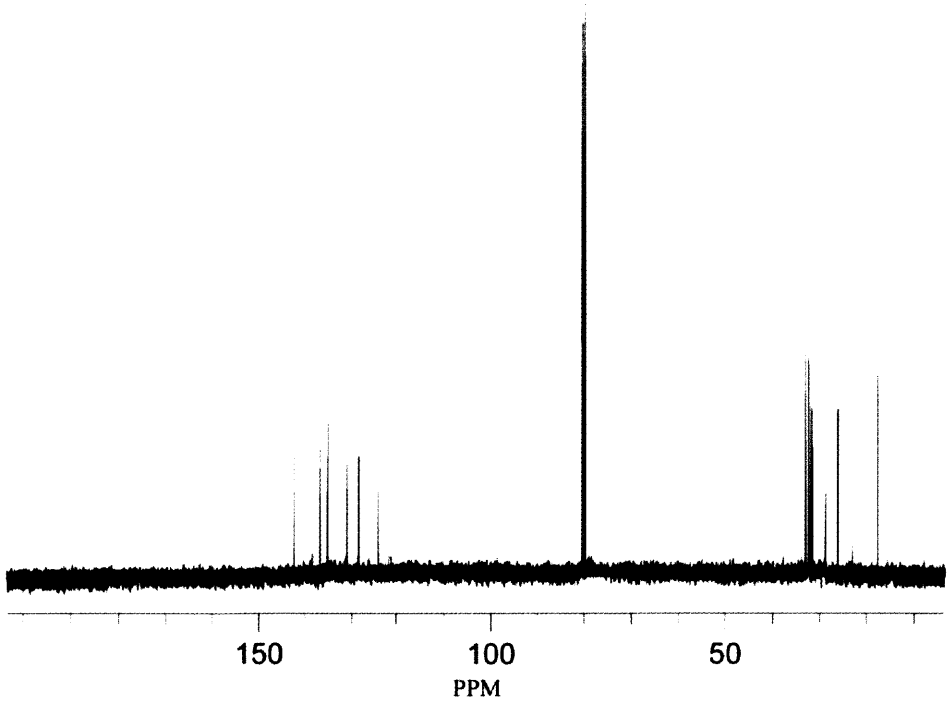

^{13}C-NMR spectrum ($CDCl_3$) of **4**

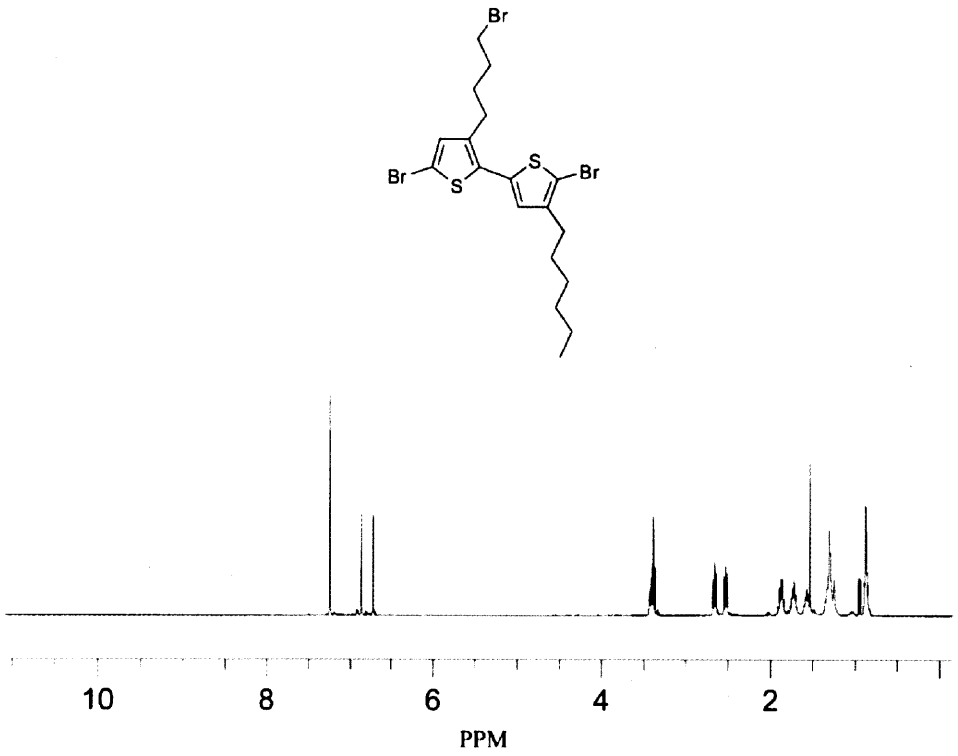

^{1}H-NMR spectrum ($CDCl_3$) of **M0**

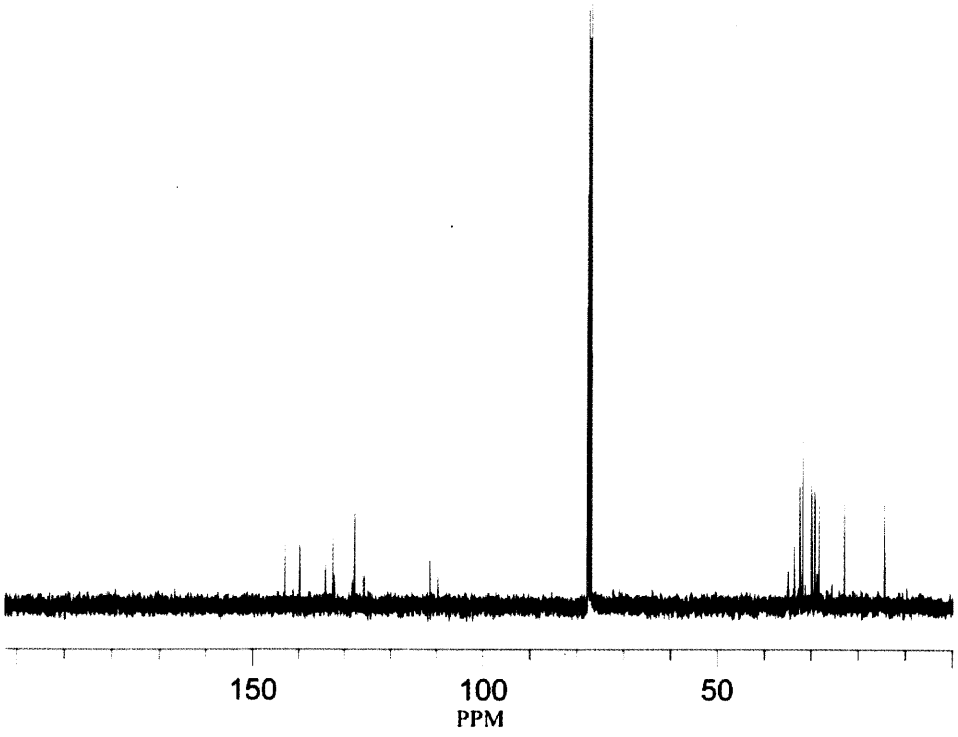

^{13}C-NMR spectrum ($CDCl_3$) of **M0**

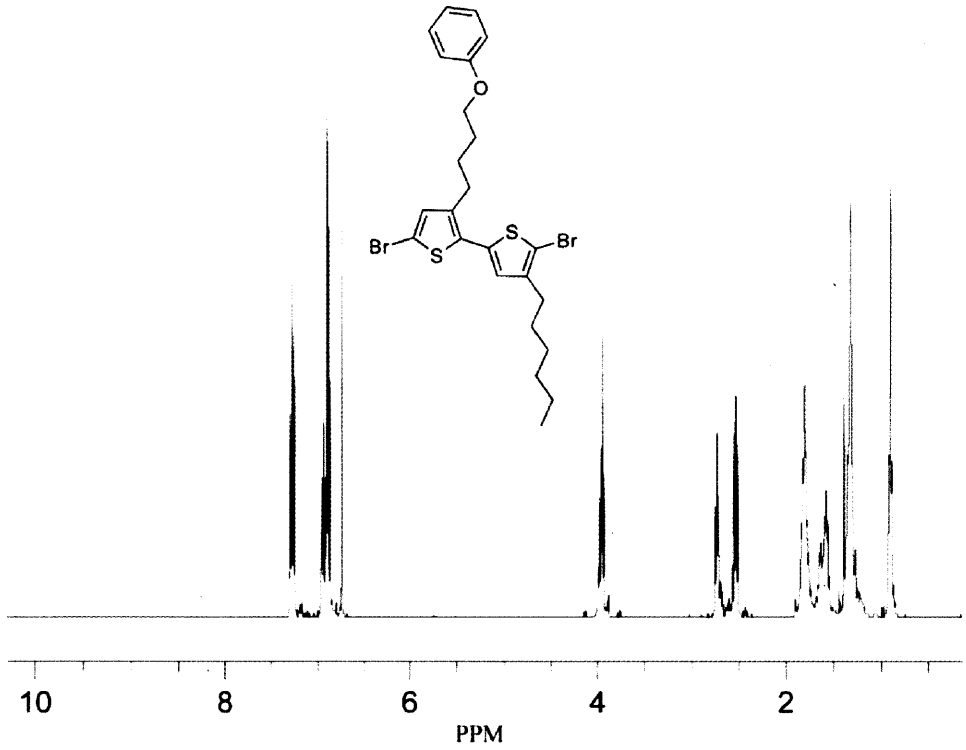

^{1}H-NMR spectrum ($CDCl_3$) of **M1**

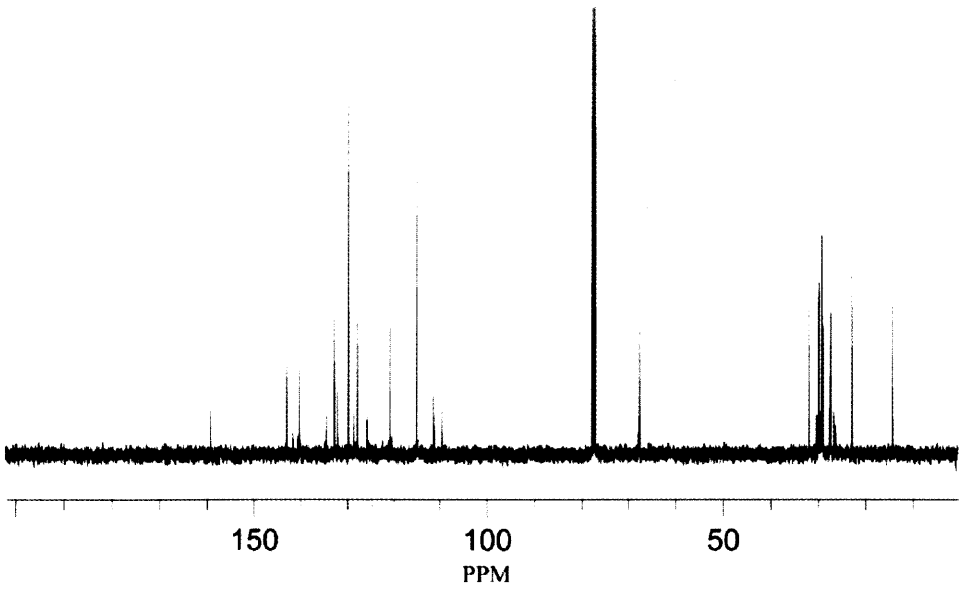

^{13}C-NMR spectrum ($CDCl_3$) of **M1**

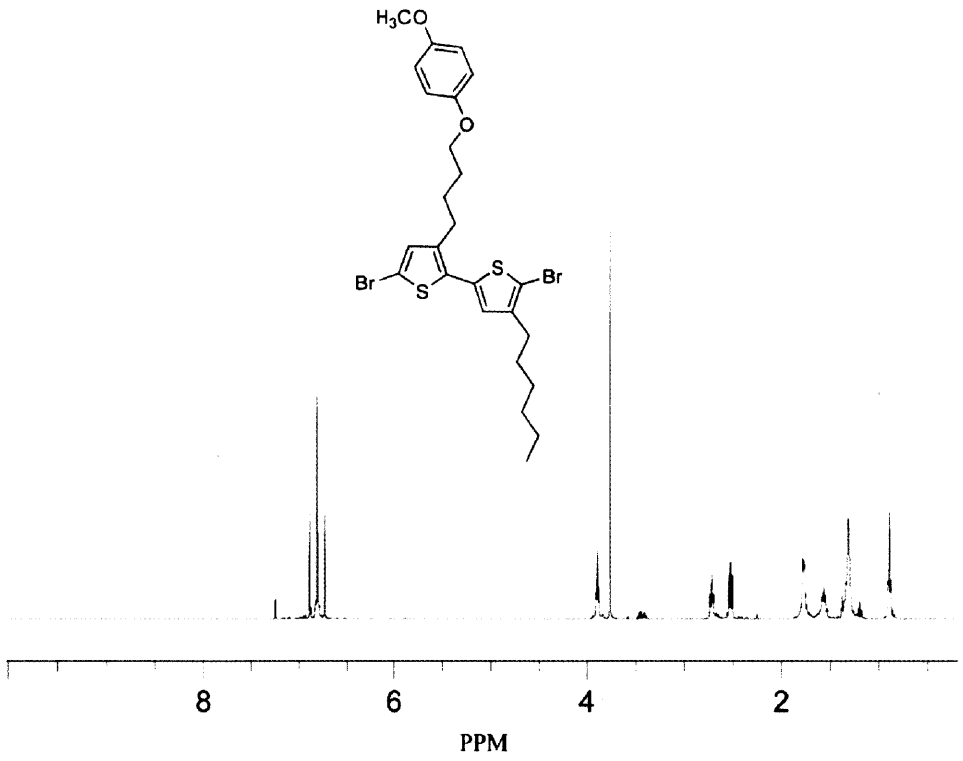

^{1}H-NMR spectrum ($CDCl_3$) of **M3**

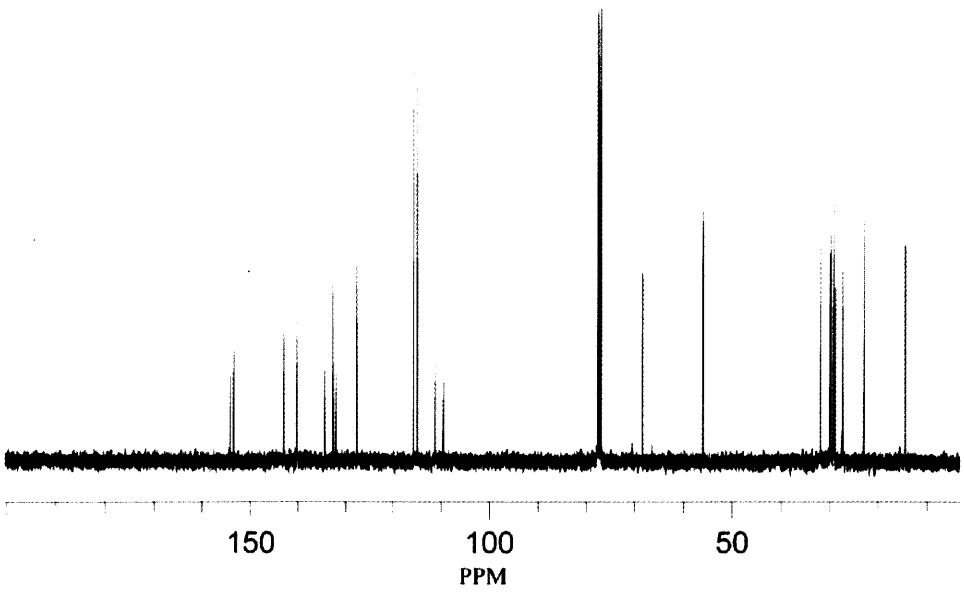

^{13}C-NMR spectrum ($CDCl_3$) of **M3**

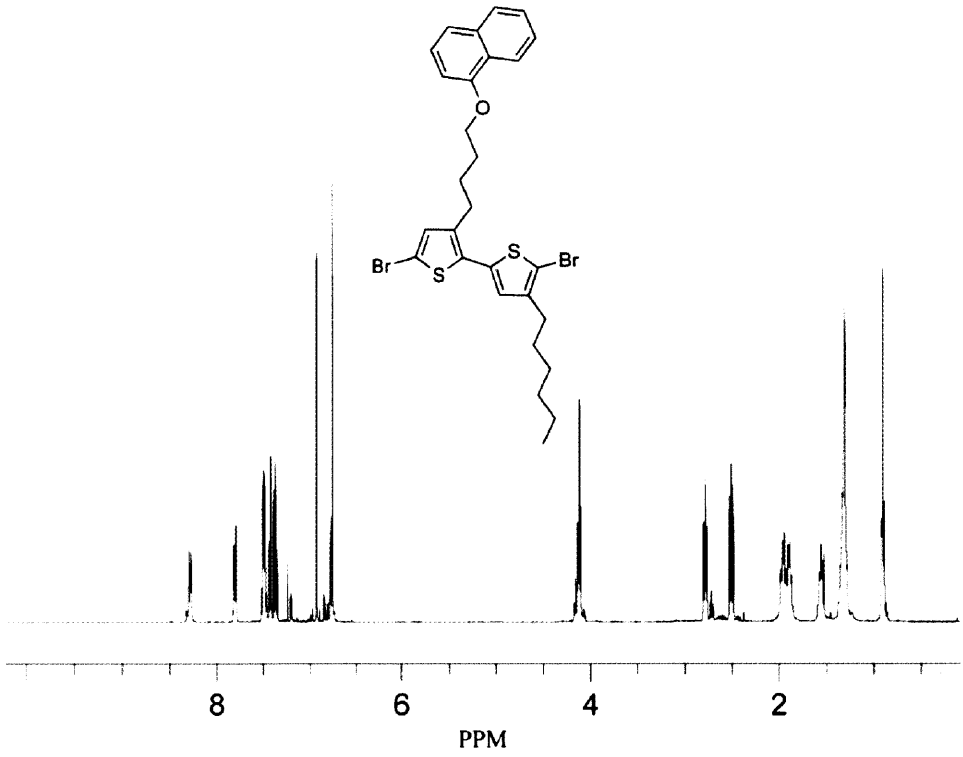

^{1}H-NMR spectrum ($CDCl_3$) of **M4**

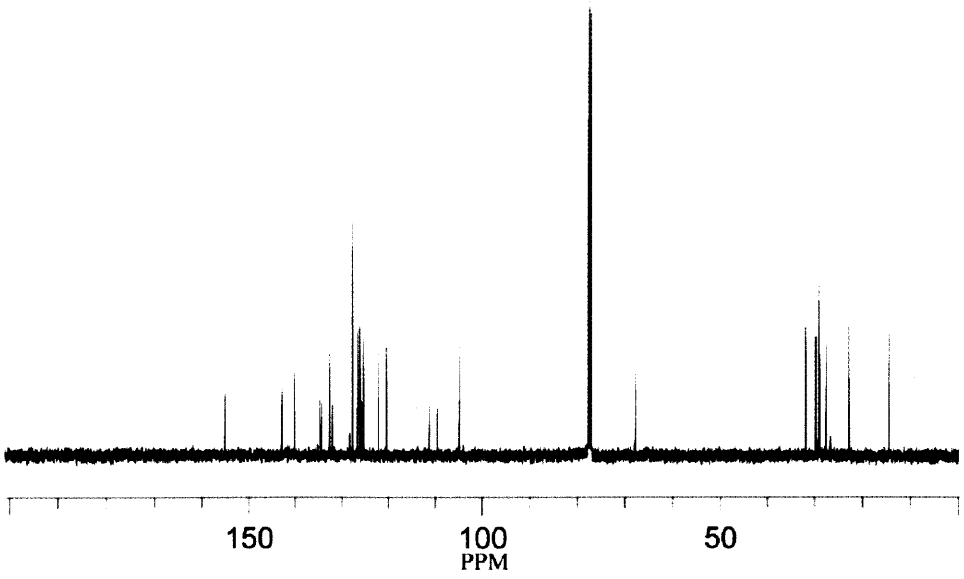

^{13}C-NMR spectrum ($CDCl_3$) of **M4**

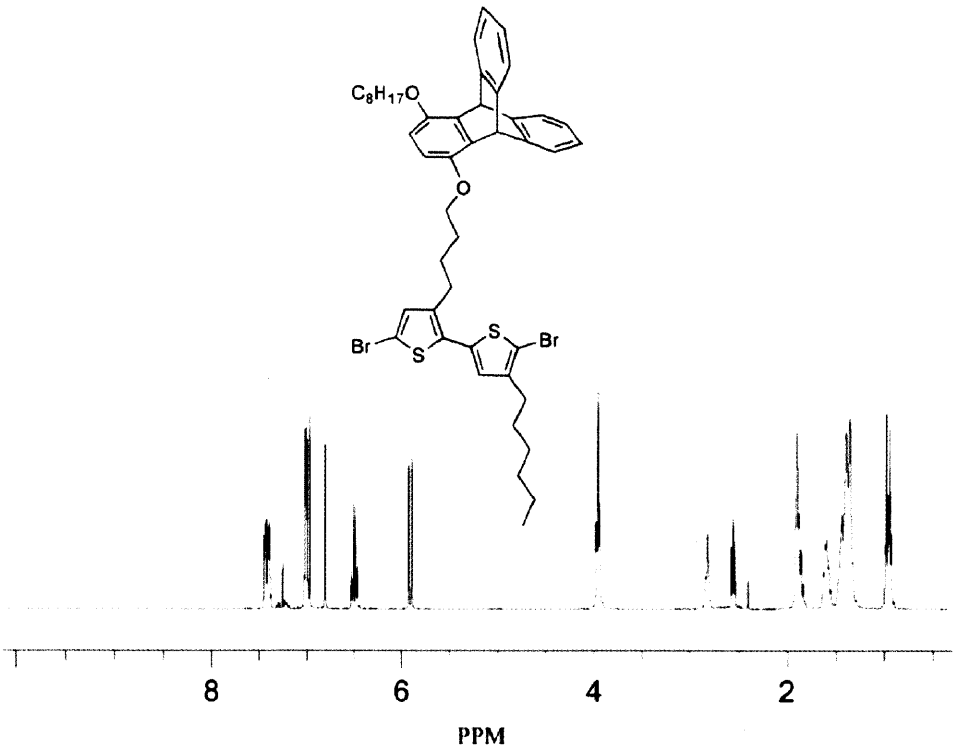

^{1}H-NMR spectrum ($CDCl_3$) of **M5**

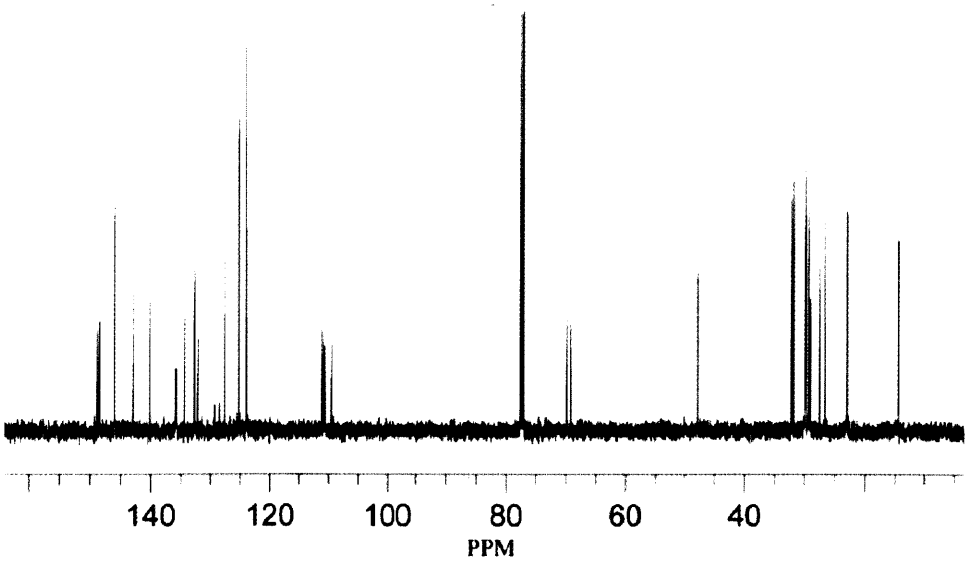

^{13}C-NMR spectrum ($CDCl_3$) of **M5**

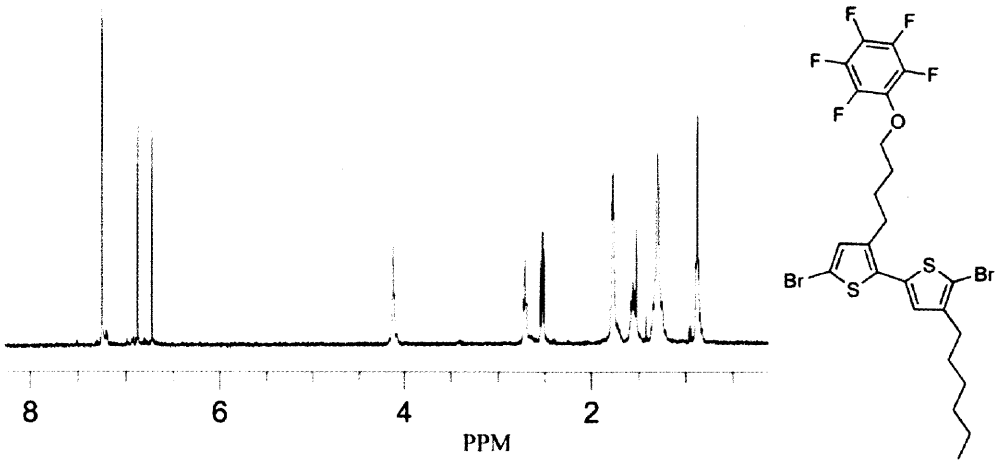

^{1}H-NMR spectrum ($CDCl_3$) of **M6**

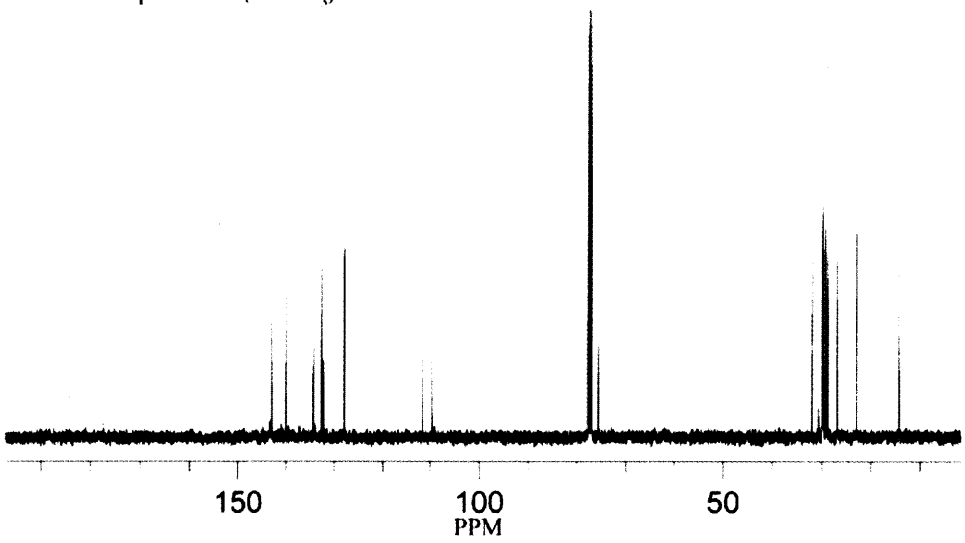

^{13}C-NMR spectrum ($CDCl_3$) of **M6**

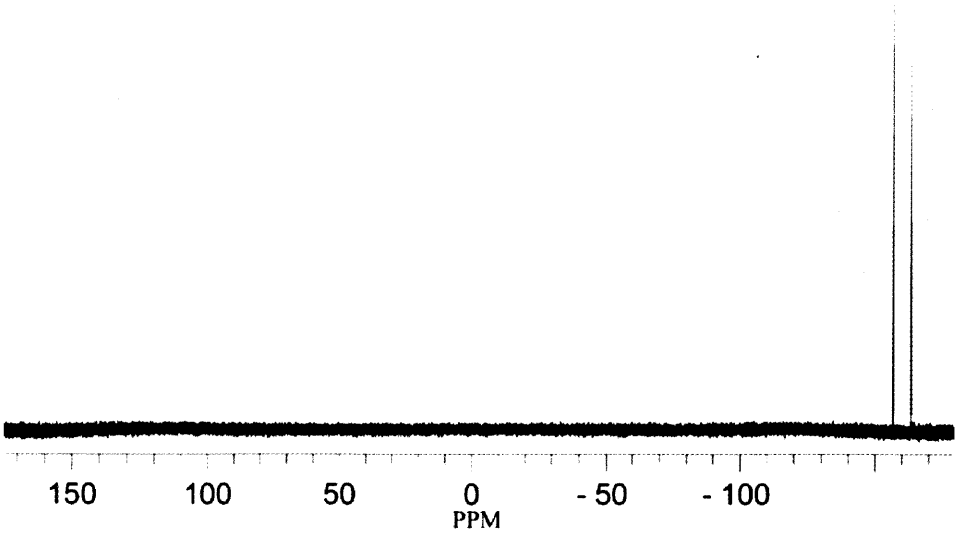

^{19}F-NMR spectrum ($CDCl_3$) of **M6**

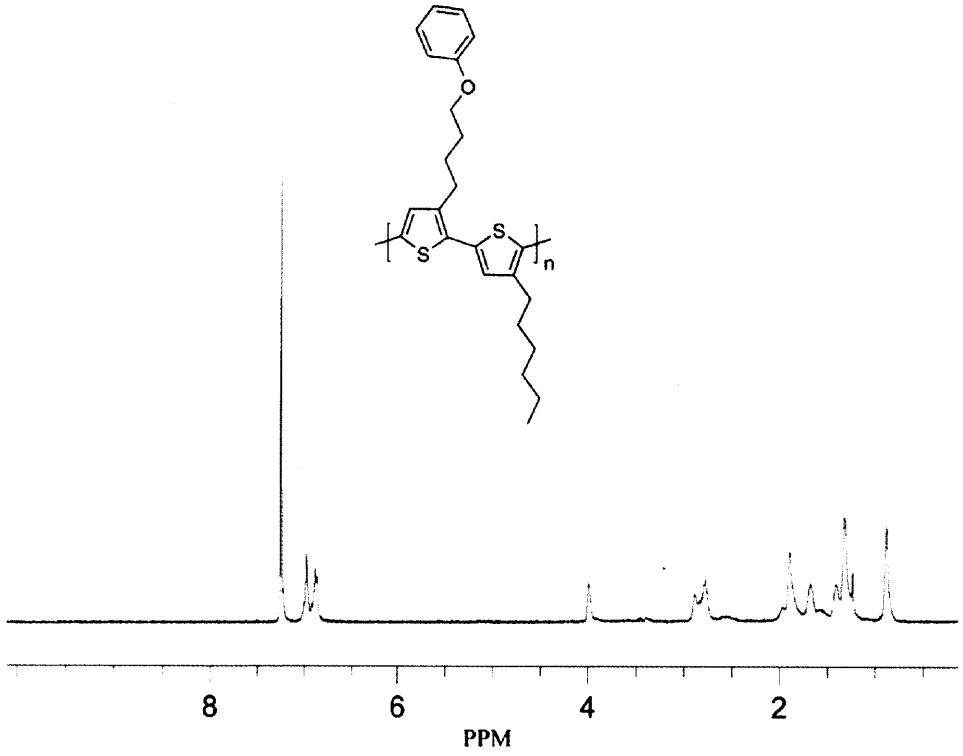

^{1}H-NMR spectrum ($CDCl_3$) of **P1**

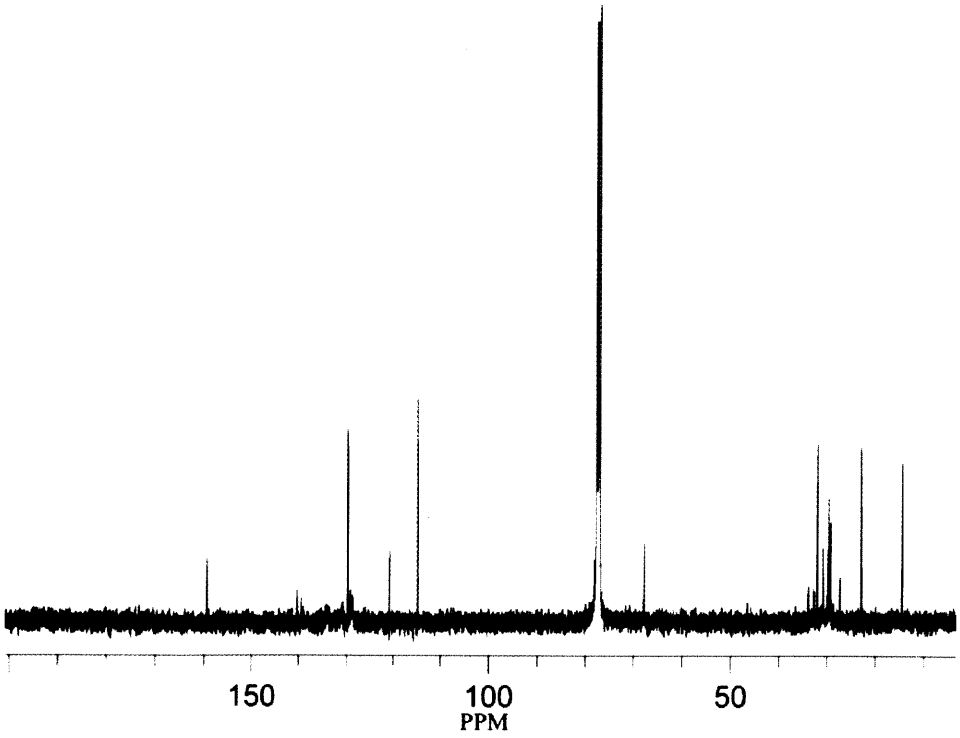

^{13}C-NMR spectrum ($CDCl_3$) of **P1**

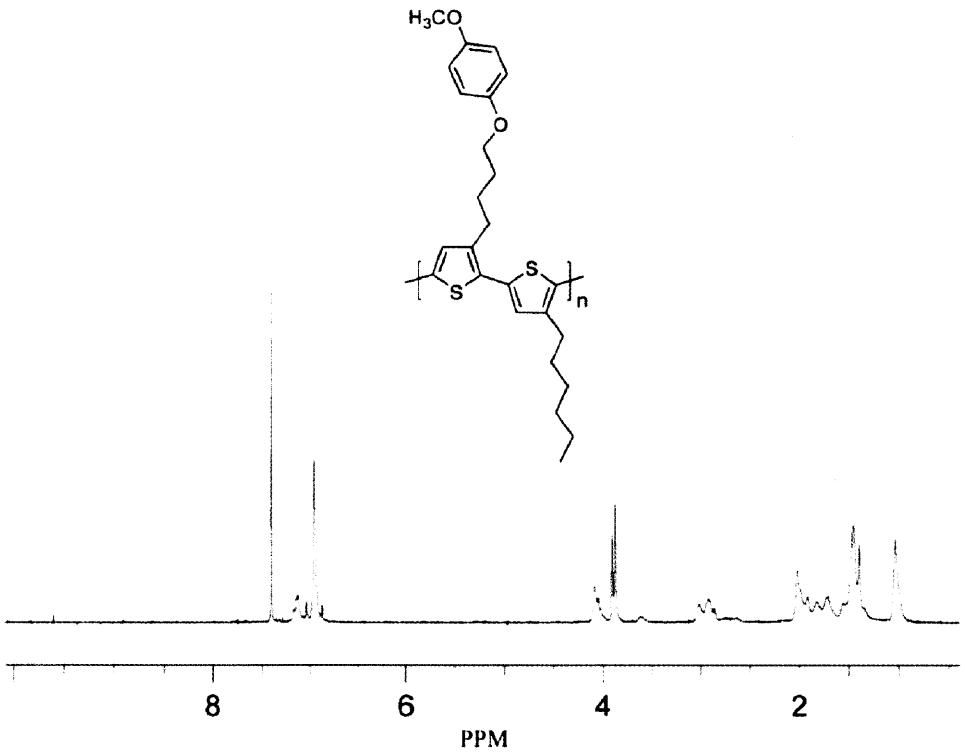

^{1}H-NMR spectrum ($CDCl_3$) of **P3**

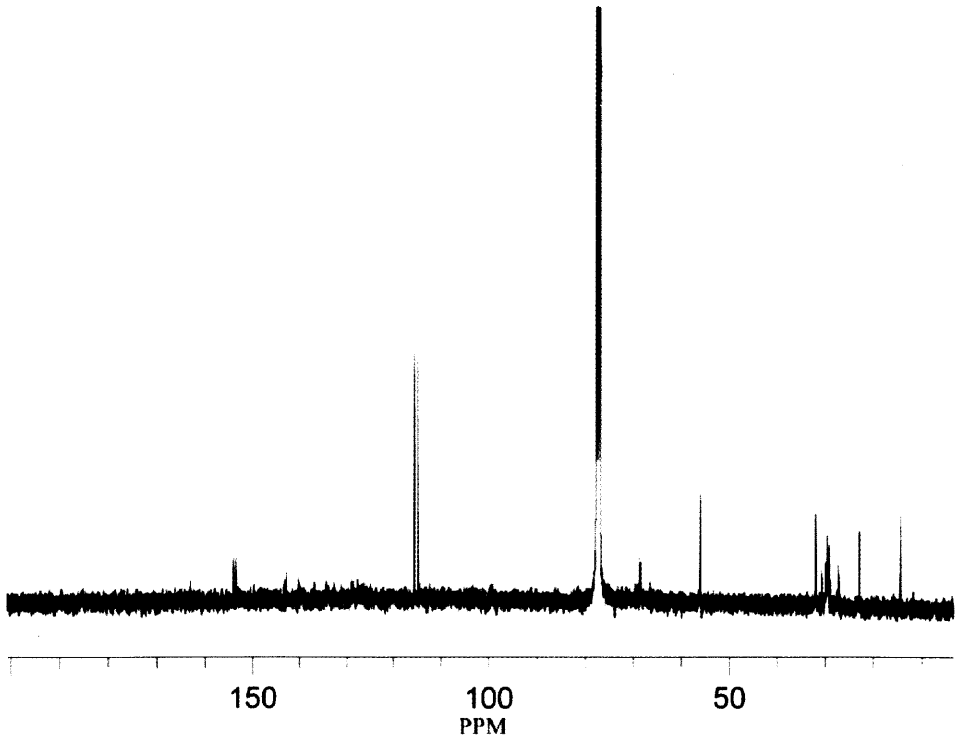

^{13}C-NMR spectrum ($CDCl_3$) of **P3**

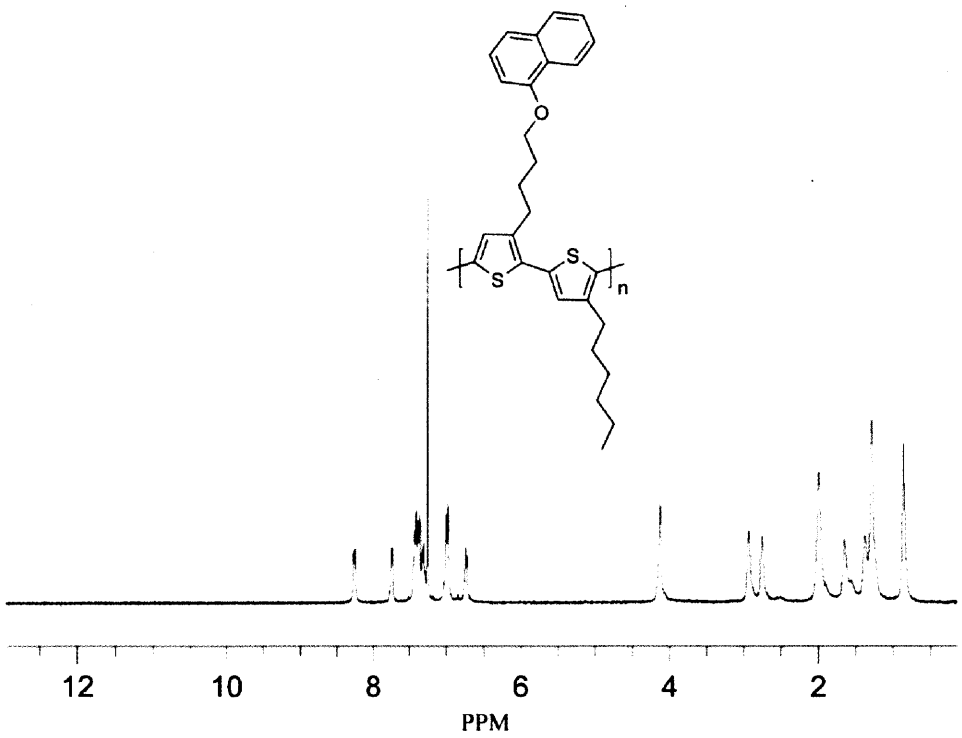

^{1}H-NMR spectrum ($CDCl_3$) of **P4**

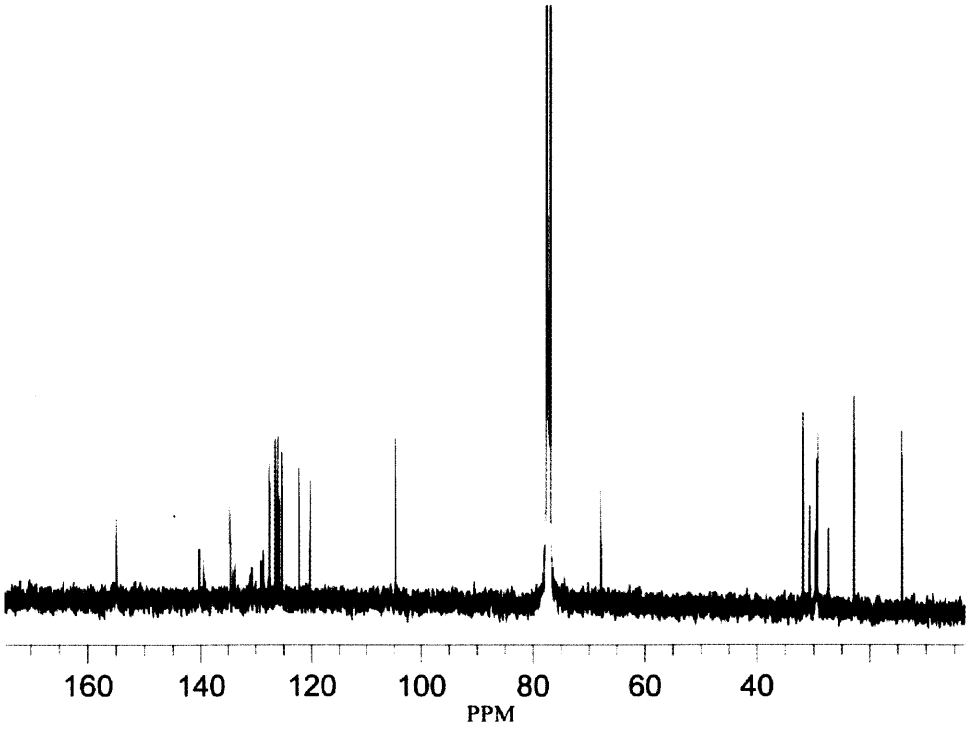

^{13}C-NMR spectrum ($CDCl_3$) of **P4**

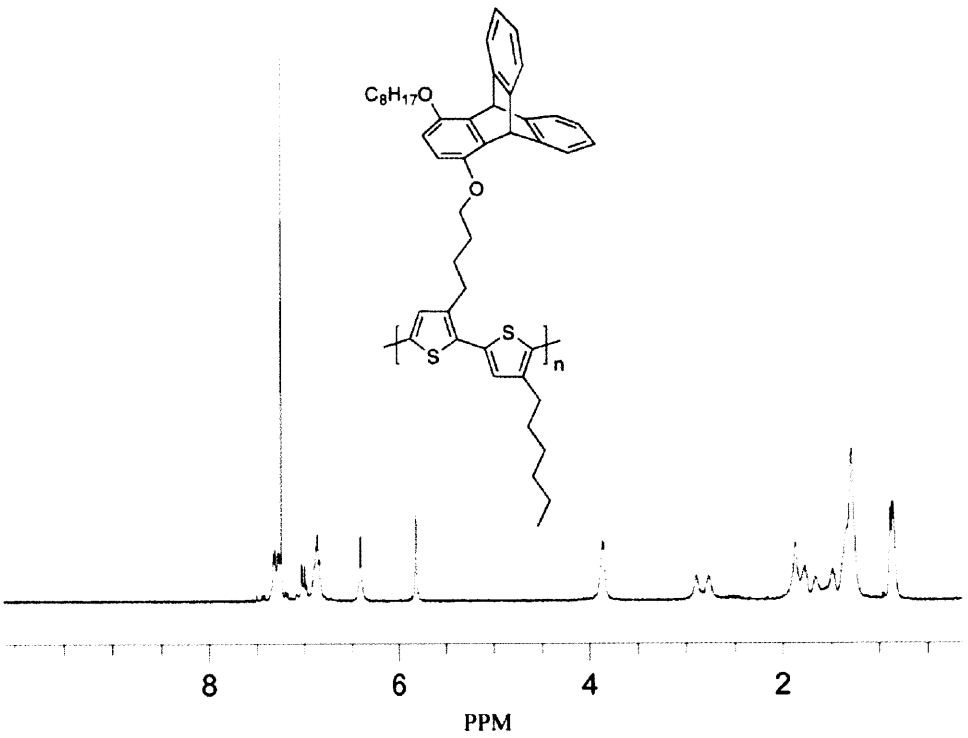

^{1}H-NMR spectrum ($CDCl_3$) of **P5**

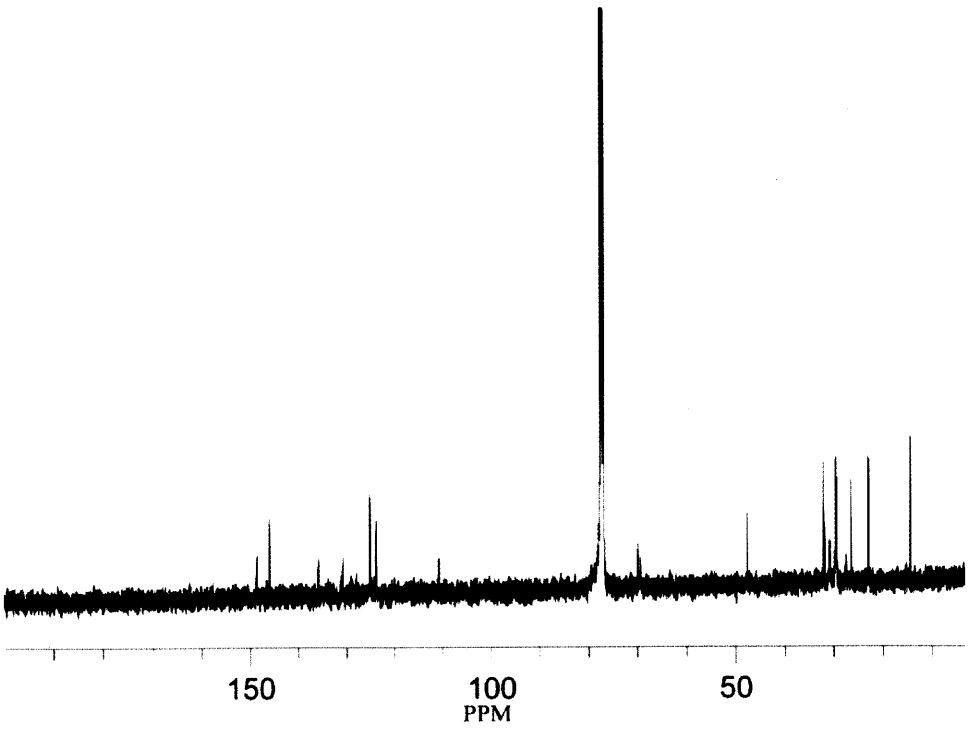

^{13}C-NMR spectrum ($CDCl_3$) of **P5**

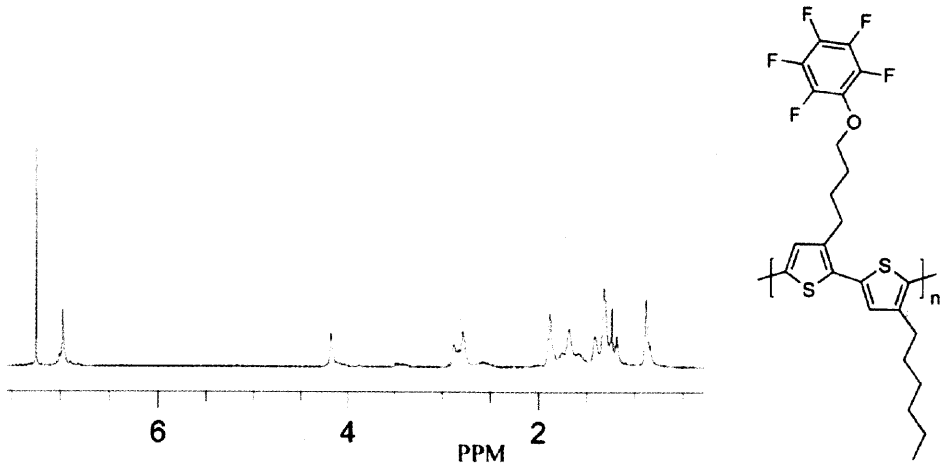

^{1}H-NMR spectrum ($CDCl_3$) of **P6**

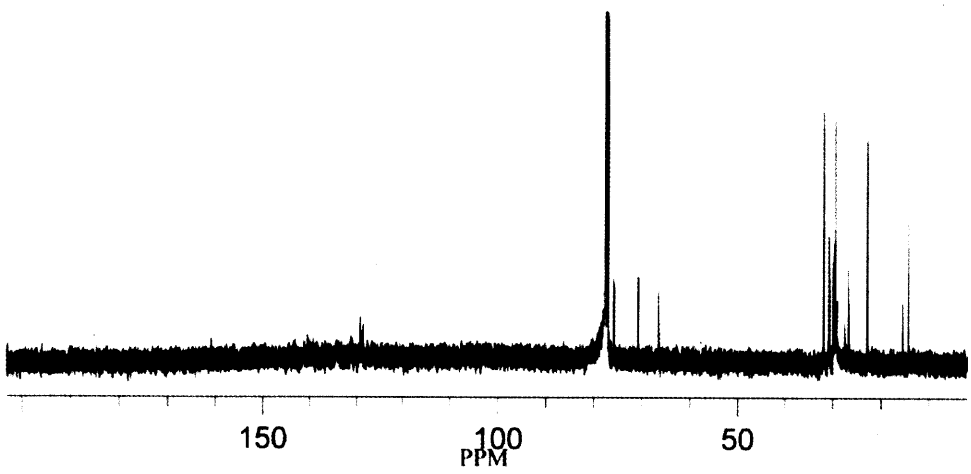

^{13}C-NMR spectrum ($CDCl_3$) of **P6**

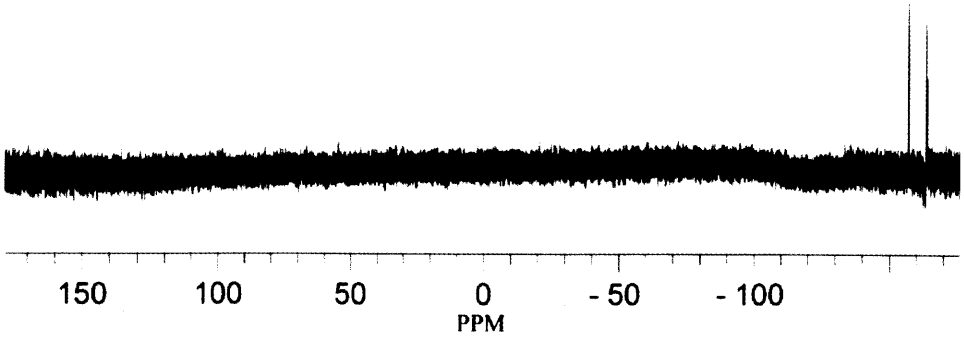

^{19}F-NMR spectrum ($CDCl_3$) of **P6**

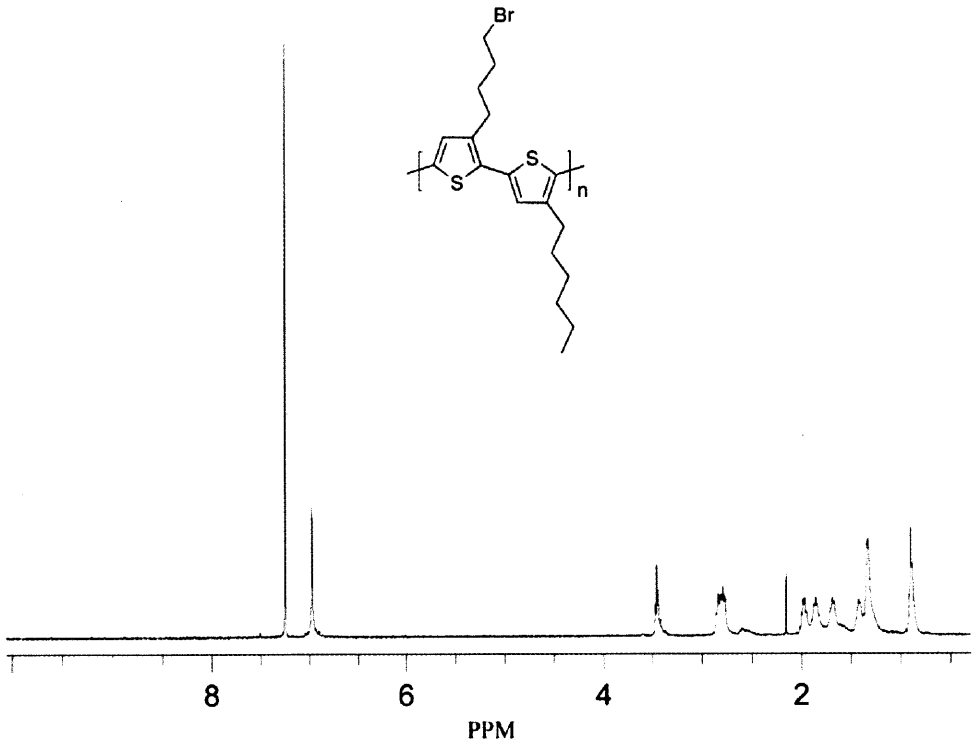

^{1}H-NMR spectrum ($CDCl_3$) of **P7**

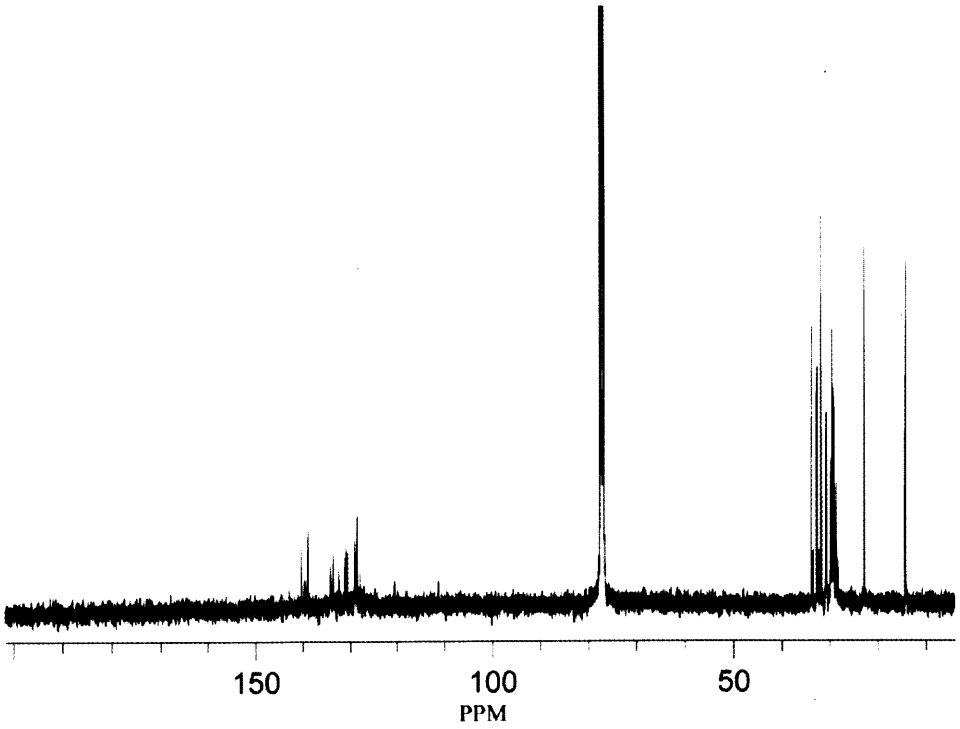

^{13}C-NMR spectrum ($CDCl_3$) of **P7**

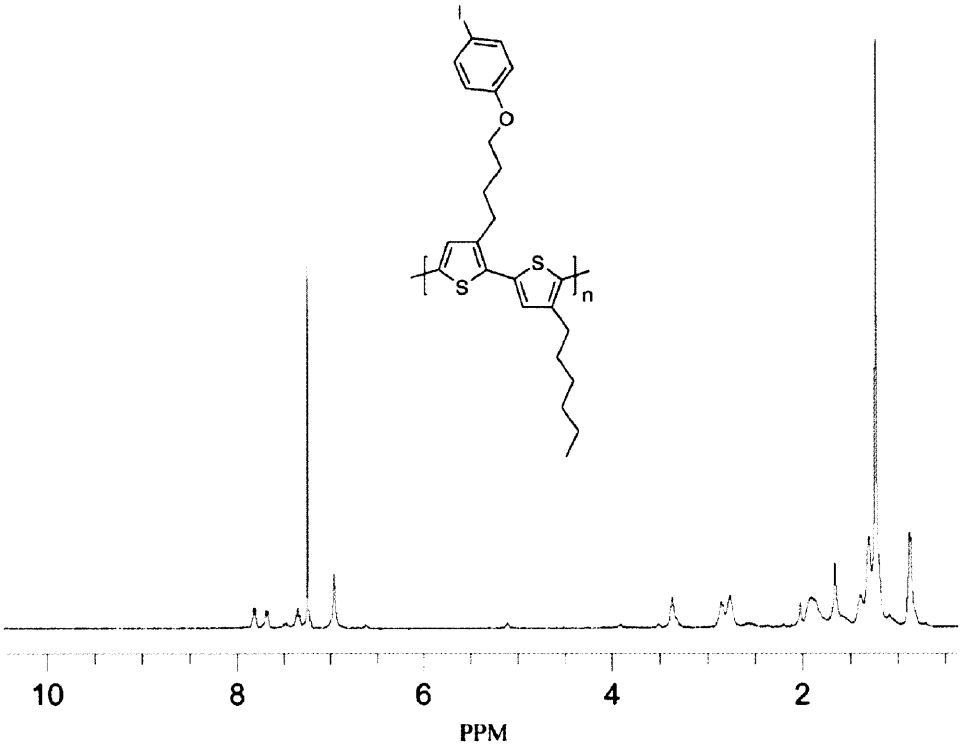

^{1}H-NMR spectrum ($CDCl_3$) of **P2**

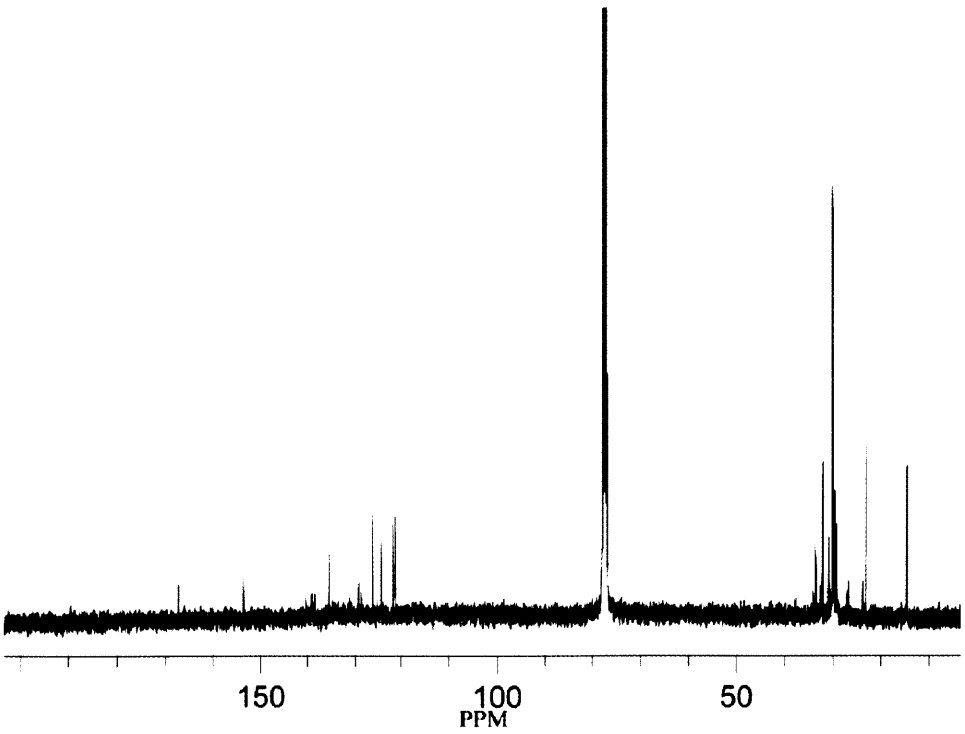

^{13}C-NMR spectrum ($CDCl_3$) of **P2**

APPENDIX 4

NMR Spectra for Chapter 4

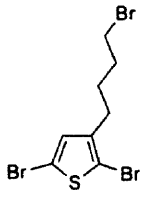

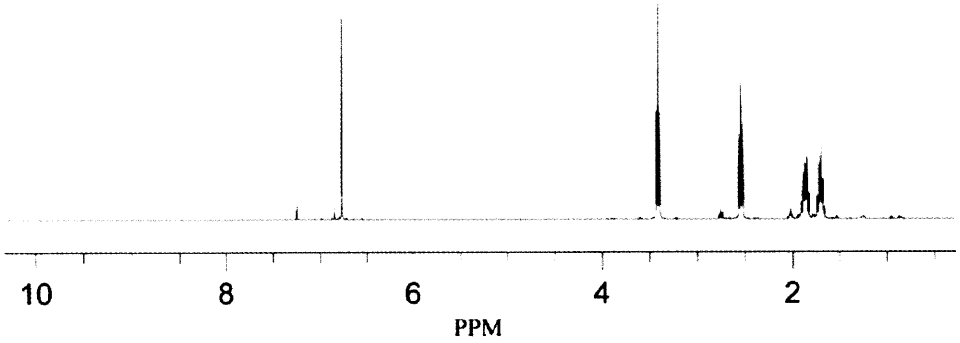

^{1}H-NMR spectrum ($CDCl_3$) of **2**

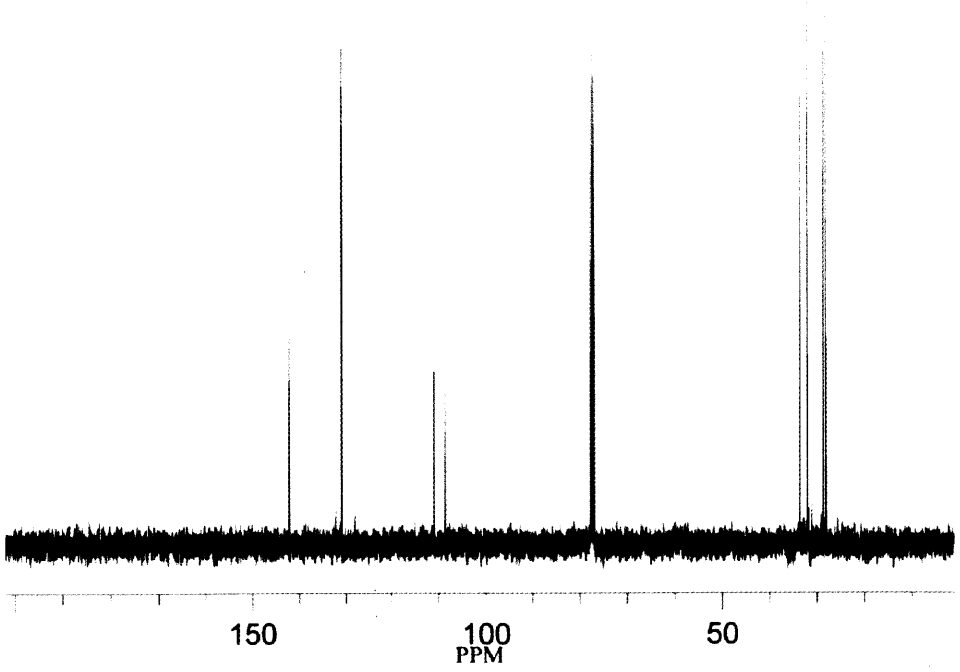

^{13}C-NMR spectrum ($CDCl_3$) of **2**

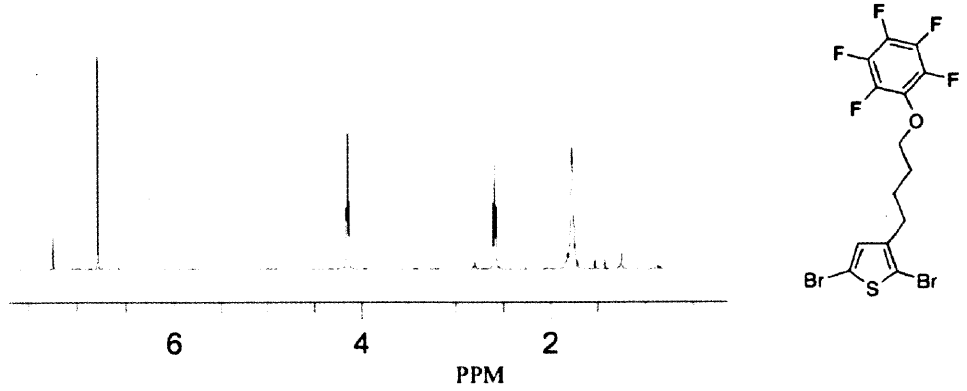

^{1}H-NMR spectrum ($CDCl_3$) of **3**

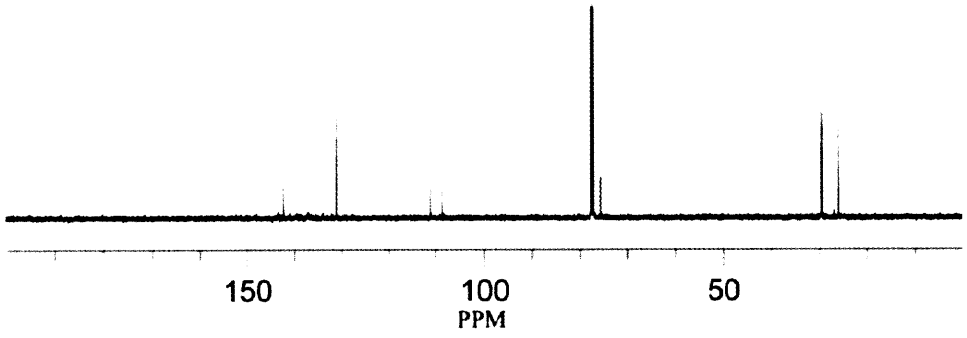

^{13}C-NMR spectrum ($CDCl_3$) of **3**

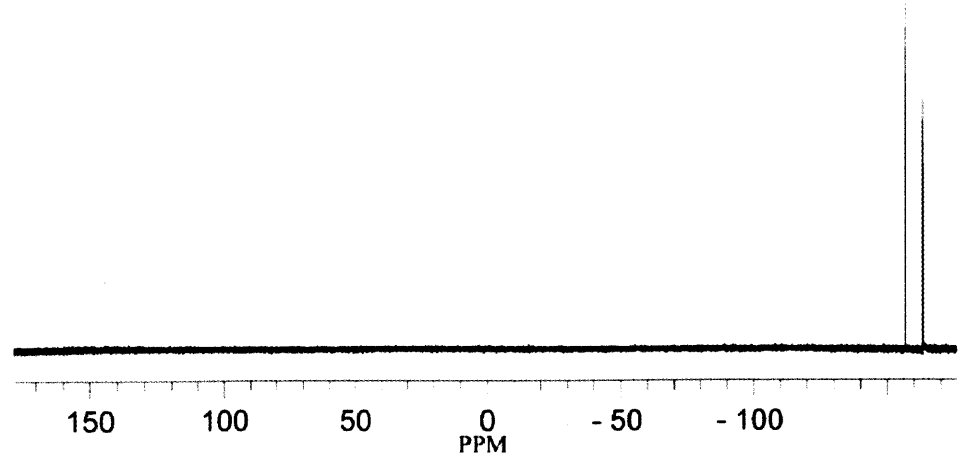

^{19}F-NMR spectrum ($CDCl_3$) of **3**

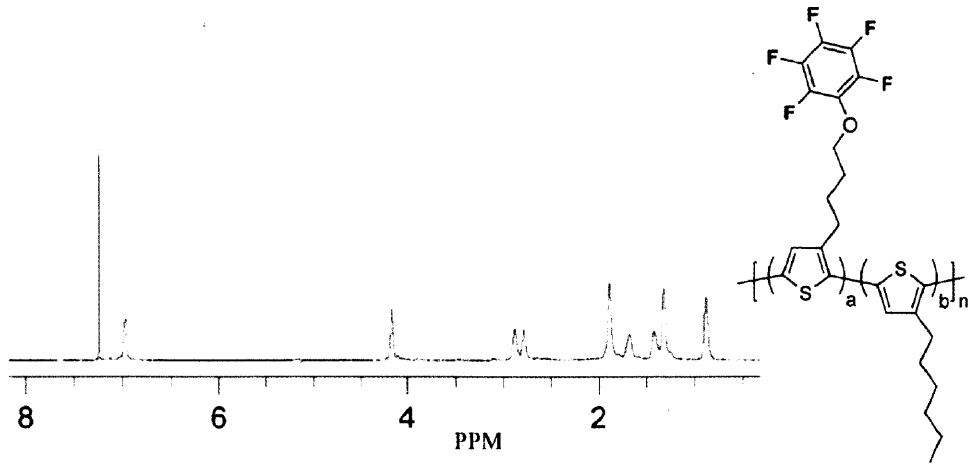

^{1}H-NMR spectrum ($CDCl_3$) of **P6a**

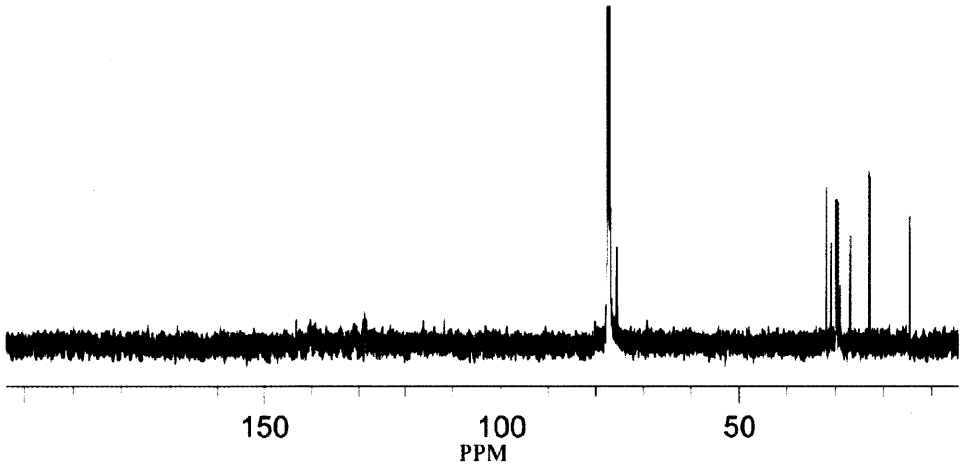

^{13}C-NMR spectrum ($CDCl_3$) of **P6a**

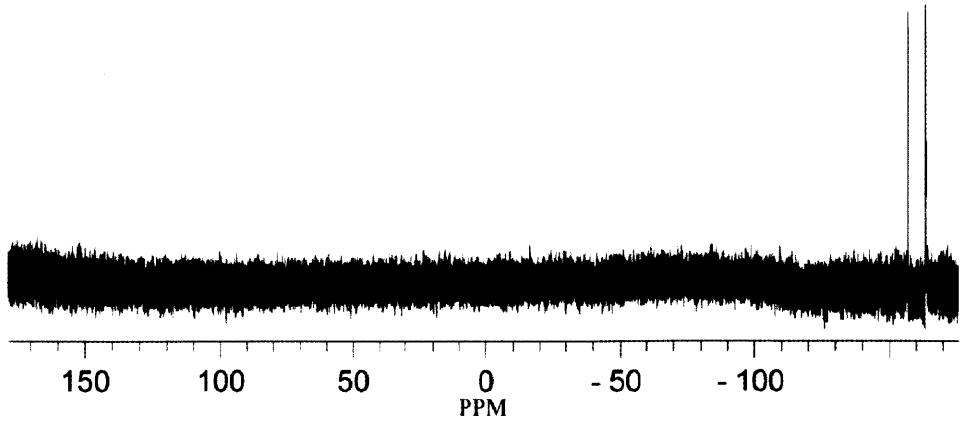

^{19}F-NMR spectrum ($CDCl_3$) of **P6a**

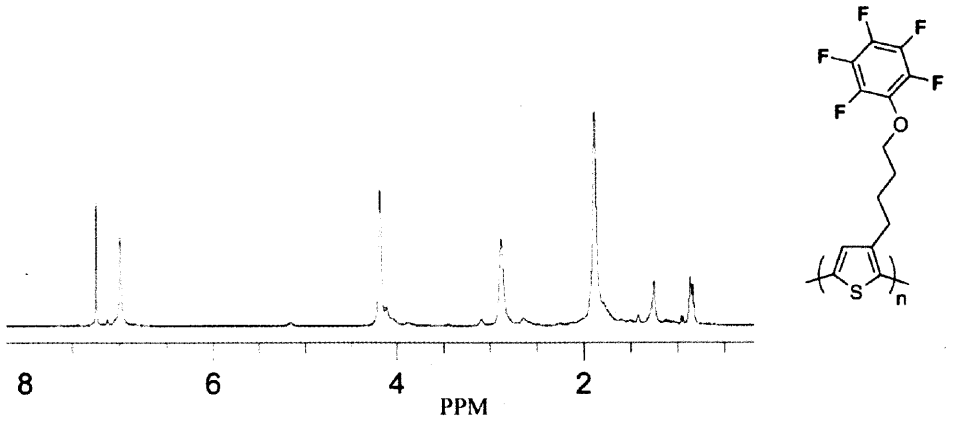

^{1}H-NMR spectrum ($CDCl_3$) of **P6b**

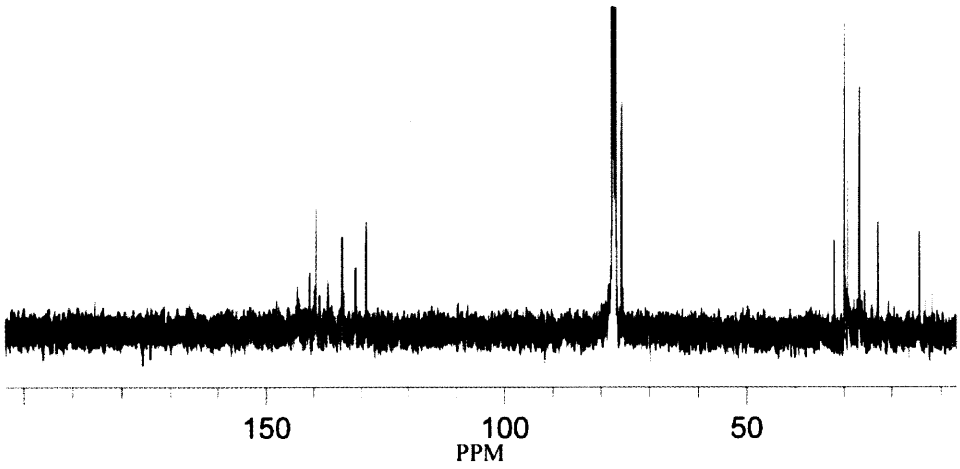

^{13}C-NMR spectrum ($CDCl_3$) of **P6b**

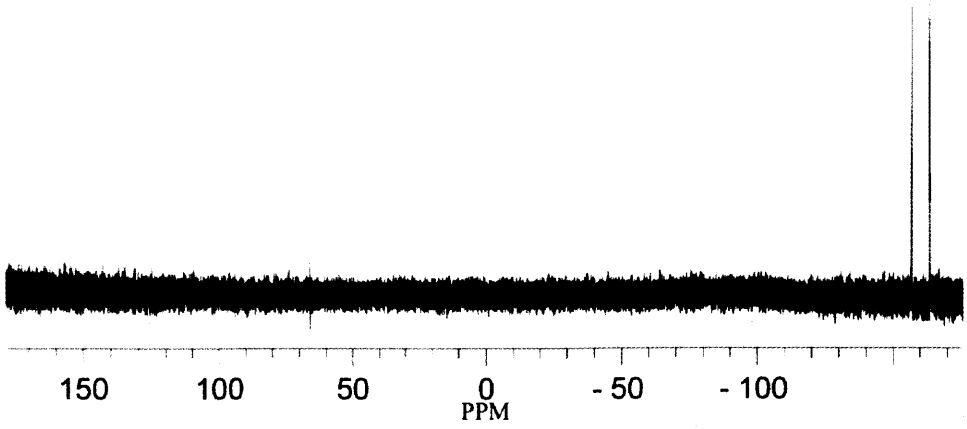

^{19}F-NMR spectrum ($CDCl_3$) of **P6b**

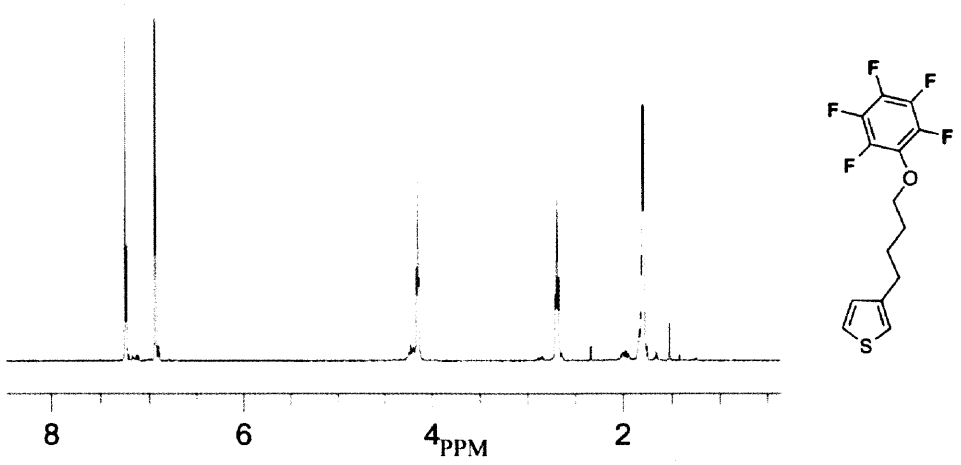

^{1}H-NMR spectrum ($CDCl_3$) of **4**

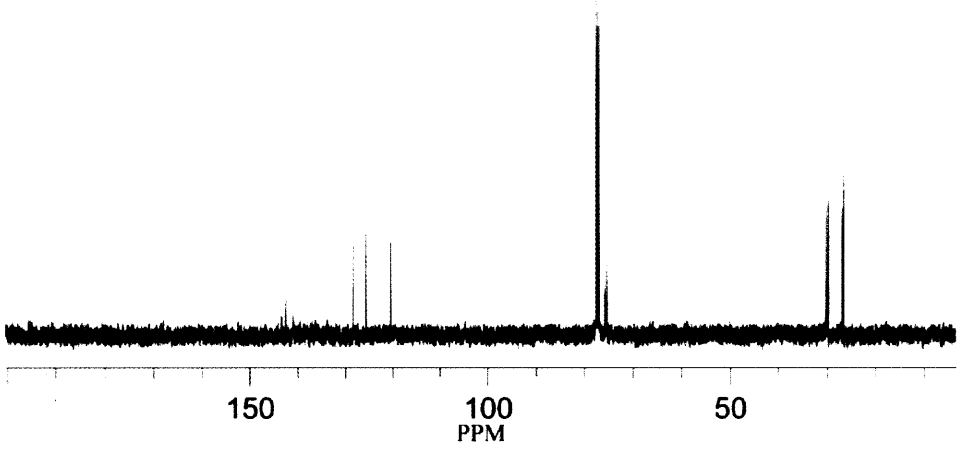

^{13}C-NMR spectrum ($CDCl_3$) of **4**

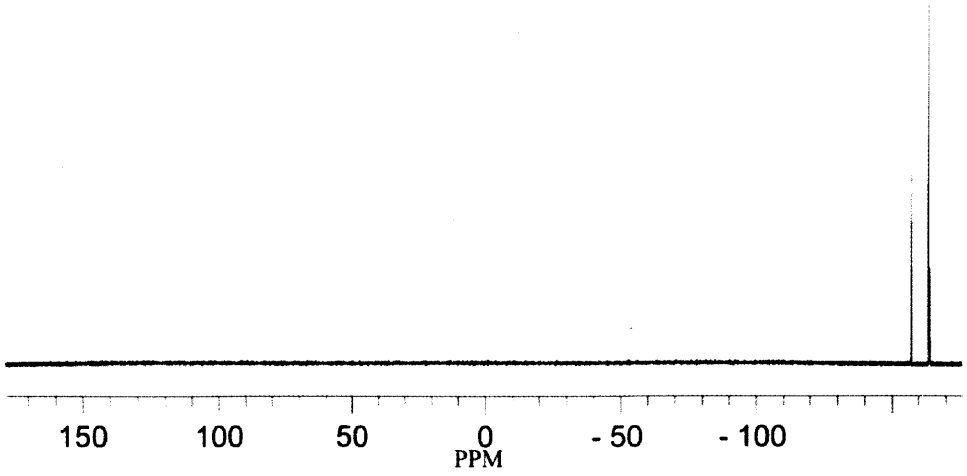

^{19}F-NMR spectrum ($CDCl_3$) of **4**

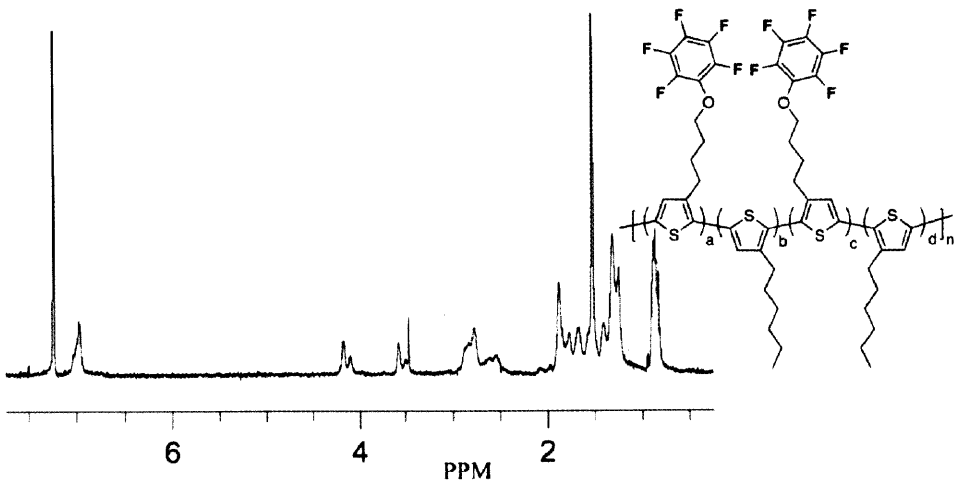

^{1}H-NMR spectrum ($CDCl_3$) of **P6c**

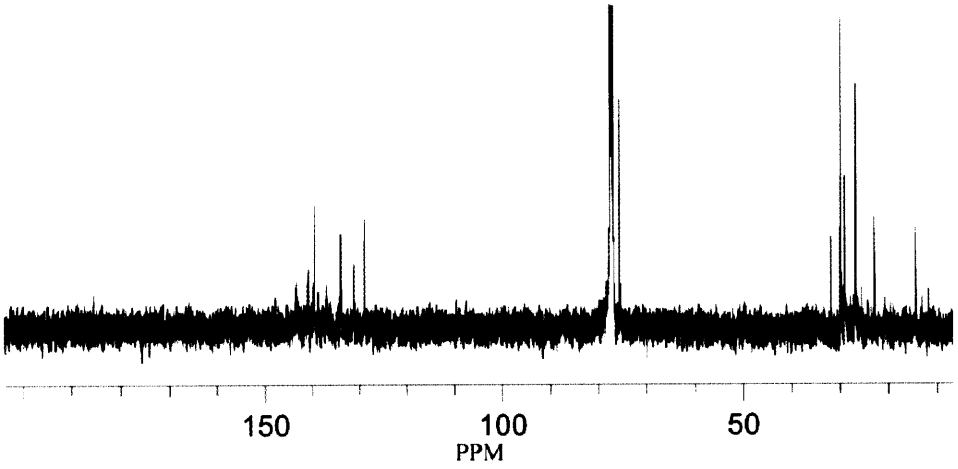

^{13}C-NMR spectrum ($CDCl_3$) of **P6c**

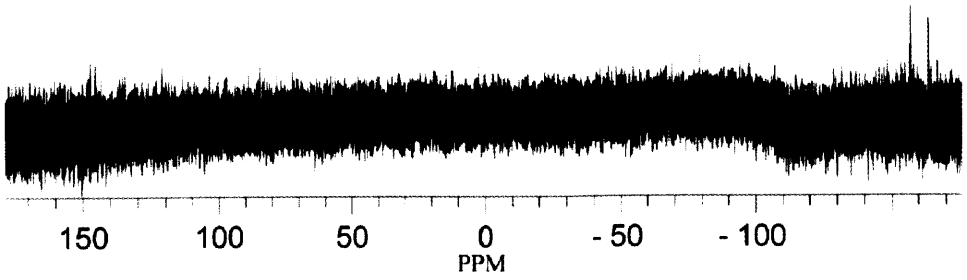

^{19}F-NMR spectrum ($CDCl_3$) of **P6c**

APPENDIX 5

NMR Spectra for Chapter 5

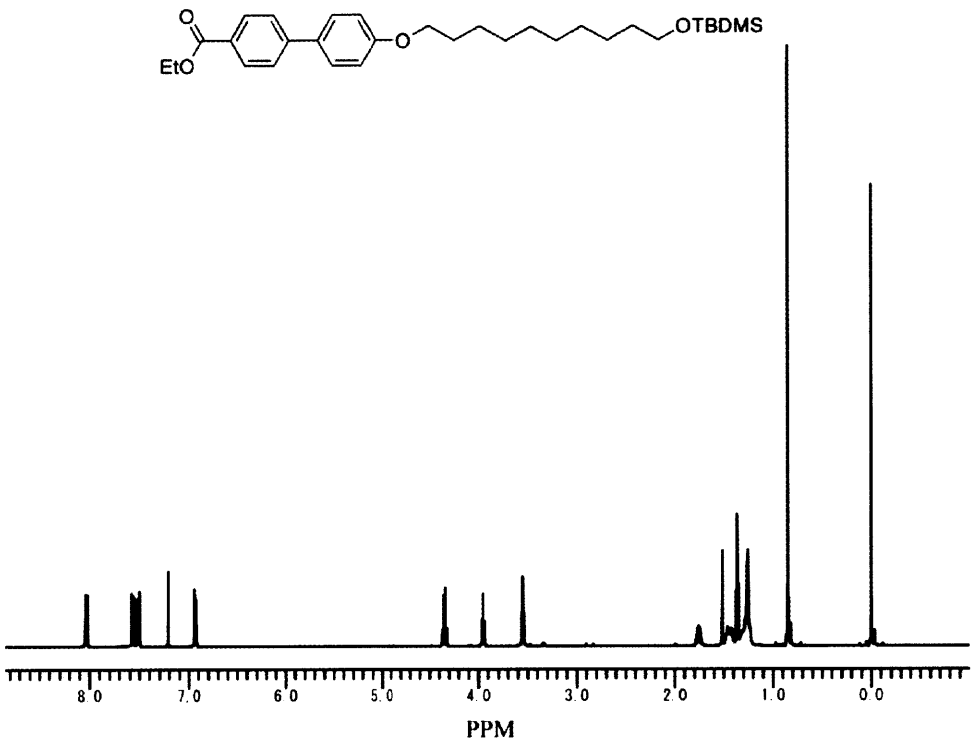

^{1}H-NMR spectrum ($CDCl_3$) of **6**

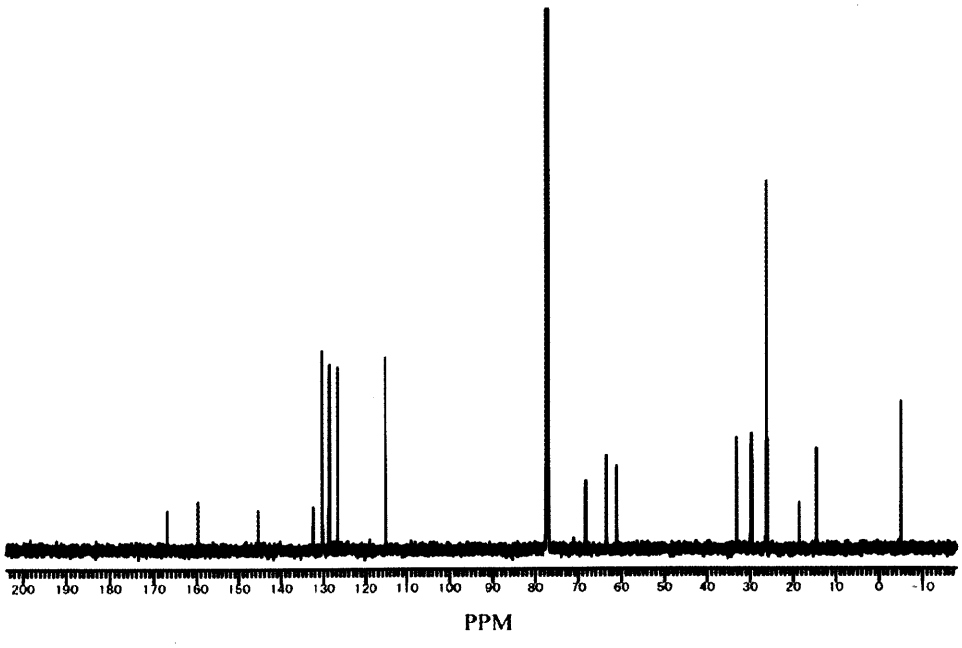

^{13}C-NMR spectrum ($CDCl_3$) of **6**

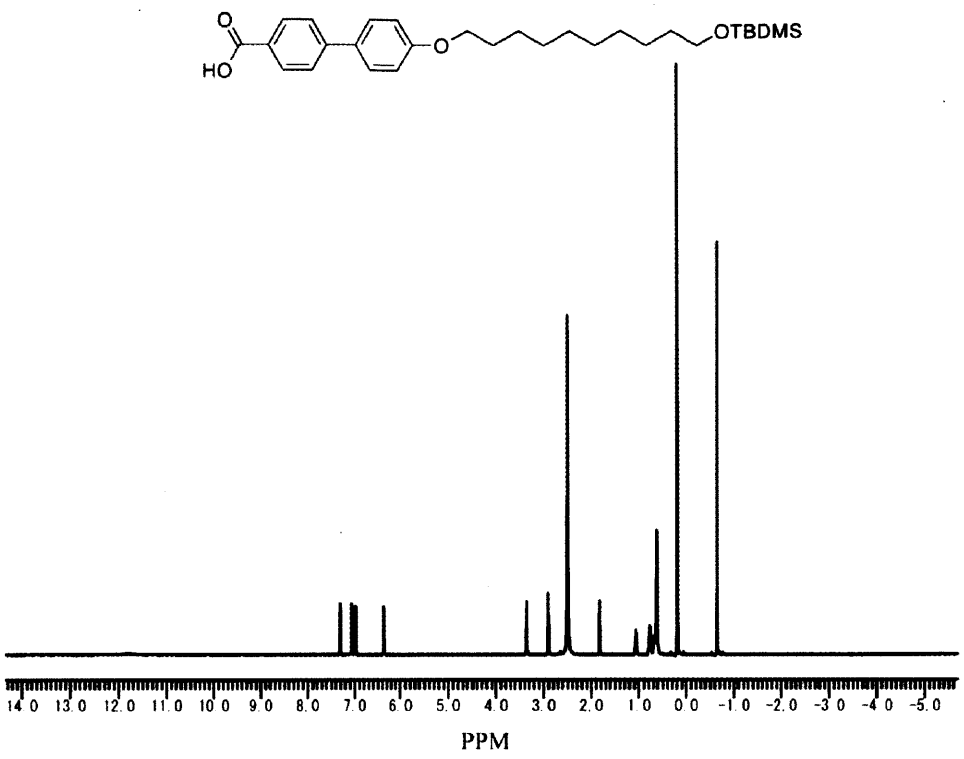

^{1}H-NMR spectrum (DMSO-d^{6}) of **7**

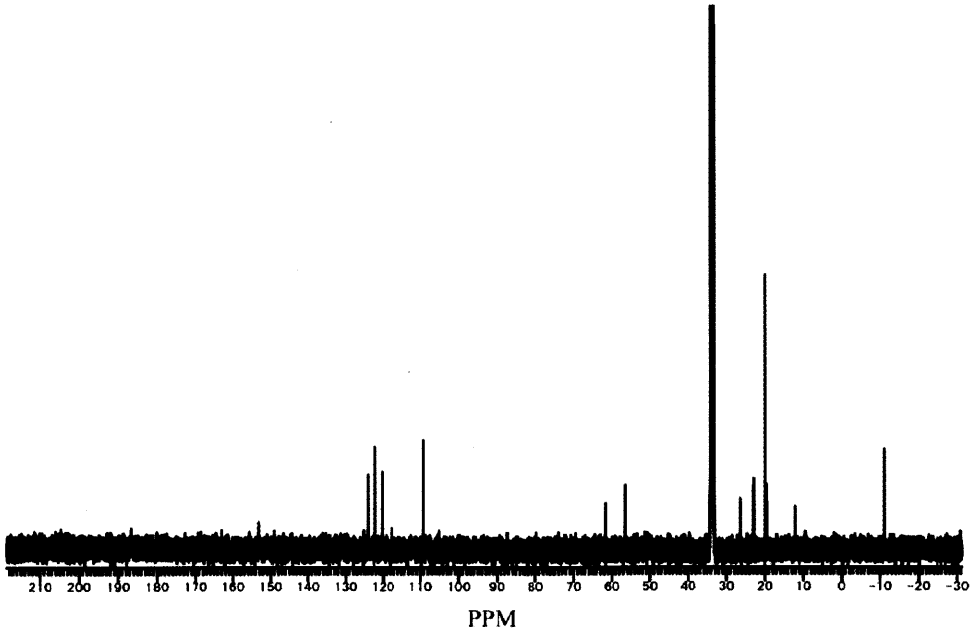

^{13}C-NMR spectrum (DMSO-d^{6}) of **7**

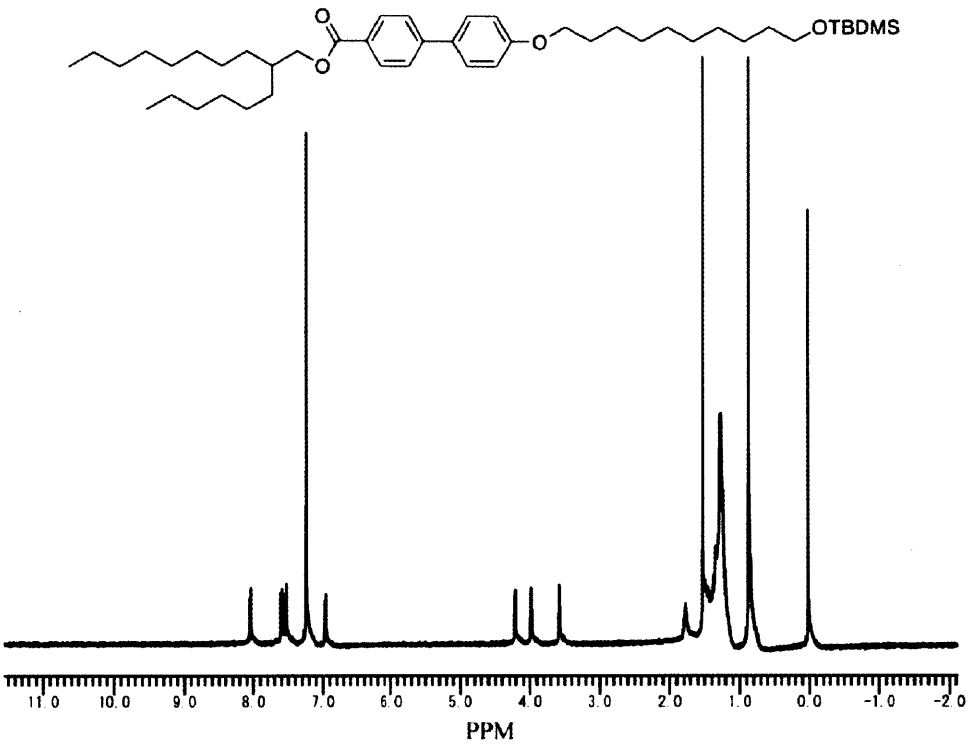

^{1}H-NMR spectrum ($CDCl_3$) of **8**

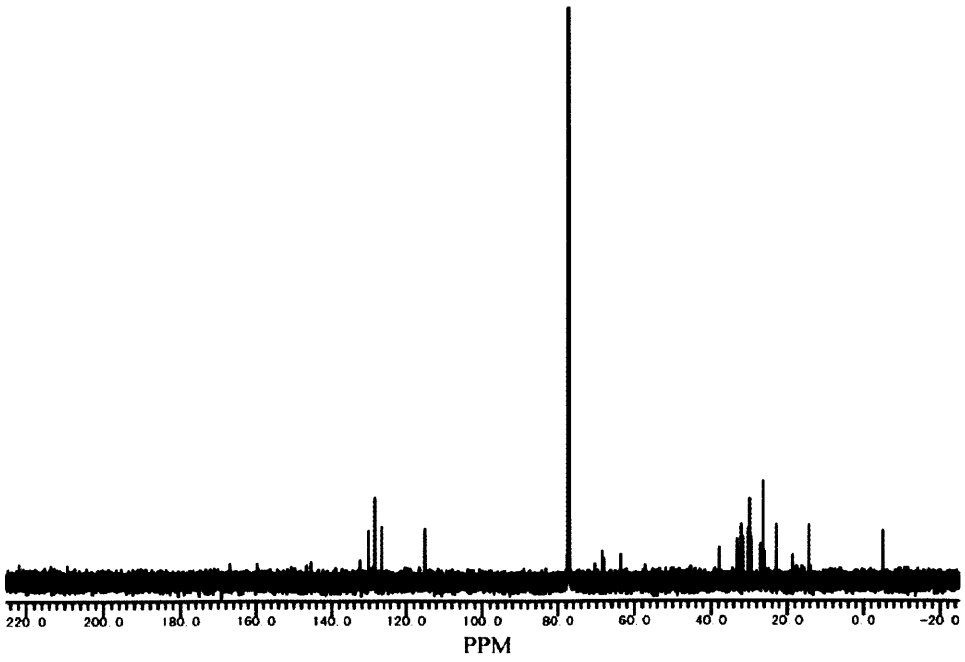

^{13}C-NMR spectrum ($CDCl_3$) of **8**

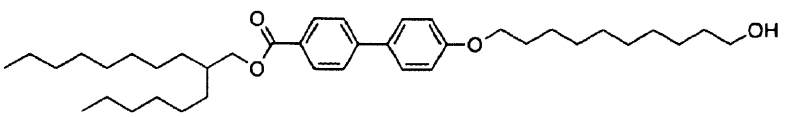

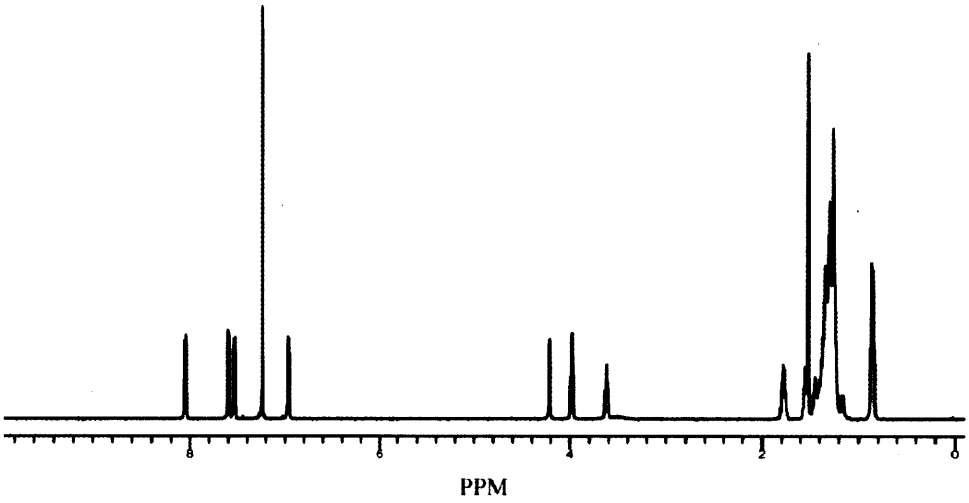

^{1}H-NMR spectrum ($CDCl_3$) of **9**

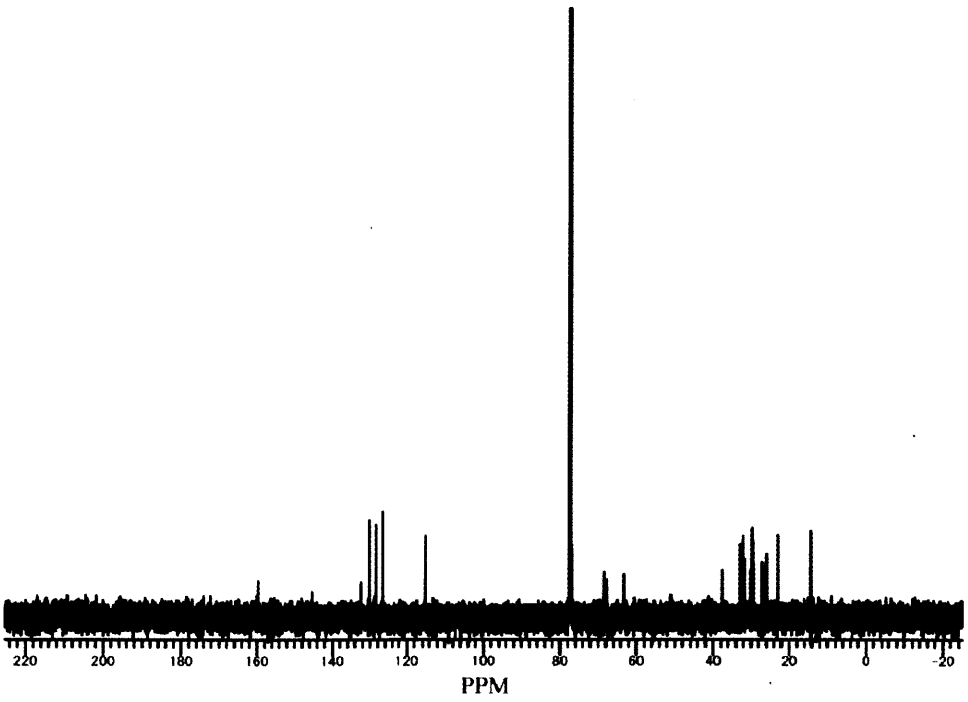

^{13}C-NMR spectrum ($CDCl_3$) of **9**

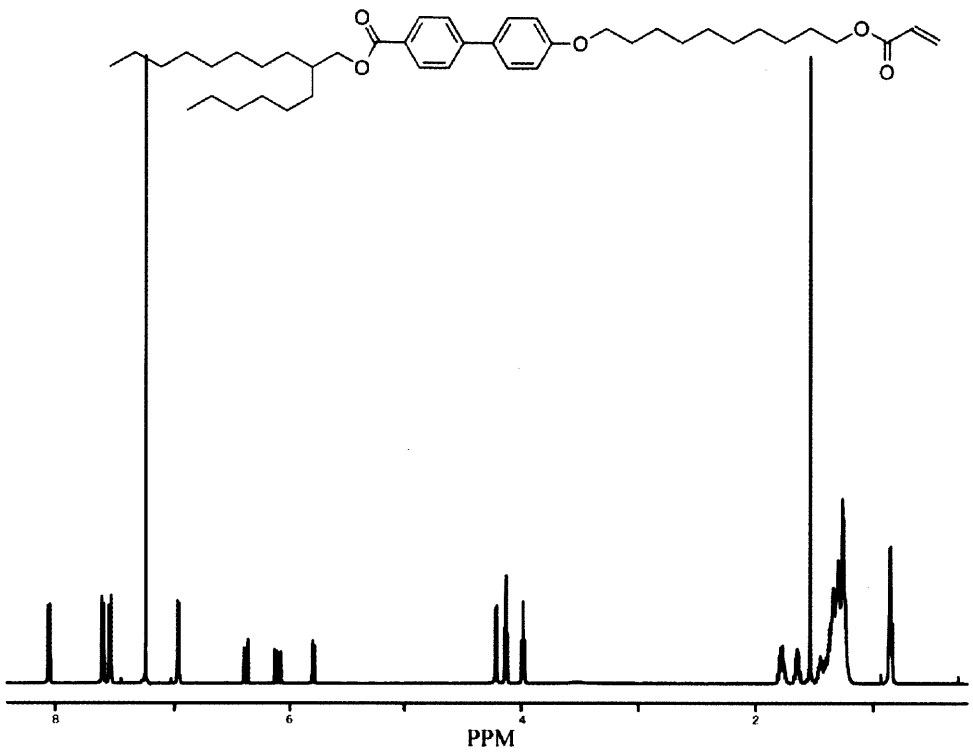

^{1}H-NMR spectrum ($CDCl_3$) of Monomer **1**

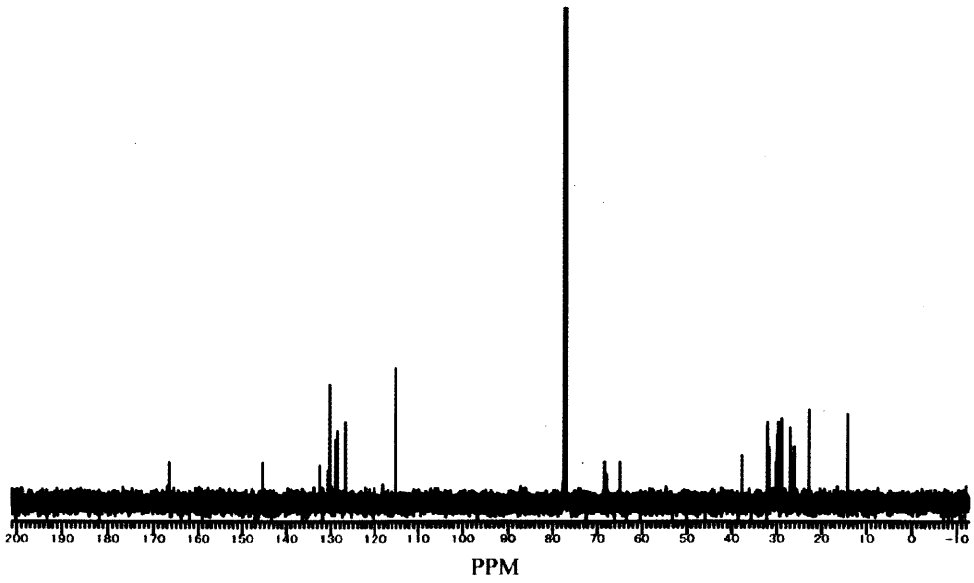

^{13}C-NMR spectrum ($CDCl_3$) of Monomer **1**

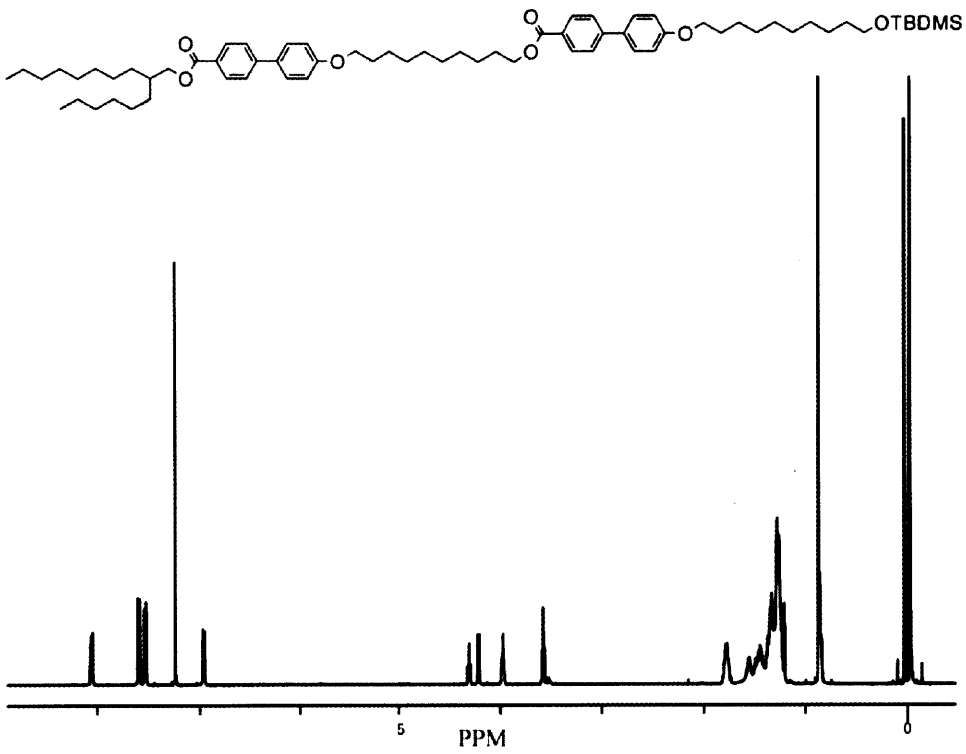

^{1}H-NMR spectrum ($CDCl_3$) of **10**

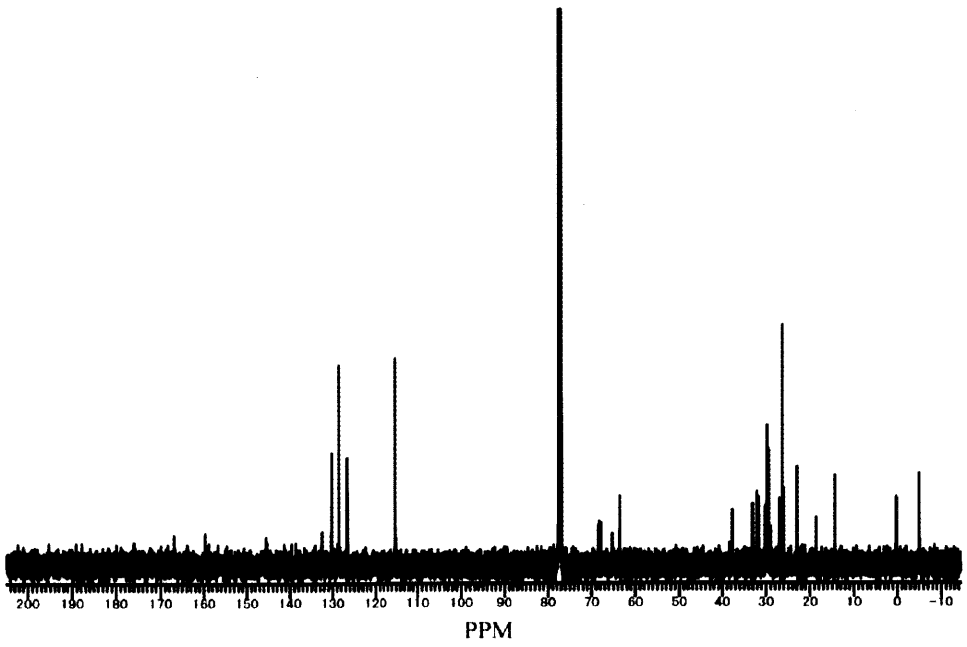

^{13}C-NMR spectrum ($CDCl_3$) of **10**

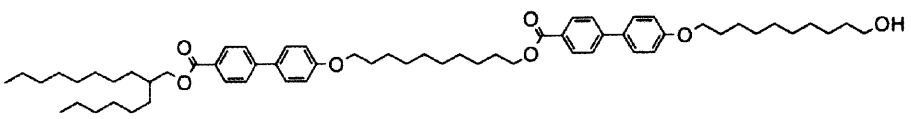

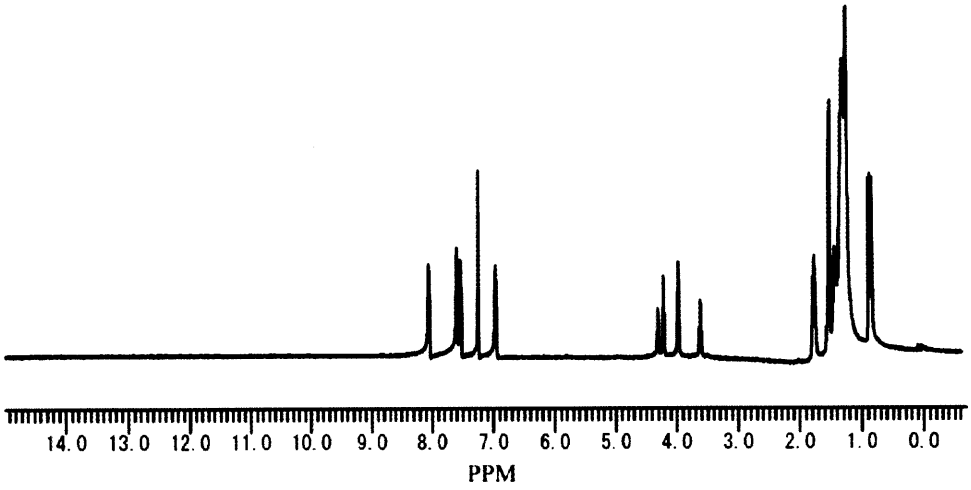

^{1}H-NMR spectrum ($CDCl_3$) of **11**

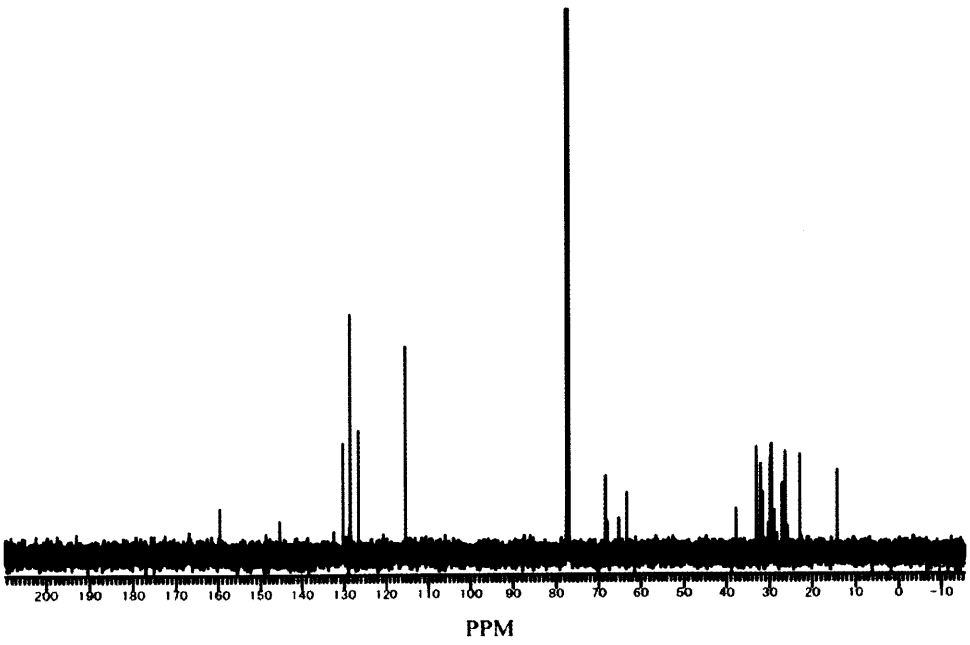

^{13}C-NMR spectrum ($CDCl_3$) of **11**

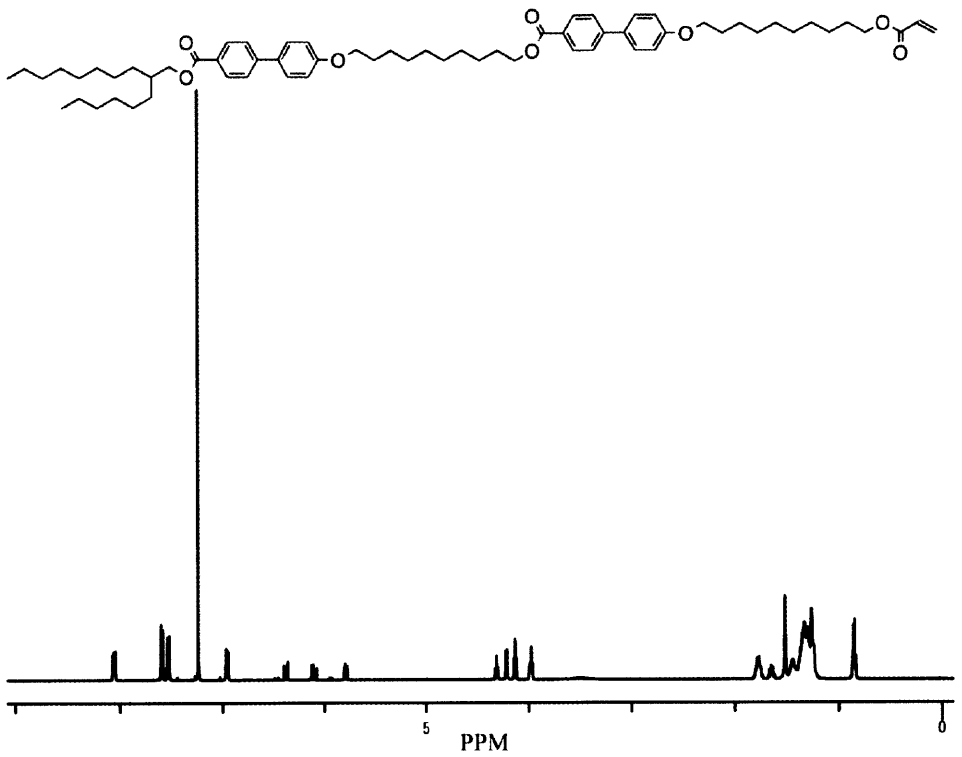

^{1}H-NMR spectrum ($CDCl_3$) of Monomer **2**

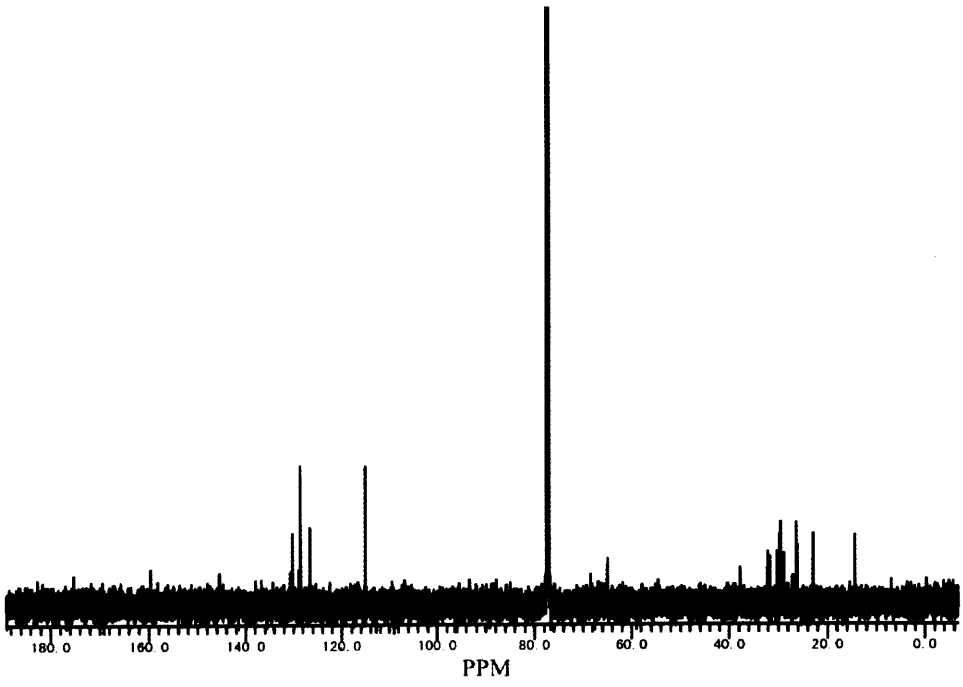

^{13}C-NMR spectrum ($CDCl_3$) of Monomer **2**

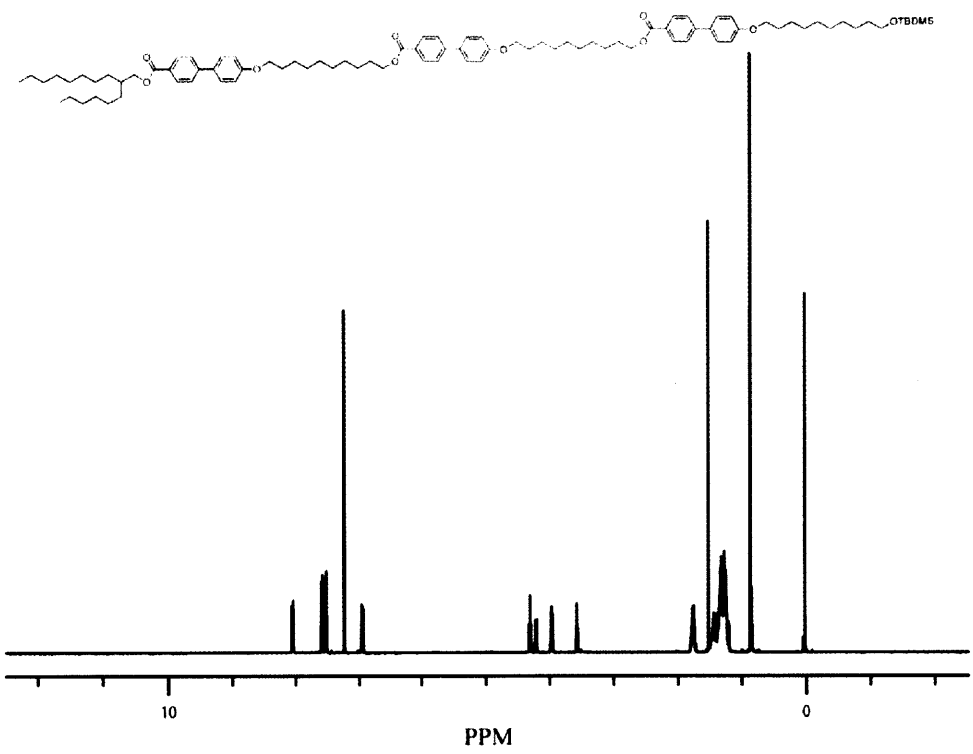

^{1}H-NMR spectrum ($CDCl_3$) of **12**

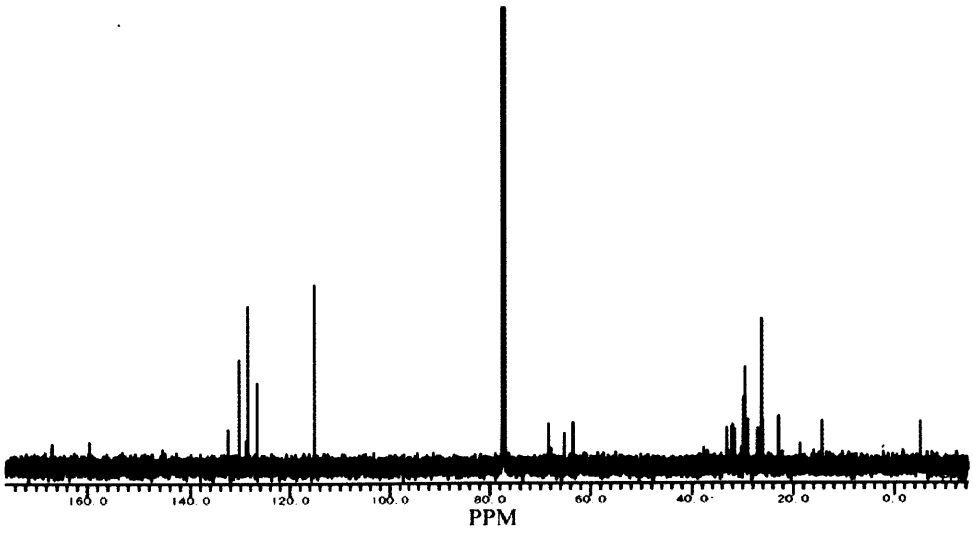

^{13}C-NMR spectrum ($CDCl_3$) of **12**

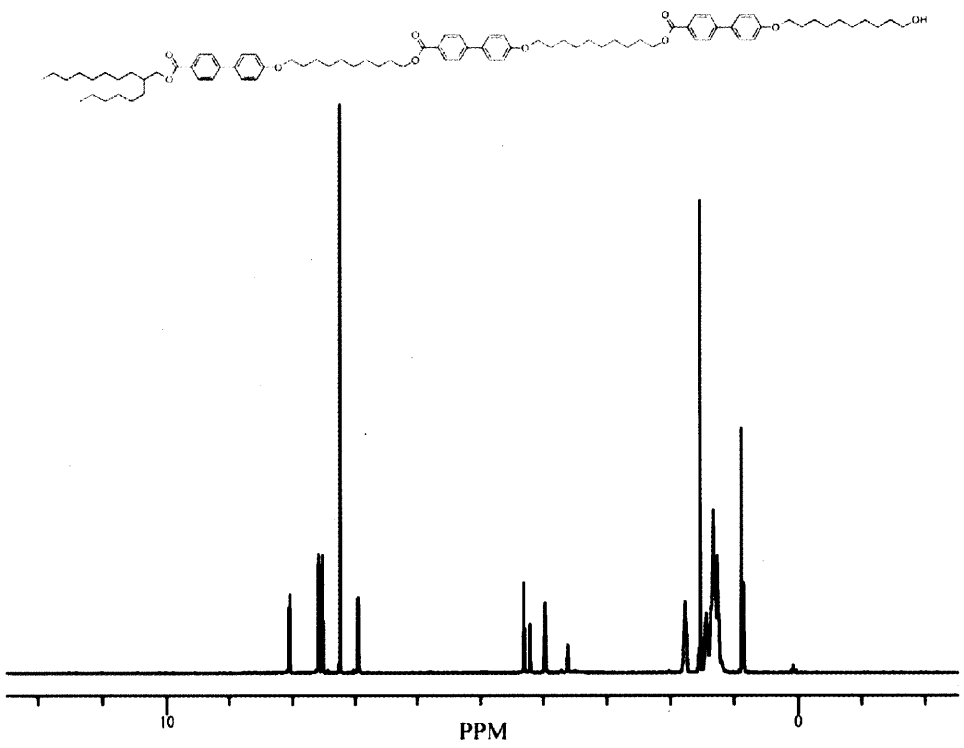

^{1}H-NMR spectrum ($CDCl_3$) of **13**

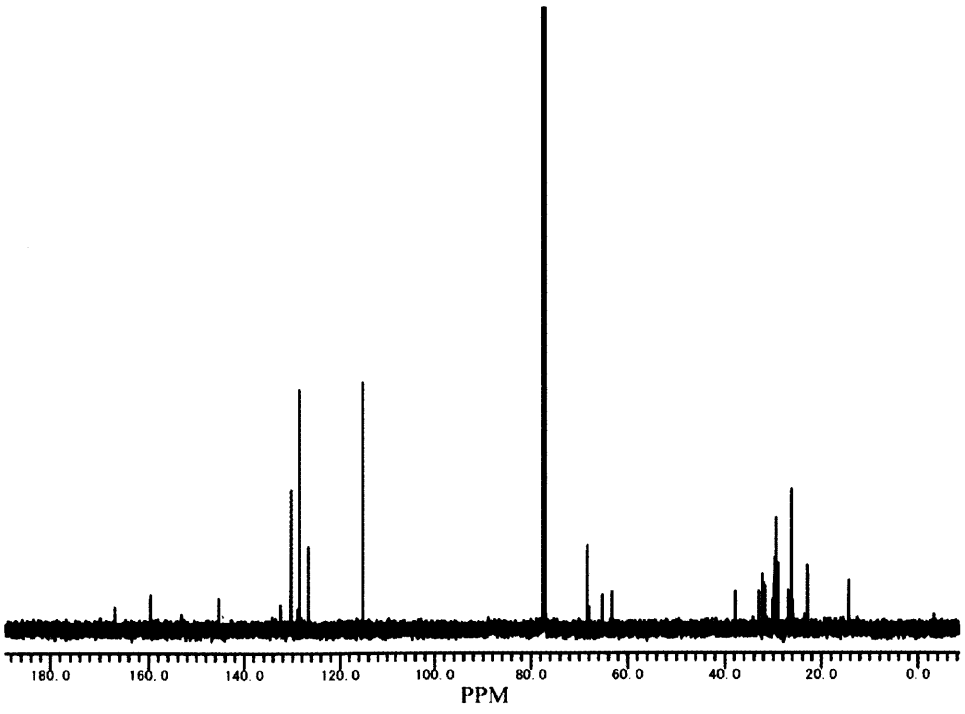

^{13}C-NMR spectrum ($CDCl_3$) of **13**

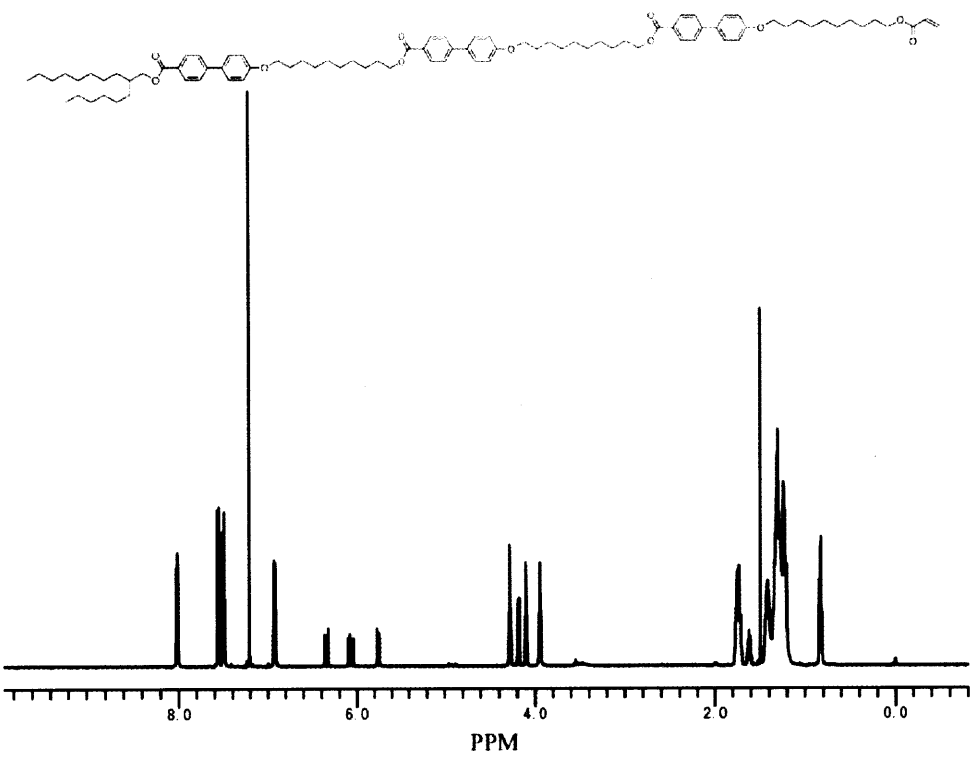

^{1}H-NMR spectrum ($CDCl_3$) of Monomer **3**

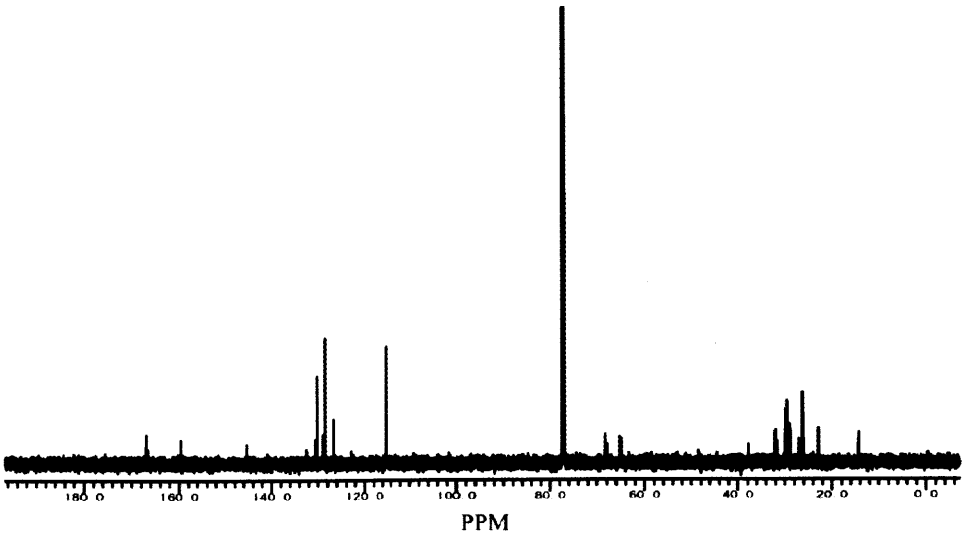

^{13}C-NMR spectrum ($CDCl_3$) of Monomer **3**

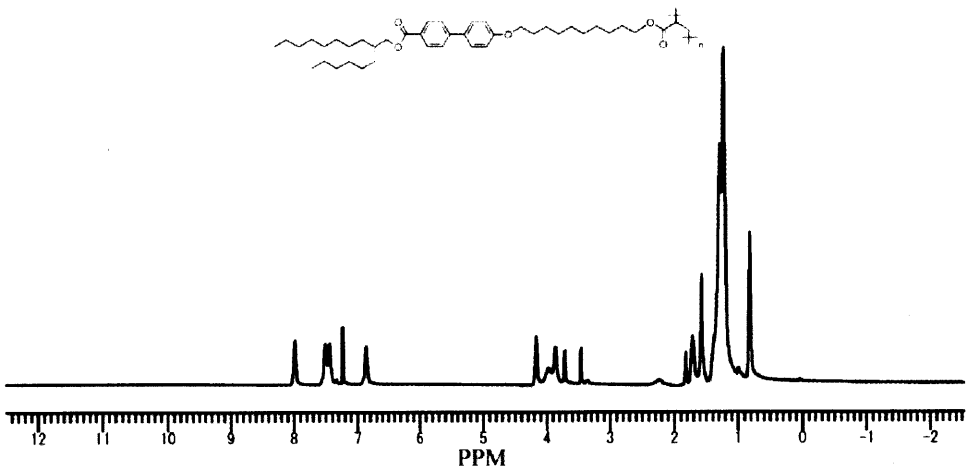

^{1}H-NMR spectrum ($CDCl_3$) of **P1**

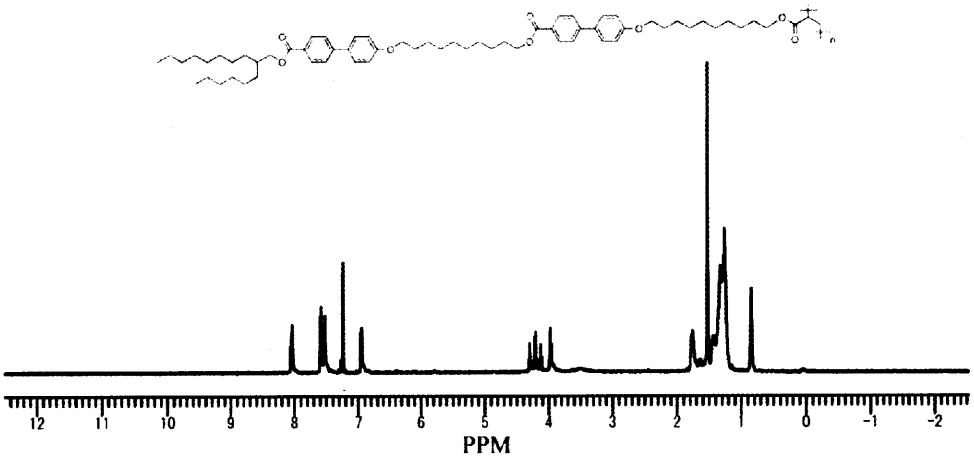

^{1}H-NMR spectrum ($CDCl_3$) of **P2**

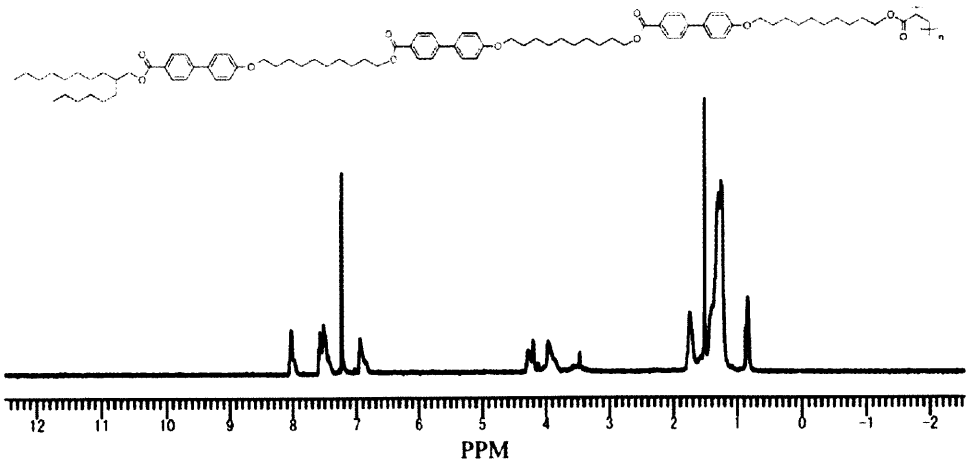

^{1}H-NMR spectrum ($CDCl_3$) of **P3**

CURRICULUM VITAE
JOSE M. LOBEZ

Education

08.2007–04.2012 **MASSACHUSETTS INSTITUTE OF TECHNOLOGY (MIT)** **USA**
Ph.D. in Chemistry
Research Advisor: Timothy M. Swager

07.2003–09.2006 **UNIVERSIDAD DE ZARAGOZA** **Spain**
Postgraduate Degree on Computer and Communication Tools

09.2001–09.2006 **UNIVERSIDAD DE ZARAGOZA** **Spain / Germany**
Lic. (MS/BS) in Chemistry. Premio Extraordinario / Premio Nacional – Mencion Especial
Erasmus at the Universität Bayreuth
Research Advisor: Günter Lattermann

Experience

08.2007–present **MASSACHUSETTS INSTITUTE OF TECHNOLOGY (MIT)** **USA**
Research Assistant (Swager Lab)
- Designed, synthesized and applied polymers for sensing, smart materials, solar cell and lithography applications
- Gained extensive experience in multi-step synthesis of small molecules and polymers, characterized polymeric materials by amperometry, mechanical testing, fluorescence spectroscopy, UV-Vis, FT-IR, NMR, Raman, 4-point probe, SEC/GPC, DSC, TGA-MS, profilometry, DLS, AFM, SEM, TEM, EDX, XPS, polarized optical microscopy

Teaching Assistant
- Organized and taught 2 recitations of 15 students and a lab of 40 students

Editorial Collaborator
- Independently reviewed papers for the journal Macromolecules
- Analyzed the impact papers to be highlighted in the journal Synfacts

Mediation Program (ChemREFS)
- Mediated between different parties in conflict within the Department of Chemistry (MIT)
- Confidentially counseled students, post-docs and staff in conflict or under high-stress

06.2011–09.2011 **UNIVERSITY OF TOKYO (東大) / RIKEN** **Japan**
Visiting Scholar (Aida Lab)
- Coordinated and oversaw research team efforts and developed new project directions
- Received an International Leadership Award (Friends of Todai) for fostering international collaboration

01.2007–08.2007 **QUEEN'S UNIVERSITY** **Canada**
Research Assistant (Crudden Lab) / Teaching Assistant
- Developed mesoporous silica and fiber optics detectors for heavy metals
- Organized and taught a course of 20 students

01.2006–09.2006 **UNIVERSITÄT BAYREUTH** **Germany**
Research Assistant (MCI Lab)
- Created magnetic hydrogel polymers for anti-cancer treatments

06.2005–09.2005 **BAYER AG** **Germany**
Intern (Bayer CropScience)
- Synthesized, characterized new insecticides based on heterocycles

06.2004–09.2004 **BASF AG** **Germany**
Intern (Fine Chemistry Research Department)
- Completed an individual project on polymers for cosmetics

Publications

PATENTS

1) Swager T. M., **Lobez J. M.**, Wang, F. "Compositions, Methods, and Systems Comprising Poly(Thiophenes)" U.S. Pat. Apl. Serial No. 61/387,851
2) Swager T. M., **Lobez J. M.** "Method and apparatus for determining radiation" Intl. Pat. No.: WO2011/044221

PEER-REVIEWED PUBLICATIONS

1) Takeda, Y., Andrew, T., **Lobez J. M.**, Mork, J. A., Swager T. M. "An Air-Stable Low-Bandgap n-Type Organic Polymer Semiconductor with Selective Solubility in Fluorous Solvents", *manuscript in preparation*
2) **Lobez J. M.**, Andrew, T. L., Bulovic, V., Swager T. M. "Side-Chain Functionalized Polythiophene Additives for Improved Efficiency in Bulk Heterojunction Solar Cells", ACS Nano 2012, *DOI: 10.1021/nn204589u* Highlighted on C&EN, Mar. 8, 2012
3) Cheong L. L., **Lobez J. M.**, Moon E. E., Hastings J. T., Smith H. I. "Secondary-Electron Signal Level Measurements of Self-Assembled Monolayers for Spatial-Phase-Locked Electron-Beam Lithography", J. Vac. Sci. B, 2011, 29, 06F308
4) **Lobez J. M.**, Swager T. M. "Smart Elastomers: Poly (Olefin Sulfone) – Silicone Composites with Switchable Mechanical Properties", Macromolecules, 2010, 43, 10422-10426
5) **Lobez J. M.**, Swager T. M. "Radiation Detection: Resistivity Responses in Functional Poly(Olefin Sulfone)/Carbon Nanotube Composites" Angew. Chem. Int. Ed. 2010, 49, 95-98 Highlighted as Hot Paper in Angewandte Chemie. Highlighted on C&EN, 87(50), Dec. 14, 2009
6) Du J., Cipot-Wechsler J., **Lobez J. M.**, Loock H.-P., Crudden C. M. "Periodic Mesoporous Organosilica Films: Key Components of Fiber Optic-Based Heavy Metal Sensors" Small, 2010, 6, 1168-1172

Presentations at International Conferences

1) **Nihon Kagakkai** (Oral Presentation) Lobez, J. M., Swager, T. M. " Efficiency Improvement of Organic Bulk Heterojunction Solar Cells by Functionalized Polythiophene Additives"
2) **MRS Fall Meeting 2011** (Poster) Lobez, J. M., Swager, T. M. "Efficiency Improvement of Organic Bulk Heterojunction Solar Cells by Functionalized Polythiophene Additives"
3) **ACS Fall National Meeting 2011** (Invited Lecture, Student Award Symposium) Lobez, J. M., Swager, T. M. "Side-Chain Azide-Functionalized Poly (Olefin Sulfone)s for Recyclable Materials and Radiation Sensing"
4) **MRS Fall Meeting 2010** (Poster) Lobez, J. M., Swager, T. M. "Carbon-based Composites for Sensing Applications"
5) **ACS Fall National Meeting 2010** (Oral Presentation) Lobez, J. M., Swager, T. M. "Functional Polymeric Blends for Sensing Applications"
6) **Canadian Society for Chemistry 2010** (Oral Presentation) Lobez, J. M., Swager, T. M. "Polymer/Carbon nanotubes sensors for ionizing radiation detection"
7) **Functional π-Electron Systems 9, 2010** (Poster) Lobez, J. M., Swager, T. M. "Polymer/Carbon nanotubes sensors for ionizing radiation detection"
8) **ACS Spring National Meeting, 2010** (Oral Presentation) Lobez, J. M., Swager, T. M. "Polymer/Carbon nanotubes sensors for ionizing radiation detection"

Awards and Honors

- 2012 MIT Polymer Day Poster Award
- 2012 MISTI China (CETI) International Program Fellow
- 2012 MISTI 2.0 International Program Fellow
- 2011 International Leadership Award, Friends of Todai
- 2011 AkzoNobel Polymer Student Award selected
- 2011 MISTI Japan International Program Fellow
- 2010 Morse grant, MIT Department of Chemistry
- 2007 Student Award for Best Poster at Materials and Nanotechnology Symposium
- 2006-2009 "La Caixa" Fellowship for International Post-graduate studies
- 2006 Spain National Award for top student in Chemistry Studies (class of 2006) Special Mention.
- 2006 Extraordinary Award for top student in University Science Studies (class of 2006)

Languages

English (Fluent), **Spanish** (Native Speaker), **German** (Fluent), **Japanese** (Intermediate)

ACKNOWLEDGEMENTS

First of all I must thank my thesis advisor, *Prof. Tim Swager*. You have not only been a magnificent mentor and teacher these past years, but also a role model, both scientifically and personally. I have been very lucky to work for you as a graduate student: you have allowed me to work on cutting-edge and really interesting projects that have opened my eyes to many different facets of science. You have also provided room for my independence to grow, pursuing my own goals and ideas both in and outside of chemistry. There are certainly not many environments where I would have been able to accomplish everything I have, and only somebody as brilliant and unique as you could have provided this. Thank you for everything.

I would also like to thank my thesis committee, *Prof. Steve Buchwald* and *Prof. Paula Hammond*: your advice and direction has been extremely helpful, both for my graduate and professional careers. *Prof. Vladimir Bulovic* also deserves special mention for all his help and guidance in the later stages of my PhD. *Prof. Takuzo Aida* at the university of Tokyo/RIKEN was my temporary advisor for a brief period of time. I would like to thank him for being so welcoming and making a research stay in his group possible. This experience changed me forever, as well as the way I see science and the world as whole.

MIT is an amazing place and the institute has been incredibly good to me. I have been able to do things I could have only dreamed of, and to meet some of the most important people of my life. These last years have been very intense, both scientifically and emotionally, and I could not have made it this far without a wonderful network of friends who have always been there to support me and to cheer for me, both in the good and in the less good times:

Prof. Trisha Andrew, so many things to thank you for: I could not have dreamt of a more generous, better friend and collaborator. Your dedication and hard work have been a constant source of admiration and inspiration to me, and a big part of this thesis would not have been possible without your help and advice. I have shared many wonderful experiences, trips and eureka moments with you. You are the smartest person I have ever met. Dream big and fly high, and try to find out whether they have Cold Stone in Stockholm.

Rebecca Parkhurst, I will always remember the popcorn, cheese and many coffees shared over laughter and tears. You are one of the most special people I have ever met, and will always remain my best friend at MIT. Our friendship started over a beer in Cambridge and will continue over dog breakfast in the streets of Asia. You opened the doors of your home to me, which has provided many precious moments that I will always keep in my memory. Even though I have never been able to remember the exact date of your birthday, I will fondly remember the holidays and evenings spent with your family. It is hard for me to imagine a work place where I cannot walk up to your desk to tell you about the latest developments in my life. Also, with whom am I going to argue in the future?

The always cheerful and smiling *Olesya Haze*: thank you for all the support, good times, and good hot pot. Having you in lab has been a privilege. In the future. I will think back on us sitting on the grass, watching happy horses chase each other around.

Susan Zultanski, thank you for being my cigar bar companion, weekend girlfriend replacement and German noise music co-groupie. I have thoroughly enjoyed talking with you about chemistry, the future, the republican primaries and Myanmar. See you in LA really soon.

Daniel Suess, thank you for being there to support me in many aspects of my life (RuPaul, Lady GaGa and gambling related). I wish you could have been there for the whole duration of my PhD!

Herr Jan Schnorr, vielen dank für deine Hilfe, nicht nur als Freund aber auch als Deutsch Lehrer! Es hat ganz viel Spass gemacht, mit dir zusammen zu arbeiten, und in dem selben Büro zu sein. Hoffentlich können wir irgendwann, irgendwo wider zusammenzuarbeiten.

The whole Swager lab (both past generations and its current members), but particularly *Caitlin McDowell* (thank you for being so awesome at your job! I will be waiting to read your papers soon) *Kathy Sweeney*, *Julian Chan*, *Shuang Liu*, *Brett VanVeller*, *Joel Batson*, *Barney Walker*, my office-mates: *Jeewoo Lim*, *Duncan den Boer*, *Yi Wei*, *Kelvin Frazier*, the Spanish mafia *Carlos Cordovilla* and *Balta Bonillo*.

Some of my MIT friends outside from lab who helped me with my science and with life in general, mainly over Starbucks coffees include *Nicole Davis*, *Julia Kohzhuk* and *Charlene Tsay*.

My collaborators at the Computer Science and Electrical Engineering Department in the Smith Lab at MIT: *LinLee Cheong* and *Euclid Moon*, with whom I had much fun talking about different fields of science and engineering. Thanks for the opportunity to learn a great deal about lithography and nanofabrication techniques.

During the last part of my PhD I had the privilege of spending some time doing research in Japan, and for that I must thank the MISTI crew which made the funding for this stay possible, particularly *Michelle Kern* as well as everybody at Friends of Todai (FOTI). I count the time I spent in Japan among the happiest I have had in my life and that was possible thanks to:

SwagerLab のメンバー: *Yumiko* 様, *Shoji* 君, *Fumi* 先生, *Yohei* 先生, *Daisuke* 様, *Eiji* 様, Hitoshi 様, 本当にお世話になりました！いつも日本語やまんがや日本の文化について教えってくださって、ありがとうございました！楽しかったです！

My dear friends with whom I shared many fun and ridiculous moments, as well as delicious しあぶしあぶとまぐろ中落ち：*Yuki Hori*, *Sarah Abraham*, *Shoko Takemoto*. I would also like to thank my Fuji-san climbing companion *Megan Brewster*.

I must thank everybody at RIKEN who helped me one way or another during my stay, particularly my direct supervisors *Fukushima* 先生 and *Kajitani* さん, and also *Chan* 先生, *Kosaka* さん, *Bruce* and *Joon* 様.

Prior to my time at MIT I had the chance to work for some wonderful scientists who expanded my scientific horizons and helped me get to where I am today. I would like to thank particularly *Prof. Günter Lattermann*, for whom I worked as an undergrad at the University of Bayreuth, and *Prof. Cathleen Crudden*, who generously opened the doors of her group and Canada to me. These and my prior experiences in industry started my interest in materials and polymer chemistry.

I have been lucky enough to be able to experience many wonderful moments in the past years not only in Boston but also in New York City and its surroundings, in great part thanks to *Juan Ley* and *Ryan McGlone*. Thank you for always being there for me, being extremely fun, offering wise advice and bearing with my problems. You are just incredible and I could not have asked for better friends.

I really need to thank obra social de "*LaCaixa*", which generously awarded me with one of their postgraduate fellowships to fund the beginning of my PhD at MIT. With the aid of *LaCaixa* I was not only able to embark on my journey at MIT, but I also had the opportunity to meet some of my dearest friends, role models, and the king of Spain. For this, I will always be grateful.

Por supuesto tampoco hubiera llegado hasta aquí sin el apoyo incondicional de mi familia. He tenido la suerte de tener unos padres maravillosos, que siempre me han dado todas las oportunidades a su alcance y mas allá, y respetado por lo que soy. Mis hermanos *Victor* y *David*, así como *Ciarica* también han estado siempre disponibles para ayudarme, a veces en la distancia, y muchas otras en mi presencia, corriendo cual Ninja o quemando la tarjeta de crédito - gracias por vuestras repetidas visitas. También querría agradecerles a mis primos *Jorge* y *Paula*, y a *Virginia*, los momentos tan divertidos que hemos compartido mayormente en bodas, comuniones y otras celebraciones. Mis tíos favoritos, *Carmen* y *Pachi*, también me han ayudado en incontables ocasiones a lo largo del camino que me ha llevado hasta este momento de mi vida. Soy la persona que soy y estoy orgulloso de ello en gran parte por vuestro ejemplo, ayuda y consejo. Siempre os he considerado como un modelo a imitar.

Por ultimo me gustaría darle las gracias a *Rodrigo*. Me resulta imposible imaginar cuan diferente hubiera sido mi vida si no te hubiera conocido en aquel frío verano de aire acondicionado de Indiana. Durante estos años contigo he aprendido, crecido, cambiado, evolucionado y mejorado, todo ello gracias a tu ayuda. Me has completado, equilibrado, escuchado cuando lo he necesitado, y siempre ofrecido sabio consejo. No creo que hubiera podido superar estos últimos años sin ti a mi lado; finalizar este doctorado ha sido posible en gran parte gracias a ti. Tanto en los momentos buenos y en los malos, siempre he mejorado a raíz de las experiencias que he compartido contigo, y por eso siempre te querré y estaré agradecido.